NANOCOMPOSITES AS ELECTROCATALYSTS FOR THE USE IN FUEL CELL AND ELECTROLYZER REACTIONS

Léonard Jean Moriau

Doctoral Dissertation
Jožef Stefan International Postgraduate School
Ljubljana, Slovenia

Supervisor: Prof. Nejc Hodnik
Department of Materials Chemistry, National Institute of Chemistry, Ljubljana, Slovenia
Jožef Stefan International Postgraduate School, Ljubljana 1000, Slovenia

Evaluation Board:
Prof. Goran Dražič, Chair, Jožef Stefan International Postgraduate School, Ljubljana, Slovenia
Prof. Tom Breugelmans, Member, University of Antwerp, Antwerpen, Belgium
Dr. Marjan Bele, Member, National Institute of Chemistry, Ljubljana, Slovenia

MEDNARODNA PODIPLOMSKA ŠOLA JOŽEFA STEFANA
JOŽEF STEFAN INTERNATIONAL POSTGRADUATE SCHOOL

Léonard Jean Moriau

NANOCOMPOSITES AS ELECTROCATALYSTS FOR THE USE IN FUEL CELL AND ELECTROLYZER REACTIONS

Doctoral Dissertation

NANOKOMPOZITI KOT ELEKTROKATALIZATORJI ZA UPORABO V REAKCIJAH V GORIVNI CELICI IN ELEKTROLIZATORJU

Doktorska disertacija

Supervisor: Assoc. Prof. Dr. Nejc Hodnik

Ljubljana, Slovenia, January 2023

"You can never know everything, and part of what you know is always wrong. Perhaps even the most important part. A portion of wisdom lies in knowing that. A portion of courage lies in going on anyway."
Robert Jordan, Winter's Heart.

Acknowledgments

First and foremost, I would like to thank Petra and Janez Matos who hosted me the first time I visited Slovenia as a volunteer. Without them, I would not have had the opportunity to visit the National Institute of Chemistry where I conducted the work presented below and meet my future colleagues.

Following up, I would like to thank Dr. Marjan Bele for hosting me during this particular first visit and for the collaborations during my Ph.D. His enthusiasm for science is very communicable and a source of motivation when you feel down while his prolific synthesis was the starting point of many studies, projects or scientific discussions.

Of course, I am thankful to my supervisor Prof. Nejc Hodnik who accepted me as a Ph.D. student. The "guided" freedom he gave to me had allowed me to explore diverse materials and reactions but also to focus on my own scientific interests. He also always made himself available from when we were 5 in the group to more than twenty in the newly formed Electrocat laboratory.

Additionally, I kindly thank the members of the commission for the evaluation of my work and for the time they dedicated to it.

I am also grateful to all my colleagues from D-13 and D-10, and especially to my office mate, for the friendly work environment and the insightful discussions, scientific or not. The same is true for all the people I had the pleasure of collaborating with. To name a few, I would like to thank Dr. Primož Jovanovič for the great articles' correction and general advice on how to write scientific publications, Dr. Matija Gatalo who is a great friend and is always ready to start and push new projects and collaboration. His dedication to work was inspirational and this work would not be the same without him. Additionally, I wish to extend my sincere thanks to Dr. Martin Šala, Dr. Francisco Ruiz-Zepeda and all the people from HI-ERN in Germany (where I went as a visiting Ph.D. student) for sharing their knowledge and specific techniques. A special thanks goes to Ivana Maver, who took care of all the administration which helped me focus on science, and to Urška Kavčič, who was always available to help with any issues in the lab.

Furthermore, I would like to express my gratitude to my family and friends for their unconditional support. I am also thankful to my girlfriend Sorour, who pushed me to finish this dissertation when I was getting distracted by too many side projects and articles.

Finally, I would like to thank all the people that participated in this work, directly or indirectly, and that I might have forgotten to mention.

Abstract

Electrochemical energy conversion devices such as fuel cells (FCs) and water electrolyzers (WE) have attracted attention from the scientific community for their unique ability to store electrical energy in the form of hydrogen and then generate electricity by the reverse process. Unfortunately, those devices rely on a significant amount of precious platinum group metals (PGMs) – rare and expensive raw materials – to catalyze the reactions involved, i.e. platinum-based catalysts for oxygen reduction reaction (ORR) and hydrogen oxidation reaction (HOR) in proton exchange membrane (PEM) FCs and iridium for oxygen evolution reaction (OER) on one side of WE and Pt for hydrogen evolution reaction (HER) on the other side. The high prices and scarcity of materials are a bottleneck for the widespread application of those technologies and slowing down the transition to clean energy. Therefore, reducing the cost and consumption of PGMs while keeping the same performances (activity and stability) is of primordial importance. Several strategies have been commonly used to optimize the utilization of PGMs, like the deposition of precious metals as nanoparticles on high surface area support or alloying with less noble metals. In the case of PEMFC (ORR and HOR), these methods have been proven effective and Pt-M (M: Co, Cu, Ni or Fe) supported on carbon black is becoming the state-of-the-art catalyst. Nonetheless, no suitable support has been widely accepted as the state-of-the-art support for OER catalysts in acidic media as carbon cannot be used in the highly oxidative environment of OER where it oxidizes to CO_2. Moreover, alloying Ir with some less-noble metals leads to heavy leaching during OER and poisoning in the WE. Therefore, a conductive, high surface area and stable support still needs to be found. Another possibility to decrease the overall price of these technologies is by combining them into one unitized regenerative fuel cell (URFC) able to perform as FC when electric energy is needed and as WE when a surplus of energy is available. In this device, one catalyst should be able to perform both HOR and HER, i.e. an ultra-low amount of Pt supported on carbon. On the other side, for ORR and OER, the current state-of-the-art bifunctional catalyst is a physical mixture of unsupported Pt and Ir powders. The former one is currently not suitable for large-scale production as it still requires significant amounts of PGMs. Nonetheless, Pt/Ir nanoparticles deposited on appropriate support, able to withstand OER conditions, would ideally allow a decrease in the price of the technology while keeping the same performances. Hereby, we investigate possible support for OER and bifunctional catalysts. The material chosen as potential support was titanium oxynitride ($TiON_x$). TiO_2 is stable under OER conditions but not conductive while TiN is conductive but not as stable. Therefore, $TiON_x$ was investigated as it could exhibit the best properties of both. First, this support was studied in combination with Ir nanoparticles for OER. Modification by adding a carbon template was used to additionally increase the surface area of the catalyst. Finally, different metal nanoparticles able to catalyze both ORR and OER catalysts were deposited on our carbon-modified $TiON_x$ and the performance of this bifunctional nanocomposite was investigated. The choice of the compounds for ORR catalyst was made after a careful comparison of different Pt-alloys while Ir + Ru was used for OER.

Povzetek

Naprave za elektrokemično pretvorbo energije, kot so gorivne celice (FC) in vodni elektrolizatorji (WE), so pritegnile pozornost znanstvene skupnosti zaradi svoje edinstvene sposobnosti shranjevanja električne energije v obliki vodika in nato ustvarjanja električne energije z obratnim procesom. Na žalost so te naprave odvisne od znatne količine plemenitih kovin platinske skupine (PGM) – redkih in dragih surovin – za kataliziranje vključenih reakcij, tj. katalizatorjev na osnovi platine za reakcijo redukcije kisika (ORR) in reakcijo oksidacije vodika (HOR) v protonsko izmenjevalno membrano (PEM) FC in iridij za reakcijo sproščanja kisika (OER) na eni strani WE in Pt za reakcijo sproščanja vodika (HER) na drugi strani. Visoke cene in pomanjkanje materialov so ozko grlo za široko uporabo teh tehnologij in upočasnjujejo prehod na čisto energijo. Zato je izrednega pomena zmanjšanje stroškov in porabe PGM ob ohranjanju enakih zmogljivosti, aktivnosti in stabilnosti. Za optimizacijo uporabe PGM se pogosto uporablja več strategij, kot je uporaba nosilca z visoko površino, odlaganje plemenitih kovin kot nanodelcev ali zlitje PGM z manj plemenitimi kovinami. V primeru PEMFC (ORR in HOR) so se te metode izkazale za učinkovite in Pt-M (M je Co, Cu, Ni ali Fe), podprt na sajah, s PtCo postaja najsodobnejši katalizator že v uporabi v avtomobilih. Kljub temu nobena ustrezna podpora ni bila splošno sprejeta kot najsodobnejša podpora za katalizatorje OER v kislih medijih. Dejansko ogljika ni mogoče uporabiti v zelo oksidativnem okolju OER, kjer oksidira v CO_2. Poleg tega zlitje Ir z nekaterimi manj plemenitimi kovinami povzroči močno izpiranje med OER in zastrupitev v WE. Zato je še vedno treba najti prevodno visoko površino in stabilno podporo. Druga možnost za znižanje skupne cene teh tehnologij je njihova združitev v eno enotno regenerativno gorivno celico (URFC), ki lahko deluje kot FC, ko je potrebna električna energija, in kot WE, ko je na voljo presežek energije. V tej napravi bi moral biti en katalizator sposoben izvajati tako HOR kot HER, in sicer katalizator z ultra nizko količino Pt na ogljiku. Po drugi strani pa je za ORR in OER trenutni najsodobnejši bifunkcionalni katalizator fizikalna mešanica nepodprtih Pt in Ir praškov. Prvi trenutno ni primeren za velikoserijsko proizvodnjo, saj še vedno zahteva znatne količine PGM. Kljub temu bi nanodelci Pt/Ir, odloženi na ustrezno podlago, ki lahko prenese pogoje OER, v idealnem primeru omogočili znižanje cene tehnologije ob ohranjanju enakih zmogljivosti. Material, izbran kot potencialna podpora, je bil titanov oksinitrid ($TiON_x$). Dejansko je TiO_2 stabilen v pogojih OER, vendar ni prevoden, medtem ko je TiN prevoden, vendar ni tako stabilen. Zato je bil $TiON_x$ raziskan, saj bi lahko pokazal najboljše lastnosti obeh. Najprej so to podporo proučevali v kombinaciji z Ir nanodelci za OER. Modifikacija z dodajanjem karbonske šablone je bila uporabljena za dodatno povečanje površine katalizatorja. Končno so bili različni kovinski nanodelci, ki lahko katalizirajo katalizatorje ORR in OER, naneseni na naš z ogljikom modificiran $TiON_x$ in raziskana je bila učinkovitost tega bifunkcionalnega nanokompozita. Izbira spojin za katalizator ORR je bila narejena po natančni primerjavi različnih Pt-zlitin, medtem ko je bil Ir + Ru uporabljen za OER.

Contents

List of Figures

List of Tables

Abbreviations

AFCs ... Alkaline Fuel Cells
A1 ... Anodic dissolution peak for Pt
A1' ... Anodic dissolution peak for M in Pt-M/C catalysts
A2' ... Anodic second dissolution peak for M in Pt-M/C catalysts
ADF ... Annular Dark Field
ADT ... Accelerated Degradation Test
ATO ... Antimony doped-Tin Oxide
BET ... Brunauer-Emmett-Teller
BoL ... Beginning of Life
C1 ... Cathodic dissolution peak for Pt
C1' ... Cathodic dissolution peak for M in Pt-M/C catalysts
CA ... ChronoAmperometry
CHNS ... Carbon, Hydrogen, Nitrogen and Sulphur content analysis
CP ... ChronoPotentiometry
CRMs ... Critical Raw Materials
CV ... CycloVoltametry
DOE ... Department Of Energy
EC-MS ... Electrochemical Cell – Mass Spectrometry
ECSA ... Electrochemical Surface Area
EDXS ... Energy Dispersive X-ray Spectroscopy
EELS ... Electron Energy Loss Spectroscopy
EFC ... Electrochemical Flow Cell
EIS ... Electrochemical Impedance Spectroscopy
EMSI ... Electronic Metal-Support Interaction
EoL ... End of Life
FC ... Fuel Cell
FCS ... Fuel Cell Store
FTO ... Fluorine doped-Tin Oxide
GONRs ... Graphene Oxide NanoRibbons
HER ... Hydrogen Evolution Reaction
HOR ... Hydrogen Oxidation Reaction
H_{upd} ... Hydrogen underpotential deposition
ICP-MS ... Inductively Coupled Plasma-Mass Spectrometry
ICP-OES ... Inductively Coupled Plasma-Optical Emission Spectrometry
IL-TEM ... Identical Location-Transmission Electron Microscopy
IPA ... Isopropanol
IPCC ... Intergovernmental Panel on Climate Change
ITO ... Indium doped-Tin Oxide
JM ... Johnson Matthey
M ... Transition Metal (Co, Cu, Ni, Fe)
MA ... Mass-normalized Activity

MCFC ... Molten Carbonate Fuel Cell
MQ ... Milli-Q water
MWNTs ... MultiWall NanoTubes
NR ... NanoRibbons
OER ... Oxygen Evolution Reaction
ORR ... Oxygen Reduction Reaction
PAFC ... Phosphoric Acid Fuel Cell
PCA ... Platinum Catalyst Activation
PEEK ... Polyether Ether Ketone
PEMFC ... Proton Exchange Membrane Fuel Cell
PGMs ... Platinum Group Metals
PTFE ... Polytetrafluoroethylene
RDE ... Rotating Disk Electrode
RDS ... Rate Determining Step
rGONRs ... Reduced Graphene Oxide NanoRibbons
RHE ... Reversible Hydrogen Electrode
Rpm ... Rotation per minute
RT ... Room Temperature
SA ... Specific surface area-normalized Activity
SEM ... Scanning Electron Microscopy
SMSI ... Strong Metal-Support Interaction
SOFC ... Solid Oxide Fuel Cell
STEM ... Scanning Transmission Electron Microscopy
Ta-TO ... Tantalum doped-Tin Oxide
TEM ... Transmission Electron Microscopy
TF-RDE ... Thin Film-Rotating Disk Electrode
TKK ... Tanaka Kikinzoku Kogyo
UPL ... Upper Potential Limit
URFC ... Unitized reversible Fuel Cell
V_{RHE} ... Potential against the reversible hydrogen electrode
WE ... Water Electrolyzer
XPS ... X-Ray Photoelectron Spectroscopy
XRD ... X-Ray Diffraction

Chapter 1

Introduction

1.1 Hydrogen Cycle

In the last few years, the effects of global warming have become more visible as the number of natural disasters has increased all over the world[1]. These events, not only more frequent but also more intense (fires, storms, floods, droughts, etc.), are due to the steep increase of CO_2 emissions in the last 70 years (Figure 1.1a)[2]. On the 9th of August 2021, the intergovernmental panel on climate change (IPCC) released the first report of the 6th assessment on global warming where the experts highlighted the rapid evolution of our climate due to human influence and the urge to tackle the incoming/present crisis by reducing the emission of greenhouse gases[3]. At the same time, the overall worldwide energy demand is expected to rise, and thus new, greener, efficient sources of energy are needed more than ever[4, 5].

The main three energy demanding sectors are industry, residential/commercial powering (e.g. housing, heating and cooling) and transport[6]. While the first two can in principle be sustained by renewable stationary stations, transport needs a mobile energy carrier. Therefore, conversion and storage processes need to be developed alongside the worldwide establishment of sustainable energy technologies. Unfortunately, renewable energy sources with the most extension potential, i.e. wind and solar, have major drawbacks. Indeed, such supplies of energy vary in the amount of electricity produced and obey to some cycle (e.g. day/night, summer/winter cycles for solar power, Figure 1.1b)[7]. Thus, an efficient energy conversion process would not only benefit the transport sector but also make intermittent renewable energy sources like wind and solar more reliable and ease their implementation.

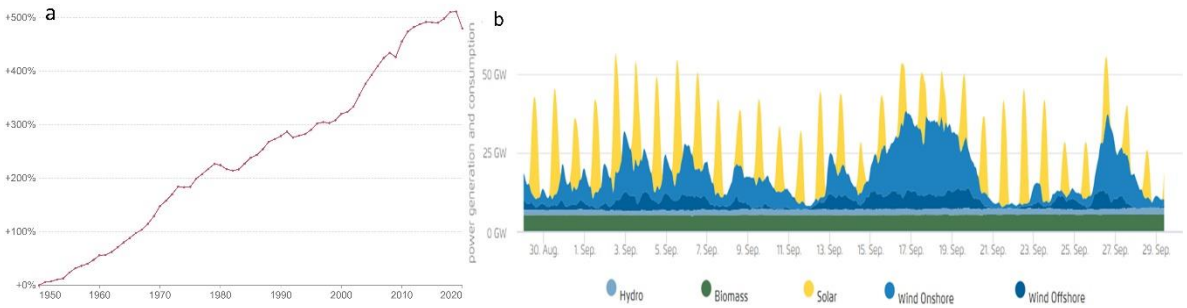

Figure 1.1: a) Augmentation of annual CO_2 emission since 1950[2]. b) Energy production from renewable sources in Germany during September 2022[7].

Hydrogen is particularly interesting as an energy carrier as it possesses the highest weight-specific energy density (142 MJ/kg)[8]. Currently, almost all of the hydrogen is produced via steam reforming of fossil fuels, producing CO and CO_2 in addition to H_2 and is therefore not a green process (called gray hydrogen)[9, 10]. If hydrogen is to be used as a green energy carrier, a cheap, competitive, and sustainable production of hydrogen needs to be implemented (Figure 2a)[11]. A promising green technique to produce hydrogen is the electrochemical splitting of water to its prime compounds, hydrogen and oxygen (oxygen evolution reaction, OER), in a water electrolyzer (WE)[12, 13]. The only requirement is to provide energy from renewable sources in a form of electricity and water. It has the advantage to produce purer H_2 compared to steam reforming where CO contamination is an issue[14]. Moreover, H_2 and O_2 can then be combined again (oxygen reduction reaction, ORR) in a proton exchange membrane fuel cell (PEMFC) which will produce energy and have only water and some heat as a side product[13]. These two reactions formed the so-called hydrogen cycle, which is the base of a hydrogen economy[15].

In the case where the energy supply to break down water comes from renewables, the hydrogen cycle is a perfectly green process as there are no pollutants and the only product/reagent besides electrons are water and heat, which can also be used. In this case, hydrogen becomes the perfect green energy carrier for the transition from fossil fuel-based energy society (Figure 1.2b).

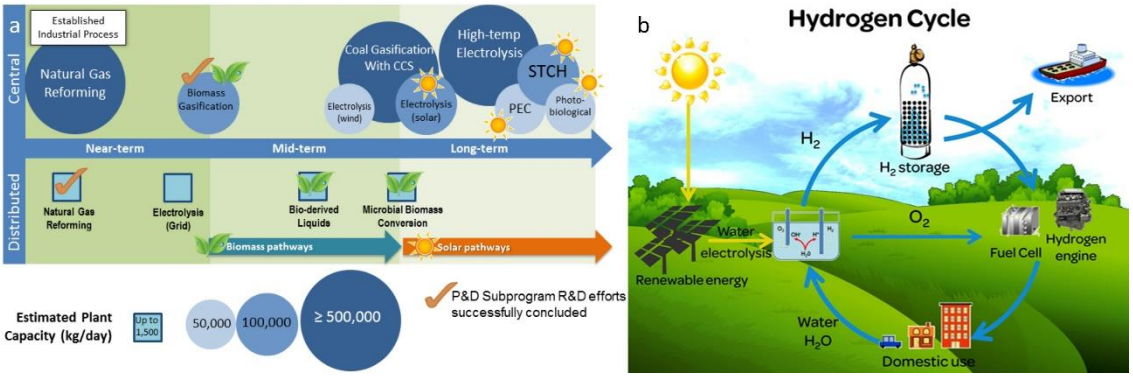

Figure 1.2: a) Objective of the U.S. Department of Energy in terms of hydrogen production[11]. b) Schematic of the hydrogen cycle economy[16].

The overall reaction of the hydrogen cycle can be written as (Eq. 1).

$$O_2 + 2\ H_2 \rightleftharpoons 2\ H_2O + \text{energy} \qquad E = 1.23\ V_{RHE} \quad (1)$$

The thermodynamic/equilibrium cell potential (E) of this reaction is 1.23 V_{RHE}. In practice, an overpotential is observed for every electrochemical reaction. It means that additional energy needs to be applied to run the reactions due to the sluggish kinetics[17] and the binding strength (free energy of adsorption) of the intermediates[18, 19]. Therefore, the OER occurs at a more positive potential than 1.23 V_{RHE} (around 1.5 – 1.7 V_{RHE}) while the ORR is happening at a more negative potential (0.9 - 0.6 V_{RHE}). Catalysts are required to limit the overpotentials and be as energy efficient as possible[13]. The best ones currently known are based on precious and rare platinum group metals (PGMs) which present an important cost and supply bottleneck in the production of WE and FC. Due to their scarcity and usefulness the European Union declared the PGMs as critical raw materials (CRMs)[20]. Therefore, their usage must be optimized or even omitted if possible. The detailed reaction and state-of-the-art of these devices, their catalysts, and the different options to efficiently increase the PGMs utilization are presented below.

1.1.1 Fuel cell

A fuel cell is a device able to combine hydrogen and oxygen gas to produce electricity. It is composed of two electrodes (anode and cathode) which are separated by an electrolyte. Specific ions can be transferred through the electrolyte/membrane from one electrode to the other. Several technologies exist and they are differentiated by the electrolyte pH, ions travelling from one electrode to the other, and operating temperatures[21, 22]. Namely, alkaline fuel cells (AFCs) and (usually) molten carbonate fuel cell (MCFC) have a high pH electrolyte while proton exchange membrane fuel cells (PEMFCs) and phosphoric acid fuel cell (PAFC) have an acidic electrolyte but operate at various temperatures (Figure 1.3). In solid oxide fuel cell (SOFC), O2- ion is passing through a solid electrolyte (ceramic). They operate at the highest temperature among all the fuel cells.

Alkaline fuel cells have several advantages over their acidic counterpart[23]. They use cheap and abundant materials as catalysts which drastically decreases the production cost[24]. They have high energy efficiency (electricity produced/hydrogen consumed) and can be operated at low (ambient) temperatures. However, due to the problem of electrolyte poisoning by CO_2 (formation of CO_3^-), high maintenance cost, high risk operation (crossover of H_2 and O_2), and stability issues, the acidic devices are seen as more promising and thus they are the state-of-the-art FC[23, 25].

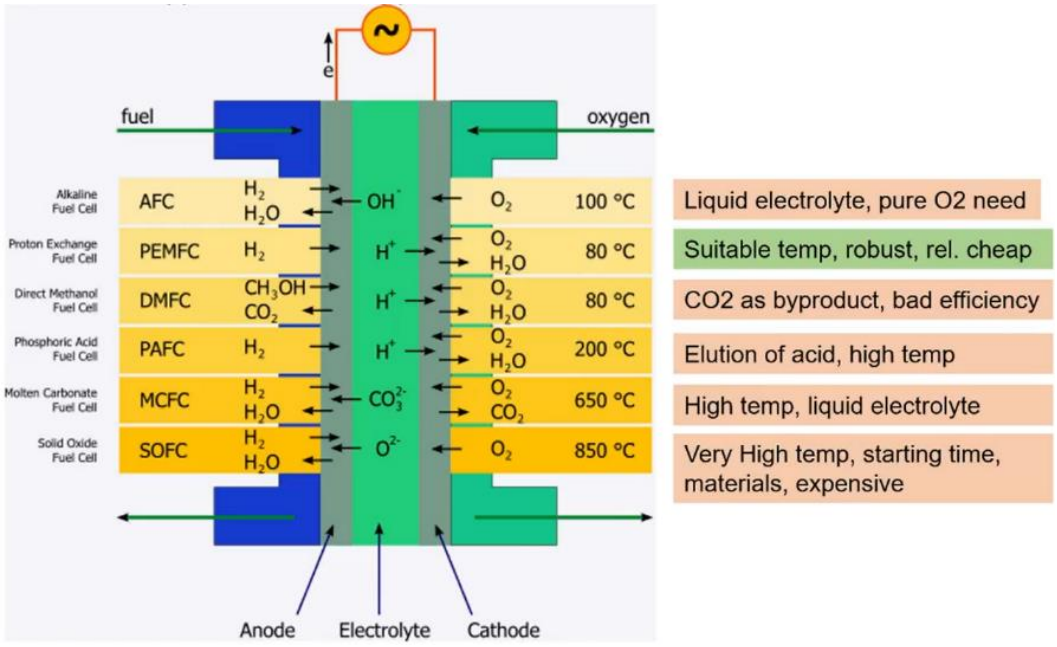

Figure 1.3: Schematic of the different type of fuel cells and their basic properties[26].

Among the various fuel cells, PEMFC is the only one that operates with a good efficiency at moderated temperature (around 80°C, while 200°C for PAFC, 600-700°C for MOFC and 500-1000°C for SOFC), which increases the durability of materials and makes them more suitable for transport applications[22]. Moreover, The PEMFC also has a shorter start-up and transient response than the high temperature fuel cells (sec/min vs hours)[27]. Therefore, they became the most studied fuel cell and are the most promising technology using the hydrogen cycle in transport applications[28].

Nonetheless, the principle of operations is similar for all the acidic fuel cells. Hydrogen is split into H^+ (Hydrogen Oxidation Reaction, HOR, Equation 2) on the anode. The protons then travel through the membrane to the cathode side. At this electrode, the

protons are combined with O_2 to produce water (ORR, Equation 3) as schemed in Figure 1.4.

$$2\ H_2 \rightarrow 4\ H^+ + 4\ e^- \qquad E°(H^+/H_2) = 0\ V_{RHE} \quad (2)$$

$$O_2 + 4\ H^+ + 4\ e^- \rightarrow 2\ H_2O \quad E°(O_2/H_2O) = 1.23\ V_{RHE} \quad (3)$$

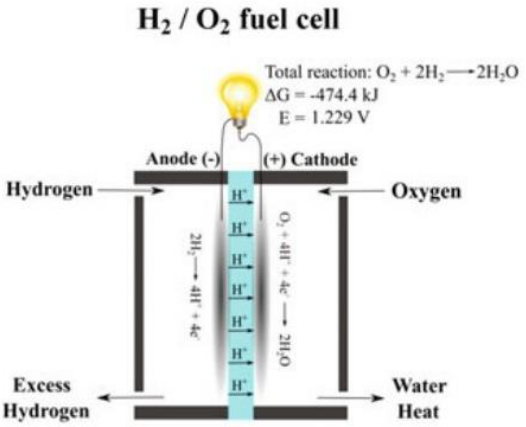

Figure 1.4: Representation of a fuel cell system[12].

In order to improve the kinetics of the reaction, catalysts are used on both electrodes. HOR on the anode is already fast and only a low amount of Pt deposited on carbon is used as catalyst (0.025 mg_{Pt}/cm^2)[29]. On the other side, the ORR exhibits slower kinetics. It is the limiting reaction in the fuel cell and the efficiency of the device depends on the efficiency of this reaction. Currently, the state-of-the-art catalyst is also Pt supported on carbon, but to compensate for low ORR activity, higher loading is needed[30].

The catalysts are evaluated based on the potential needed to reach a certain current density or, oppositely, based on the current density provided at a specific potential. In the case of ORR, the mass- and/or electroactive surface area-normalized current density at 0.9 V_{RHE} is the comparison point[31].

1.1.1.1 Hydrogen oxidation reaction

The hydrogen oxidation reaction generates 2 electrons and implies two elementary steps. Two different pathways are possible, and the mechanism of reaction follows either the Tafel/Volmer or the Heyrovsky/Volmer pathway[32] (Figure 1.5).

General reaction: $H_2 \rightarrow 2\ H^+ + 2\ e^-$ $E = 0\ V_{RHE}$ (4)

First, Hydrogen dissociates via either the Tafel or the Heyrovsky step.
Tafel step (dissociative adsorption of H_2):

$$H_2 + 2* \rightarrow 2\ H^{ads} \quad (5)$$

Where * is a free adsorption site.
Or the Heyrovsky step (dissociation ionization):

$$H_2 \rightarrow H^{ads} + e^- + H^+ \quad (6)$$

And the adsorbed H is then transformed into proton with the loss of an electron in the Volmer step (oxidative desorption):

$$H^{ads} \rightarrow H^+ + e^- \quad (7)$$

For an ideal catalyst, the binding of H^{ads}, H_2 and H^+ is the same. Theoretically, if the binding of H^{ads} is too strong, the Volmer step limits the reaction. On the other hand, if the binding is too weak, the Tafel/Heyrovsky step is the limiting step[12, 33]. According to the latest research, in acidic media with a Pt catalyst, the rate of the hydrogen adsorption and HER reactions is so high that the rate determining step is actually the mass-transport[34]. Only low amounts of Pt are needed (0.025 mg_{Pt}/cm^2)[29] and thus, the anode does not contribute much to the overall price of PEMFC compared to the ORR electrode.

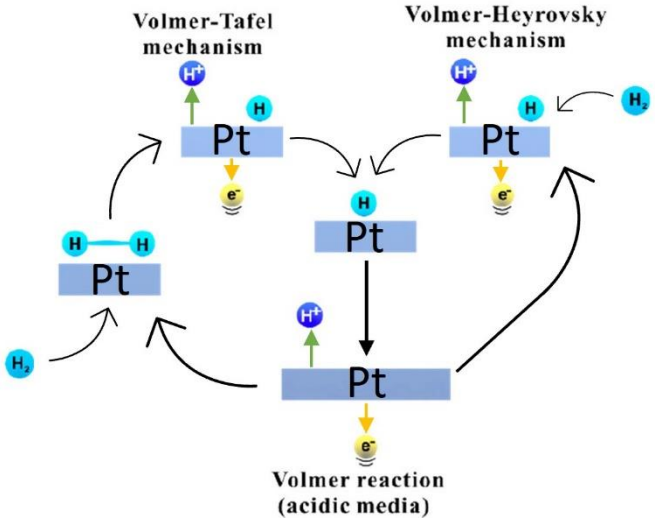

Figure 1.5: Scheme of the proposed HOR mechanisms in acidic medium. Modified from[35].

1.1.1.2 Oxygen reduction reaction

The oxygen reduction reaction is a more complex process that involves multiple steps and the transfer of up to 4 electrons. Wroblowa *et al.* proposed the following mechanism pathways (Figure 1.6)[36].

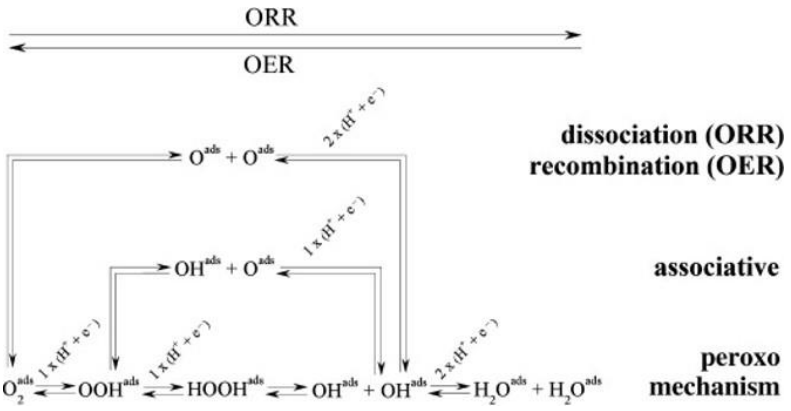

Figure 1.6: Scheme of the proposed ORR and OER mechanisms[13].

Different mechanisms can occur, the two electrons pathway, also called the peroxo mechanism (or second associative, Figure 1.7) as it involves the formation of H_2O_2 as intermediate, and two pathways involving a transfer of four electrons, associative or dissociative mechanisms[13, 36, 37]. The 4 electrons pathways are desired in a fuel cell as the peroxide produced in the 2 e^- mechanisms can decompose in radical species which degrade the components of the fuel cell (e.g. the membrane)[38]. The peroxide route also has a lower energy conversion efficiency[39]. The Pt-based catalysts used are propitious to lead to the 4 e^- pathway[19]. At low current densities, the dissociative mechanism is predominant[19, 40]. It can be written with three different steps. First, oxygen breaks during the adsorption and 2 atomic O are adsorbed.

$$O_2 + 2* \rightarrow 2\ O^{ads} \tag{8}$$

Where * is a free adsorption site
Then, the atomic O further gains two electrons in two consecutive steps

$$O^{ads} + H^+ + e^- \rightarrow OH^{ads} \tag{9}$$

$$OH^{ads} + H^+ + e^- \rightarrow H_2O + * \tag{10}$$

At higher current density range (and thus higher overpotentials), the associative mechanism becomes prevalent. It could be due to the increasing O coverage of the electrodes[40, 41], and thus a decrease in O_2 dissociation rate (first step of dissociative mechanism). In the associative mechanism, the first step is the adsorption of oxygen on the surface without breaking the O-O bond.

$$O_2 + * \rightarrow O_2^{ads} \tag{11}$$

Afterwards, OOH^{ads} is formed which then breaks into O^{ads} and OH^{ads}.

$$O_2^{ads} + H^+ + e^- \rightarrow HOO^{ads} \tag{12}$$

$$HOO^{ads} \rightarrow O^{ads} + OH^{ads} \tag{13}$$

Then, O^{ads} is transformed in another OH^{ads},

$$O^{ads} + H^+ + e^- \rightarrow OH^{ads} \tag{9}$$

Finally, water is formed by the combination of OH^{ads} and a proton, freeing the adsorption sites,

$$OH^{ads} + H^+ + e^- \rightarrow H_2O + * \tag{10}$$

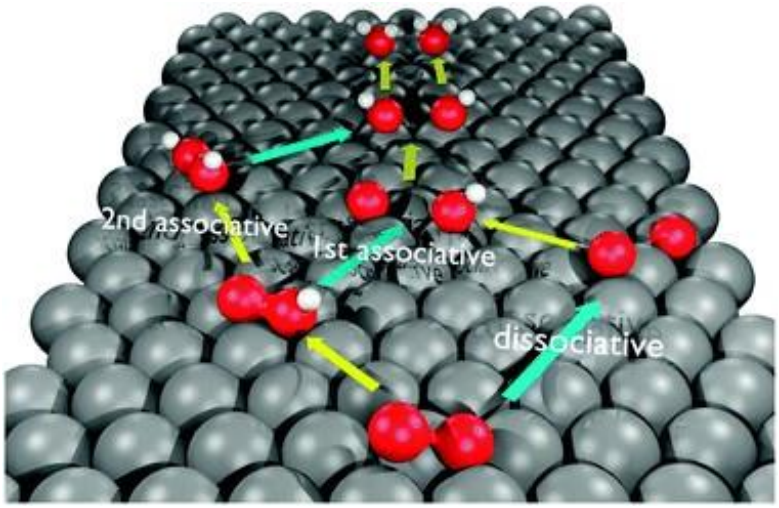

Figure 1.7: Illustration of the proposed ORR mechanisms in acidic media[37].

The formation/removal/binding of the different oxygen species (O^{ads}, OH^{ads}, OOH^{ads}) is rate-determining for ORR and defines the catalyst performance[19]. The binding energy of these species is linearly related to each other. Thus, the binding energy of one species is a sufficient descriptor to describe the activity of the catalyst, the so-called scaling relationship[17, 42]. In the case of the 4 e^- pathways, the ORR is limited by the formation of OOH^{ads} species (Equation 12) or by the removal of OH^{ads} (Equation 10)[18, 43]. Sabatier principle enounces that the adsorption of these two species on the catalyst should not be too strong nor too weak[44]. Therefore, a Volcano-plot can be constructed and the materials at the left of it bind oxygen species too strongly (OH^{ads} removal is the limiting step), the ones at the right bind oxygen species not strongly enough (OOH^{ads} formation is limiting) while the ones at the top are the best catalysts for ORR (Figure 1.8)[19, 45].

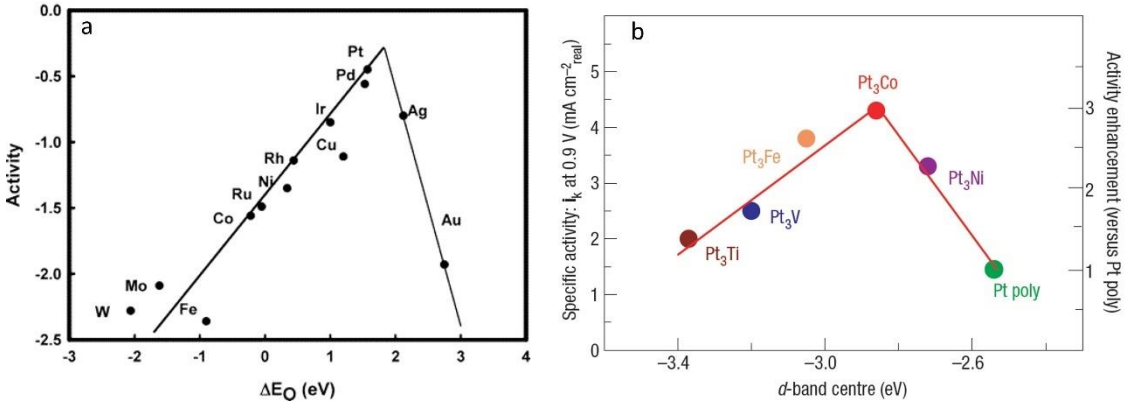

Figure 1.8: a) Volcano-type relationship for the ORR activity versus the oxygen binding energy in acidic media[19]. b) Relationships between the electronic structure and the catalytic properties of Pt_3M alloys[45].

While Pt is the closest to the top among the pure metal, alloying it with less noble metals allows for even better balance between the biding of oxygen species adsorbed of surface Pt[46, 47]. The special structure of the alloy, with a Pt shell on the surface while the less noble metal is in the core. This causes a downward shift of the d-band center (increasing d-band vacancy) resulting in a weakened Pt-O bond[13, 46]. In addition to this electronic effect, a strain effect participates in the activity improvement. The distance

between Pt-M (M is a transition metal) and Pt-Pt is different and thus the surface atoms are compressed, inducing a reduction of the d-band level and thus improving ORR activity (Figure 1.8b)[48, 49]. Another huge advantage of the alloying process is the reduction of Pt needed in the catalyst. Indeed, the scare and expensive Pt is diluted in the core of the nanoparticles and thus less of it is needed for the same or even better electrochemically active surface area (ECSA), and thus electrochemical performances[50, 51].

Another way to increase the Pt utilization is by supporting the nanoparticles on a high surface area, conductive, and stable support[52]. The most common one for ORR catalysts is carbon[52]. It presents all the necessary characteristics for electrocatalyst support. Moreover, the support can also help to improve the activity through the well-known strong metal support interaction (SMSI)[53] and/or electronic metal-support interaction (EMSI)[54]. The EMSI has recently been proposed by Campbell as a more precise metal-support interaction (MSI)[54]. It is used to specifically describe the electronic perturbations (charge transfer) at the metal-support interface oppositely to the SMSI which refers to any change in chemisorption properties of the active metal while supported on another material[53, 55]. However, the EMSI was mostly described for single atoms and small nanoparticles and becomes increasingly difficult to characterize with bigger nanoparticles[56, 57]. Distinction between the two is difficult without specific characterization and thus the term SMSI will be used indifferently for all the interactions between the support and the active nanoparticles in the rest of the text.

The Pt-based catalysts on carbon reached the top of the volcano thanks to the activity enhancements due to support and alloying. Hence, any further impressive activity improvement is unlikely to happen in the future and, consequently, the biggest challenge in the ORR community is to improve long-term stability. Therefore, understanding the degradation of Pt-based catalysts is primordial to design new catalysts with better stability. Several mechanisms have been identified as the degradation processes of Pt-based catalysts[58, 59] (Figure 1.9). They fall into two categories, the primary degradation mechanisms, related to the operational conditions, and the secondary degradation mechanisms, happening due to the primary degradations[60].

In the first category, the most important processes are the dissolution of Pt nanoparticles, with a Pt-O exchange mechanism[61], and the corrosion of the carbon support[62, 63]. The reshaping of the nanoparticles and the dealloying of the less noble metal are also primary degradation processes[64]. Those induce the other degradation processes. Namely, Ostwald ripening, detachment, and agglomeration of particles[65, 66]. Similarly to dealloying, leaching of the less noble metal is a secondary degradation process as some fresh transition metal atoms are exposed to the electrolyte (and thus to possible dissolution) after the dissolution of Pt. Reshaping is a primary degradation but can also be considered as a secondary process due to Ostwald ripening and agglomeration.

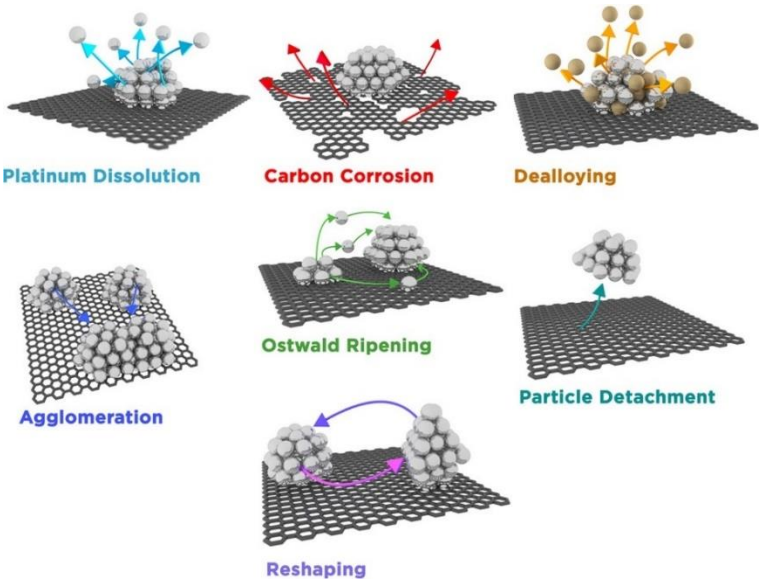

Figure 1.9: Illustration of the different degradation mechanisms of ORR catalyst, carbon corrosion, dissolution, Ostwald ripening, agglomeration and detachment[58].

Even if Pt/C is still considered as the state-of-the-art catalyst for ORR, activity improvement has been possible through alloying with less noble metals while reducing the cost. The major drawback of Pt-M/C catalysts is the stability and extensive studies are performed to understand the differences between different alloys and how to improve their stability[67-69].

1.1.2 Water electrolyzer

A water electrolyzer is a device that uses electrical energy to electrocatalytically split water into hydrogen and oxygen. Under acidic conditions, water is split at the anode into oxygen and protons (oxygen evolution reaction, OER, Equation 14). The proton then travels through the membrane to reach the cathode where it is evolved into hydrogen gas (hydrogen evolution reaction, HER, Equation 15).

$$2\ H_2O \rightarrow O_2 + 4\ H^+ + 4\ e^- \qquad E = 1.23\ V_{RHE} \quad (14)$$

$$4\ H^+ + 4\ e^- \rightarrow 2\ H_2 \qquad E = 0\ V_{RHE} \quad (15)$$

Again, the theoretical potentials are shown, and they are identical to those in PEMFC as it represents the reverse process. In practice, an overpotential is also observed in a WE. The overpotential of HER is slightly more negative (few mV) due to Pt being an extremely good catalyst for this reaction, even with low amounts[29]. Therefore, the reaction limiting the WE efficiency is the oxygen-involved one, the OER, and overpotentials of a few hundred mV are observed even with the best catalysts[12, 70]. Consequently, the potential needed to reach a current density of 10 mA/cm^2 is commonly used to compare the studied materials[71]. Another option is to compare the mass-normalized current density obtained at a specific potential, usually, 1.51, 1.55 and 1.6 V_{RHE} are employed but various other potentials are also used[72, 73].

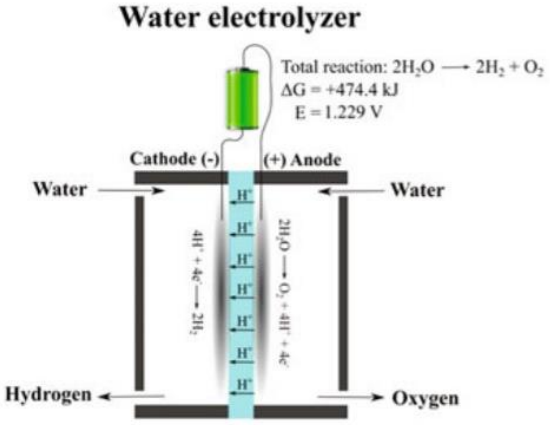

Figure 1.10: Representation of an electrolyzer system[12].

1.1.2.1 Hydrogen evolution reaction

The hydrogen evolution reaction in acid follows the same possible pathways as HOR but in the reverse directions[12]. Namely, the general reaction is

$$2\ H^+ + 2\ e^- \rightleftharpoons H_2 \tag{16}$$

The first step is the Volmer step:

$$H^+ + e^- \rightarrow H^{ads} \tag{17}$$

Followed by either the Heyrovsky step:

$$H^{ads} + H^+ + e^- \rightarrow H_2 + * \tag{18}$$

Or the Tafel step:

$$2\ H^{ads} \rightarrow H_2 + 2* \tag{19}$$

Where * is an active site.

First, Trasatti used the work function of the catalyst as a descriptor for the HER activity[33]. This was based on the observation of a linear relationship between the logarithm of the exchange current density of HER and the work function. Later, Norskov et al. generated a volcano-plot by plotting the experimental exchange current densities as a function of the calculated hydrogen chemisorption energies[74] (Figure 1.11).

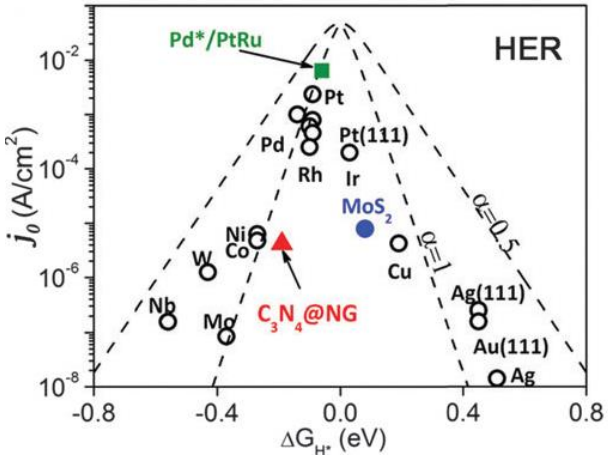

Figure 1.11: Volcano-type relationship for the HER current densities versus the hydrogen binding energy[75].

Identically to HOR, Pt is the state-of-the-art catalyst for HER. It presents a high activity, with low overpotential, and the rate of the reaction is extremely fast. Therefore, the reaction is quickly limited by the diffusion of H^{+}[12]. The scarcity of Pt is not a bottleneck in commercialization as loadings of 0.5 - 1.0 mg/cm^2 are sufficient for good efficiency of the WE[76].

1.1.2.2 Oxygen evolution reaction

The oxygen evolution reaction pathway in acid is opposite to the ORR pathways (see Figure 1.6). In short, three pathways are conceivable[77]. The first step is always the formation of an OH^{ads} species from the adsorbed water.

$$H_2O + * \rightarrow OH^{ads} + H^{+} + e^{-} \tag{20}$$

a) Afterwards, in the recombination pathway (opposite of dissociation for ORR), also known as the oxide path, two OH^{ads} can release a water molecule and form a O^{ads}

$$2\ OH^{ads} \rightarrow O^{ads} + * + H_2O \tag{21}$$

The third step of this pathway is the formation of O_2 from two O^{ads} species.

$$2\ O^{ads} \rightarrow O_2^{ads} \tag{22}$$

b) In the second possible mechanism, the electrochemical oxide path, opposite to the associative for ORR, the OH^{ads} loses one proton without the formation of water. This step can occur twice to form two O^{ads}.

$$OH^{ads} \rightarrow O^{ads} + H^{+} + e^{-} \tag{23}$$

The following step is then similar to the oxide path.

$$2\ O^{ads} \rightarrow O_2^{ads} \tag{22}$$

c) The last mechanism is the electrochemical metal peroxide path. It involves the formation of a peroxide and starts similarly to the oxide path (Equation 21). The second step is the reaction between O^{ads} and H_2O which is then followed by the loss of a proton.

$$2\ OH^{ads} \rightarrow O^{ads} + * + H_2O \quad (21)$$

$$O^{ads} + H_2O \rightarrow HOOH^{ads} \quad (24)$$

$$HOOH^{ads} \rightarrow OOH^{ads} + H^+ + e^- \quad (25)$$

Finally, the additional loss of a proton leads to O_2 formation.

$$OOH^{ads} \rightarrow O_2^{ads} + H^+ + e^- \quad (26)$$

The mechanism taking place depends on the catalyst itself but also on the applied potential as seen by the switch in Tafel slope in different potential windows (Figure 1.12a)[77]. The Tafel slope relates the rate of an electrochemical reaction to the overpotential[78]. The Tafel slope is determined by the rate-determining step (RDS) and thus a different Tafel slope indicates different RDS in the OER mechanism[79]. However, a similar Tafel slope is not sufficient to identify the RDS or mechanism. Indeed, different RDS in different mechanisms can have the same Tafel slope[70].

Comparably to the ORR, a volcano plot can be built from the oxygen species binding energy (Figure 1.12b)[80]. Either OOH^{ads} can be adsorbed too strongly or O^{ads} is too weakly adsorbed, determining the rate of the reaction[18]. However, oppositely to ORR, the conditions of the reaction (potential above 1.23 V_{RHE}) imply that the reaction is taking place on metal oxides and not on pure metal[80, 81].

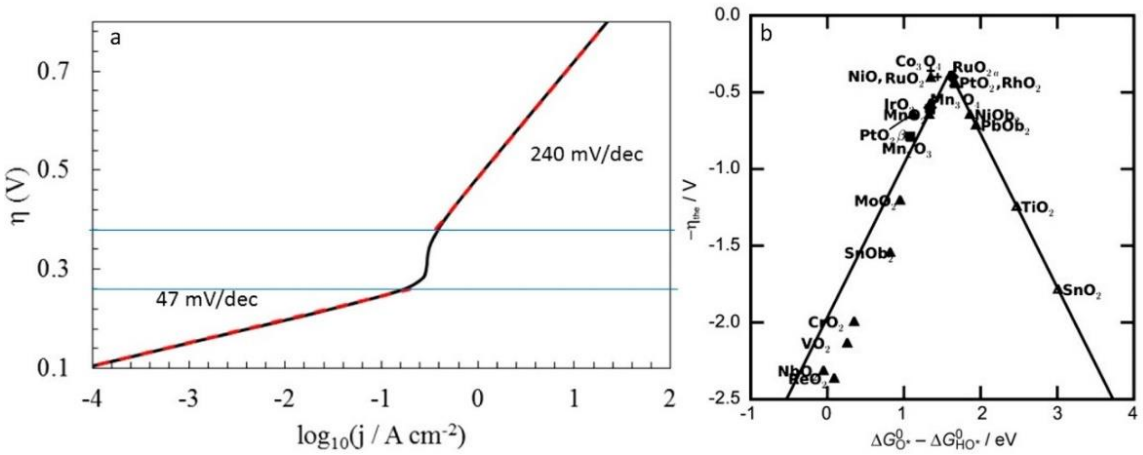

Figure 1.12: a) Tafel plot for OER on IrO_2 (110) calculated by DFT. The red dots highlight the linear regions in the Tafel plot[77]. b) Volcano-type relationship for the OER activity versus the oxygen binding energy[80].

It can be seen in Figure 1.12 that the materials the closest to the top (and thus the most active ones) are Ru-oxides and not the state-of-the-art catalysts, Ir-oxides[80]. This is explained by the stability of the materials. Indeed, stability is also an important parameter for electrocatalysts and, unfortunately, Ru-oxides dissolve constantly at OER conditions[82, 83]. At similar potentials to OER, Ru-oxides transition from a lower to a higher oxidation state (e.g. RuO_2 to RuO_4). RuO_4 species are gaseous and thus induce Ru dissolution which makes Ru unsuitable as a catalyst for WE without improved stability[82]. Therefore, the

current state-of-the-art catalysts are Ir-oxides as they present the best activity/stability tradeoff[12].

Unfortunately, iridium is considered as a CRM thus WE will never reach worldwide commercialization if bulk iridium is used as the OER catalysts[20, 76]. Therefore, Ir utilization should be optimized. Similarly to Pt-based catalysts, few studies of alloying Ir with less expensive and more abundant transition metal (Ni, Co) were published but the dissolution of the transition metal during OER operations was rarely addressed[84-88]. In fact, the improved activities recorded were often ascribed to an increase of the ECSA after a massive de-alloying instead of some other explanation like a strain and/or electronic effect due to the less noble metal[84, 87]. The other method to increase the utilization is by using a high surface area support to disperse nanoparticles of the precious metal. However, the classic carbon support commonly used is not stable under OER conditions[89]. Several other materials have been studied as potential support for OER catalysts but not many materials meet the requirements of electrocatalysts support under the harsh conditions of OER[90]. Indeed, the carbides[91, 92], pervoskites[93], nitrides[94, 95], and metal oxides[96-102] proposed as potential supports usually lack one of the necessary characteristics of electrochemical support, namely stability, high surface area or conductivity[90]. These properties can be tuned to a certain extent through doping but often to the cost of other features. For example, the doping of the tin-based supports, the most studied support material for OER catalysts[98, 103-105], can increase their conductivity but at the expense of lower stability due to the dissolution of the doping element[106, 107]. Another possibility is to increase conductivity by using high loadings of Ir (over 60 wt% of the catalyst[108]) but then the goal of ultra-low loadings of PGMs will not be reached[90]. Currently, no material has been accepted as benchmark support for OER.

1.1.3 Unitized reversible fuel cell

A fuel cell can produce electrical energy by combining oxygen and hydrogen while a water electrolyser device uses the surplus of electrical energy to split water into its basic components, H_2 and O_2. The unitized reversible fuel cell (URFC) device is able to function in both modes, fuel cell to produce electricity and electrolyser to convert it into chemical bonds[109]. This results in an overall smaller device than the separate FC + WE. It proves itself useful in some cases like space exploration where saving weight is primordial[110]. It also reduces the cost of the overall catalysts. Indeed, instead of having Pt/Pt (anode/cathode) catalysts in fuel cell plus Ir/Pt (anode/cathode) catalysts in WE, bifunctional catalysts are used in URFC, resulting in a lower amount of precious metals[109]. However, the state-of-the-art bifunctional catalysts are simple physical mixtures of Pt and Ir, allowing a lot of space for improvement[111].

A URFC can be constructed in two different ways (Figure 1.13)[112]. In the first mode (mode A, on the left in Figure 1.13), the electrodes are exposed to the same gases (hydrogen for one, oxygen for the other) in both FC and WE mode[113]. The advantage is straightforward gas management. Each electrode will act as a cathode in one mode and as the anode in the other one. On the hydrogen electrode, a small amount of Pt on carbon is enough as it is an excellent catalyst for both HOR and HER. On the oxygen electrode, Pt and Ir are mixed to provide activity for ORR and OER, respectively[114]. In mode B (right in Figure 1.13), the oxidation processes will take place on the same electrode (anode) in both FC and WE, and the reduction reactions will take place on the other electrode (cathode) each time. The cathode catalyst is Pt on carbon, a good catalyst for ORR and HER (reduction processes). However, higher loading is needed than on the hydrogen electrode of mode A due to the ORR. On the anode, the bifunctional mix Pt+Ir is sufficient for OER and HOR (oxidation processes).

URFC built on the model A are more frequent because they are safer and easier to build. Model B requires one to switch from oxygen to hydrogen and vice-versa every time you change between FC and WE mode, which can be dangerous and purging with inert gas in between is needed. However, it presents higher performances in FC mode and equal performances in WE than the mode A[112].

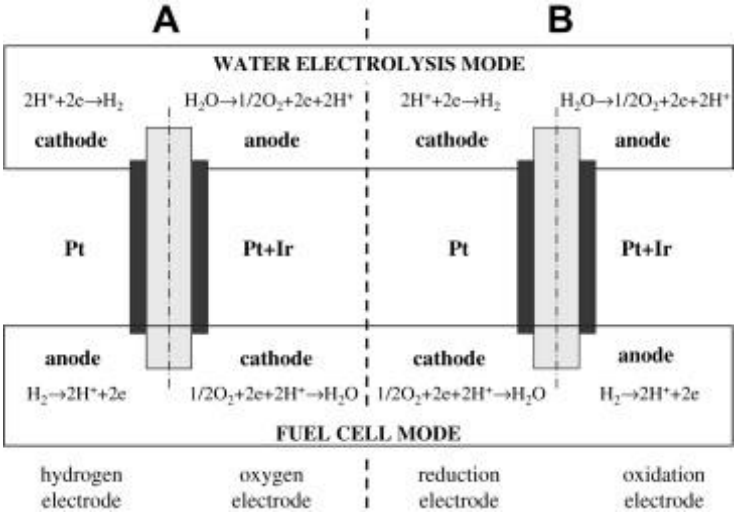

Figure 1.13: Representation of the two possible modes of operation of a URFC[112].

Even if the overall amount of PGMs used in URFC is lower than for FC/WE duo, the bifunctional catalyst involved in OER still required a considerable amount of Ir and Pt. The solution to better utilization is the introduction of suitable support. Electrocatalyst support should have a high surface area, good conductivity, and be stable in the range of operational conditions[91, 115]. Currently, no material presents these three characteristics for OER in WE/URFC (around 80°C, pH 1 and a highly oxidizing environment). The usual carbon used as a support for Pt (ORR, HER, HOR) is oxidized to CO_2 at this potential, leading to high degradation of the catalyst[89]. Even so, some graphitized carbons, a more stable form of carbon, have been proposed as potential support for bifunctional catalysts[116-118]. The same materials proposed for single OER catalysts can be considered such as the electrically conductive transition metal-based materials as Ebonex (mostly composed of the suboxide Ti_4O_7)[119], $Ti_{0.9}Nb_{0.1}O_2$[101], doped-SnO_2 (ATO, ITO, FTO, Ta-TO)[97, 98, 99, 105], TiC[92] and TiN[94]. However, all of the proposed materials currently lack one of the requirements for good electrocatalyst support, namely high surface area, good conductivity, and good stability. Therefore, there is still room for improvement of the PGMs utilization in bifunctional catalysts in URFC, notably through the development of a high surface area, conductive and stable support.

Chapter 2

Motivation and Objectives

To reach commercialization of URFC, the overall price of the devices has to be reduced drastically[31]. The most expensive parts are the catalysts for oxygen reactions due to the high amount of PGMs needed. The cost can be decreased by improving catalyst utilization, i.e. maximizing the exposed surface area or its activity per gram of PGM. It can be achieved by alloying PGMs with a cheaper transition metal. This approach has been proven effective for ORR catalysts made out of Pt-M alloys (M: Co, Ni, Fe, Cu)[47]. However, the stability of the less noble metal is already problematic during ORR[67] and it is expected to be worst during OER[72]. Another tactic to boost the utilization of precious metals is by supporting them on a high surface area support[52]. However, no material has been proven to achieve all the requirements for good ORR and OER catalyst support.

This work focuses on the thorough investigation of potential bifunctional catalysts for URFC. Two main aspects must be considered. First, which materials to use as catalysts for ORR and OER. Many different Pt-M alloys can be employed for ORR while Ir and Ru are the two common options for OER. At the beginning, an extensive study of benchmark Pt-alloys was performed to analyze the differences due to the less noble metal. At the same time, this research was used to establish a protocol on how to appropriately characterize and evaluate an electrocatalyst. Indeed, many techniques and parameters need to be accounted for while comparing electrocatalysts with each other and with the literature data. For some reactions/materials, benchmark protocols that facilitate the comparison are implemented. This is, however, not true for all the investigated reactions/materials. Therefore, it is important to present our groups' approach to electrocatalysts studies and how to understand the differences between them.

Secondly, a stable, conductive, and high surface area material was proposed as a support for URFC. Hereby, we studied titanium-based support able to withstand OER conditions and thus suitable for bifunctional catalysts. The $TiON_x$ support proposed is a combination of TiO_2 and TiN parts which provide good stability (property of TiO_2) and sufficient conductivity (property of TiN) even at low PGMs loading. Unfortunately, $TiON_x$ – made from TiO_2 – tends to not provide a high surface area. This problem was addressed by investigating different morphologies of the support, and ultimately graphene was used to improve the dispersion and thus surface area of the support. In summary, the following topics are discussed in this work:

(i) Case study of ORR catalyst – Pt-alloys, establishing a protocol to study electrocatalyst and which alloy to choose (Chapter 4)?

(ii) $TiON_x$ as potential support for OER (Chapter 5).

(iii) Effect of $TiON_x$ morphology on OER activity and stability (Chapter 5.3).

(iv) Using a graphene-based template for $TiON_x$ to enhance OER (Chapter 5.4).

(v) Optimizing bifunctional catalysts (Chapter 6).

Chapter 3

Materials and Methods

This chapter presents the various experimental techniques and methods used to synthesize materials, prepare samples and study catalysts' performances and characteristics. The work described below was performed in collaboration with many scientists and experts in their field. The details can be found in the corresponding chapter.

3.1 Material Preparation

MilliQ water (18.2 MΩ.cm) was used for catalysts synthesis and for electrolyte preparation. Benchmarks materials (various Pt/C; various Pt-M/C from Fuel Cell Store (FCS); Ir, and IrO_2, Alfa Aesar) were used as-received without further treatment.

3.1.1 Synthesis

3.1.1.1 $Ir/TiON_x$ materials and Ir/C (Chapter 5.2)

Iridium nanoparticles deposited on two different titanium oxynitrate supports; $Ir/TiON_x$ ($Ir/TiON_x$-NR and $Ir/TiON_x$-P25); and on carbon (Ir/C) were prepared.

The titanium oxynitride nanoribbons ($TiON_x$-NR) were synthesized by weighting 225 mg of the hydrogen titanate nanoribbons in a quartz boat which was then placed in an oven and heated to 800°C at a ramp rate of 7.2°C/min. The heating was performed in a NH_3(g)/Ar(g) atmosphere, with a flow ratio of 30/10 mL/min. The sample was maintained at the selected temperature for 3 h before cooling down to room temperature (RT). The iridium nanoparticles were prepared by dissolving 22 mg of iridium (III) bromide hydrate (Sigma-Aldrich, St. Louis, MO) in 0.6 mL of water at 50°C. The solution was then mixed with 30 mg of the prepared support at 50°C until evaporation of the solvent. Afterwards, the obtained mixture was annealed in a 5% H_2/Ar atmosphere. The annealing was performed at 400°C for 1h with an increasing temperature rate of 2°C/min and a cooling down rate of 3°C/min to RT. The final composite material (Ir-$TiON_x$-NR) contained 23 wt% of iridium.

Another $TiON_x$ substrate was prepared from commercial TiO_2 nanoparticles (P25, Degussa). The received TiO_2-P25 nanoparticles were heated in a NH_3 atmosphere (flow rate, 50 mL/min) at 800°C for 6h. The same procedure as for Ir-$TiON_x$-NR was employed to deposit Ir nanoparticles on the newly prepared support. The final composite ($Ir/TiON_x$-P25) contained 22 wt% of Ir after thermal treatment.

The same procedure was employed to synthesize Ir nanoparticles on a carbon support. The Ir particle size distribution was comparable to the $Ir/TiON_x$ materials.

3.1.1.2 $TiON_x$-nh-Ir (Chapter 5.3)

Three different $TiON_x$-nh-Ir catalysts were prepared following the procedure shown in Figure 3.1. Firstly, a previously cleaned (with acetone and ethanol in an ultrasonic bath) titanium foil (200 µm thick, 99.8%, Baoji Lyne Metals Co., Ltd) was anodized in a 0.3 wt% NH_4F (99.99%, Sigma-Aldrich) and 2 vol.% deionized water in ethylene glycol (99.5%, Carlo Erba Reagents) electrolyte. The foil was anodized at a constant potential of 60 V in a two-electrode electrochemical cell using a stainless-steel counter electrode for 1h, 3h and 6h. The newly grown amorphous TiO_2 nanotubes were washed with deionized water and ethanol and then detached from the titanium substrate by bending the anodized foil. Afterwards, the amorphous TiO_2 was converted to $TiON_x$ by thermal treatment in NH_3 (50 mL/min) at 700°C for 10h. 70 mg of iridium (III) bromide hydrate precursor (Sigma-Aldrich, St. Louis, MO) dissolved in 1 mL of water (50°C) was mixed with 100 mg of $TiON_x$ powder at 50°C. After evaporation of the solvent, the mixture was thermally treated for 1h at 450°C in a 5% H_2/Ar atmosphere. The heated rate was 2°C/min while the cooling down rate to RT was 3°C/min. The final composites contained around 11 wt% of iridium. The samples were named as $TiON_x$-nh-Ir, where n is 1, 3 or 6 depending on the anodization time.

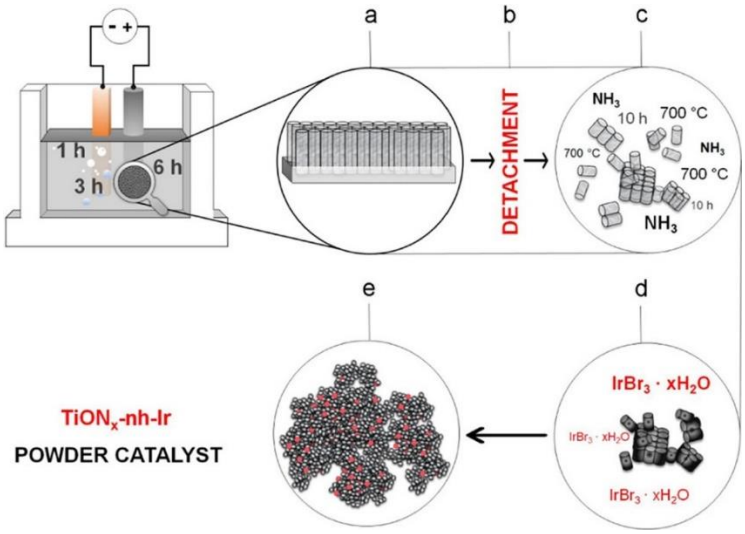

Figure 3.1: Procedure for $TiON_x$-nh-Ir catalyst preparation. a) Anodic oxidation of titanium foil. b) Detachment of TiO_2 nanotubes. c) Annealing of detached TiO_2 nanotubes in ammonia. d) Deposition of Ir onto $TiON_x$ nanotubes. e) The final $TiON_x$-nh-Ir powder catalyst.

3.1.1.3 Ir/$TiON_x$/rGONRs (Chapter 5.4)

Three different Ir/$TiON_x$/rGONRs composites were synthesized with different $TiON_x$/rGONRs precursors ratios.

First, the graphene nanoribbons (GONRs) were synthesized according to a modified previously published method[120]. Multiwall carbon nanotubes (NanoTechLabs C-Grade MWNTs) (2 g) were added to a mixture of concentrated acid (H_2SO_4/H_3PO_4, 9/1 volume ratio, 135/15 mL). Then 6 aliquots of 2g of $KMnO_4$ were added to the stirred solution, producing a slight exothermic reaction, heating up the mixture to 35-40°C. The reaction was stirred at RT for 10 days. The reaction slurry was then quenched by pouring it onto

ice (400mL). Then, 30 vol% H_2O_2 was added dropwise (3 mL) to deactivate the remaining $KMnO_4$. The mixture was then centrifuged for 15 min (3000 rpm). The supernatant obtained was decanted away and the leftover solid was washed with water (10 times) and methanol (1 time) before a new session of centrifugation (3000 rpm, 15min, removal of supernatant). The material left (3.8g) was freeze-dried and stored at RT.

Various amounts of titanium isopropoxide precursors (86 mg, 345 mg, and 1,38 g) were stirred in 3.9 g of isopropanol in an agate mortar. Afterwards, 500 mg of the prepared GONRs were added and mixed until a thick paste was formed. Milli-Q water (360 mg) was then added dropwise until a very thick paste was formed. The obtained nanocomposite paste was transferred to a glass vessel and spread around to make a thin film. This film was left to dry at RT for over 4h and then freeze-dried. The three different ratios between Ti precursor and GONRs lead to three TiO_2/GONRs composites. Namely molar ratios of 1/140 (Low-$TiON_x$/rGONRs), 1/35 (Middle-$TiON_x$/rGONRs) and 1/8.75 (High-$TiON_x$/rGONRs) of Ti/rGONR were used.

The TiO_2/GONRs composites were reduced in NH_3 atmosphere (50 mL/min) with the following heat treatment: i) RT to 120 °C (7 K/min), ii) hold at 120 °C for 1 h, iii) 120 °C to 700 °C (heating rate 5 K/min), iv.) hold at 700 °C for 10 h, and v) 700 °C to RT (5 K/min).

The Ir nanoparticles deposition was done by dispersing $TiON_x$/rGONRs (100 mg) and $IrBr_3xH_2O$ (70 mg) in 1 mL of Milli-Q water. Ir as a nominal wt% in the catalysts of 10 %. The mixture was annealed in an Ar/H_2 atmosphere using the following protocol: i) RT to 120 °C (7 K/min), ii) hold at 120 °C for 1 h, iii) 120 °C to 450 °C (2 K/min), iv) hold at 450 °C for 1 h, and v) from 450 °C to RT (3 K/min). A temperature of 450°C was chosen as Da Silva et al. showed that Ir reaches the best catalytic performances after a thermal treatment between 400 and 500°C[121]. After annealing, the catalyst powders were dispersed in 10 mL of Milli-Q water and sonicated for 5 min. Afterwards, the black suspensions were filtered through a 220 nm pore size PTFE membrane filter. The filter cake was additionally rinsed before being transferred to a glass bottle and dried in an oven for 4h at 110°C. This purification step was necessary to ensure no presence of contamination salt (KBr).

3.1.1.4 Bifunctional catalyst (Chapter 6)

The graphene oxide template was prepared from a modified version of Marcano's synthesis[120]. Namely, 6g of graphite flakes were added to a stirred mixture of acid (H_2SO_4/H_3PO_4, 720/80 mL). 6 equivalents per 6g of $KMnO_4$ were slowly added to the mixture (one equivalent per day). The mixture was stirred for 14 days and then cooled to RT. The resulting solution was poured onto the ice with 10 mL of 30% H_2O_2. The product was centrifuged and washed with milli-Q (2 times), 5% HCl (3 times) and methanol (5 times).

The following step of the synthesis was to embed $TiON_x$ on graphene. Ti isopropoxide (Aldrich, 97%) was mixed with the previously prepared graphene in an isopropanol/water (70/30) solvent (isopropanol, Honeywell, 99,8%). The mixture is then annealed at 800°C for 6 h in NH_3 atmosphere (50 mL/min, heating rate of 2°C/min and cooling down of 3°C/min).

Afterwards, Pt and Cu precursors (27 mg of $Pt(NH_3)_4(NO_3)_2$, Alfa Aesar and 45 mg of $Cu(NO_3)_2.3H_2O$, Sigma-Aldrich, 98%, respectively) were dissolved in 1 mL of Milli-Q water. 100 mg of the prepared support (TiON-graphene) was added to the solution. The mixture was then dried in air at 50°C. This allows good alloying between Pt and Cu. Afterwards, 15 mg of Ru precursor ($RuCl_3.H_2O$, Apollo Scientific) dissolved in 1 mL of ethanol was added to the dried composite. The new solution was dried again before thermal treatment at 800°C (2°C/min from RT) under NH_3 atmosphere (50 mL/min). Pt, Cu and Ru

precursors during the same annealing step allow for good proximity between PtCu alloy and Ru nanoparticles.

Finally, 18 mg of $IrBr_3.H_2O$ (Alfa Aesar, St-Louis, MO) was added to 84 mg of the previously obtained composite in 1 mL of water at 50°C. After drying, a thermal treatment under NH_3 atmosphere (50 mL/min) was performed. The temperature was heated up to 450 °C (2°C/min). After 1 hour, the final catalyst was cooled down to RT (3°C).

3.1.2 Electrode preparation

First, the catalyst inks were prepared by accurately weighing approximately 1 to 3 milligrams of the powder samples with an analytical scale (Sauter). After that, a defined volume of milliQ water (18.2 MΩ.cm) was added (exactly the same ml as the weight milligrams) in order to reach a catalyst concentration of 1 mg/mL.

Afterwards, the ink was sonicated in an ultrasonic bath for a few minutes to assure homogeneity and 20 µL was drop-casted on 0.196 cm^2 glassy carbon electrode embedded in Teflon (Pine) and left to dry overnight. 5 µL drop of 1:50 v/v Nafion:IPA solution was deposited on the dry film to stabilize it. Several films were prepared every time and only the best ones were selected for experiments in rotating disk electrode (RDE).

3.2 Electrochemistry

Electrochemistry experiments were performed to evaluate the performances (i.e. activity and stability) of the catalysts for a specific reaction (ORR or OER). The electrochemical evaluations were performed in a thin film rotating disk electrode (TF-RDE) set-up. The experiments were conducted in a standard two-compartment cell in a 0.1 M $HClO_4$ (Merck, Suprapur, 70%, diluted by Milli-Q water, 18.2 MΩ.cm) electrolyte with a three-electrodes system controlled by a potentiostat (Figure 3.2a). The cell was boiled for at least 30 min in between different samples. The electrolyte was exchanged and replaced with a fresh one in between different protocols (i.e. activation, activity and stability protocols).

The TF-RDE system is conventionally used to measure steady-state electrochemical reactions. The control rotation rate allows the control of the diffusion layer thickness, and the electrochemical reactions can be evaluated during the kinetics-control regime, depending on the electrocatalyst deposited on the working electrode[122] (Figure 3.2b).

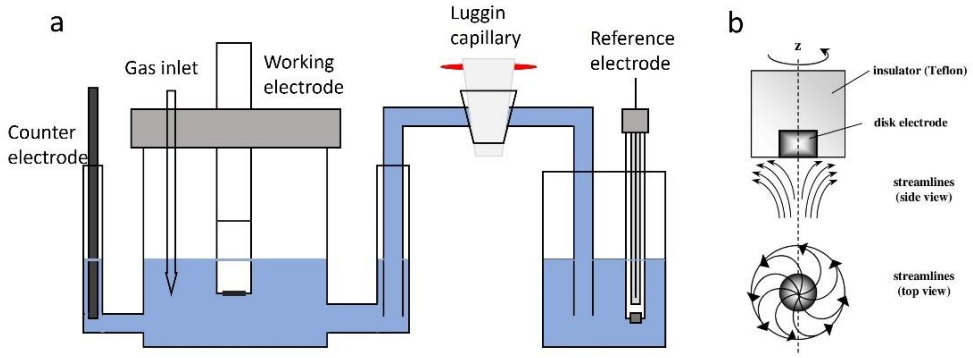

Figure 3.2: a) Scheme of a three-electrode system with the reference separated from the rest of the cell by a Luggin capillary. b) Sketch of a rotating disk electrode with the streamline in the electrolyte. Top view and side view at the bottom[123].

An Ag/AgCl electrode was used as a reference. Its potential against the reversible hydrogen electrode (RHE) was determined by saturating the electrolyte with H_2 and measuring the OCP with a Pt working electrode. The reference is separated from the rest of the system by an electrolyte bridge and/or Lugging capillary to avoid Cl- contamination. A Pt wire was used as a counter electrode during the activity measurement, but it was replaced by a carbon rod during stability measurement to avoid any dissolution/redeposition of the Pt from the counter on the working electrode.

Various electrochemical techniques were employed to analyze the performance of the catalysts, namely cyclovoltammetry (CV), chronoamperometry (CA) and chronopotentiometry (CP). Beforehand, electrochemical impedance spectroscopy (EIS) was performed to measure the resistance of the solution which was then accordingly compensated during the activity measurement[124]. Different protocols were applied depending on the reactions (ORR or OER) and materials (Pt-based, Ir-based or multimetallic) investigated. However, regardless of the protocol, the CV measurement is used to activate the catalyst, measure ECSA, record activity and perform accelerated degradation tests (ADT). On the other hand, the CA (constant potential, measure of the current) and the CP (constant current, measure of the potential) protocols were solely used for ADT. The protocols performed during the diverse studies presented in this work are listed below.

Pt-M/C catalysts (Chapter 4): The electrode with the best film was mounted in the three-electrodes set-up with an Ar-saturated electrolyte and under a potential control of 0.05 V_{RHE}. An activation protocol of 200 cycles between 0.05 and 1.2 V_{RHE}, at 300 mV/s and a rotation rate of 600 rpm was applied (Platinum catalysts activation, PCA). After replacing the electrolyte, the ORR-activity measurement was performed, and polarization curves were recorded between 0.05 and 1.0 V_{RHE} in an O_2-saturated electrolyte at 20 mV/s and 1600 RPM. The kinetic parameters were calculated at 0.9 V_{RHE} after subtraction of the background current. The ECSA was evaluated by integrating the charged in a CO electrooxidation experiment[125] performed after the activity measurement. Therefore, the electrolyte was purged with CO for at least 5 min under potentiostatic mode (0.05 V_{RHE}) to ensure sufficient CO-adsorption. Afterwards, the electrolyte was saturated with Ar and the CO electrooxidation was performed between 0.05 and 1.0 V_{RHE} at 20 mV/s, without any rotation. In the case where an ADT was performed, the activated electrocatalysts were subjected to 5000 cycles between 0.4 and 1.2 V_{RHE} at 1 V/s. The activity and ECSA measurements were performed in a freshly changed electrolyte after the ADT. All the experiments were reproduced at least 3 times. In the case where further characterization was needed (e.g., ex-situ TEM), the films after activity measurements or ADT were suspended in 0.5 mL of isopropanol by placing the working electrode in an ultrasonic bath (Iskra Sonis 4) for few seconds.

Ir-based catalysts (Chapter 5.2): Exceptionally, a gold disk electrode (diameter of 4 mm) was used as the working electrode on which the catalyst powders were deposited. For all the samples, 20 µL of the 1 mg/mL ink were drop-casted on the working electrode resulting in iridium loading of 12.9 µg/cm^2 for Ir/TiON$_x$-NR, 13.52 µg/cm^2 for Ir/TiON$_x$-P25 and 58.78 µg/cm^2 for IrO_2-AA and Ir-Black. An activation protocol consisting of 100 cycles between 0.05 and 1.6 V_{RHE} at 300 mV/s and 600 RPM was carried on to electrochemically oxidize iridium. The OER-activity measurement followed by cycling the catalyst in the same potential range but at 20 mV/s and 1600 RPM. The stability test was performed according to a widely used protocol[71, 126]. Namely, a CP treatment of 0.1 A/mg$_{Ir}$ was applied for 5 hours.

Ir/TiON$_x$-NR catalysts (Chapter 5.3): The potential was cycled between 0.05 and 1.6 V_{RHE} at 1600 RPM and 20 mV/s until a stable CV was obtained. The stable CV was used to estimate the OER-activity of the catalyst. A preliminary stability test was conducted

by applying a constant current of 1 mA/mg_{Ir} (CP protocol) for 1 or 2 hours[126]. The activity was measured again after replacing the electrolyte.

Ir/$TiON_x$/rGONRs catalysts (Chapter 5.4): An activation protocol of 10 cycles between 0.05 to 1.6 V_{RHE} under O_2 atmosphere and at 20 mV/s and 1600 RPM was conducted in order to electrochemically oxidize the iridium nanoparticles. Afterwards, the electrolyte was saturated with Ar and the activity was measured under the same cycling conditions. The activity was evaluated after correcting CVs for the capacitive current (half the current at 1.1 V_{RHE}). Two different stability tests were performed on different films, i.e. cycling and CP. In the first case, 5000 cycles in the OER potential region (1.2 to 1.6 V_{RHE}) were conducted at 1 V/s. For the CP protocol, a constant current of 2 mA/cm^2_{geo} was applied for 2 hours, corresponding to 0.291, 0.288, 0.302 and 0.217 $mA/\mu g_{Ir}$ in a 20 µL drop of Ir/rGONRs, Ir/Low-$TiON_x$/rGONRs, Ir/Middle-$TiON_x$/rGONRs and Ir/High-$TiON_x$/rGONRs, respectively. After replacing the electrolyte, the activity was tested again.

Multimetallic catalysts (TiON-RuPtCu-Ir, Chapter 6): First, the films were activated by 200 cycles between 0.05 and 1.2 V_{RHE} in an Ar-saturated electrolyte at 300 mV/s. This step is particularly important for Pt-alloys as Cu leaches out of PtCu particles and improves the activity for ORR compared to pure Pt (activation step)[64, 127, 129]. Then, the ORR activity was tested by cycling between 0.05 and 1 V_{RHE} in O_2-saturated electrolyte at 20 mV/s and 1600 RPM. Afterwards, the OER activity was examined by cycling between 0.05 and 1.6 V_{RHE} at the same speed and RPM but in an Ar-saturated electrolyte. Fresh films were used to study HER. Cycles between 0.1 and 0.6 V_{RHE}, 20 mV/s and 1600 RPM were performed in a H_2-saturated electrolyte. Three different ADTs were performed according to the reaction of interest. Namely, one ADT was performed in the ORR region, "ORR degradation", which consists of 10 000 cycles between 0.4 and 1.0 V_{RHE}. The "OER degradation" means that 10 000 cycles are conducted between 1.0 and 1.6 V_{RHE}. The last protocol is the ORR & OER degradation" (also called "ALL degradation") which is 10 000 cycles in both reaction regions, i.e. between 0.4 and 1.6 V_{RHE}. All the ADTs were performed under Ar and at 1 V/s. Similarly to the previous study, the films of interest for ex-situ characterization were dispersed in 0.5 mL of isopropanol.

3.3 Electrochemistry Coupled with Other Techniques

In addition to activity and stability measurements, electrochemistry techniques can be coupled with other characterization techniques to get in-situ information about mechanisms, notably degradation processes.

3.3.1 Online Inductively Coupled Plasma - Mass Spectrometry

An electrochemical flow cell (EFC, Figure 3.3) coupled with an inductively coupled plasma – mass spectrometry (ICP-MS) (Agilent 7900x, Agilent technology, Palo Alto, CA) was used to study the dissolution of catalysts under electrochemical protocols. The ICP-MS was equipped with a MicroMist glass concentric nebulizer and a Peltier cooled Scott-type double-pass quarts spray chamber. A forward radio frequency power of 1500 W was used with Ar gas flows: carrier 0.85 L/min; makeup 0.28 L/min; plasma 1 L/min; cooling 15 L/min. The electrochemical flow cell was custom-made in PEEK based on the design of a crossflow metallic cell (BASi, USA). The counter and the working electrodes are glassy carbon (3mm diameter) embedded into PEEK material (ALS dual type electrode for crossflow cell, 25x25 mm). The electrolyte is flowing in a direction to first reach the counter electrode and then the working electrode to assure no redeposition can occur on the counter. The reference electrode (Ag/AgCl (MW-2030, BASi) potential vs RHE was determined in

a separated three-electrode set-up prior to the EFC-ICP-MS experiments. The flow of the electrolyte was ensured to be at a constant 400 µL/min by a syringe pump (AL-1000, World Precision Instrument, USA). A diagonal 4-way flow valve (PEEK, V-100D, Idex) was used to switch different electrolytes (water and 0.1 M $HClO_4$) without stopping experiments. The working electrodes were prepared by drop-casting 5 µL of a 1 mg/mL sonicated suspension, resulting in a catalyst loading of 70.74 mg/cm^2. The film was let to dry overnight and a drop of a Nafion 1:50 solution was deposited on it. Standard solutions (1, 2, 5, 10, 20, 50, 100 ppb) were prepared from certified, single element, ICP grade standards (Merck CertiPUR) and measured to convert the recorded signals of the catalysts from counts to ppb. The electrochemical protocols were applied with an Ivium potentiostat and no ohmic drop compensation was used. Different protocols were applied depending on the investigated material. At the end of every protocol, a sequence of potential pulses was applied to synchronize the ICP-MS signal and the electrochemical experiment. The protocols used for each catalyst are presented below.

Pt-M/C catalysts (Chapter 4): Milli-Q water was initially pumped through the cell before switching to the 0.1 M $HClO_4$ so as to notice any dissolution due to acid contact. After reaching a stable background level, slow cycles (5 mV/s) from 0.05 V_{RHE} to an increasing upper-potential limit (1.0, 1.2 and 1.4 V_{RHE}) were performed to as-purchased electrocatalysts. Two cycles were repeated for each upper potential limit. The same protocol was replicated on a fresh film after an electrochemical activation protocol, i.e. 200 cycles between 0.05 and 1.2 V_{RHE} at 300 mV/s.

Ir/$TiON_x$/rGONRs catalysts (Chapter 5.4): First, an activation/cleaning step was performed by fast cycling the samples 10 times between 0.05 and 1.2 V_{RHE} at 200 mV/s. This step was followed by two cycles between 1.2 and 1.6 VRHE at 20 mV/s and the Ir and Ti dissolution was monitored.

Multimetallic catalysts (TiON-RuPtCu-Ir, Chapter 6): The experiment started with an activation protocol of 200 cycles between 0.05 and 1.2 V_{RHE} at 300 mV/s. It was followed by slow cycles (20 mV/s) in five different potential windows; 0.4 to 1.0 V_{RHE}; 1.2 to 1.6 V_{RHE}; 0.4 to 1.6 V_{RHE}; 0.0 to 1.6 V_{RHE} and −0.1 to 1.0 V_{RHE}. Three minutes of OCP were implemented between each potential window in order to reach a stable background.

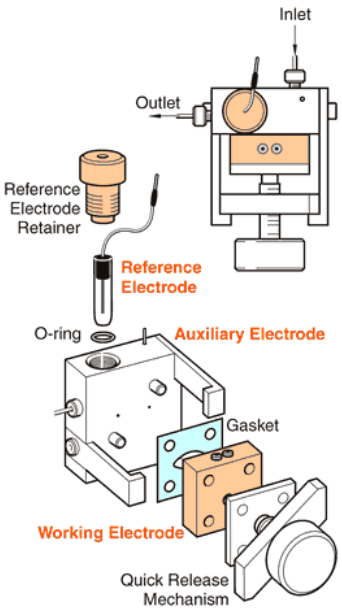

Figure 3.3: Schematic illustration of an electrochemical flow cell (EFC) used for the EFC-ICP-MS experiments[129].

3.3.2 Electrochemistry mass spectrometry

An electrochemical cell coupled with a mass spectrometer (EC-MS, Spectro Inlets) was used to analyze the evolution of volatile species at the working electrode during electrochemical tests of Ir/$TiON_x$/rGONRs (Chapter 5.4).

The working electrode was prepared by drop-casting 20 mL of a 1 mg/mL catalyst ink on a previously polished (with 0.05 mm alumina paste) and washed glassy carbon disk electrode. The ink was sonicated 10 min before the deposition to assure good dispersion and homogeneity of the catalyst. No Nafion was added to the electrode. The working electrode was used in a thin-layer cell configuration, placed parallelly at 100 mm of a porous chip membrane that leads to the MS detector (quadrupole, Pfeiffer Vacuum, PrismaPro QMG 250 M2). The counter and the reference electrodes were a graphite rod and a reversible hydrogen electrode (Hydroflex, Gaskatel), respectively. The electrolyte (0.1 M $HClO_4$) was deaerated and saturated with the carrier gas (He) prior to the experiment. A Biologic SP-300 channel potentiostat was used to perform the electrochemical protocol. No iR compensation was applied.

The experiment started with 5 min at OCP to determine the background MS signal. Afterwards, a pretreatment of 10 cycles between 0.05 and 1.2 V_{RHE} at 200 mV/s was performed. The pretreatment protocol was followed by three different short degradation protocols separated from each other by 5 min at 1.2 V_{RHE} to let the signal go back to the background. The first degradation was a cycling degradation (100 cycles, 200 mV/s, from 1.2 to 1.5 V_{RHE}, corresponding to 5 min of cycling). The second one was chronopotentiometry (CP, 100 mA, 5 min) and the last one was chronoamperometry (CA, 1.5 V_{RHE}, 5 min). Low current and a limit of 1.5 V were chosen to avoid extensive O_2 bubble formation which would block the thin-layer cell.

The m/z ratios of 32 and 44 were tracked down as they correspond to O_2 and CO_2, respectively. O_2 is the product of OER, and CO_2 is formed if the carbon support degrades. At least two measurements for each sample were performed.

3.4 Materials Characterizations

3.4.1 Conductivity Measurements

Conductivity measurements were performed in the early stage of research on $TiON_x$ as a potential electrocatalyst support material. For conductivity measurements, two types of samples were prepared from the synthesized $TiON_x$ materials (without the presence of Ir). The first sample type was pressed at a loading of 2 T to form a pellet. The typical pellet thickness was from 1 to 2 mm and the surface area 0.5 cm^2. The second type of sample was first treated the same way as the first one and then heated ("sintered") in gaseous ammonia for 10 h at 700°C. The electrical measurements were carried out by placing the pellet between two copper foils, which were then pressed together with external weight (5 kg) in order to maintain good electrical contact with the pellet. The conductivities were calculated based on the voltage response and pellet geometry.

3.4.2 BET Measurements

The Brunauer−Emmett−Teller (BET) surface-area and nitrogen-sorption measurements for the samples in Chapter 5.3 were recorded using a Tristar 3000 automated gas-adsorption analyzer (Micromeritics Instrument Corp.) recording at -196 °C. Before the adsorption analysis, the samples were outgassed under vacuum for 12 h at 120 °C.

3.4.3 X-Ray Diffraction Analysis

The powder X-ray Diffraction (XRD) measurements were carried out with an X-ray powder diffractometer PANalytical X'Pert PRO MPD (PANalytical B.V., Almelo, The Netherlands) with Cu Kα1 radiation (λ = 1.5406 Å). The 2θ range of the diffractograms varies depending on the study but always comprised between 10° and 90°. A step of 0.04° per 1s was used. The samples were prepared on a zero-background Si holder and the X'pert Highscore plus software was used to analyze the spectrum.

3.4.4 Scanning Electron Microscopy

Scanning electron microscopy (SEM) was carried out using a Zeiss Supra TM 35 VP microscope (Carl Zeiss, Oberkochen, Germany) equipped with an energy dispersive X-Ray spectrometer (EDX, Oxford Instruments, Model Inca 400). The distance between the sample and the gun was 4.5 mm. The operating voltage was set to 2-7 kV. Three areas were analyzed for statistical relevance.

Width measurements of nanoribbons were evaluated using ImageJ software. At least five pictures and 15 different nanoribbons were used to measure the width of the nanoribbons of each sample (Chapter 5.3).

The powder samples were deposited on a conductive carbon tape which was then placed on an aluminum SEM holder. In the case of identical location SEM (IL-SEM), 5 mL of the catalyst ink was deposited on a carbon rod marked with an X. Pictures were taken for the "as-prepared" samples, then the carbon rod was mounted on the rotating disk electrode (RDE) set-up as the working electrode (Chapter 6).

3.4.5 Transmission Electron Microscopy

Scanning transmission electron microscope (STEM) imaging, Energy dispersion X-ray spectrometry (EDXS) and Electron energy loss spectroscopy (EELS) were performed with a Cs-corrected microscope (Jeol, CF-ARM 200) equipped with 100 mm^2 SDD Jeol EDX spectrometer and Gatan Quantum ER DualEELS system. Operating voltages of 80 or 200 kV were used.

For the "as-prepared" images, the samples were prepared from the catalyst ink. The initial 1 mg/mL suspension was sonicated for 15 min and diluted 10 times in Milli-Q water. The new suspension was then sonicated for 5 additional minutes and 5 µL was deposited on a TEM Au grid. In order to perform identical location TEM (IL-TEM) experiments, the same Au grid was mounted on a glassy carbon disk embedded in Teflon. The glassy carbon disk with the grid was then used as a working electrode in a typical three-electrode electrochemical set-up. After electrochemical measurements, the grid was rinsed with Milli-Q water, dried and then examined again.

In the case where no IL-TEM was performed, the electrochemical experiments were performed with a classic three-electrode set-up. Afterwards, the working electrode was sonicated in 1 mL of isopropanol for 10 s to detach the film. Then 5 µL was deposited on a TEM grid.

3.4.6 Inductively Coupled Plasma - Optic Emission Spectrometry

Inductively coupled plasma - optical emission spectrometry (ICP-OES) was used to determine the amount of metal in the samples. The samples were weighted (approximately 10 mg) before being digested in 3/1 v/v HCl/HNO_3 solution using a microwave-assisted digestion system (CEM MDS-2000). The digested samples were cooled down to room temperature and diluted with a 2% v/v HNO_3 until their concentration reached the desired

range for ICP-OES measurements. The measurements were performed with a Varian 715-ES instrument. In-house standards prepared from traceable, certified, ICP-grade, single-element standards (Merck CertiPUR) were used for calibration.

3.4.7 Raman Spectroscopy

Raman spectroscopy of Ir deposited on $TiON_x$/Carbon support (Chapters 5.3 and 5.4) was carried out with a WITec alpha 300 confocal Raman spectrometer. A silicon wafer was used as a substrate for the powdered samples and a green laser light (532 nm) with a power of 4 mW was used for recording the spectra. The chosen power enables us to see the characteristic bands of $TiON_x$ and graphene oxide carbon support while lower power provides only the G and D bands of carbon. The spectra were measured at four different positions using a 20x objective and at least four individual Raman spectra were recorded for each sample. The spectrum approaching most of the average value of all spectra was plotted.

3.4.8 CHNS Analysis

A CHNS/O elemental analyzer (PerkinElner 2400 Series II) was used to determine the amount of carbon in Ir/$TiON_x$-rGONRs (Chapter 5.4). The temperature of combustion and of detection was set at 975°C and 81.5°C, respectively.

3.4.9 X-ray photoelectron spectroscopy

X-ray photoelectron spectroscopy (XPS) was employed to characterize the first few layers (3-5 nm) of Ir/$TiON_x$ catalysts (Chapter 5.3). A PHI-TFA XPS spectrometer (Physical Electronics Inc) equipped with an Al-monochromatic source was used to record the spectra. The analysis area was 0.4 mm in diameter and at least two measurements were performed on every sample. Carbon was not considered while calculating the surface composition as it could only originate from contamination.

Chapter 4

Studying and Comparison of Electrocatalysts for ORR

Parts of the following section have been previously published under the title: "Resolving the nanoparticles' structure-property relationships at the atomic level: a study of Pt-based electrocatalysts"[69]

L. Moriau, A. Hrnjić, A. Pavlišič, A.R. Kamšek, U. Petek, F. Ruiz-Zepeda, M. Šala, L. Pavko, V. S. Šelih, M. Bele, P. Jovanovič, M. Gatalo, and N. Hodnik.

L. Moriau as the first author conducted all the electrochemical studies in RDE set-up as well as all the online-ICP-MS experiments and participated in discussion and interpretation of the results with M. Gatalo. The conceptualization was done by P. Jovanovic, M. Gatalo and N. Hodnik.

4.1 Introduction

One of the remaining grand challenges in the PEMFC field is to achieve high activity and stability at low PGMs loadings. Currently, Pt-based electrocatalysts account for almost half of the total PEMFC manufacturing cost[130]. Therefore, decreasing the overall price of the catalysts and reaching low PGMs loading while keeping the same performances is primordial. The approach which is the closest to the production phase is alloying Pt with less expensive transition metals (Cu, Ni, Fe, Co) on a high surface area support[29, 131]. Alloys not only have the advantages of optimizing the Pt utilization by diluting the core of the particles[132], but they also enhance the intrinsic activity. The electronic structure of the Pt surface is influenced by the incorporation of the less noble metal, leading to a ligand/strain effect that modifies the bond strength of oxygen species and improves the ORR activity[48, 133-135].

These improvements (lower cost and higher activity) in most cases come with the price of lower stability. The transition metal (M) is thermodynamically unstable at the ORR acidic conditions[136] and dissolves inside the PEMFC. An activation protocol, either chemical (acid washing) or electrochemical one[137, 139], can deplete the surface and subsurface (and sometimes also from bulk) of M and thus form a Pt-rich protective layer. The activation step can slow down the dissolution of the less noble metal but not hinder it totally. These metals can then cause problems in the PEMFC when diffused in the different parts of the device[139-141]. Therefore, the biggest challenge is the stability of these Pt-M

catalysts and the limitation of M leaching[142]. For this, the phenomena leading to M leaching need to be understood at a fundamental level for each different Pt-alloy.

Unfortunately, the transition metal alloyed with Pt is not the only parameter that can influence the activity (and stability) of the catalyst, thus making its study difficult. It has been shown that the structure of the particles (or shape) greatly influences the activity even for "simple" Pt catalysts (Figure 4.1a)[143-145]. This is due to the different facets exposed for catalytic activity, which have atoms with distinct generalized coordination numbers (number of neighbors present in the first and second sphere, with a weight for each first-nearest neighbor corresponding to their own coordination number)[146], and thus different activity. Moreover, in the real world where particles are not perfectly shaped, defects play an important role in the activity of catalysts, making a comparison with theoretical study (which used perfectly shaped nanoparticles) difficult (Figure 4.1b)[147].

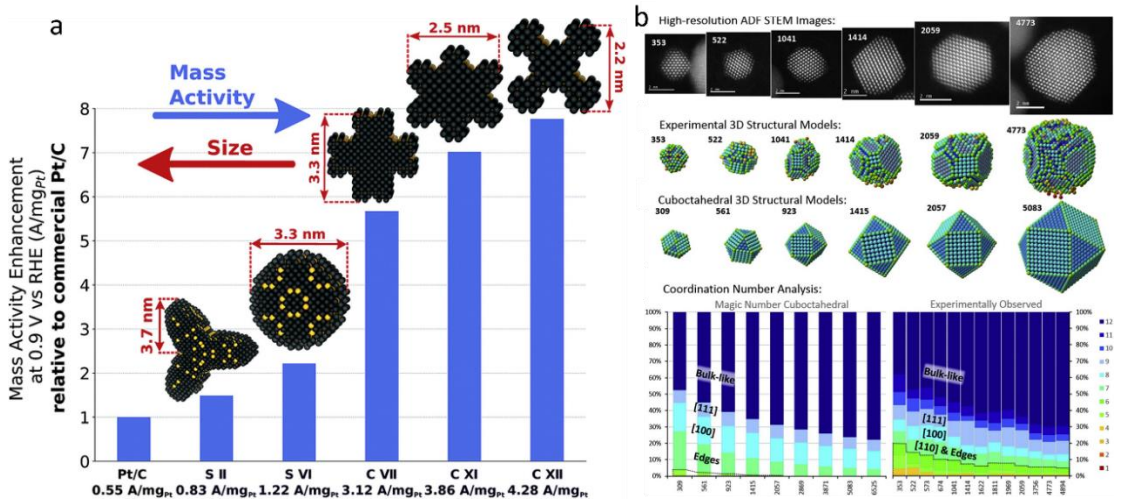

Figure 4.1: a) Shape-ORR activity relationship of Pt catalysts[148]. b) HR-STEM images, 3D structural models and coordination number analysis[147].

For alloys, the complexity is even higher as other parameters take place like the chemical composition[135, 149], the degree of ordering[150], the thickness of Pt-shell or the amount of less noble metal retained[48]. Therefore, understanding the structure-property relationship that governs both activity and stability is even more difficult[151]. In addition, the surface is not stagnant under operation and is dynamically changing, moving the real world even further from the idealized models used in theoretical studies (Figure 4.2).

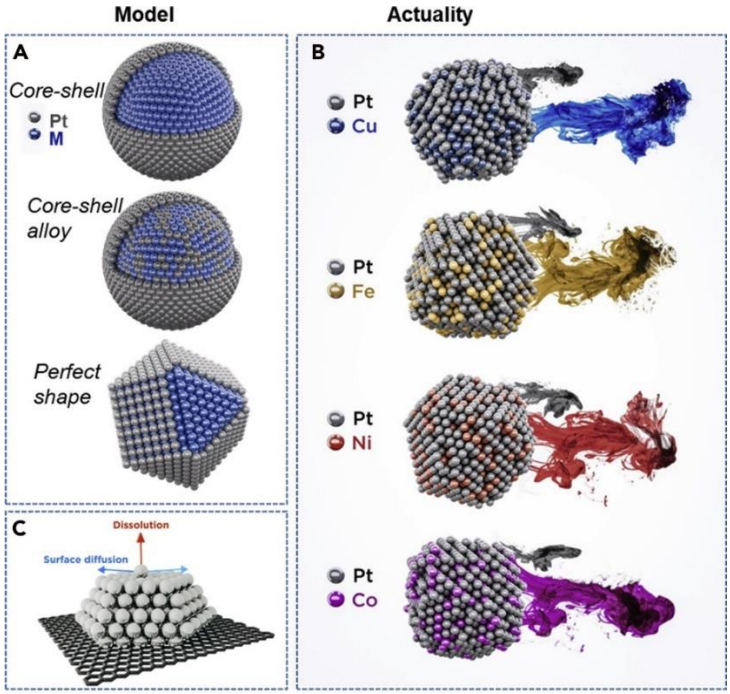

Figure 4.2: a) Model structures of Pt-alloys nanoparticles. b) Real structures of Pt-alloys nanoparticles. c) Representation of surface atoms movement and removal.

The activation step is necessary to remove M from the surface and near-surface region, thus decreasing or better eliminating its leaching later in PEMFC and improving the stability of nanoparticles. It also has the consequence of changing the structure of the nanoparticle[152] and this potentially creates new very active structures[153, 154]. The final structure depends on many different parameters (shape, native composition, etc.). Overall each Pt-M alloy possesses unique properties and fair comparisons of activity and stability become complicated without a good understanding of their differences and consequently different structure-properties relationship. Moreover, there is no database of the shape transformation of the nanoparticle after annealing and/or activation[155, 156].

In this work, we aim to understand better the differences between Pt/C catalysts and Pt-M/C catalysts as well as the impact of M on activity and stability. For this, we have compared benchmarks and at the same time, we point out the difficulty of evaluating seemingly comparable systems. Four different Pt/C electrocatalysts (from Umicore, TKK and JM) have been compared with each other for Pt benchmarks and four Pt-M/C electrocatalysts (M = Cu, Fe, Ni, Co, purchased from Fuel Cell Store) for Pt-alloys. The idea behind using benchmarks was to, first, use comparable catalysts that are widely used in different laboratories over the world, and second, to limit as much as possible the different synthesis parameters which could influence the catalysts' structure/shape/morphology (for the alloys that were advertised to have the same carbon support, metal loading, composition and particle size distribution). In addition, comparing benchmarks was a good way to introduce our methodology to evaluate and understand the activity and stability of electrocatalysts. Several techniques were used to systematically characterize the physical, chemical, and electrochemical properties of the catalysts. Some of these techniques (like XRD, TEM, RDE, etc.) allow fast and reliable comparison of general characteristics like general structure, activity, surface area or stability but are limited for deeper understanding which is more precise, but also more costly, in terms of time and processes, methods are needed (e.g. IL-TEM).

4.2 Results and Discussion

4.2.1 Physical characterization

Pt/C: Firstly, the Pt/C benchmarks were investigated with TEM (Figure 4.3). The three catalysts present inhomogeneity in the particle size and in the dispersion of the nanoparticles on the support. This is due to the synthesis method and the relatively high Pt loadings (over 40 wt%)[157, 158].

Pt-M/C: Based on the product description (20% Pt-M, ratio 1:1, Vulcan XC-72 support, the average particle size of 2-3 nm)[159], the only expected difference was the type of alloying metal M (Ni, Fe, Co, and Cu). ICP-OES digestion confirmed the 1:1 ratio and the total loading of approximately 20 wt% while XRD spectra (Figure 4.3d) and especially TEM analysis (Figures 4.3e-h) reveal characteristic differences between the Pt-M/C catalysts, specifically for PtCo/C.

The XRD spectra uncover different crystal phases for the different alloys. Pt-Co/C (Ref. code 03-065-8968) and Pt-Ni/C (Ref. code 03-065-9445 in "Powder diffraction file") show the same Fm-3m crystal structure while Pt-Fe/C (Ref. code 03-065-9121) and Pt-Cu/C (Ref. code 00-042-1326) exhibit ordered P4/mmm and R3-M phases, respectively. The different crystal structures are expected as the analyzed Pt-M have unique phase diagrams. The XRD spectra also reveal the presence of pure M phases (particles ranging from 20 to 500 nm) for alloys containing Fe, Co, and Ni.

After examination of the XRD spectra, (S)TEM analysis provides additional clues about the samples. For example, encapsulation of pure M phase in a graphitic shell can be observed (Figure 4.3f). This phenomenon is well-known from the chemical vapor deposition technology and is due to the solubility of carbon in M phase at high temperature, which then forms a graphitic shell when cooled down[134, 160-162].

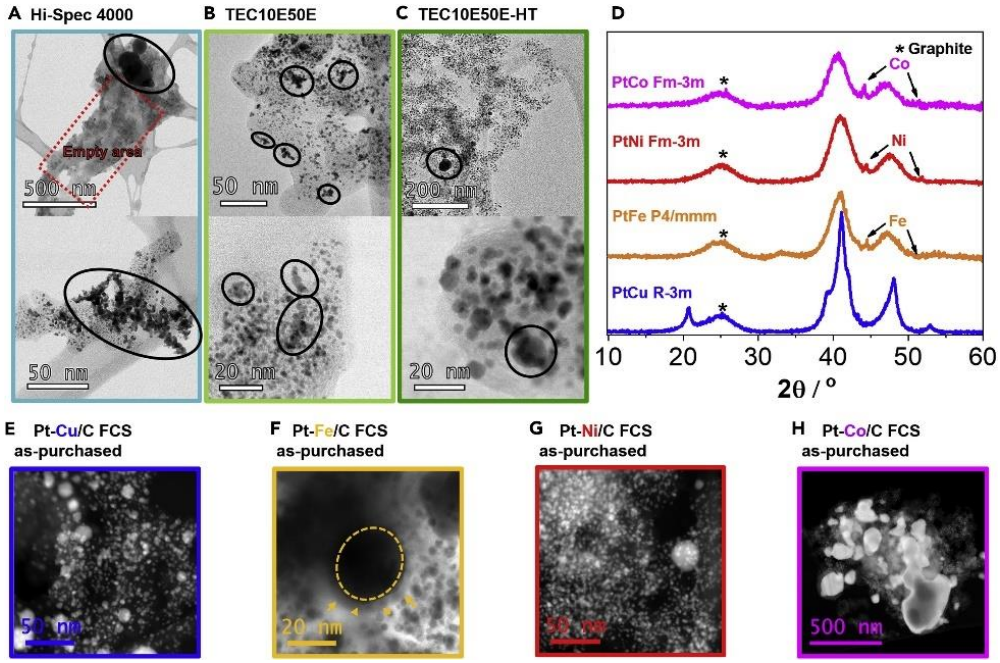

Figure 4.3: a-c) TEM analysis of commercially available Pt/C electrocatalysts (Hi-spec 4000 from JM-teal, TEC10E50E from TKK-light green and TEC10E50E-HT from TKK-green; d) XRD analysis of as-purchased Pt-M/C electrocatalysts from FCS. e-h) STEM analysis of all four Pt-M/C electrocatalysts in the as-purchased state. The colors (Pt-Cu

= blue, Pt-Fe = orange, Pt-Ni = red and Pt-Co = magenta) correspond to the ones used for the graphs and borders in all of the figures.

This is not observed for Cu as the solubility of carbon in this metal is a few orders of magnitude lower than for the other transition metal[163], explaining the absence of pure Cu peaks in XRD. The presence of pure M particles means that the 1:1 (atomic) ratio of nanoparticles stated by the producer and confirmed by ICP-OES is not correct. The active Pt-alloy nanoparticles are more Pt rich. Using EDX, two types of samples area were analyzed. First, the areas with mostly small nanoparticles (2-3 nm) show around 60-65 at% Pt (Figure 4.4), thus higher than the 50 at% expected for a 1:1 ratio. On the other hand, the areas with larger nanoparticles (over 10 nm) contain a higher amount of M (above 50 at% and up to 97 at%) (Figure 4.5).

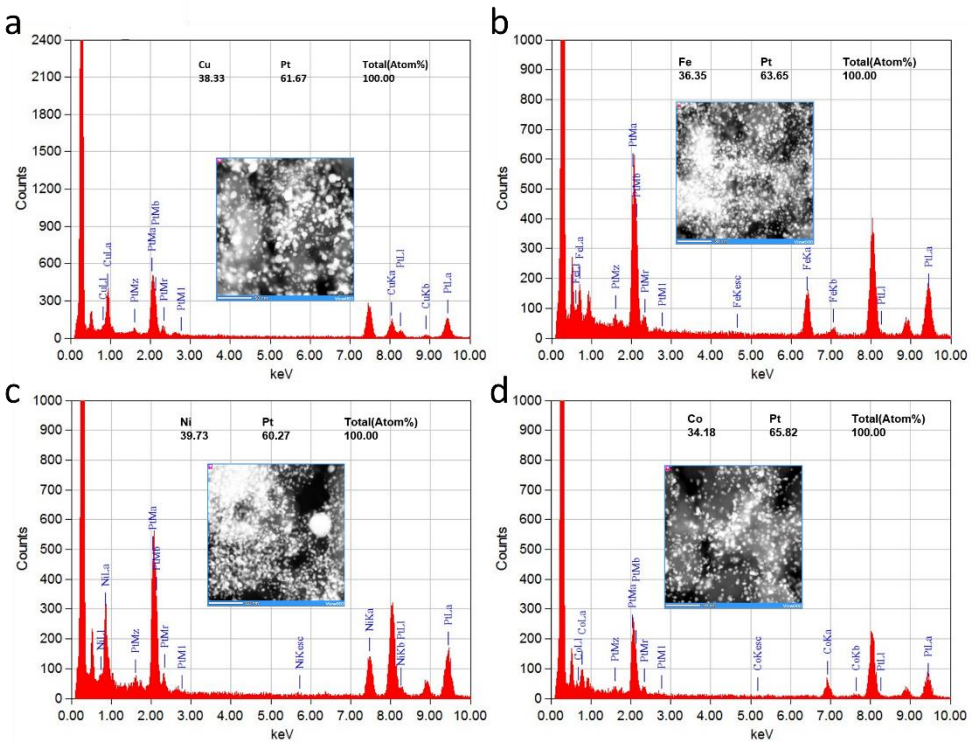

Figure 4.4: EDX-TEM energy spectra with an inlet of the HAADF image of the analyzed area of the as-purchased Pt-M/C (FCS) electrocatalysts. Area with mostly small nanoparticles. a) PtCu/C. b) PtFe/C. c) PtNi/C. d) PtCo/C.

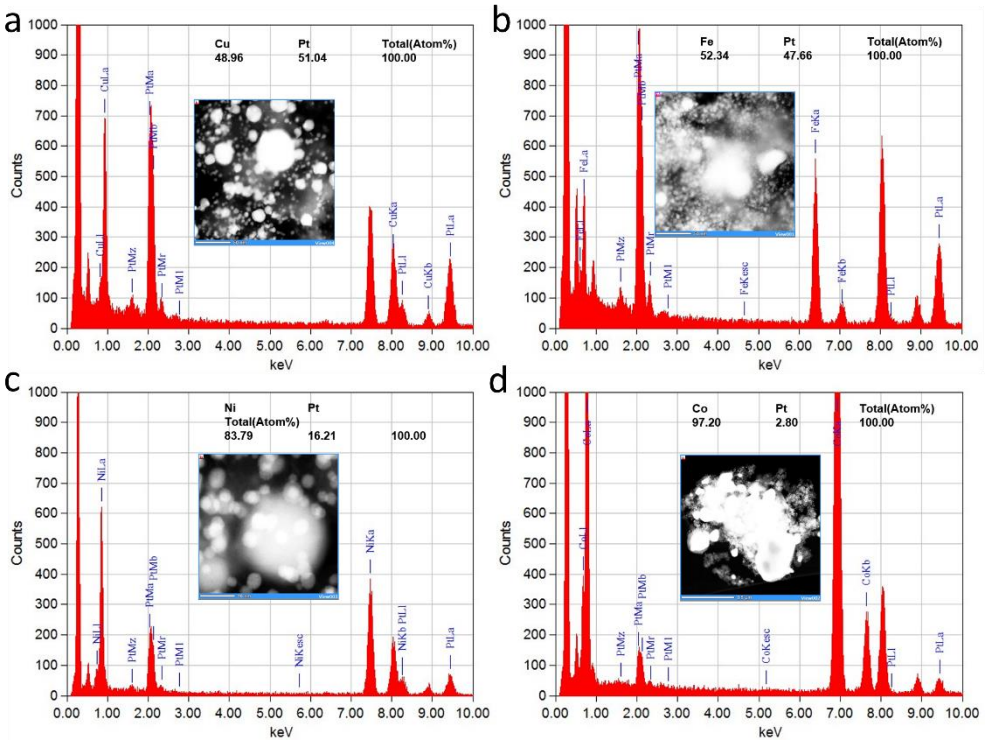

Figure 4.5: EDX-TEM energy spectra with an inlet of the HAADF image of the analyzed area of the as-purchased Pt-M/C (FCS) electrocatalysts. Area with mostly big nanoparticles. a) PtCu/C. b) PtFe/C. c) PtNi/C. d) PtCo/C.

4.2.2 Electrocatalytic performances

The electrochemical performances of Pt-based ORR catalysts are usually screened with a RDE set-up. Before checking the activity, an activation protocol is needed (200 cycles between 0.05 and 1.2 V_{RHE}, at 300 mV/s). The benchmark protocol was taken from the DOE (Department of Energy, USA) report in 2013[164]. Afterwards, a slow cyclic/linear voltammetry is applied to the catalysts and the normalized (per mass or per surface area) activity (mA/cm^2_{Pt} or mA/mg_{Pt}) is checked at 0.9 V_{RHE}. For mass normalization, the precise amount of Pt (Pt loading in catalyst) needs to be measured, which can easily be done with ICP-OES. On the other hand, the electroactive surface area (ECSA) of Pt can be measured by two different methods (Figure 4.6); the underpotential deposition of hydrogen (H_{upd}) and the CO-stripping. CO-stripping is preferred over H_{upd} measurement in the case of Pt-alloys because H_{upd} adsorption is suppressed on the Pt-skin of Pt-alloys (shifted to the HER region) while the CO-stripping is similar to pure Pt (no critical overlapping with other reactions), favoring this technique for the determination of ECSA[165]. In addition, the ECSA determination allows the comparison of the catalysts with different particle sizes. The stability is tested by recording the activity before and after the accelerated degradation test (ADT).

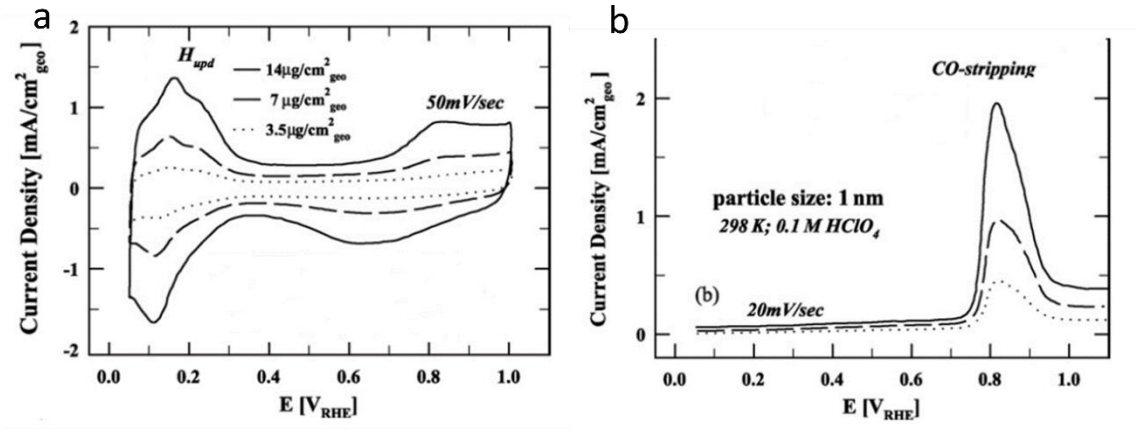

Figure 4.6: a) CV of Pt catalyst in 0.1 M $HClO_4$[166]. b) CO stripping of Pt catalysts in 0.1 M $HClO_4$[166].

Pt/C: The electrochemical performances of the four catalysts also vary significantly as seen in Figure 4.7. It is important to point out that while the activity normalized by geometric area (Figure 4.7a) looks very similar for all catalysts, this is another story when the mass activity or the specific activities are compared (Table 1). Enhancing the importance of normalization for proper comparison.

The two non-thermally annealed Pt/C electrocatalysts (Hi-Spec 4000 and TEC10E50E) present a similar specific activity (SA) of around 0.6 mA/cm^2_{Pt} while having different $ECSA_{CO}$. Hi-Spec 4000 has an ECSA of ~ $53 m^2/g_{Pt}$ while TEC10E50E presents an ECSA of ~ 80 m^2/g_{Pt}. This difference could be due to the different carbon support used. In the case of Hi-Spec, a Vulcan XC-72 was used as a support oppositely to the Ketjen black EC300J used for TEC. The second carbon (Ketjen black) has a more than 3 times higher surface area (800 vs 250 m^2/g for Vulcan). Pointing out the importance of having a high surface area support to effectively deposit nanoparticles without any surface area loss due to agglomeration.

For the two thermally annealed catalysts (TEC10E50E-HT and Elyst Pt50 0550), the SA and the ECSA are both similar, ~ 0.4 mA/cm^2_{Pt} and ~ 50 m^2/g_{Pt}, respectively. They are both supported on Ketjen black EC300J. Although those non-thermally treated catalysts have better SA, the thermally annealed ones (TEC10E50E-HT and Elyst Pt50 0550) are considered as benchmarks. Indeed, the thermal treatment step is primordial for the improved stability of the electrocatalysts that is needed for reliable operation of PEMFC[129, 157]. This step provides a higher resistance against Pt dissolution and improved stability of the carbon support.

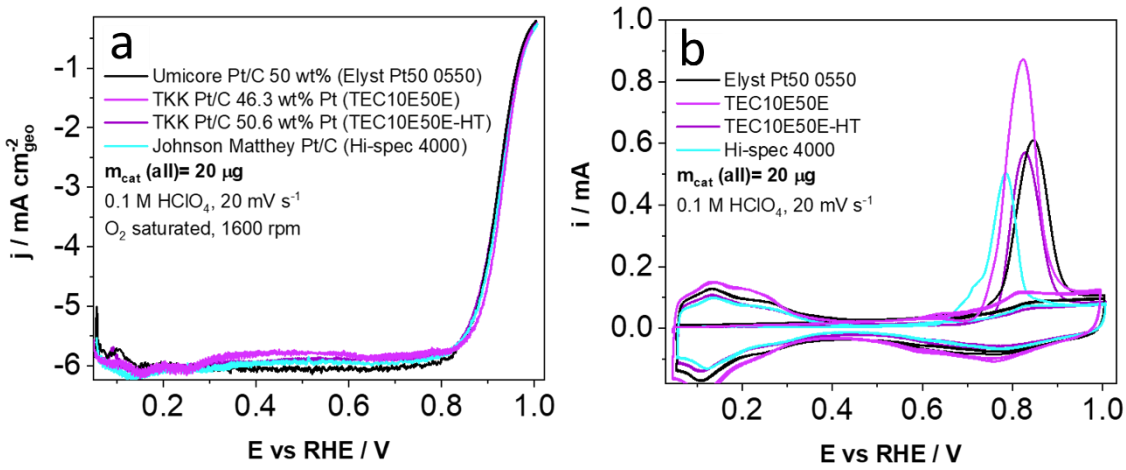

Figure 4.7: a) ORR activity normalized by geometric surface area of the RDE for various commercial Pt/C catalysts. b) CO stripping of various commercial Pt/C catalysts.

Table 1: Electrocatalytic performances of commercially available Pt/C electrocatalysts for PEMFC.

Producer	Name	Pt wt%	ECSACO (m^2/g_{Pt})	SA @ 0.9 V_{RHE} (mA/cm^2)	MA @ 0.9 V_{RHE} (mA/mg_{Pt})	Type of carbon support	Thermally annealed
Johnson Matthey	Hi-Spec 4000 Pt/C	40	53.5	0.64	0.34	Vulcan XC72	No
Umicore	Elyst Pt50 0550 Pt/C	50	56.76	0.42	0.24	Ketjen Black EC300J	Yes
Tanaka Kikinzoku Kogyo	TEC10E50E Pt/C	46.3	79.7	0.6	0.48	Ketjen Black EC300J	No
Tanaka Kikinzoku Kogyo	TEC10E50E-HT Pt/C	50.6	50	0.42	0.21	Ketjen Black EC300J	Yes

Pt-M/C: Figure 4.8 compares the electrocatalytic performances (SA, $ECSA_{CO}$, and the MA) of Pt-M/C catalysts after an activation protocol (PCA, 200 cycles in 0.1 M $HClO_4$, 0.05–1.2 V_{RHE}, 300 mV/s, Ar saturated, 600 rpm) and after the degradation test (ADT; 5000 cycles in 0.1 M $HClO_4$, 0.4–1.2 V_{RHE}, 1 V/s, Ar saturated, 600 rpm). From the four catalysts, PtNi/C clearly exhibits a higher SA (1.6 mA/cm^2_{Pt}) than the three other alloys (1.1 – 1.2 mA/cm^2_{Pt}) (Figure 4.8a). At the same time, all the catalysts present similar ESCA values (Figure 4.8b). Therefore, the MAs follow the same trends as SAs with Pt-Ni/C exhibiting higher activity than the three other ones, with 1.1 A/mg_{Pt} and 0.8 - 0.9 A/mg_{Pt}, respectively.

After the degradation test, Pt-Cu/C retains the most activity with a SA around 1.1 mA/cm^2_{Pt} while the three other ones display an activity around 0.8 – 0.9 mA/cm^2_{Pt} (Figure 4.8a). Pt-Fe/C and Pt-Ni/C present the highest relative loss of SA after ADT while Pt-Cu/C and Pt-Co/C have a lower, comparable loss. However, the decrease in ECSA for all the samples is quite similar. Consequently, MAs after ADT follow again the same trend as SAs, with MAs ranging from 0.4 to 0.6 A/mg_{Pt}.

The activity decrease after ADT of Pt-alloys is usually attributed to the dissolution of the less noble metal, and thus the loss of M positive effect on the activity[134]. However, if electrocatalytic tests in RDE are good to evaluate the activity and stability of the catalysts, they are not helpful to understand the reasons for the difference in said activity and stability. Previous XRD and (S)TEM analyze have shown that the Pt-M/C catalysts were too different to attribute the observed activity and stability differences to one feature.

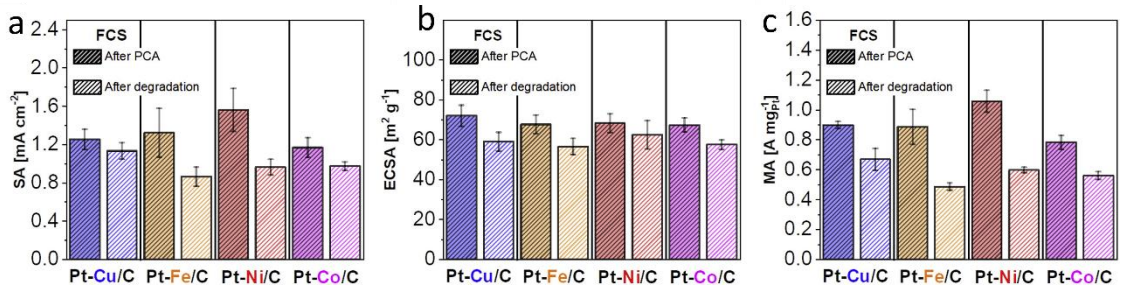

Figure 4.8: Electrocatalytic performances of Pt-M/C alloys from FCS after activation and after degradation. a) Specific activity. b) Electroactive surface area. c) Mass activity.

EDXS-STEM can be used after PCA and ADT in order to get a better understanding of the changes of the catalysts (Figure 4.9). However, the previously discussed inhomogeneity of the samples makes the analysis questionable or subjective as only a fraction of the catalyst, which might not be representative of the whole sample, is examined.

Figure 4.9a reveals the composition of the areas with small nanoparticles (as seen in Figure 4.4) and deliberately without pure M phases of the as-purchased catalysts. During activation, the less noble metals dissolve (dealloying) and a core-shell structure and/or porosity are formed[64, 138, 156]. Under ADT, the catalysts undergo a similar phenomenon as during PCA but to a higher extent. Therefore, it is hypothesized that a higher loss of the less noble metal in the relative chemical composition would correlate with a higher loss of the positive effect on activity (ligand/strain) and thus a higher decrease of SA. This correlates nicely for Pt-Ni/C. This catalyst experienced a big loss in Ni content (Figures 4.9b and 4.9c) and the highest one in SA. However, the same is not true for Pt-Fe/C and Pt-Cu/C. In both cases, the loss of M (Cu or Fe) was insignificant after ADT while a loss of SA was observed. Once again, this points to the difficulty of understanding and comparing seemingly comparable electrocatalysts.

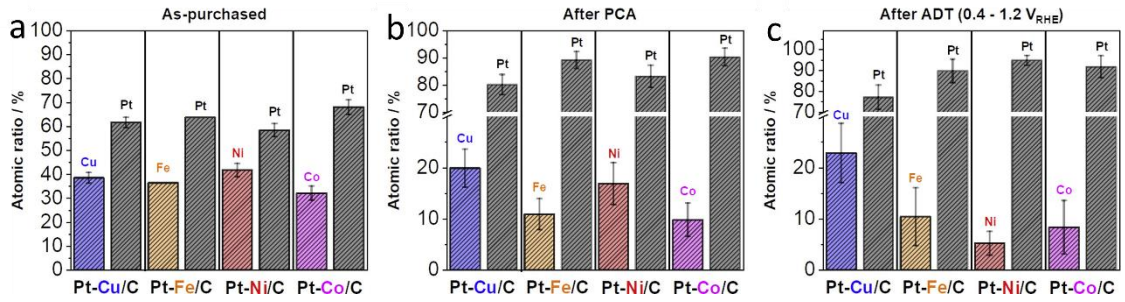

Figure 4.9: Atomic percent of M and Pt in Pt-M/C alloys from FCS as obtained by EDXS measurement. a) Atomic percent in the as-purchased catalysts. b) Atomic percent in the activated catalysts. c) Atomic percent in the degraded catalysts.

The (S)TEM analysis after PCA (Figures 4.10a-d) reveals how the same activation protocol induces various phenomena for different Pt-alloys. For example, Pt-Cu/C shows a mix of smaller (~2–10 nm) and larger nanoparticles (> 10 nm) while Pt-Fe/C and Pt-Ni/C present a more uniform particle size distribution. In the case of Pt-Co/C, the same mix of sizes as for Pt-Cu/C is observed but in addition, it also displays nanoporosity. This is observed despite the similar chemical composition of the as-purchased catalysts.

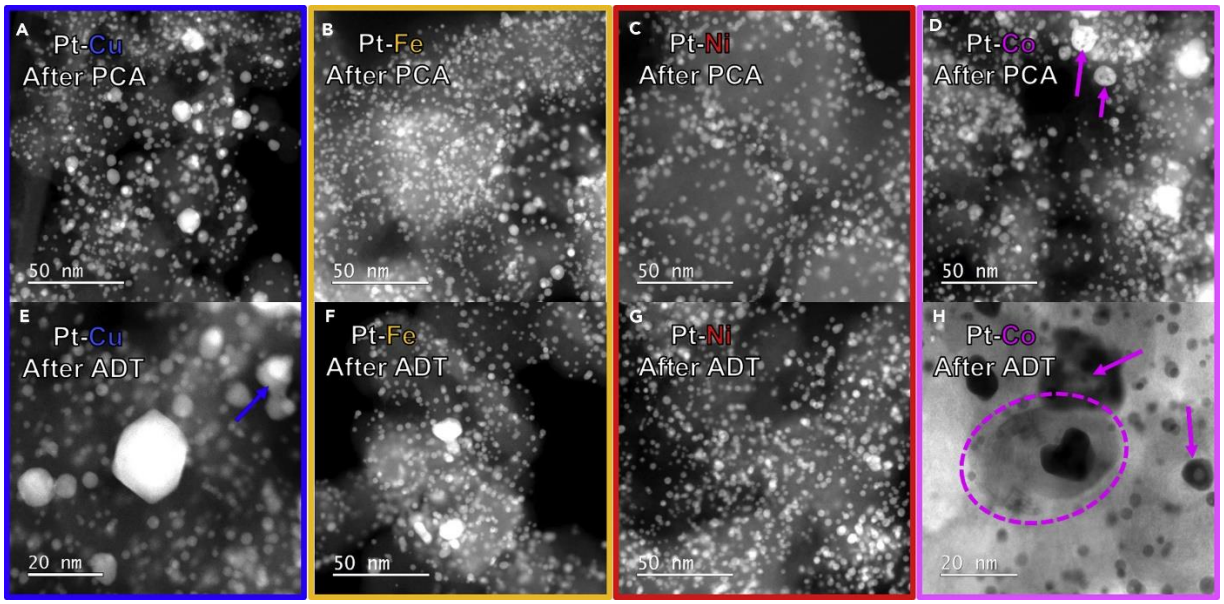

Figure 4.10: STEM comparison of Pt-M/C alloys from FCS. a-d) After activation. e-h) After degradation. The color code is: Pt-Cu = blue, Pt-Fe = orange, Pt-Ni = red and Pt-Co = magenta.

The same (S)TEM analysis after ADT provides more information (Figures 4.10e-h). In the case of Pt-Cu/C, in addition to the previously observed mix of particle size, necking and agglomeration were also observed. This explains the loss of ECSA observed in RDE (Figure 4.8b). However, no Cu is lost during the degradation as seen in Figure 4.9c. For Pt-Fe/C, agglomeration was noticed after ADT which correlates with the loss of ECSA observed (Figure 4.8b). Oppositely, Pt-Ni/C does not present major structural change, accordingly to the almost constant ECSA before and after ADT. Nonetheless, a lot of Ni was lost during ADT, causing a loss of activity. Finally, Pt-Co/C shows similar features

after PCA. Namely, a mix of small and large nanoparticles with core-shell or porous structure. In addition, a carbon nanotube was observed growing out of a nanoparticle. However, without knowing the history of the particle, it is impossible to know at which step this phenomenon happened.

Hereby, it was shown that comparing Pt-M/C alloys with only M as a varying parameter is impossible. Many differences were exposed that affect the structure-property relationship and thus performances of the catalysts. All the different alloys look promising and further on, "online" techniques were performed on the different Pt-M/C catalysts to understand better the mechanism of dissolution and attempt to differentiate them.

4.2.3 Online metal dissolution of Pt-M/C electrocatalysts

Classic analytical methods provide information about the difference in the behavior of Pt-M/C electrocatalysts. However, advanced methods are needed to get deeper insight and understanding. Therefore, we investigated the online dissolution of the four alloys at a ppb range resolution using an electrochemical flow cell coupled to an inductively coupled plasma mass spectrometer (EFC-ICP-MS)[129, 167, 168]. Both Pt and M dissolution are followed during slow cyclovoltammetry.

Two sets of measurements were performed (Figure 4.11). First, the dissolution of the Pt-alloys in the as-purchased state (without any prewashing or activation) was monitored during slow cycles from 0.05 to 1.X V_{RHE} (where X =0, 2, 4; at 5mV/s). During the second set of measurements, the same protocol was applied but after an activation step. Thereby, insights into the intrinsic dissolution mechanisms of the Pt-alloys in their "pristine" state could be gained and then compared with the activated versions, with richer Pt surfaces.

The Pt dissolution (in black in Figure 4.11) is in accordance with the literature[61, 129, 138, 169, 170]. Namely, the cathodic dissolution peak (C1) is higher than the anodic peak (A1) while cycling to 1.4 V_{RHE}. The anodic dissolution provokes surface structure roughening caused by the oxide place exchange mechanism[61], which creates defects. These defects are not passivated by oxide formation and can dissolve. The cathodic dissolution is due to restructuration of the surface and creation of unstable low coordinated sites which occur during the reduction of Pt-oxides[169]. The less noble metal dissolution follows the dissolution of Pt. Every time Pt dissolves, the previously protected M atoms are now exposed and prone to dissolution[138]. This is common to all Pt-M alloys, and it is observed in both anodic and cathodic directions (A1' and C1' for M, respectively). Therefore, stabilizing Pt would suffice to improve the stability of Pt-M alloys[171-174]. However, an unrelated M dissolution peak can also be observed, A2'. This peak is either due to the direct dissolution of un-alloyed M (Pt-Ni, Pt-Co, and Pt-Fe) or due to a strong interaction between M and Pt surface (the transition metal under potential deposition, M_{upd}, particularly visible for Pt-Cu).

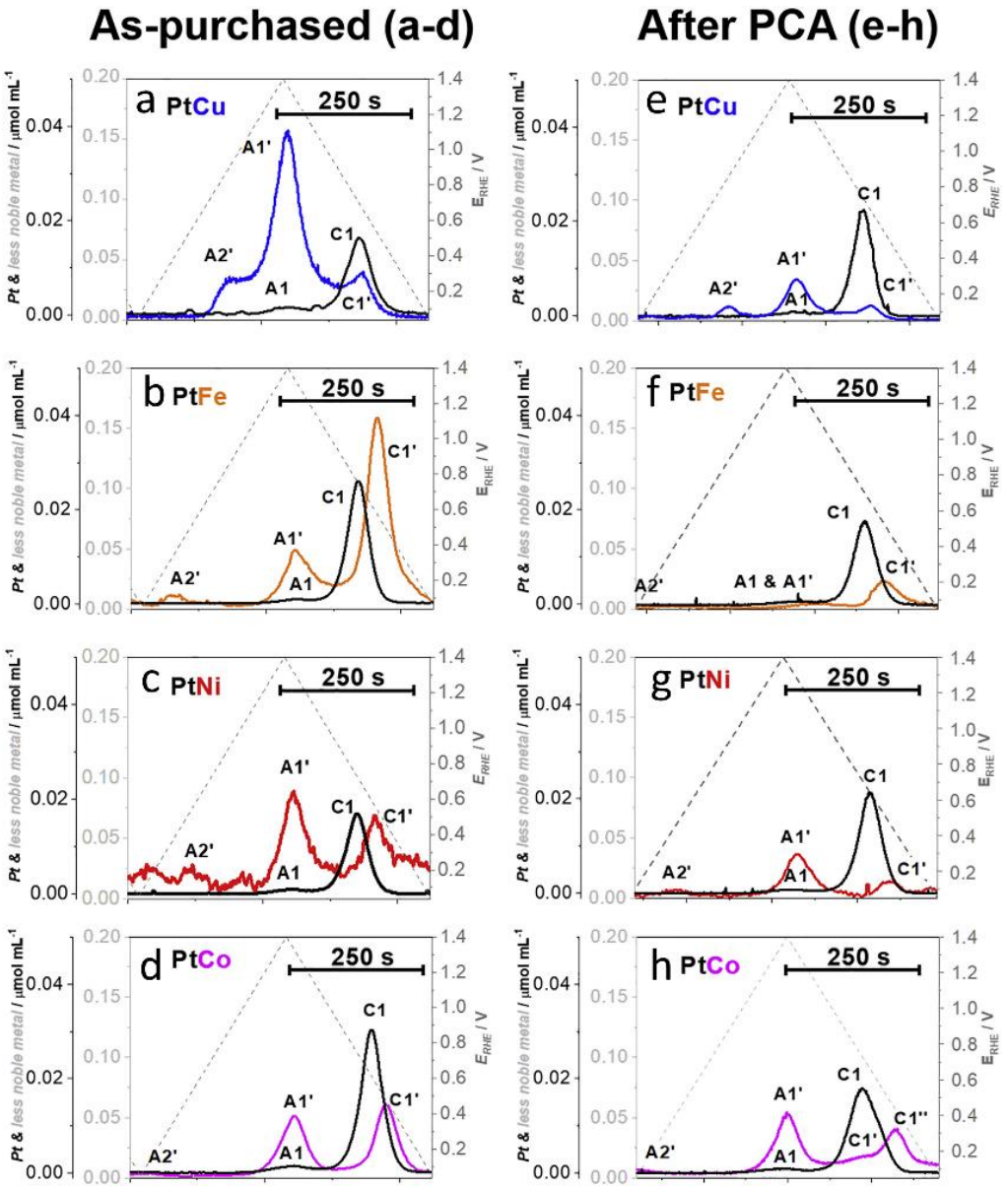

Figure 4.11: Online dissolution of Pt (black) and M (colored) in Pt-M/C alloys from FCS. a-d) As-purchased state. e-h) After activation protocol.

The four Pt-M analogues can be divided into two groups based on which peak becomes the dominant peak for M (anodic or cathodic). In other words, which peaks among A1' and C1' grows the most while increasing the upper potential limit (UPL) up to 1.4 V_{RHE}. In the first group, anodic dissolution is predominant over cathodic dissolution (A1'>C1') when increasing the UPL. This is observed for Pt-Cu and Pt-Ni. In the second group, for Pt-Fe and Pt-Co, the trend is reversed, and the cathodic peak becomes more important when UPL increases (C1'>A1') (Figure 4.12).

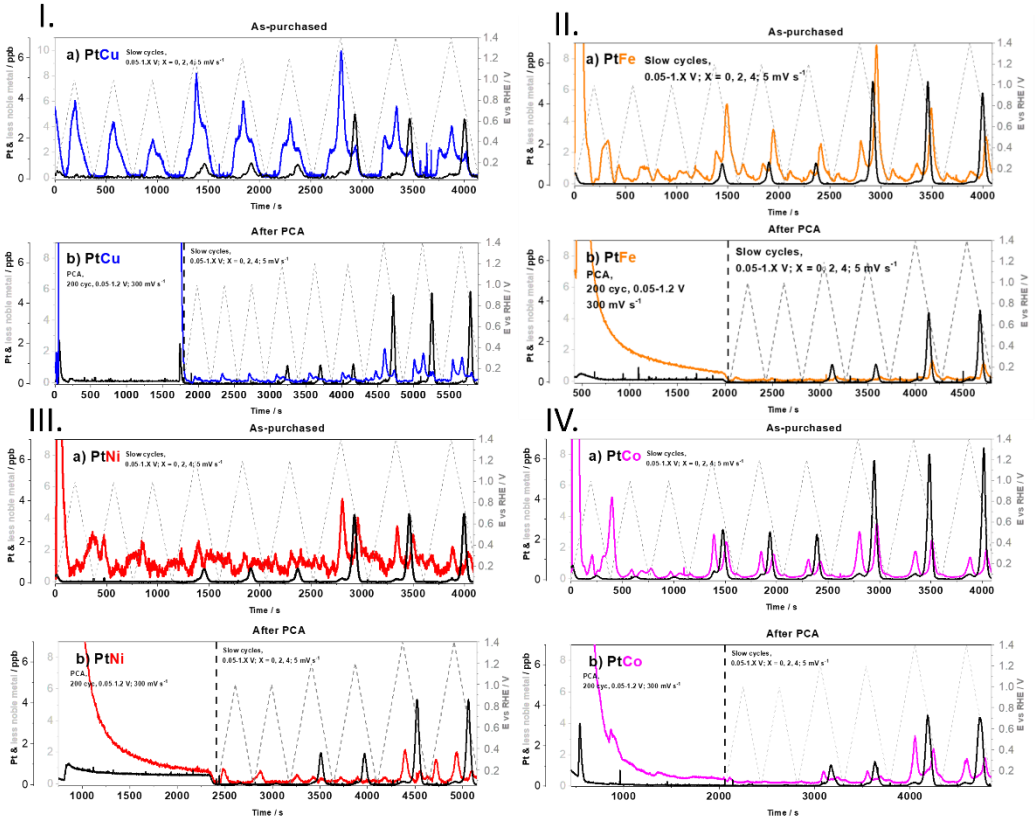

Figure 4.12: Online dissolution of Pt-M/C alloys from FCS during cycling from 0.05 to 1.X V_{RHE}, where X is 0, 2, 4. a) As-purchased. b) After an activation protocol. I. PtCu/C. II. PtFe/C. III. PtNi/C. IV. PtCo/C.

Interestingly, after PCA, the mechanism for each alloy is similar to before and thus the previous separation into two groups is still valid. In other words, the intrinsic mechanism of dissolution does not change even after the removal of M from the near-surface region. Moreover, while M dissolution decreases drastically for the activated samples (as expected), the Pt dissolution stays in the same order of magnitude. Once again, the dissolution of Pt is followed by the dissolution of M, pointing out that the stability limiting factor is the stability of Pt.

Therefore, each alloy possesses its own benefits and restrictions for applications (in PEMFC). Each transition metal brings strong and weak points while alloyed with Pt, the pros and cons of each Pt-M/C catalyst are presented below.

1. Pt-Cu alloy presents the best resilience toward the leaching of M, and extremely good long-term ORR activity (Figure 4.8). In addition, the intermetallic phase is easily formed[127, 138, 175], slowing down the leaching of M[152]. Moreover, the encapsulation of Pt-M nanoparticles with a carbon shell due to the high temperature treatments is not a concern for Pt-Cu due to the low carbon solubility in Cu[163]. Therefore, Pt-Cu looks like one of the best choices for application in RDE studies. However, Cu has been shown to have a negative effect in real devices[176, 177]. Thus, to transmit the performances of Pt-Cu from the lab to real application, the leaching of Cu needs to be eliminated. One option is through more complicated alloys (ternary alloys) that focus on the stability of M[172, 178].
2. Pt-Fe presents the same benefits as Pt-Cu. Namely, easy formation of intermetallic phases[179, 180], and rather good keeping of M during operations. However, Fe ions are

even worse than Cu if present in PEMFC. Indeed, Fe ions can catalyze the formation of radicals (Fenton reaction)[181] which heavily degrade the membrane in PEMFC. Therefore, even more than for Pt-Cu, the leaching of Fe needs to be prevented before reaching the application.

3. Pt-Ni does not form intermetallic phases as easily as the two previously discussed alloys. The carbon solubility in Ni is an order of magnitude higher than for Cu[163] (and Fe) and thus one hypothesis is that it prevents facile crystallization due to the ternary nature of the Pt-Ni-C phase system where carbon acts as an impurity in the crystal lattice. The high solubility of carbon also leads to a thick carbon shell during the synthesis if high temperature treatments are used, limiting the usable synthesis parameters[45]. Furthermore, the carbon shell has a negative effect on the performance at high current density in PEMFC, possibly affecting the O_2 transport resistance[182]. It also requires an additional effort of removing the shell during chemical activation compared to other alloys[183]. On the positive side, the Ni ions have a less negative effect on PEMFC compared to Fe or even Cu ions[180], even if it was shown that Ni ions still negatively affect the O_2 transport resistance and the water uptake of the ionomer[140]. Pt-Ni could be a viable candidate, it has already been demonstrated[139, 142, 184], but its synthesis is more challenging than for other alloys and, as for all alloys, the leaching of M should be significantly decreased.
4. Pt-Co is the closest alloy to end-user products, its presence in some devices has already been shown[185, 186]. Indeed, it has many advantages. First, the encapsulation issue with carbon shell is not as problematic as for Ni. Secondly, the formation of intermetallic phases is possible[150, 187]. Furthermore, Co^{2+} ions in PEMFC behave similarly to Ni ions, with relatively low impact[140, 188]. However, the Co sources and mining practices are extremely controversial, as already highlighted in the Li-ion battery sector, which is going to eliminate the use of Co[189]. If a fair-trade origin becomes available for Co, it could be the best option. Although, Co leaching needs to be tackled, as for all Pt-alloys, before deployment of end-user products.

Pt-Co looks like the best option in terms of performance but the access to its raw precursors needed for synthesis is controversial at best. On the other hand, Pt-Fe is not considered before extreme improvements due to the extremely problematic Fe ions in the real device. Therefore, Pt-Cu and Pt-Ni are the two options considered, with different problems. Decreasing Cu ions leaching is more important for PEMFC stability while Pt-Ni presents more synthesis challenges.

4.2.4 Corrosion of the carbon support

The dissolution of metal nanoparticles is not the only material of the electrocatalyst that can be responsible for degradation. The carbon support can also degrade, and its degradation leads to further agglomeration and/or detachment of Pt-based nanoparticles[60]. Many properties of carbon support play a role in its stability but also in Pt activity. For example, the porosity size and type of the carbon are important since the nanoparticles located in micropores exhibit suboptimal mass transport resistances and thus lower activity[187, 190]. Among others, the degree of graphitization, surface area and functional groups have been revealed to play a crucial role in carbon stability or Pt-utilization[191-193].

The currently used carbon supports (such as Vulcan XC72 and Ketjen Black EC300J), despite being relatively stable, are already thermodynamically prone to oxide into CO_2 at a potential of 0.207 V_{RHE}[89]. In addition, the kinetics of the reaction is accelerated by Pt and by the PEMFC operation conditions (80°C)[194, 195]. Therefore, slowing down the support corrosion is a major challenge to improve the overall stability of the catalyst.

The corrosion behavior of carbon can be assessed by tracking the CO_2 released from the material under electrochemical protocol thanks to Electrochemistry Mass-Spectrometry (EC-MS)[196]. In the case of the Pt-M/C catalysts, similar carbon corrosion was observed indistinguishably from the M present in the alloy (Figure 4.13a). The carbon used for the support (Vulcan XC-72) is the same and thus a similar degradation was not surprising. It can be concluded that the type of alloy does not have an impact on the stability of the carbon. In the case of Pt/C benchmarks (Ketjen black EC300J carbon) (Figure 4.13b), the carbon corrosion is higher (higher CO_2 signal) but the Pt loading, known to accelerate carbon corrosion, is also higher.

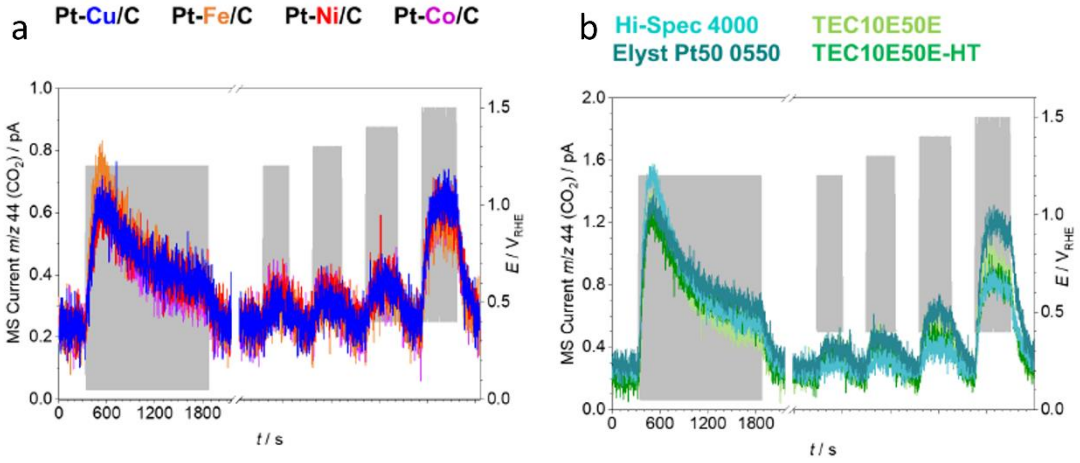

Figure 4.13: Carbon corrosion experiments. a) m/z=44 signal (CO_2) of Pt-M/C electrocatalysts. b) m/z=44 signal (CO_2) of Pt/C electrocatalysts. The protocol consists of an activation protocol followed by subsequent sets of 20 cycles with increasing UPL (0.4–1.X V_{RHE}; X = 2, 3, 4, 5; 100 mV/s).

4.2.5 High Resolution Identical Location TEM

Although the presented methods (RDE, XRD, ICP-OES, EFC-ICP-MS and EC-MS) provide useful information about the average structure properties and electrocatalytic performances, other techniques are more interesting for an in-depth understanding of local structural change. For example, high-resolution identical-location TEM (IL-TEM) allows to see the history of the exact same nanoparticles before and after electrochemical treatment[156, 197, 198], and thus to reliably understand the processes happening.

The IL-TEM was performed before and after PCA on Pt-Co/C as a showcase of the technique. Figure 4.14 shows the differences for the same nanoparticles of Pt-Co/C samples and three nanoparticles were studied at atomic resolution. Atomic resolution is needed as "low magnification" IL-TEM pictures do not reveal significant changes except for coarsening of largest nanoparticles as seen in Figure 4.14. In the atomic resolution images, nanoparticle number 1 not only shrinks under PCA but also undergoes a change of morphology, with different facets exposed. Nanoparticles number 2 and 3 have shrunk more, probably due to dealloying of Co during PCA. Therefore, it seems that smaller nanoparticles are more exposed to degradation processes/dealloying than bigger ones. This exemplifies the benefits of directly looking at the same particles before and after electrochemical treatment to understand the ongoing processes and not the average results.

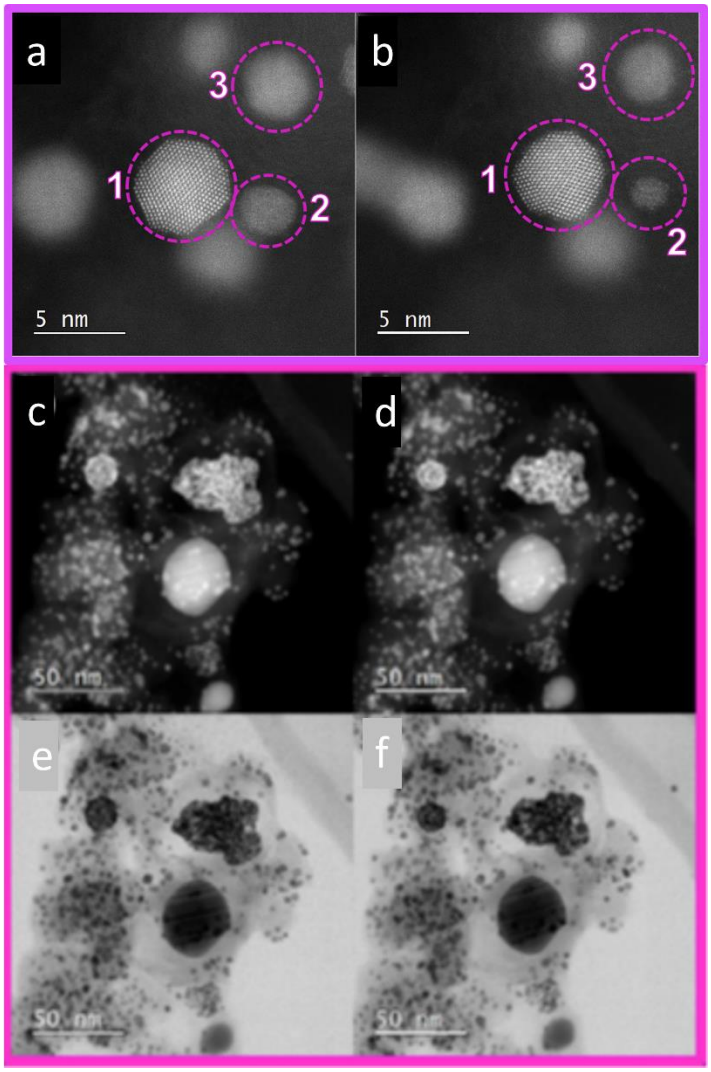

Figure 4.14: IL-STEM comparison of PtCo/C from FCS electrocatalyst before and after PCA. a, c and e) Before activation. b, d and f) After activation.

To go further, an in-depth analysis can be performed on a single nanoparticle. This allows us to directly see which facets disappear or shrink, or new atomic columns grow due to redeposition. Moreover, some calculations can be performed to measure the displacement of atomic columns and observe a change in strain in the nanoparticle or to figure out the coordination number of surface atoms[199, 200].

This knowledge is useful for understanding structure-relation properties and in the future to optimize and design the next generation of catalysts with improved properties, but it goes out of the scope of this chapter and work in general and the interested reader is invited to read the reference [69].

4.3 Conclusions

In the present study, differences in seemingly comparable Pt/C and Pt-M/C commercially available benchmark catalysts were exposed. In doing so, the complexity of the structure of real ORR catalysts was uncovered together with the fact that the conventional analytical methods for electrocatalysts (RDE, XRD, TEM) are limited to average materials characteristics. Therefore, the observed differences, notably in alloys, cannot be explained

by the average-out material properties (e.g. metal loading, Pt/M composition, carbon support, particle size distribution, electrochemical surface area, etc.). Online methods such as EFC-ICP-MS or EC-MS provide a better understanding of ongoing mechanisms, especially stability-wise. This is sufficient to analyze pros and cons of Pt-M/C for application in PEMFC or URFC, but we wish to emphasize that it is not enough to understand at a deeper level the processes happening. For this, an atomic level study should be conducted using a method such as IL-TEM.

Nonetheless, Pt-Co/C was shown to be the most promising alloy, but the controversial sources of its precursors lead us to rule it out. Among the three other alloys, Pt-Fe was excluded due to the Fenton reaction catalyzed by Fe ions in PEMFC. Pt-Ni and Pt-Cu were both good candidates as ORR catalysts in the further bifunctional catalyst. They both present good activities, with PtNi > PtCu, and stabilities, particularly for PtCu. The main decisive feature of the selection between the two alloys were the challenges in the PtNi synthesis, dismissing it. Therefore, among all the Pt-alloys, Pt-Cu/C was selected as a good ORR candidate to be a part of the bifunctional catalyst.

Chapter 5

$TiON_x$ as Supporting Material for Ir During OER

Titanium oxynitride ($TiON_x$) is investigated as a potential support for iridium nanoparticles as oxygen evolution reaction (OER) electrocatalyst. Good electrocatalyst support should have sufficient conductivity, effective dispersion of the nanoparticles, highest surface area possible and be stable under demanding reaction conditions. These different parameters were studied and optimized in this chapter.

5.1 Introduction

Decreasing the amount of PGMs used in proton exchange membrane water electrolyzers is a necessity for widespread usage of this technology – a requirement to tackle down the use of fossil fuel and thus global warming. For this, the oxygen evolution reaction (OER) catalysts at the anode, involving iridium, need to be designed in a more rational way, namely, lowering the PGM loading to a minimum while keeping the same electrocatalytic performances.

One possible improvement is by finely dispersing Ir nanoparticles on a suitable support[99], similarly to Pt in a fuel cell. However, carbon used for oxygen reduction reaction (ORR) catalysts is not an option as it is not stable under OER conditions[89]. Several other materials have been proposed as potential support for OER catalysts. The most studied ones are titanium and its oxides[100, 119, 201-203] as well as metal nitrides[94, 95, 204], carbides[91, 92, 205], perovskite[93, 206] and, some other conductive oxides[92, 96-98] as antimony-, fluorine- or indium-doped tin oxide, (ATO, FTO and ITO)[99, 105, 207-209]. Unfortunately, this kind of material usually lacks sufficient conductivity[70] and therefore doping is needed to help to tune the properties of such materials. However, da Silva et al. showed that the doping element can leach out and thus decrease the stability of the support, questioning the use of such dopant[107]. In addition to lowering the overall cost of the OER catalysts, support can also improve the performance of the catalyst due to the known strong metal-support interaction (SMSI)[53, 55, 210].

The idea behind $TiON_x$ as a support is to use a cheap precursor (TiO_2 or TiN) that can either be relatively easily nitrated or oxidized to the desired $TiON_x$ compound[211]. The latter could combine the stability of TiO_2 and the good conductivity of TiN, making it suitable support under OER conditions. In addition, TiO_2 or TiN can be synthesized in various nanostructures which makes it possible to tune the morphology of the support[212-214]. Afterwards, Ir nanoparticles can be nicely dispersed on the prepared support.

Later, a graphitized carbon template was used to further improve the surface area of the support. Carbon possesses surface areas that are one order of magnitude larger than Ti-based material[91, 204, 215, 216] and thus depositing the Ti phase on a high surface area carbon allows a higher surface area than pure Ti-based support. The carbon template stability should be assessed to make sure not to introduce a weak point in the catalyst but if it is nicely covered by the $TiON_x$ flakes, the carbon would in principle not be in contact with the acidic environment and thus be protected.

5.2 Investigation of $TiON_x$ Properties as Potential Support for OER

Parts of the following text were published in ChemCatChem under the title "Towards stable and conductive Titanium oxynitride high surface area support for Iridium nanoparticles as OER electrocatalysts"[217].

M. Bele, K. Stojanovski, P. Jovanovič, L. Moriau, G. Koderman Podboršek, J. Moškon, P. Umek, M. Sluban, G. Dražič, N. Hodnik, and M. Gaberšček

As a co-author, L. Moriau participated in the electrochemical experiments, discussion, comparison with the literature, and writing of the draft. N. Hodnik and M. Gaberšček are corresponding authors and principal supervisors.

First, the basic characteristics of $TiON_x$ support were investigated. Indeed, before optimizing and studying all the parameters that could influence activity/stability, a feasibility study was conducted to first provide answers to crucial and fundamental questions: i) Is electrical conductivity of the support ($TiON_x$) sufficient for the electrocatalytic application? (ii) Can the support host active nanoparticles (Ir) in a finely dispersed form? (iii) How does the performance of the new catalytic composite ($Ir/TiON_x$) compare to the state-of-the-art composites?

5.2.1 Structural characterization

SEM, STEM, and XRD were performed on the prepared $Ir/TiON_x$ samples (see Chapter 3.1.1.1), and the results are shown in Figure 5.1. The observed diffraction peaks of $Ir/TiON_x$ samples are characteristics of cubic iridium $2\,\theta = 41.0°$and $47.6°$ (International Centre for Diffraction Data, Ref: 00-001-1212), and of the cubic titanium oxynitride: $2\,\theta = 37.2°$and $43.2°$ (TiO_xN_y with $x+y \approx 1$)[212] (Figure 5.1d). Broad iridium diffraction peaks are due to the small particle size of the nanoparticle as seen in the STEM micrographs (Figures 5.1b and 5.1c). The $TiON_x$-Nanoribbon (NR) shown in SEM and STEM is in the form of partly crystallized, up to 1 micrometer-sized irregular ribbons.

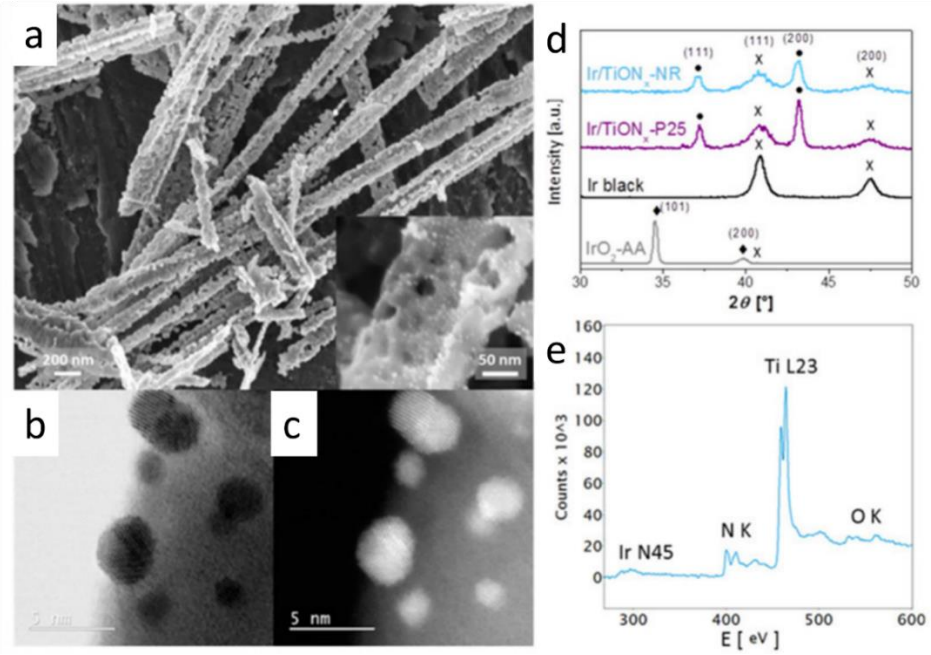

Figure 5.1: a) SEM image showing typical morphology of prepared $TiON_x$-NR sample with the insert of Ir/$TiON_x$-NR. HAADF-STEM micrographs of individual Ir nanoparticles on $TiON_x$-NR support are shown in b) bright field and c) dark field. d) XRD spectra for Ir/$TiON_x$-NR, Ir/$TiON_x$-P25, homemade Ir black and IrO_2-AA. Peaks (X) correspond to iridium, peaks (*) to titanium oxynitride and peak (◆) to IrO_2 (rutile structure). d) EELS spectrum of Ir/$TiON_x$-NR where Ir N4,5, Ti L2,3 and O K edges are visible.

The support is uniformly covered with spherical, well-crystallized iridium nanoparticles with a mean particle size of 3.3 nm (Figure 5.2a). The mean particle size for Ir/$TiON_x$-P25 is slightly lower with a size of 2.6 nm (Figure 5.2b). In both cases, the particles are smaller than unsupported benchmarks Ir catalysts. The IrO_2 (Alfa Aesar) has an average particle size of 8.8 nm while Ir-black (Alfa Aesar) has the biggest particle size with 9.8 nm (Figures 5.2c and 5.2d). In addition, the latter presents significant agglomeration due to sintering which further reduces the accessible Ir surface. The Ir nanoparticles supported on $TiON_x$ do not present any agglomeration which indicated that the nanoparticles are firmly anchored onto the substrate. Therefore the interaction with the support prevents surface migration during annealing. The BET specific area of both $TiON_x$ composites, NR and P25, is similar with a value of 48 m^2/g and 52 m^2/g, respectively. Therefore, the formation of well-dispersed, small nanoparticles on both supports is attributed to the novel synthesis procedure, namely the use of iridium (III) bromide precursor. The latter is highly soluble in ethanol at 50°C and thus it precipitates rapidly during drying. This helps slow down the mobility and growth of Ir nanoparticles.

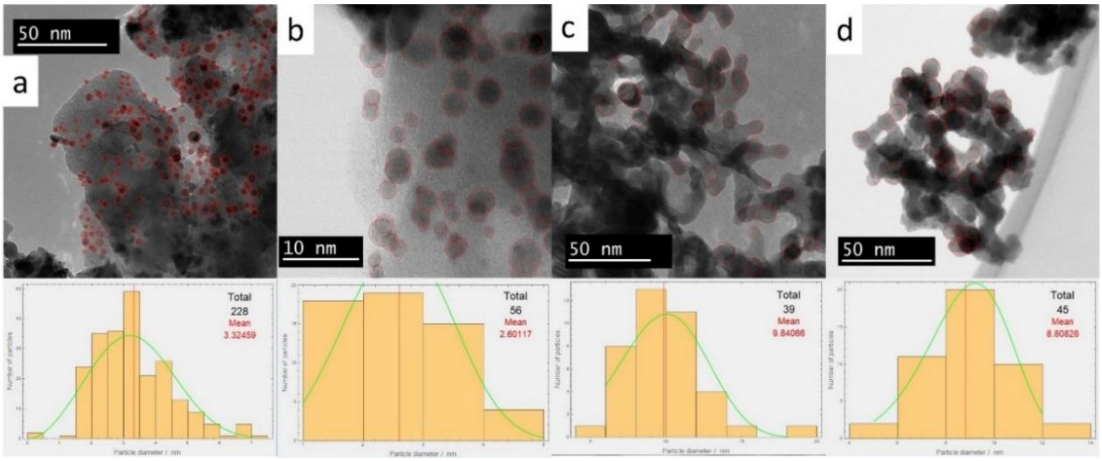

Figure 5.2: TEM pictures and iridium nanoparticles average size distribution of a) Ir/$TiON_x$-NR. b) Ir/$TiON_x$-P25. c) Ir-black. D) IrO_2.

To be conductive, the support needs to possess sufficient nitride parts. EELS spectrum, displayed in Figure 5.1e, shows Ti L2,3 lines, Ir N4,5 as well as N K and O K lines. Based on the intensities of the lines, one can conclude that the content of nitrogen is higher than that of oxygen while the absence of t_{2g} and e_g splitting of Ti L3 and Ti L2 lines due to crystal field in octahedrally coordinated titanium ion indicate that most of the titanium is in the Ti^{3+} valence state. Nonetheless, the electrical conductivity was measured by pressing the samples in the form of pellets. Ohmic-like behavior was measured in a wide span of applied currents (current scan) from 1 $\mu A/cm^2$ up to 1 A/cm^2. Conductivity of as-synthesized, pure (without Ir) $TiON_x$ substrates ($TiON_x$-NR, $TiON_x$-P25) is shown in Table 2, as well as some different carbon substrates or potential oxide-based support. The conductivity of $TiON_x$ substrates is similar to the carbons when the samples are prepared in the same way (i.e. based on pressed and heat-treated powder). The preparation of the sample influences the measured conductivity due to the quality of inter-particle contact and is usually lower than the intrinsic conductivity of bulk material in preferential crystallographic direction (e.g. data for graphite). The conductivity of $TiON_x$, without the presence of Ir nanoparticles, fills the requirement for electrocatalysts support. In fact, it is notably higher than the conductivity of the most study potential support, antimony-doped SnO_2 (ATO)[126].

Table 2: Comparison of room temperature specific conductivities of present $TiON_x$ substrate with conductivities of selected carbon materials.

Materials	Conductivity, σ ($\Omega^{-1}.cm^{-1}$)
Graphite, a axis[218]	$2.6.10^4$
Graphite, c axis[218]	1.10^2
Polycrystalline graphite[218]	$1.3.10^3$
Glassy carbon[219] [220] [52]	$(1\text{-}3).10^2$ $(2\text{-}10).10^2$ $(0.47\text{-}0.69)^a$
Acetylene black[221]	24^b
Pure TiO_2, pressed pellet (2T) [222]	2.10^{-10}
$TiON_x$, pressed pellet (2T)	3.3
$TiON_x$, pressed pellet (2T) and sintered	7.8

Sb-doped SnO_2 (ATO), pressed pellet[223]	0.11

a. Special form of glassy carbon with open porosity. b. After treatment at 1000°C in N_2.

5.2.2 Electrochemical Performances

Figure 5.3 displays the electrochemical performances of the catalysts before (beginning of life, BoL) and after (end of life, EoL) degradation. The mass activity of both $Ir/TiON_x$ samples largely surpasses the activity of IrO_2. $Ir/TiON_x$-P25 shows the best activity while $Ir/TiON_x$-NR presents an activity close to the second benchmark, Ir-black. The better activity of $Ir/TiON_x$ catalysts is in line with better utilization of iridium, i.e. more electrochemical surface area exposed, due to the smaller average particle size (2.6 for $Ir/TiON_x$-P25 and 3.3 nm $Ir/TiON_x$-NR). Commercial rutile IrO_2 powder exhibits a lower activity, according to literature[224, 225]. Importantly, the activity of blank $TiON_x$ substrates was negligible (Figure 5.3c).

After initial OER activity measurements, the stability of the materials was tested. A CP protocol was applied to all samples, namely a current of 0.1 A/mg_{Ir} for 5h, and then the activity was measured again (EoL). Apart from IrO_2 which is known to be stable, the most stable catalyst is $Ir/TiON_x$-NR while $Ir/TiON_x$-P25 shows the lowest activity retention. The great difference in stability between the two $Ir/TiON_x$ composites is ascribed to, on one hand, the loss of electrical conductivity due to surface oxidation at the contacts between individual $TiON_x$ particles in the case of $Ir/TiON_x$-P25. On the other hand, due to the unique elongated morphology of $Ir/TiON_x$-NR sample, it exhibits statistically fewer contacts and thus less passivation of the surface-related problems (Figure 5.4). Nonetheless, the support can sustain the OER conditions even if its morphology plays a role in the stability. This parameter (morphology of the support) will be studied later as here the fulfilling of electrocatalyst support requirements by $TiON_x$ is investigated.

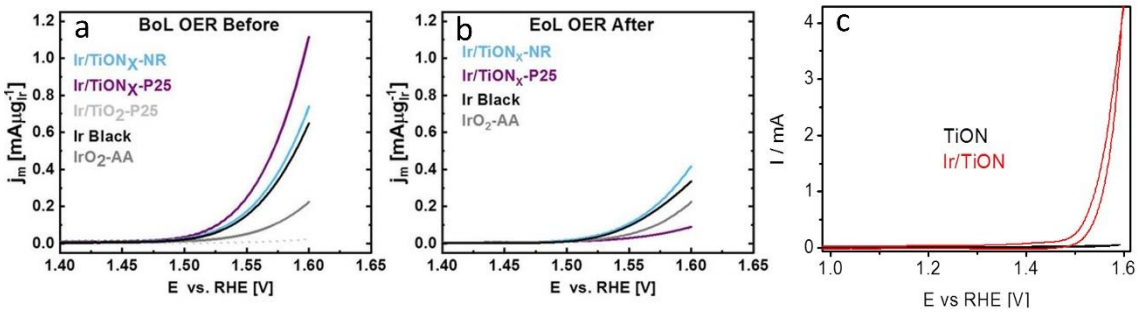

Figure 5.3: OER activity polarisation curves (anodic branch) of the studied catalysts at 20 mV/s, 1600 RPM in 0.1 M $HClO_4$. a) Before a 5-h chronopotentiometric degradation protocol (0.1 A/mg_{Ir}) (Beginning of life, BOL). b) After (End of life, EOL). c) Comparison of current response under OER conditions of $TiON_x$ support and the $Ir/TiON_x$-NR analogue.

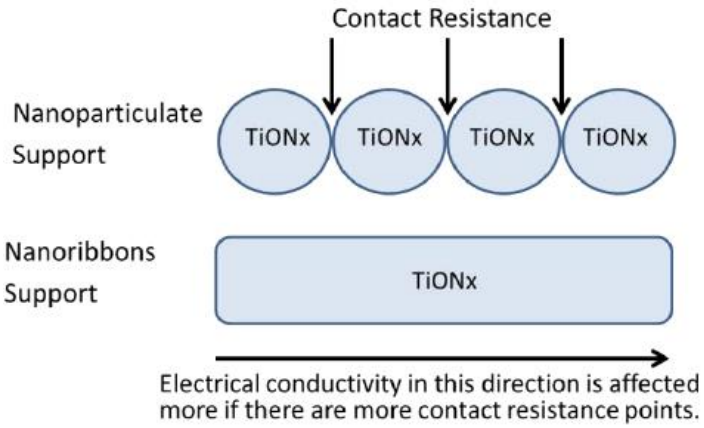

Figure 5.4: Scheme of the contact difference between nanoribbons – $TiON_x$ and nanoparticle – $TiON_x$

Ir nanoparticles have been nicely dispersed on $TiON_x$. The support has also shown to be reasonably stable, depending on the morphology. In addition, in some cases, the support affects the catalyst activity through the so-called strong metal support interaction, SMSI [53, 55, 210]. The potential presence of this effect between Ir and $TiON_x$ was investigated by fast potentiodynamic CVs. For this purpose, Ir/$TiON_x$ was compared to another homemade catalyst with a different support material, i.e. Ir/C. The particle size distribution on Ir/C was similar to Ir/$TiON_x$. By alterations of the characteristic iridium voltammetric features during fast cycling, several differences in electrochemical behavior of Ir/$TiON_x$-NR and Ir/C can be observed (Figure 5.5), these disparities are related to the interaction between Ir and the different supports[98].

The H_{upd} feature, which can be seen below 0.4 V_{RHE} for metallic Ir, remains visible throughout the entire protocol for Ir/$TiON_x$-NR while it gradually disappears for Ir/C. It means that the availability of Ir metals to protons is decreasing more rapidly for Ir/C than for Ir/$TiON_x$-NR. One can assume that there is either no oxide in the Ir/$TiON_x$-NR or that the oxide layer structure is significantly different in the two samples. For example, a fast decrease of the H_{upd} peak could point to a thinner layer of hydrous oxide in the case of Ir/C in comparison to the Ir/$TiON_x$-NR analogue[226]. According to extensive work on iridium oxides, only the compact "inner" oxide gets reduced in the cathodic sweep while hydrous oxide does not. Therefore, the hydrous oxide layer remains and grows with cycling number. Hydrous oxide is a very porous solid or gel-like structure and thus lets protons pass through. As H_{upd} feature is still observed for Ir/$TiON_x$-NR, it is assumed that hydrous layer grows on the Ir nanoparticles while "inner" oxide, impermeable to protons, grows on Ir/C. This is further supported by the reversible CV peak at around 1.15 V_{RHE} that corresponds to the formation of Ir (IV) and is visible throughout 200 voltammetric cycles in the Ir/C sample.

The results in Figure 5.5 indicate that an interaction between $TiON_x$ support and Ir nanoparticles exists, and it is inhibiting the growth of "inner" oxide or boosting the formation of hydrous porous oxide. This inhibition of "inner" oxide has been observed with in-situ techniques for other supports like ATO[227] or TiN[94]. It affects the activity and stability according to the literature. Indeed, amorphous hydrous oxides are the most active OER catalysts in the family of Ir-based materials[228-231]. They have overall lower oxidation states compared to IrO_2[229]. The presence of electrophilic oxygen in the Ir (III/IV) oxyhydroxides are optimal precursor sites for the nucleophilic attack of (preadsorbed) water during the O-O bond formation[232, 233].

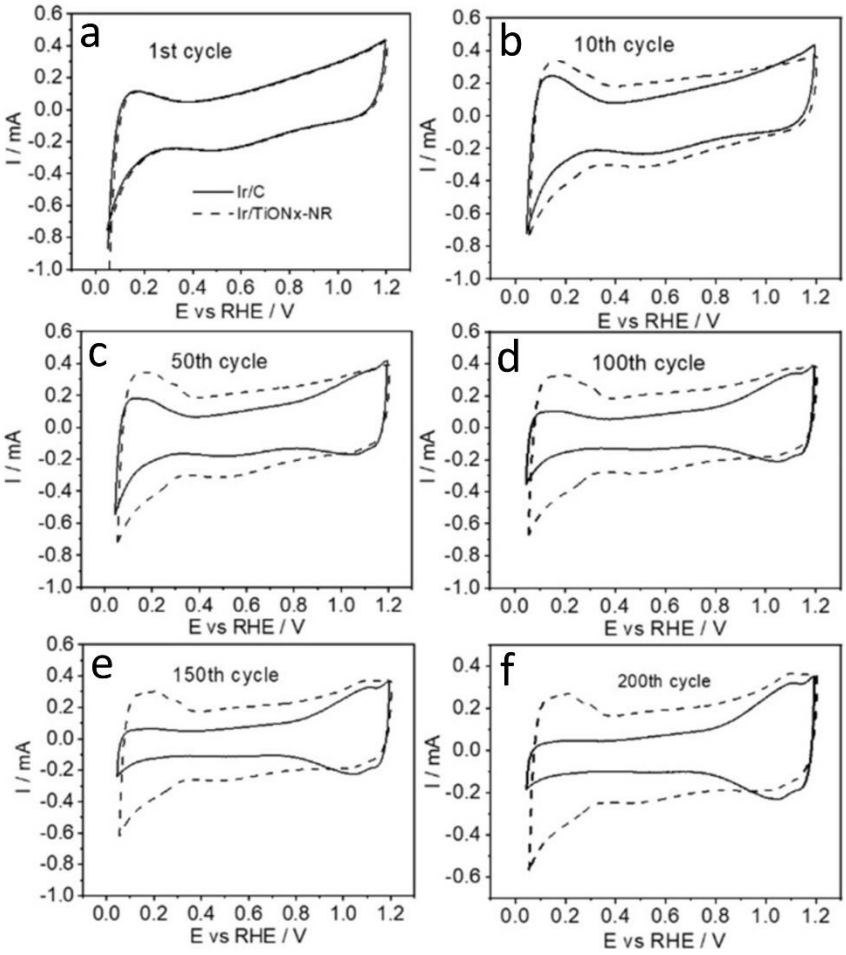

Figure 5.5: Inspection of the SMSI effect during potentiodynamic treatment (300 m/Vs, between 0.05–1.2 V_{RHE}. a-f) sequential cycles are selected for better clarity.

5.2.3 Conclusion

Titanium oxide enriched with nitrogen ($TiON_x$) can be prepared in a form that is suitable as a support for OER electrocatalysts. First, the average macroscopic conductivity of $TiON_x$ (without Ir) can reach sufficient values (between 3 and 8 S/cm) that are comparable to carbon support with similar morphology and higher than the ATO material proposed as a potential OER support. Secondly, small Ir nanoparticles can be deposited on $TiON_x$ and finely dispersed. Finally, the iridium activity and stability, when dispersed on $TiON_x$, are equal or even better than benchmark catalysts.

The improved performances can be explained by various effects such as the very good utilization of Ir (uniform dispersion of nanoparticles), retention of electric conductivity (for $Ir/TiON_x$-NR), and possibly of SMSI effect. However, several parameters can still be investigated to improve the electrochemical performances of $Ir/TiON_x$. Some hints give indications that the morphology of the support can influence the activity and stability. It could also influence the particle size or the oxidative state of Ir.

5.3 Morphological Effect of the Support on the Performances of Iridium Nanoparticles Towards OER

Parts of the following text were published in ACS Catalysis under the title "Effect of the morphology of the high surface area support on the performance of the OER for iridium Nanoparticles"[234].

L. Moriau, M. Bele, Ž. Marinko, F. Ruiz-Zepeda, G. Koderman Podboršek, M. Šala, A. K. Šurca, J. Kovač, I. Arčon, P. Jovanovič, N. Hodnik* and L. Suhadolnik**

As the first author, L. Moriau conducted the electrochemistry measurements and analyzed the results. He also assembled the various other results and wrote the initial draft in collaboration with L. Suhadolnik.

$TiON_x$ fills the requirement of electrocatalysts support, namely sufficient conductivity, stability under operations conditions, effective surface area, and fine dispersion of the nanoparticles anchored on it. In addition, the $TiON_x$ support has an impact on the activity of Ir through the SMSI effect. However, the morphology of the support can also play a role in those parameters and needs to be investigated. Hereby, we developed a new, anodic oxidation-based synthesis process for the cost-effective fabrication of high-performance OER catalysts, Ir-$TiON_x$. The anodization time during the TiO_2 growth step of the synthesis influences the morphology, structure, and composition of the support. The differences were studied using various state-of-the-art characterization methods such as X-ray photoelectron spectroscopy (XPS), scanning electron microscopy (SEM), scanning transmission electron microscopy (STEM), and X-ray diffraction (XRD). We show that the electrochemical activity and stability can be substantially enhanced, compared to the commercial benchmark IrO_2 material and other best OER catalysts in the literature, exclusively by modifying the $TiON_x$ support morphology.

5.3.1 Characterization of $TiON_x$-nh-Ir electrocatalysts

The morphology of the catalyst layer has an important influence on the performances of gas-evolving electrocatalysts[235-237]. Notably because of electrical contact and bubble management problems[238, 239]. In the case of supported electrocatalysts, the overall morphology of the catalyst layer is due to the morphology of the support. Therefore, supports with various morphology were synthesized by changing the anodization time and proceeding of a milling step, which influences the support morphology differently. In order to assure that the morphology was the only changed feature, extensive techniques (SEM, STEM, BET, XRD, XPS, and ICP-OES) were performed to characterize the synthesized catalysts.

The amorphous TiO_2 nanotubes were synthesized by anodization of titanium foils for one, three and six hours. The immobilized nanotubes were detached, and their morphology was not affected by the removal process as shown by the SEM picture in Figure 5.6b. Similarly, the nitridation process (see Chapter 3.1.1.2 for more details) does not affect the overall morphology of the clusters of nanotubes (size and shape) as seen in Figure 5.6c. However, the appearance of the nanotubes is modified, becoming rougher. This is due to the formation of some small $TiON_x$ nanofragments with cracks and pores. Consequently, the surface area increases after the nitridation from 14.231 ± 0.075 m^2/g for amorphous

TiO_2 to 36.279 ± 0.172 m^2/g for $TiON_x$ in the case of the samples anodized for six hours ($TiON_x$-6h) as determined by BET measurement.

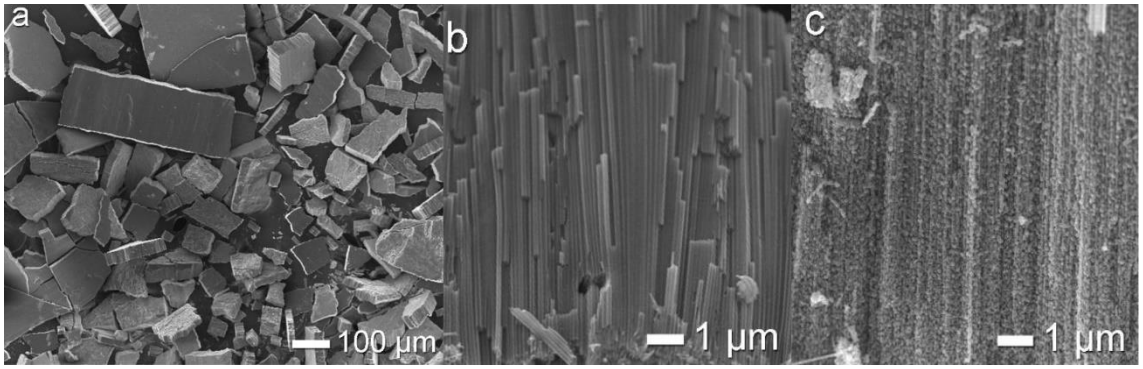

Figure 5.6: SEM pictures. a) Amorphous TiO_2 nanotube powder at low magnification. b) The cross-section of amorphous TiO_2 after detachment. c) TiO_2 after annealing in ammonia and transformation in $TiON_x$. All micrographs show the 3 h samples.

Moreover, the longer anodization results in a longer nanotube length with thinner walls, and thus lower mechanical stability. The average length of the nanotubes after anodization is 3.5 µm, 13 µm and 27 µm for one, three and six hours, respectively. The anodization time also affects the thickness of the wall. For all anodization time, the wall thickness depends on the part of the nanotube, which is measured, as seen in Figure 5.7. For example, the sample anodized for six hours exhibits a wall thickness of approximately 5 nm at the top and approximately 55 nm at the bottom part (Figures 5.7a and 5.7b). The reason for the formation of a more than ten times thinner wall at the top part of the nanotubes is that this part forms first and is etched during the entire anodization time[240]. The thickness of the wall influences the size of the nanofragments that can form during the nitridation process and/or milling. For example, the top part of the nanotubes anodized for 6 hours (± 5nm) results in nanofragments with a diameter of around 30 nm while the bottom part (± 55 nm) gives nanofragments with a diameter of approximately 100 nm (Figures 5.7c and 5.7d). In addition, the etching time also affected the morphology of the wall. The thinner walls at the top were smoothed out, while at the bottom, the walls are noticeably thicker (rippled).

The length of the nanotubes in the cluster is maintained. However, some portions of nanotubes that have grown with longer anodization are more brittle due to the thinning of the nanotube wall and thus more likely to break down into smaller nanotubes and clusters or even nanoparticles.

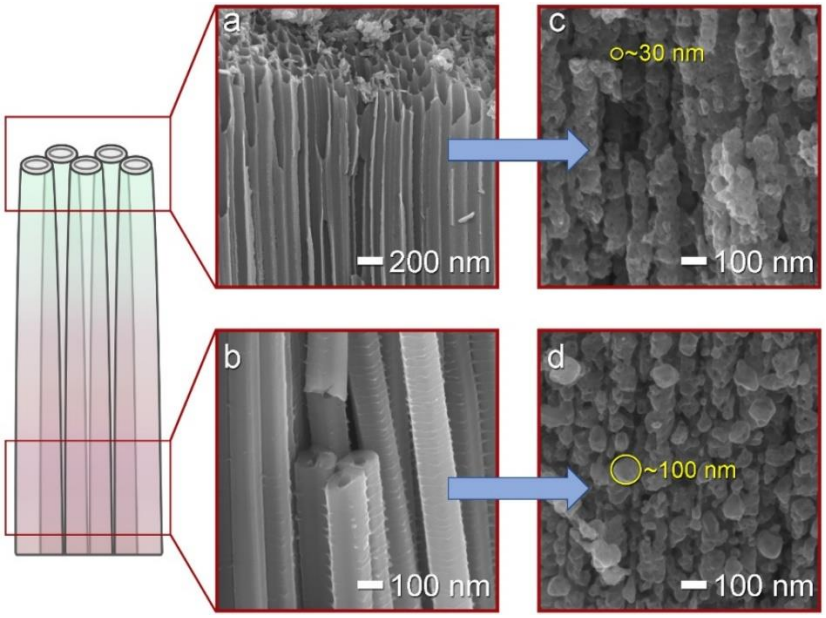

Figure 5.7: SEM micrographs of the TiO_2 nanotubes anodized for 6h. a) At the top. b) At the bottom. The top parts were transformed into small $TiON_x$ nanofragments (c), while the thick nanotube walls at the bottom part resulted in large $TiON_x$ nanoparticles (d).

Afterwards, iridium nanoparticles were deposited on $TiON_x$-nh supports with a different morphology as seen in Figure 5.8. The nanotube arrays are more crushed than the as-prepared support due to the wet impregnation step of the deposition of iridium which included slight milling to obtain a homogeneous distribution. Figures 5.8a, 5.8b and 5.8c show the as-prepared samples, while Figures 5.8d, 5.8e and 5.8f show the same samples after more rigorous milling. These final catalysts are schematically shown in Figure 5.8g. It is observed that the milling procedure has a larger influence when the anodization time was longer, namely for three and six hours. This is due to the higher mechanical stability of the nanotube arrays prepared with a shorter time, especially for one hour, which exhibit shorter lengths and thicker walls of nanotubes. On the other hand, longer anodization time induces a thinner wall, and this results in greater brittleness when milling. The sample anodized for one hour consists of relatively large nanotube arrays (Figure 5.8a) which become smaller after milling (Figure 5.8d). After three hours of anodization, some clusters with a nanotubular morphology can be observed (Figure 5.8b), even after reducing the cluster size with milling (Figure 5.8e). On the other hand, almost no nanotubular morphology features can be recognized for the samples anodized for six hours, even before the rigorous milling (Figure 5.8c). And no nanotubular morphology is left after the milling for this sample (Figure 5.8f). Again, this is due to the lower mechanical stability of nanotubes formed during a longer anodization time due to etching. Nonetheless, the cluster size for the six hours samples is the largest before and after the rigorous milling. The average cluster size of the final electrocatalyst for $TiON_x$-6h-Ir is more than two times bigger than for $TiON_x$-3h-Ir with 121 ± 7 µm and 50 ± 3 µm, respectively. The difference between the electrocatalysts prepared with anodic oxidation and other synthesis procedures is the defined orientation resembling the nanotubes. However, the anodization time should not be too long, or the top surface loses the nanotube morphology. In this case, the nanotubes start turning into nanoparticles which end in an electrocatalyst with a similar morphology as if prepared from commercial nanopowders.

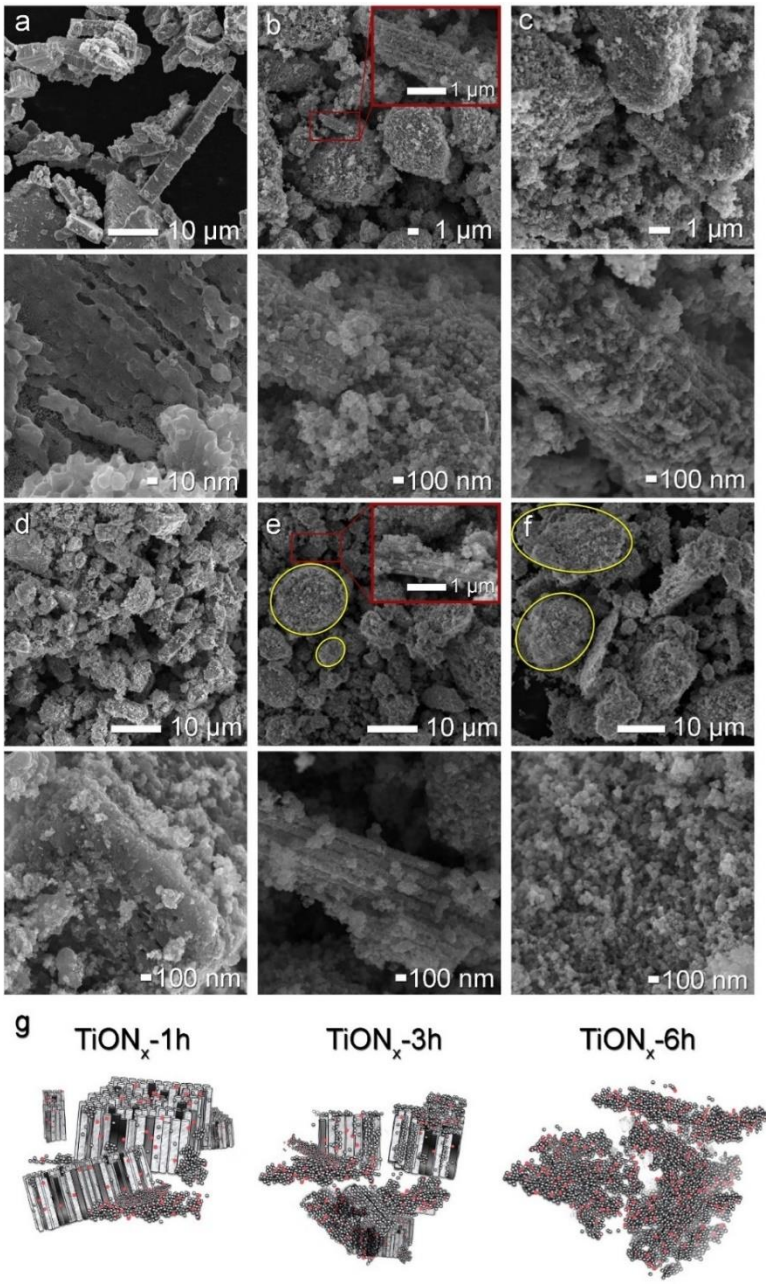

Figure 5.8: SEM micrographs of the synthesized catalysts: a) TiON$_x$-1h-Ir. b) TiON$_x$-3h-Ir. c) TiON$_x$-6h-Ir. d) Milled TiON$_x$-1h-Ir. e) Milled TiON$_x$-3h-Ir. f) Milled TiON$_x$-6h-Ir. Inset figures (b) and (e) show the nanotubular morphology of the TiON$_x$-3h-Ir sample. g) A schematic presentation of all three milled catalysts with iridium. The yellow circles highlight the nanoparticular morphology.

The deposition of small iridium nanoparticles was observed with STEM (Figure 5.9). The nanoparticles are also nicely dispersed on the support. The iridium nanoparticles' average size was monodispersed and between 3.1 and 3.4 nm for all the samples (Figures 5.9c, 5.9f, 5.9i and Table 3).

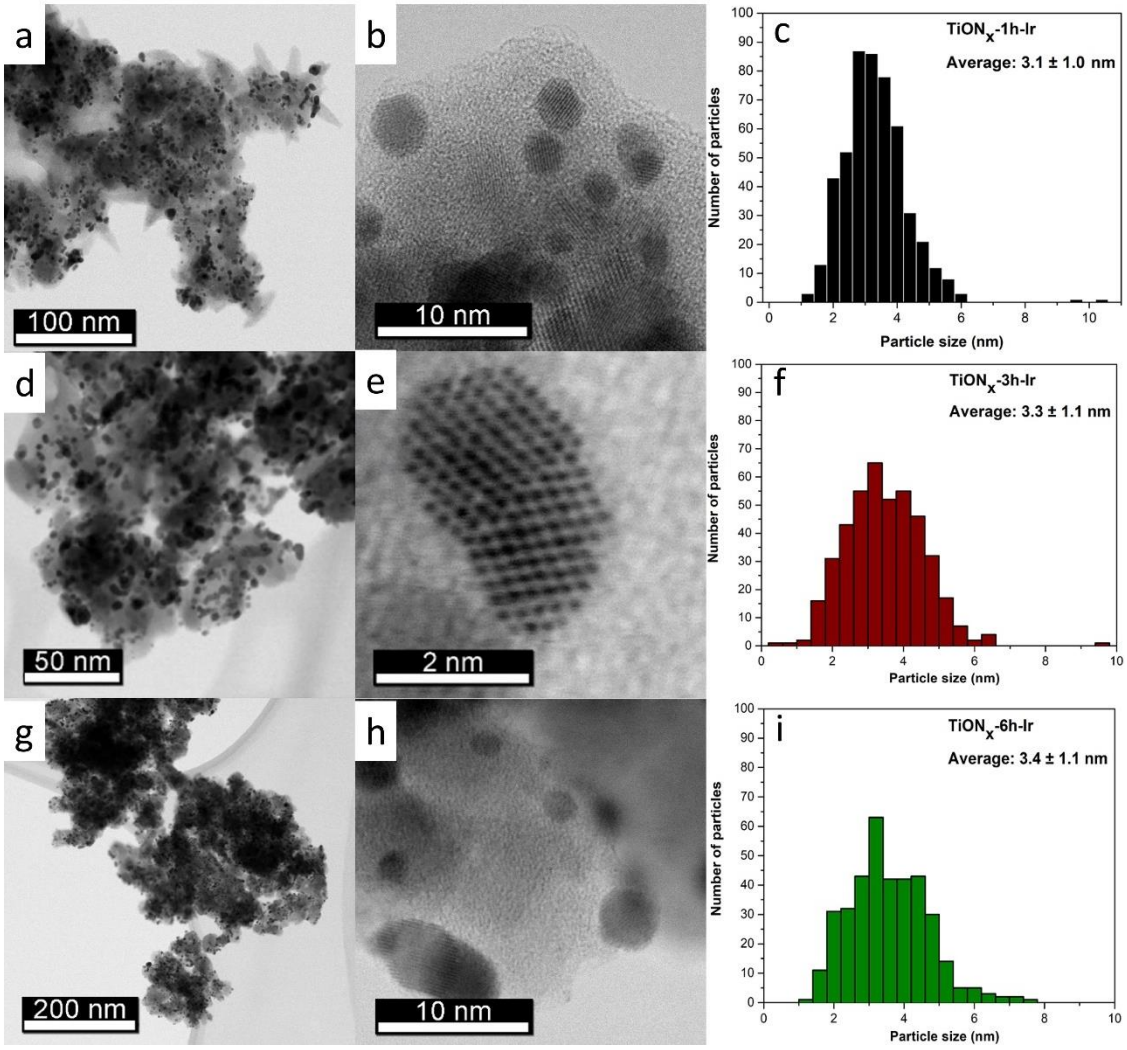

Figure 5.9: STEM pictures. Low resolution (a), high resolution (b), and particle size distribution (c) of $TiON_x$-1h-Ir. Low resolution (d), high resolution (e), and particle size distribution (f) of $TiON_x$-3h-Ir. Low resolution (g), high resolution (h), and particle size distribution (i) of $TiON_x$-6h-Ir.

The EELS and XPS results indicate that the compositions of all the samples are very similar (Table 3). The XPS results show that the surface concentration of all elements (Ti, O, N, and Ir) is independent of the anodization time (Figure 5.10a). However, a difference in the O/N ratio measured by XPS (between 3.3 and 4.1) and by EELS (between 1.5 and 2) is observed. This is explained by the oxidation of the $TiON_x$ surface (upper 3-5 nm) that likely occurred during milling. The XPS spectra (Figure 5.10b) reveal a characteristic peak of TiO_2 (Ti^{4+} at 458.6 eV), Ti-ON (457.2 eV) and TiN (455.7 eV)[241]. Around 65% of the Ti is in TiO_2 state, 20% is in Ti-ON and 15% is in TiN state. The XPS spectra of Ir 4f are similar for all the samples (Figure 5.10c). They consist of the characteristic peaks for Ir0 (60.9 eV and 63.9 eV)[242] with a possible minor portion of Ir4+ or Ir3+. The metallic state of iridium is expected from the synthesis procedure as no oxidation step was introduced; however, it changes with electrochemical oxidation.

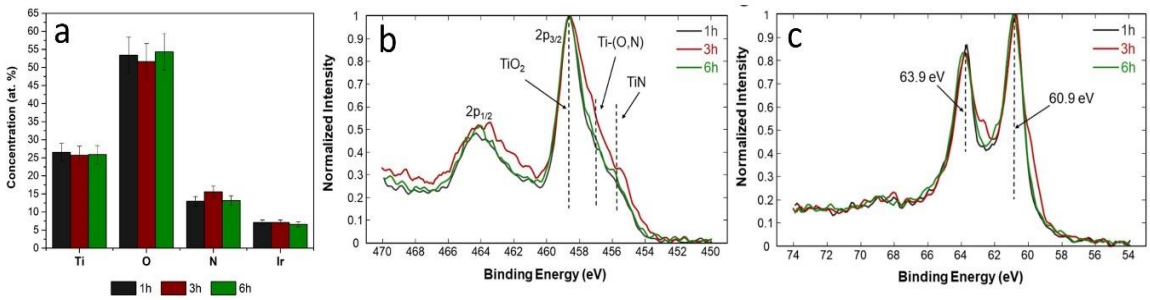

Figure 5.10: a) Surface composition in at. % determined with XPS on $TiON_x$-nh-Ir samples. b) Normalized XPS spectra of Ti 2p of $TiON_x$-nh-Ir samples. c) Normalized spectra of Ir 4f of $TiON_x$-nh-Ir samples.

Table 3: Average particle size as determined by the STEM image analyses and the amount of nitrogen and oxygen in the $TiON_x$ support for the $TiON_x$-nh-Ir samples, as determined with EELS and XPS.

	$TiON_x$-1h-Ir	$TiON_x$-3h-Ir	$TiON_x$-6h-Ir
Average particle size (nm)	3.1 ± 1.0	3.3 ± 1.1	3.4 ± 1.1
$TiON_x$ support composition determined with EELS (at%)			
N	20 ± 3	19 ± 5	22 ± 3
O	34 ± 4	34 ± 4	32 ± 3
O/N	1.71 ± 0.46	1.98 ± 0.77	1.5 ± 0.36
$TiON_x$ support composition determined with EELS (at%)			
N	13 ± 1.3	15.6 ± 1.6	13.2 ± 1.3
O	53.4 ± 5	51.6 ± 5	54.3 ± 5
O/N	4.11 ± 0.41	3.31 ± 0.33	4.11 ± 0.41

Independently, the presence of TiO_2 was also confirmed by Raman Spectroscopy (Figure 5.11). The bands at 144 (E_g), 197 (E_g), 399 (B_{1g}), 515 (A_{1g}, B_{1g}), and 625 (E_g)cm^{-1} are characteristic for TiO_2 in anatase form and are present for all the samples[243]. However, the intensities vary among the catalysts, but also at different sites of the same samples. The Raman spectra shown in Figure 5.11 are the most representative ones out of at least four, with the arrows marking the measured range of the 144 cm^{-1} band intensities. A larger ordering of the anatase phase was observed for $TiON_x$-3h-Ir as indicated by the highest intensities (and the smallest spread between different sites). On the other hand, $TiON_x$-1h-Ir exhibits lower intensities, suggesting that TiO_2 is closer to the amorphous state in this sample. The spectra of $TiON_x$-6h-Ir reveal the largest spread of the spectral intensities, indicating that the long-range ordering in anatase could be in any state between the one-hour and three-hour samples.

The basis of the anatase bands increases with an increase in the band intensity which has been ascribed to the nanometric size[244]. A debate has been going on about the possible presence of TiN and $TiON_x$ bands in the same region as TiO_2. TiN is characterized by a broad double band at 190-350 cm^{-1} and an additional one between 550 and 565 cm^{-1} [245, 246]. The relative ratios among those bands change with the deficiencies in the nitrogen TiN_x[247]. Moreover, Prokes et al. studied nitride TiO_2 and suggested the presence of $TiO_{2-x}N_x$ due to the appearance of the shoulder ban near 550cm^{-1} [248]. Therefore, the described TiN, TiN_x,

$TiON_x$ bands could be superimposed in the considered spectral range. A similar assumption as Prokes can be made for our $TiON_x$-nh-Ir samples since a band at 552 cm^{-1} can be observed. The Raman spectroscopy confirms the XPS results with the higher amount of Ti-(O,N) and TiN in the $TiON_x$-3h-Ir catalyst. Nonetheless, the exact determination of $TiON_x$ and TiN bands is not feasible yet and will be addressed in future work.

Another interesting feature visible in the Raman spectra is the shoulder band at around 715 cm^{-1}. This band could confirm the presence of Ir^{4+} state as observed by XPS. Indeed, literature reports the appearance of IrO_2 bands at 561 and ~720 cm-1 in chemical-vapor-deposited and sputtered samples[249]. The deviation compared to IrO_2 single crystal (561 (E_g), 728 (B_{2g}) and 752 (A_{1g})) was ascribed to the nanometric size effects and residual stress effects. Therefore, the band at 715 cm^{-1} could reflect the presence of Ir^{4+}. The other bands could be blurred by the anatase bands between 515 and 552 cm^{-1}.

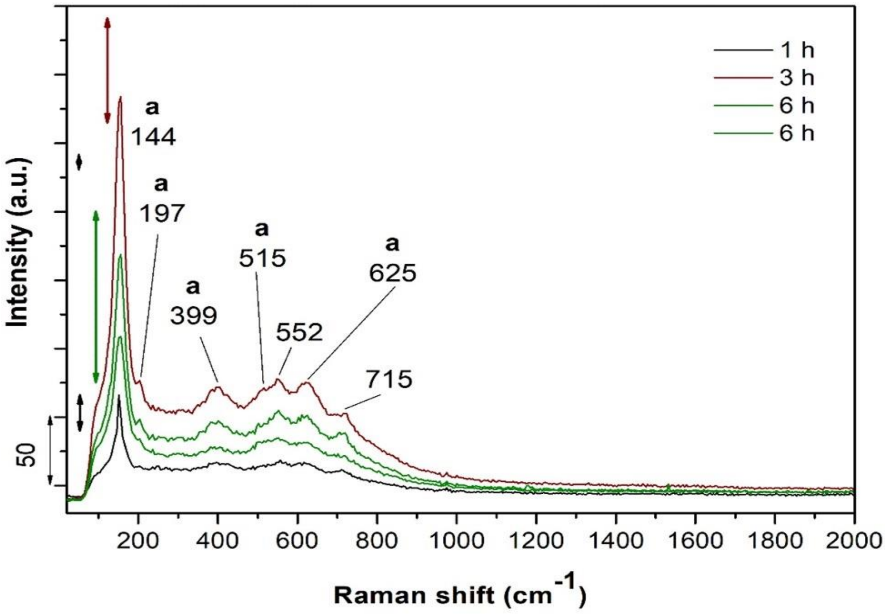

Figure 5.11: Raman representative spectra of $TiON_x$-nh-Ir powders. Two representative spectra are presented for the $TiON_x$-6h-Ir sample due to the largest spread of the intensity values. The arrows denote the intensity ranges of the 144 cm^{-1} anatase bands detected for each type of sample.

ICP-OES was performed to measure the total amount of Ir in the catalysts. This information is primordial to determine the exact mass activity of each sample and thus to have a fair comparison. The amount of Ir in all the samples was approximately 11 wt%. Therefore we can claim that the morphological differences of the supports did not influence the amount (and particle size) of deposited iridium nanoparticles.

The chemical structure of all the samples was determined with XRD. The spectra of the various stages of the $TiON_x$-3h-Ir preparation are shown in Figure 5.12. The TiO_2 nanotubes grown in the first step are amorphous and show no diffraction peaks. The diffraction domains of TiO_2 anatase visible by Raman spectroscopy are too small to sufficiently scatter X-rays. The annealing step at 700°C transforms the amorphous nanotubes into $TiON_x$ (Figure 5.12a, in blue). The diffraction peaks of $TiON_x$ are related to (◆) cubic titanium oxide nitride at the 37.1° (111), 43.1° (200), 62.5° (220), 75.0° (311) and 94.4° (400) angles (PDF 01-084-4872)[250]. Afterwards, Ir nanoparticles were deposited on the support and the XRD is shown in red in Figure 5.12a. The additional diffraction

peaks are observed at the 40.7° (111), 47.3° (200), 69.1° (220), 83.4° (311) and 88.1° (222) angles, corresponding to cubic Ir (○) (PDF 04-007-8342)[250]. The XRD spectra of $TiON_x$-1h-Ir and $TiON_x$-6h-Ir reveal the same chemical structure as $TiON_x$-3h-Ir (Figure 5.12b).

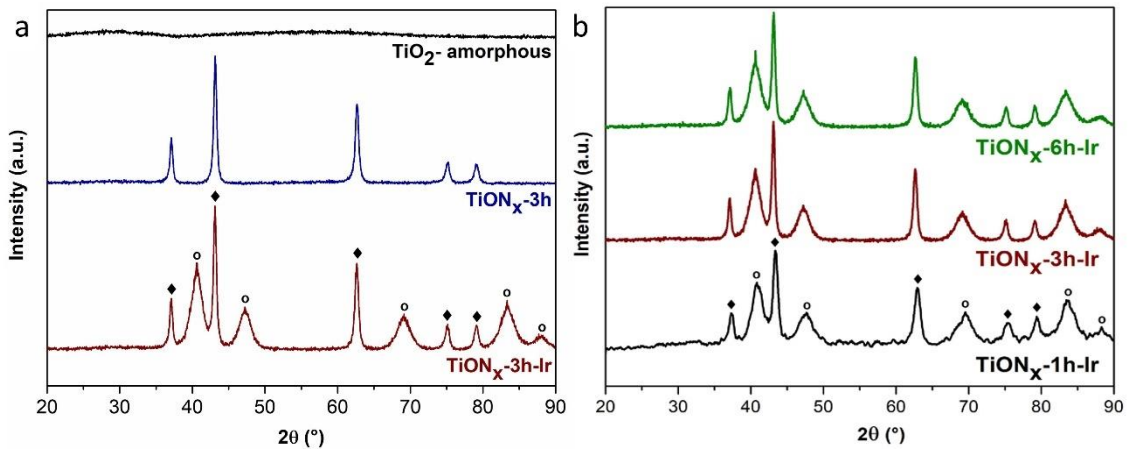

Figure 5.12: XRD spectra. a) Comparison of the XRD spectra after each synthesis step. b) Comparison of $TiON_x$-nh-Ir electrocatalysts XRD spectra. The diffraction peaks denoted with (♦) are related to cubic titanium oxide nitride (PDF 01-084-4872), whereas diffraction peaks denoted with (○) correspond to cubic Ir (PDF 00-006-0598).

5.3.2 Electrochemical activity

The OER activity was determined for the three $TiON_x$-nh-Ir samples and compared with IrO_2 (Alfa Aesar) benchmarks (Figure 5.13). The $TiON_x$-nh-Ir analogues were also compared to Ir on Ti-based support from literature (Table 4). The influence of the electrode morphology is clearly seen in Figure 5.13 with different activities observed for the samples with different support morphology. Although the morphology of the support does not affect the iridium deposition nor the dispersion of the nanoparticles, i.e. similar particle size distribution for all the anodically grown analogues, its decisive role is visible.

At low overpotential, the $TiON_x$-nh-Ir analogues activity trend is: $TiON_x$-1h-Ir > $TiON_x$-3h-Ir > $TiON_x$-6h-Ir. However, at higher potentials (> 1.52 V) this trend is altered: $TiON_x$-3h-Ir > $TiON_x$-6h-Ir > $TiON_x$-1h-Ir. To understand this trend, it should be emphasized that the OER polarization curve consists of two regimes (Figure 5.13): i) the kinetic regime at lower potentials, which is influenced by the chemical structure of active sites[251-253], surface structure[253-255], electronic interaction[254, 256], and interactions with support[94, 98, 227, 257], ii) transport regime at higher potentials, which is controlled by electron transport and mass transport/removal of the oxygen bubbles. The transport regime is due to confinement and results in an alternation of the local concentration of reactants and products. This further causes a local decrease of pH[258] or accumulation of evolved oxygen that can lead to bubble formation. The bubbles formed hinder the mass transport but also lower the number of active sites available for reactant. Thus, the effective detachment of gas bubbles is essential for good activity, especially at high potentials where more bubbles are formed. Notably, the frequency and critical bubble diameter of the detachment depend on the electrode morphology[235-238, 259, 260]. Therefore, in the kinetic regime, the nanotube-array morphology (highly present in $TiON_x$-1h-Ir) promotes the OER while during the transition to higher potentials, a combination of cluster size and nanotubular morphology (characteristic feature in $TiON_x$-3h-Ir) governs the reaction. According to the literature, the cluster size should decisively impact the OER proceeding via bubble management at higher reaction rates (i.e. higher potentials)[235-238]. However, the $TiON_x$ particle-to-particle

electron resistance through the oxidized surface contact points could lower the OER[239]. $TiON_x$-1h-Ir statistically has the lowest number of them due to its higher nanotubular morphology, this could also explain its highest OER activity at low potentials. Accordingly, $TiON_x$-6h-Ir has the lowest OER performance in the lower potentials among the three analogues, which can be ascribed to the absence of nanotubular morphology and the highest amount of oxidized contact points although it shows a more promising OER activity at higher potentials. $TiON_x$-3h-Ir has the best tradeoff between electron resistance and mass transport issues. The higher performances at high current densities compared to $TiON_x$-6h-Ir were ascribed to the lower cluster size (50 ± 3 µm vs 121 ± 7 µm).

Based on XPS, EELS and Raman analyses, the surface of the support is rich in TiO_2 phase for all three samples. Unfortunately, TiO_2 can induce passivation and influence the electron access to Ir nanoparticles (besides $TiON_x$ particle-to-particle contact points), and thus affect the kinetics of the reaction[261, 262]. Therefore, the highest amount of $TiON_x$ is needed to assure good electron conductivity. This phase is important to retain sufficient electron conductivity as $TiON_x$ is largely more conductive than TiO_2. XPS and Raman analyses reveal the highest amount of Ti-(O,N) phase in $TiON_x$-3h-Ir (Figures 5.10 and 5.11), accordingly to its higher activity. Additionally, Raman analyses also reveal the degree of TiO_2 crystallinity where $TiON_x$-3h-Ir analogue presents the most crystalline TiO_2 and $TiON_x$-1h-Ir has the most amorphous one. A correlation of the TiO_2 degree of crystallinity (3h>6h>1h analogues) and OER performances at higher potentials (3h>6h>1h analogues) indicates that TiO_2 crystallinity could play a role at high current densities, which would be in line with the better electrochemical stability of the crystalline TiO_2 compared to the amorphous one[263]. In other words, when the TiO_2 layer is not sufficiently stabilized (too amorphous), it can become too thick for efficient electron conductance/tunneling, impacting negatively the OER performance at high current densities.

More insights were obtained by performing a Tafel slope analysis. The three anodically grown analogues have a similar Tafel slope (60-65 mV/dec, Table 4) which is comparable to literature values for both rutile IrO_2 and electrochemically grown oxide[98, 264-266]. A similar Tafel slope indicates that the RDS (rate-determining step) is the same for all the catalysts. The other catalysts with Ti-based support (homemade benchmarks) present Tafel slopes slightly higher, between 70 and 77 mV/dec. Usually, if the RDS is different, a difference in Tafel slope of several decades is expected. Hereby, the difference is too small to be explained by another RDS for non-anodized samples and alternative reasoning is needed to explain the difference. The literature data for similar systems suggests that the Tafel slope can be influenced by the interaction between Ir nanoparticles and the support[98, 101, 228]. For example, unusually large Tafel slopes have been observed when Ir was supported on semiconducting support such as TiO_2 [261, 267]. Nonetheless, both groups of catalysts (with anodically and non-anodically grown support) have the same $TiON_x$ chemical composition, the steeper Tafel slope of the non-anodically group is ascribed to a more extensive TiO_2 passive surface layer[261, 267]. This attribution is based on the change in the Tafel slope after electrochemical degradation (Table 4), where the Tafel slopes of anodically grown analogues increased to values similar to the non-anodized samples. This is in line with the electrochemical oxidation of $TiON_x$ to TiO_2 during the degradation protocol[261, 262].

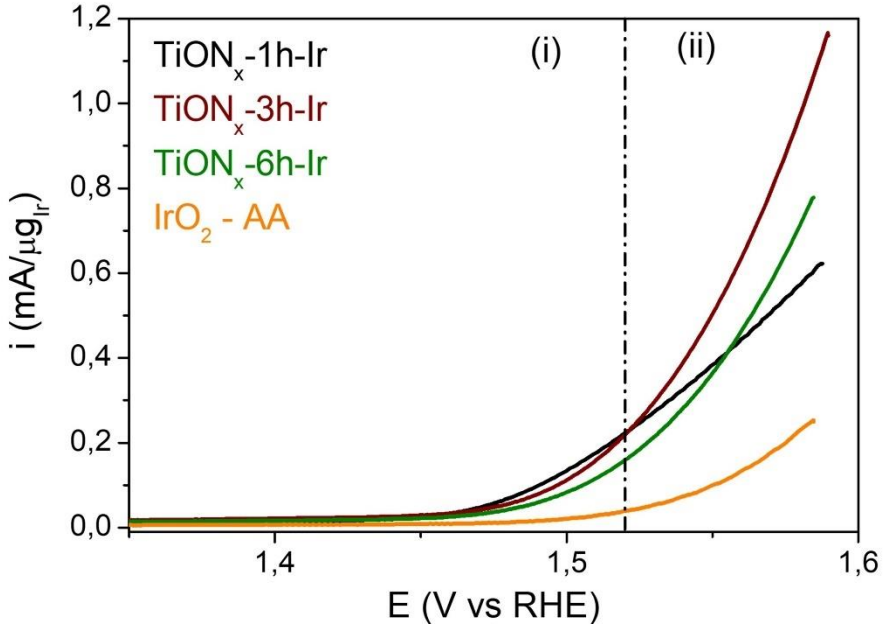

Figure 5.13: OER polarization curves. The curves were obtained at 20 mV/s, in 0.1 M $HclO_4$, 1600 rpm.

Table 4: Electrochemical performances of Ir-based catalysts (averaged over 3 measurements) and comparison with Ir on Ti-based support from literature.

Sample	Mass Activity at 1.55 V_{RHE} [A/g_{Ir}]	Tafel slope [mV/dec]
TiON$_x$-1h-Ir	360.9 ± 18.7	± 60
After degradation (2h)	*245.4 ± 12.8*	± 72
TiON$_x$-3h-Ir	520.3 ± 50.6	± 63
After degradation (1h)	*405.8 ± 39.5*	± 77
After degradation (2h)	*385.0 ± 37.5*	
TiON$_x$-6h-Ir	369.5 ± 35.1	± 65
After degradation (2h)	*223.5 ± 21.2*	±77
IrO_2-AA	99.8 ± 14.3	± 70
Ir/TiON$_x$-P25[a]	143.9 ± 12.1	± 71
Ir/TiON$_x$-NR[a]	213.2 ± 26.9	± 77
Ir/TiN[234]	147.5 ± 11.4	± 75
IrO_2@TiO_2[268]	112	
IrO_2/TiO_2 (Umicore)[268]	47	
IrO_2@Ir/TiN (60wt%)[94]	222.3	± 52.3
Ir/TiC[269]	150	± 53

a. From Chapter 5.2.2.

5.3.3 Electrochemical stability

A chronopotentiometric (CP) protocol was chosen as the degradation protocol in this study because it is more destructive than a potentiodynamic treatment[270] and thus more

appropriate for a short stability test. In addition, cycling over 1.6 V_{RHE} during the degradation can induce bubbles that block the surface of the catalyst and protect it against degradation, leading to wrong conclusions about stability[270, 271]. A short degradation was applied as a primary degradation test to minimize ruining the carbon backing electrode. A constant current of 1 mA/mg_{Ir} was applied for 2 hours on the three anodically grown analogues and the activity was recorded before and after.

Our results show that the most stable catalyst is $TiON_x$-3h-Ir, which retained 74.3% of the initial activity after 2 h (Figure 5.14). Importantly, most of the performance loss already occurs after one hour, namely a loss of 22% is observed. This suggests that after an initial loss, the catalyst – activity decay is slowing down and could sustain prolonged operation. The activity loss could originate from (i) the dissolution of Ir nanoparticles, (ii) the physical detachment of Ir nanoparticles, or (iii) the electrochemical oxidation of $TiON_x$, leading to the formation of a passive nonconductive TiO_2 layer. However, a recent study showed that Ir (i) and (ii), while potentially important in real devices, do not play a significant role during ADT under ambient conditions and in the time frame of RDE experiments[270]. Therefore, the activity loss could be ascribed to the electrochemical oxidation of the $TiON_x$ support, leading to a thicker TiO_2 layer. This is in accordance with the increase of the Tafel slope after the degradation. Another possibility for the decrease of activity during the first hour is linked to the formation of a thicker Ir-oxide layer. Indeed, Ir-oxide is less active than Ir-hydrous oxide[228-231]. However, an activation protocol has been performed before the test and thus a stable oxide layer was already formed. In addition, $TiON_x$ was shown to hinder excessive oxidation of Ir and stabilize the nanoparticles[272]. Additionally, the most stable catalyst ($TiON_x$-3h-Ir) also contains the most crystalline TiO_2 phase. The degree of crystallinity could play a role in stability, based on studies of oxide analogues[273-275] but further dedicated studies would be needed to investigate this effect.

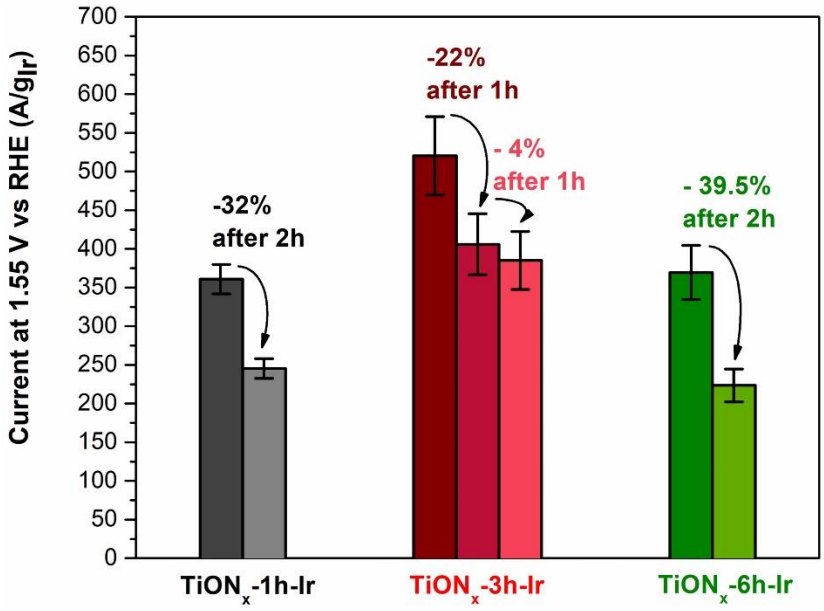

Figure 5.14: Activity remaining for the different samples after 2 hours at 0.1 A/mg_{Ir}. In black, $TiON_x$-1h-Ir, in red, $TiON_x$-3h-Ir and $TiON_x$-6h-Ir in green.

5.3.4 Conclusion

Ir nanoparticles deposited on $TiON_x$ made from anodically grown TiO_2 nanotubes exhibit a 5-times better mass activity than commercial IrO_2 and 2-times better mass activity than

Ir on $TiON_x$ from the previous study (Table 4). Among the three anodized analogues, the activity for OER was in the order $TiON_x$-3h-Ir > $TiON_x$-6h-Ir ≥ $TiON_x$-1h-Ir at 1.55 V_{RHE}. Better activity was assigned to the differences in the morphology of the support, as other properties like Ir particle size and metal loading were kept the same. At low current densities, a nanotubular morphology provides better conductivity than its nanoparticular counterpart and thus a better activity is observed for $TiON_x$-1h-Ir. On the other hand, bubble management becomes more important at high current densities and the nanoparticular morphology is more adequate. Furthermore, the ratio between O/N was also similar in all of the samples, as determined by EDX, EELS, and XPS. The amount of iridium was approximately 11%, as measured by ICP-OES, and the average Ir particle size was 3.3 nm, as observed in STEM. The best stability after the chronopotentiometry test was found for the most active catalyst, $TiON_x$-3h-Ir. Better stability was ascribed to the morphology and crystallinity of the support (anatase TiO_2 layer, as found by Raman spectroscopy) as the physical and chemical characteristics of the catalysts are (almost) identical.

Therefore, stable and active OER catalysts using $TiON_x$ as support were synthetized. The morphology of the support for the best catalyst was made of a mix of nanotubular morphology and nanoparticle clusters. This combination morphology brings the best tradeoff between electron resistance (nanoparticulate support) and mass transport problems (nanotube support). Moreover, an anatase TiO_2 layer was found on the surface and is most likely protecting the $TiON_x$ bulk from further oxidation. It is, however, also the reason for the decrease in activity after the stability test.

5.4 Support Composition Effect on the Performances of Iridium Nanoparticles Towards OER

Parts of the following text were published in Advance Material Interfaces under the title "Enhancing iridium nanoparticles OER activity and stability by adjusting the coverage of titanium oxynitride flakes on reduced graphene oxide nanoribbons support" [276].

L. Moriau, G. Koderman Podboršek, A. K. Surca, S. Semsari Parapari, M. Šala, U. Petek, M. Bele, P. Jovanovic, B. Genorio, N. Hodnik**

As the first author, L. Moriau conducted the electrochemical experiments as well as the online-ICP-MS experiments. He also planned the other characterization techniques presented in the articles in accordance with the experts. He wrote the initial draft of the manuscript.

Previously, $TiON_x$ was shown to be a suitable material as a support for OER catalysts. It not only possesses the required characteristics of electrocatalyst support but also improves the performance of the active material through the SMSI effect. Nonetheless, some features can still be enhanced like its conductivity or surface area. Therefore, we investigated a combination of $TiON_x$ nanoflakes deposited on a reduced graphene oxide nanoribbons (rGONRs) template as a carbon – ceramic nanocomposite OER electrocatalyst. The nanoribbons morphology allows a fine dispersion of the TiO_2. In addition, this specific morphology provides an efficient particle-to-particle electrical conductivity by micro-wiring of the sample as shown for $TiON_x$ in Chapter 5.2. or for pure IrO_2 catalysts[239]. In this subchapter, the influence of the composite $TiON_x$/rGONRs on the activity and stability of the catalysts was explored. Three samples with a varying $TiON_x$/rGONRs ratio (referred to as Ir/Low-$TiON_x$/rGONRs, Ir/Middle-$TiON_x$/rGONRs, and Ir/High-$TiON_x$/rGONRs for a ratio of 1/140, 1/35 and 1/8, respectively) and thus interfacial contact areas between the three phases have been synthesized and investigated in detail with classical and advanced electrochemical techniques, as well as structural characterization. In addition to the three samples with different Ti/C ratios, the same process was performed without titanium precursor to yield Ir/rGONRS.

5.4.1 Physical characterization

The results of the synthesis process (see chapter 3.1.1.3) were followed step by step by XRD (Figure 5.15). In the first step, the unzipping of multi-walled carbon nanotubes yields amorphous GONRs as seen by the diffraction spectrum in green in Figure 5.15a. The deposition of TiO_2 on the GONRs and the annealing in ammonia atmosphere lead to $TiON_x$/rGONRs analogues. The reduction of the graphene oxide is visible through the characteristic peak around 26-27° (002, ⊥) in Figure 5.15a. The two other peaks at 37° (111) and 43.1° (200) are characteristics of $TiON_x$ (●, PDF 01-084-4872)[277] and are more intense for the samples with a higher amount of Ti-precursor used during the synthesis. This indicates that either higher crystallinity or bigger grains are present in the samples with more Ti-precursor during the synthesis. Simultaneously, the rGONRs related peak (at 26–27°) decreases in intensity with an increase of Ti in the support (lower peak for High-$TiON_x$/rGONRs than for Low-$TiON_x$/rGONRs). Finally, after the deposition of Ir nanoparticles, new peaks are observed at 40.7° (111) and 47.3° (200) for all the samples (Figure 5.15c) which correspond to cubic iridium (*, PDF 04-007-8342)[277]. Finally, a sample

without $TiON_x$ was synthesized as a benchmark (Ir/rGONRs) and the characteristic peaks of graphene and of Ir were also visible (Figure 5.15d).

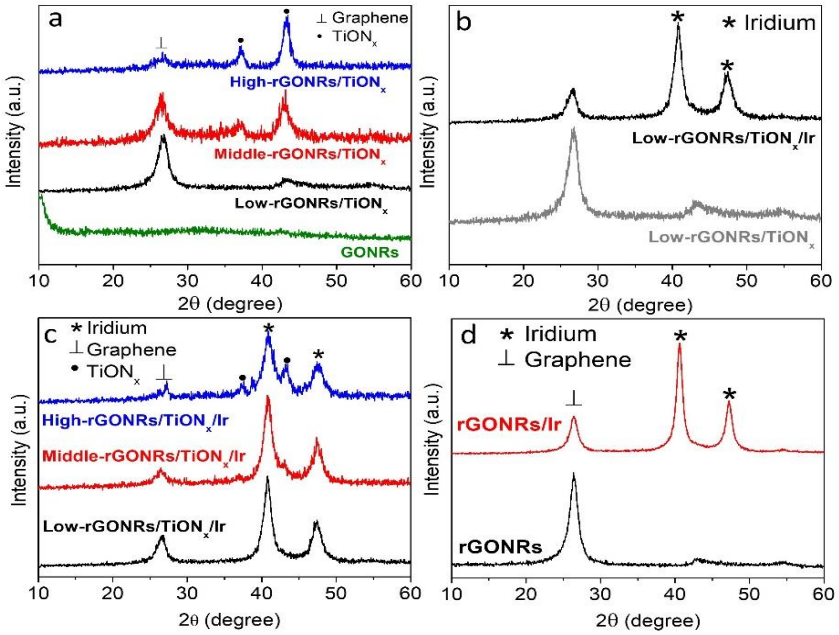

Figure 5.15: X-ray diffraction spectra. a) Comparison of the different supports. b) Materials after the addition of Ir on Low-$TiON_x$/rGONRs support. c) Comparison of the catalysts with different Ti/C ratios after deposition of Ir. d) Deposition of Ir on rGONRs.

The amount of metals was quantified with ICP-OES where Ir content of 6.81, 6.49, 9.02 and 6.74 wt% was measured for Ir/Low-$TiON_x$/rGONRs, Ir/Middle-$TiON_x$/rGONRs, Ir/High-$TiON_x$/rGONRs and Ir/rGONRs, respectively (Table 5). In the case of titanium, 2.3, 13.59, and 31.34 wt% was determined for Ir/Low-$TiON_x$/rGONRs, Ir/Middle-$TiON_x$/rGONRs, Ir/High-$TiON_x$/rGONRs and Ir/rGONRs, respectively. No titanium was found in the Ir/rGONRs sample as expected. Hence, the amount of titanium present in the sample is not linearly dependent on the ratio of the precursor. When the ratio goes from 1/140 to 1/35 ("Low" ratio to "Middle" ratio), there is a 4-time increase in precursor but around a 6-time increase in the amount of Ti in the sample, going from 2.3 to 13.6 wt%. Oppositely, when higher concentrations of Ti-precursor are used ("High" ratio), the final catalyst contains only twice the amount of Ti as in Ir/Middle-$TiON_x$/rGONRs with a 4-time higher precursor ratio.

Table 5: Physical characteristics of the Ir-based electrocatalysts with a graphene-template/$TiON_x$ support.

	Ti/C (molar ratio)	Ti wt%	Ir wt%	Nanoribbons width (nm)*	Iridium particle size (nm)
Ir/rGONRs	/	< 1	6.74	422 ± 82	2.35 ± 0.47
Ir/Low-$TiON_x$/rGONRs	1/140	2.30	6.81	292 ± 54	3.4 ± 0.47
Ir/Middle-$TiON_x$/rGONRs	1/70	13.59	6.49	288 ± 50	2.52 ± 0.33
Ir/High-$TiON_x$/rGONRs	1/35	31.34	9.02	301 ± 45	2.92 ± 0.2

*Since nanoribbons are a high aspect ratio material, both dimensions, width and length, would be of interest. The length varies significantly but is in the range of 1 to 10 µm.

Afterwards, the morphology of the catalysts was investigated by SEM and TEM. The nanoribbons' shape and structure are confirmed for all the samples (Figure 5.16). However, the Ir/$TiON_x$/rGONRs analogues exhibit some morphological changes compared to Ir/rGONRs. Firstly, the width of the nanoribbons, which decreases when $TiON_x$ was added to the graphene, for Ir/rGONRs is 422 ± 82 nm wide while the samples covered with Ir/$TiON_x$/rGONRs are 292 ± 54, 288 ± 50 and 301 ± 45 nm wide for Low-, Middle- and High- Ir/$TiON_x$/rGONRs, respectively (measured from SEM analysis). Moreover, the surface smoothness changes with the higher amount of $TiON_x$ in the sample. Ir/rGONRs look smooth while Ir/High-$TiON_x$/rGONR is the more rugged one. This could be beneficial for the catalytic performances as it in principle increases the available surface area of $TiON_x$ for Ir deposition and possibly has better anchoring ability for Ir nanoparticles. This could explain the higher amount of Ir present in Ir/High-$TiON_x$/rGONR. These morphological changes are most likely due to some interaction between $TiON_x$ and rGONRs during the synthesis (thermal annealing or hydrolysis steps). For clarity, the structures of the different catalysts are represented in Figure 5.17.

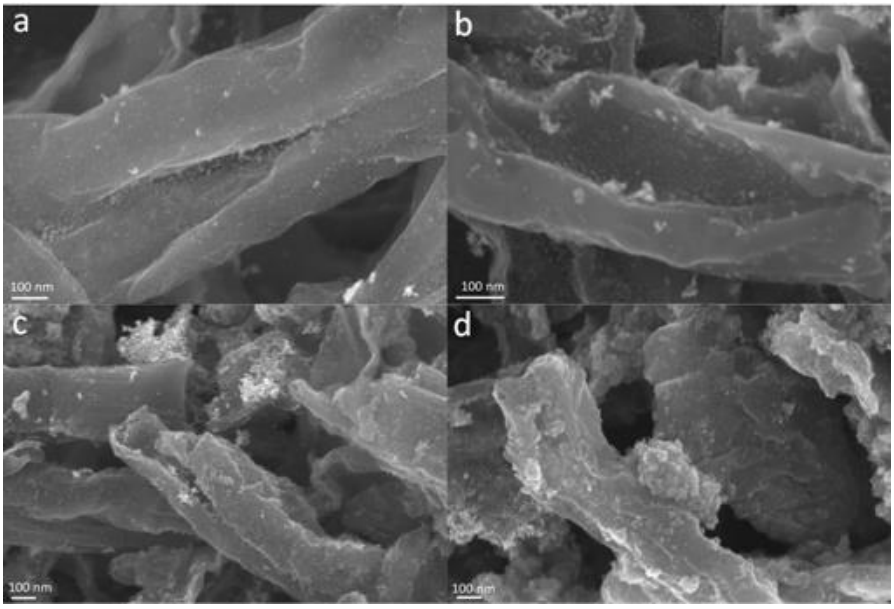

Figure 5.16: SEM pictures of supported Ir catalysts. a) Ir/rGONRs. b) Ir/Low-$TiON_x$/rGONRs. c) Ir/Middle-$TiON_x$/rGONRs. d) Ir/High-$TiON_x$/rGONRs.

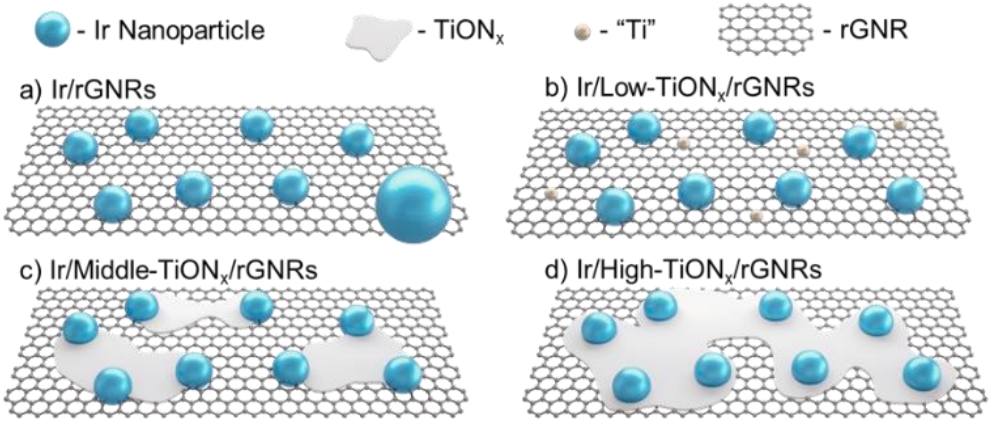

Figure 5.17: Graphical representations of supported Ir electrocatalysts. a) Ir/rGONRs. b) Ir/Low-$TiON_x$/rGONRs. c) Ir/Middle-$TiON_x$/rGONRs. d) Ir/High-$TiON_x$/rGONRs.

SEM analysis provides information about the morphology of the support while the TEM images deliver morphological details of the deposited iridium nanoparticles. In addition, EDXS-TEM mapping provides information about the composition and anchoring locations of Ir nanoparticles as well as the presence of Ti (Figure 5.18). The EDXS signal of Ti follows the trend observed in ICP-OES.

First, the signal in Ir/Low-$TiON_x$/rGONRs is low and evenly spread across the carbon, pointing more toward "doping" than a significant coverage of the carbon (Figure 5.18). From the images, it is not possible to claim if it is single atoms or clusters, but no few nm-sized Ti clusters were observed. Nonetheless, any Ti-containing clusters would be very small (not visible in TEM) or in an amorphous form (lack of XRD diffraction) and account for only 2.3 wt% of the sample. On the other hand, Ti is covering the ribbons like patches in the Ir/Middle-$TiON_x$/rGONRs sample with some bare carbon sections. These patches are described as flakes of $TiON_x$ on nanoribbons. It is observed that the Ir nanoparticles in this sample (in blue in Figure 5.18) are mostly present at the intersection between Ti (in green) and carbon (in red). Finally, for Ir/High-$TiON_x$/rGONRs, the coverage of the carbon surface by $TiON_x$ patches is larger. Subsequently, the Ir nanoparticles are principally sitting on the $TiON_x$ flakes in this catalyst. For comparison purposes, Ir/rGONRs EDXS is also shown but no Ti signal was observed (Figure 5.18). The Ir signal was seen superimposed on the Ti signal for Ir/Middle-$TiON_x$/rGONRs and Ir/High-$TiON_x$/rGONRs but careful examination of the EDXS signal of Ir/Low-$TiON_x$/rGONRs shows that Ir is also present on the Ti small signal for this sample. Hence, it looks like iridium nanoparticles preferentially grow on top or in direct contact with $TiON_x$ patches/clusters. For all samples, the size and morphology of the Ir nanoparticles could be measured from the TEM images. In the two composites with the most Ti, the Ir nanoparticles are spherical with an average diameter of 2.5 ± 0.3 and 2.9 ± 0.2 nm, for Ir/Middle-$TiON_x$/rGONRs and Ir/High-$TiON_x$/rGONRs, respectively (Table 5). On the other hand, in Ir/Low-$TiON_x$/rGONRs and Ir/rGONRs catalyst, the Ir nanoparticles are also small but more elongated. Consequently, the average particle size is more difficult to accurately measure but an estimation of 2.4 ± 0.5 nm and 3.4 ± 0.5 nm was determined for Ir/Low-$TiON_x$/rGONRs and Ir/rGONRs, respectively (Table 5). In addition, some particles up to 25 nm were observed for Ir/rGONRs. Thus, the preferential growth of Ir nanoparticles on $TiON_x$ leads to a smaller and more uniform particle size distribution.

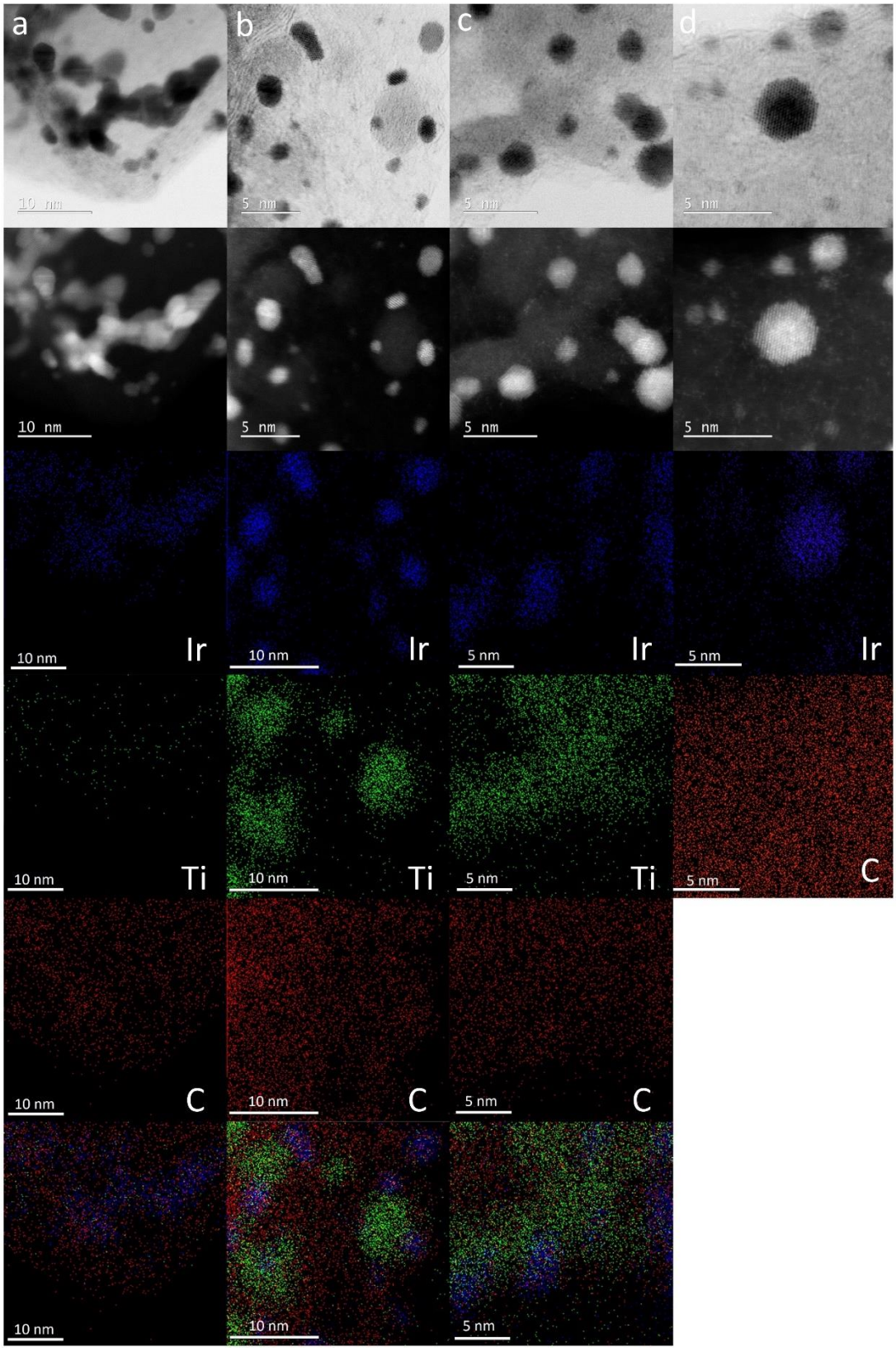

Figure 5.18: STEM (first row: bright field, second row: dark field) and EDS analysis (carbon in red, Ti in green, and Ir in blue). By columns: a) Ir/Low-$TiON_x$/rGONRs. b) Ir/Middle-$TiON_x$/rGONRs. c) Ir/High-$TiON_x$/rGONRs. d) Ir/rGONRs.

Furthermore, Raman spectroscopy confirmed the presence of $TiON_x$ on the surface of rGONRs (Figure 5.19). Spectra recorded at different z values (distance between the objective and the exposed surface of specimen) expose the surface composition. At higher z values with constant laser power, the depth signal is lower and thus the signal originates more from the surface. When z values were increased, the carbon peaks slowly disappeared (typical G and D bands at 1601 and 1354 cm^{-1}) while the typical $TiN/TiO_2/TiON_x$ features[243, 245, 246], discussed before, appeared. The IrO_2 peaks are superimposed in the same range as the ones for Ti-based compounds, specifically at 715 and 445 cm^{-1} [249]. The disappearance/appearance of peaks with z values points out that the $Ir/TiON_x$ is only present on the surface of the carbon.

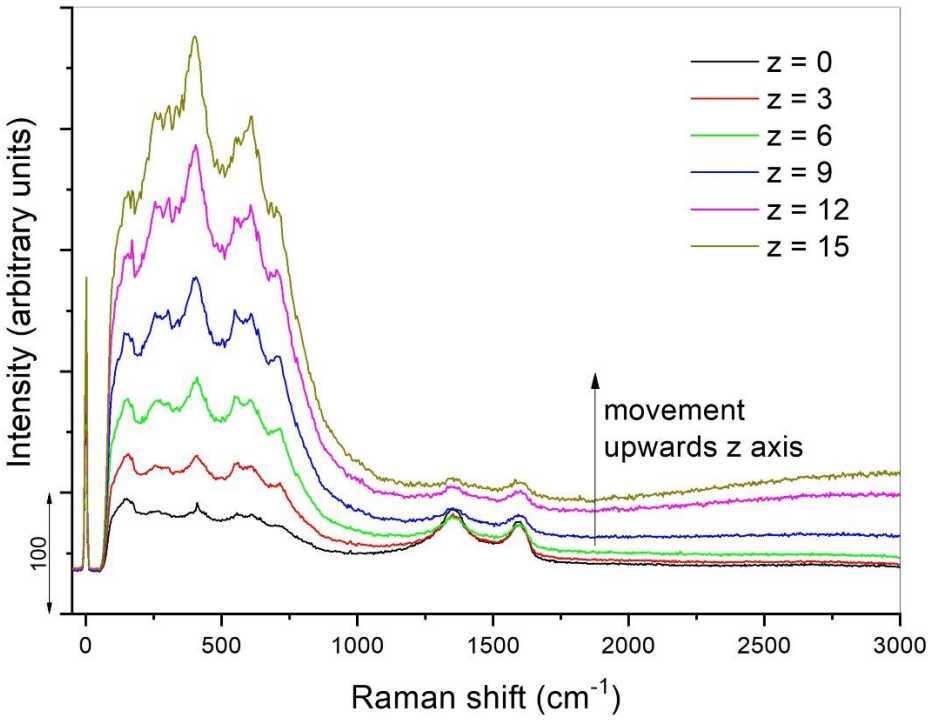

Figure 5.19: Raman spectra of Ir/Middle-$TiON_x$/rGONRs at the same site but at different z axis positions of the objective (in μm). The spectra were recorded using a constant laser power of 4 mW.

5.4.2 Electrochemical characterization

The samples were activated by cycling from 0.05 to 1.6 V_{RHE} under O_2 until a stable CV was obtained. Afterward, the electrolyte was saturated with Ar and the samples were cycled in the same potential at a slow scan rate. The activity was measured at 1.55 V_{RHE} after correcting for the capacitive contribution.

Figure 5.20 displays the anodic part of the CV for all the synthesized catalysts and a commercial IrO_2 (Alfa Aesar). The activity trend is Ir/Middle-$TiON_x$/rGONRs > Ir/High-$TiON_x$/rGONRs > Ir/Low-$TiON_x$/rGONRs > Ir/rGONRs with mass activity of 4820 ± 310, 3200 ± 250, 2910 ± 120, and 2450 ± 150 A/g_{Ir}, respectively. The IrO_2 benchmark has a recorded activity of 157 A/g_{Ir}, which is comparable to literature measurements for this benchmark[72, 85, 98, 224, 264-266]. It means that our catalysts present a 30.5, 20.4, 18.4, and 15.5 improved activity over the benchmark. The enhanced activity can be mostly ascribed to better utilization of Ir in the supported analogues over the IrO_2 benchmark, namely smaller particle size and thus higher active surface area exposed. However, while the particle size

difference and the use of support can explain the difference between the synthesized catalysts and benchmark, it does not provide a satisfying explanation for the difference of activity observed between the supported analogues. Other factors can be responsible for activity differences as an effect of the support[98, 100, 108, 126, 207, 265] or Ir-oxide composition[121, 273] (e.g., hydrous iridium oxide is more active than the crystalline oxide).

In the case of Ir/Low-$TiON_x$/rGONRs and Ir/rGONRs samples, a comparable activity is expected as they have a similar structure and composition as seen from the XRD results (black curve in Figure 5.15c and red in Figure 5.15d, respectively). The main differences between these two samples are the low amount of $TiON_x$ on graphene in the Ir/Low-$TiON_x$/rGONRs (2.30 wt%), a bit smaller average particle size (3.4 ± 0.5 nm vs 2.3 ± 0.5 nm for Ir/Low-$TiON_x$/rGONRs and Ir/rGONRs, respectively) and the presence of large particles found only in Ir/rGONRs. Intriguingly, these differences do not affect the OER activity at low potential (under 1.53 V_{RHE}), but they do have an impact at higher potentials. This difference cannot be ascribed to the small addition of $TiON_x$, as 2.30 wt% is likely not enough to induce a SMSI effect and thus an influence on the activity. However, this small addition is indeed enough to impact the stability of carbon as addressed later. Therefore, the trend shift at low and high potentials is most likely due to the presence of large particles in the Ir/rGONRs sample. At high potentials, the bubble management issue has a significant impact on the activity as mentioned before and larger particles have a lower active surface area per mass than small particles. Consequently, at high potentials, the bubble formation and release are improved on small particles. Thus, Ir/Low-$TiON_x$/rGONRs catalyst with a more homogeneous dispersion of Ir nanoparticles has better activity than Ir/rGONRs at high potentials where the bubbles management plays a more important role, and thus the particle size distribution is more critical, while it has a similar activity at low potentials. On the other hand, adding a higher amount of Ti (both 13.59 wt% and 31.34 wt%) drastically increases the activity. Several factors could explain this enhancement. First, $TiON_x$ has been shown to induce SMSI with Ir (Chapter 5.2.2) and the presence of flakes, oppositely to 2.30 wt%, is most likely enough to generate this effect. It can affect the growth of the less-active Ir-oxide and thus affect OER activity and Ir nanoparticles stability as previously shown. Secondly, the nanoparticles in Ir/rGONRs and Ir/Low-$TiON_x$/rGONRs are more elongated than the spherical ones of Ir/Middle-$TiON_x$/rGONRs and Ir/High-$TiON_x$/rGONRs catalysts. The catalytic reactions have been shown to be catalyst-shape dependent and thus this could influence the OER activity[254, 278-280]. The last possible influencing factor is the average particle size and thus Ir utilization. However, this factor is definitely not enough by itself. Indeed, Ir/Middle-$TiON_x$/rGONRs has the smallest average particle size (2.52 ± 0.33 nm) compared to the two other analogues (3.40 ± 0.47 nm and 2.92 ± 0.2 nm for Ir/Low-$TiON_x$/rGONRs and Ir/High-$TiON_x$/rGONRs, respectively), but this accounts to only a 20 % difference (based on simple geometric particle size-to-surface calculation, assuming spherical particles) while the difference in mass normalized activity is between 40 and 50 %.

The small amount of Ti in Ir/Low-$TiON_x$/rGONRs (2.3 wt%) is assumed not to induce the SMSI effect due to a doping-like presence of Ti instead of Ti-containing structures as defined by XRD and EDXS. At the same time, both Ir/Middle-$TiON_x$/rGONRs and Ir/High-$TiON_x$/rGONRs analogues should have a similar SMSI effect as they both have $TiON_x$ flakes. However, the beneficial effect obtained with the addition of a halfway amount of $TiON_x$ (13.59 wt% Ti, Ir/Middle-$TiON_x$/rGONRs) does not scale up when a higher amount of $TiON_x$ is added. Namely, Ir/High-$TiON_x$/rGONRs has a lower activity than Ir/Middle-$TiON_x$/rGONRs (around 40 %). The first look of STEM images and EDXS mapping gives the impression that Ir nanoparticles are sitting on $TiON_x$ for both High- and Middle-analogues while a closer inspection tells another story. The Ir nanoparticles are indeed anchored on top of $TiON_x$ flakes in Ir/High-$TiON_x$/rGONRs but the nanoparticles

are present on their edges in Ir/Middle-$TiON_x$/rGONRs catalyst. In the latter, the nanoparticles are in contact with $TiON_x$ and with the rGO nanoribbons simultaneously. Therefore, the heterojunction between nanoparticles and the support as well as the binding environment is not the same in both catalysts which indicates that the difference in activity could go beyond the effect of SMSI with $TiON_x$. It suggests that the notable activity increase in Ir/Middle-$TiON_x$/rGONRs occurs due to some synergistic effects due to the special position of Ir nanoparticles in contact with both $TiON_x$ flakes and carbon. This unique distribution which brings the highest activity is not present for lower Ti loading, where the Ir nanoparticles are predominantly supported on carbon, nor at higher loading, where the nanoparticles are anchored on top of $TiON_x$ flakes. Indeed, the activity can be presented as a volcano-plot where on one side, there are carbon-support catalysts, and on the other side, the catalysts with Ir are on $TiON_x$, while Ir/Middle-$TiON_x$/rGONRs, with Ir nanoparticles sitting on both $TiON_x$ and carbon, is at the top.

The Tafel slopes are similar for all the catalysts with values of 50.2, 52.4, 54.7 and 59.1 mV/dec for Ir/Middle-, High-, Low-$TiON_x$/rGONRs and Ir/rGONRs, respectively. Hereby, all the materials have the same RDS for OER. Moreover, values between 40 and 70 mV/dec are frequent for Ir-based catalysts[98, 224, 254, 264-266, 281] (Table 6).

In comparison to the literature (Table 6), Ir/Middle-$TiON_x$/rGONRs catalyst is the most active catalyst reported at 25°C. It outperforms the most active Ir-alloys catalysts reported so far by Alia et al. (3353 A/g_{Ir} and 2327 A/g_{Ir} at 1.55 V_{RHE} for Ir-Ni and Ir-Co, respectively)[85]. With an activity of 862.93 A/g_{Ir} at 1.5 V_{RHE}, it also overpasses the performance of other supported Ir catalysts (Ir/ATO, 185 A/g_{Ir} at 1.5 V_{RHE}) proposed by Hartig-Weiss et al.[103], or IrRu@Te presented by Xu et al. (590 A/g_{IrRu} at 1.5 V_{RHE})[282]. In addition, the impact of the carbon template was observed when compared with our previously made $TiON_x$-nh-Ir catalysts (Chapter 5.3). The catalysts with a carbon template have one order of magnitude higher activity. The Tafel slope is also slightly lower for the catalysts with a carbon template with a value between 50 and 55 mV/dec over the 60-65 mV/dec observed before. The RDS is similar in both groups as the difference is not big enough, but this still indicates that the kinetics is higher when the carbon template was used.

Therefore, the $TiON_x$ support can directly influence Ir nanoparticles properties like morphology, particle size or electrical contact. Moreover, it can also affect the electrochemical performances of Ir nanoparticles via many features like support interaction[272], better wiring[239] or oxygen bubble formation and removal process[237]. These will influence not only the activity but also the stability (SMSI) or the Tafel slope. The last one depends on the coverage of the catalysts by the intermediates[283-285] and thus is influenced by, among others, the oxygen bubble formation/removal, the Ir nanoparticles morphology, the adsorption energy and the Ir oxidation state.

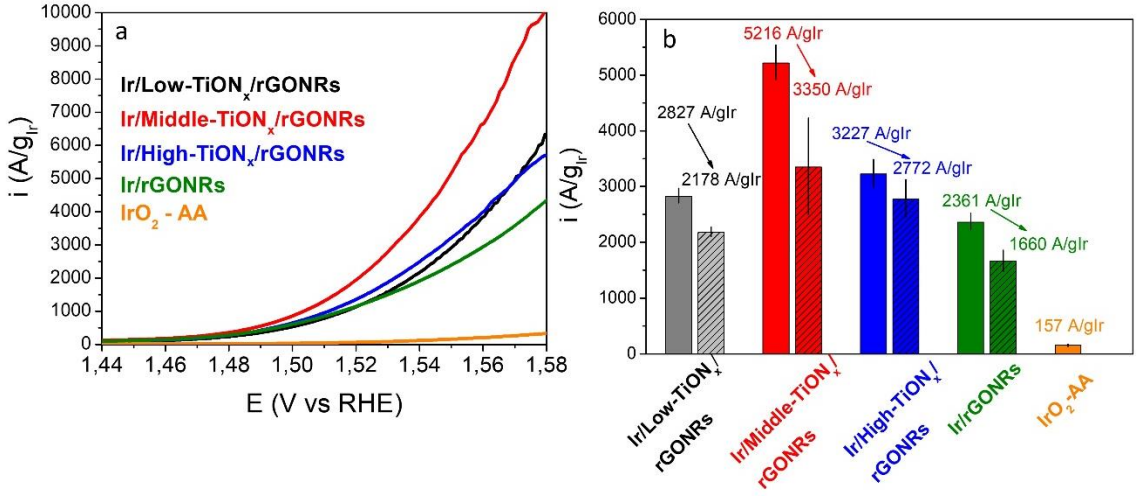

Figure 5.20: OER performance of the catalysts in Ar-saturated 0.1 M $HClO_4$. a) Positive scans after correction for the capacitive contribution of the CVs (20 mV/s, 0.05 to 1.6 V_{RHE}). b) OER mass activities at 1.55 V_{RHE} of the catalysts before (plain) and after (crosshatch) chronopotentiometry (average of three measurements).

Table 6: Comparison of electrochemical performances of Ir-based catalysts.

Samples	A/g_{Ir} at 1.5 V_{RHE}	A/g_{Ir} at 1.55 V_{RHE}	Tafel slope (mV/dec)
Ir/rGONRs	605	2361	59.1
Ir/Low-TiON$_x$/rGONRs	540	2827	54.7
Ir/Middle-TiON$_x$/rGONRs	863	5216	50.2
Ir/High-TiON$_x$/rGONRs	649	3227	52.4
IrO_2-AA	34	157	67.6
TiON$_x$-1h-Ir		361	60
TiON$_x$-3h-Ir		520	63
TiON$_x$-6h-Ir		370	65
Ir[224]		140-300	
Ir/V[224]		460	
Ir/TiO_2 [224]		70	
IrO_x [72]		689	
IrNi[85]		3353	
IrCo[85]		2327	
Ir bulk[254]			63
Ir nanoparticles[254]			64
Ir network[286]		1850*	
IrO_2/TiN[204]		< 250*	
IrO_x/ATO[98]	20*		56.8-59.4
IrRu@Te[282]	590		

* From graphs

5.4.3 Stability evaluation

5.4.3.1 Electrochemical performances and morphological change

In this case, the stability of the OER catalysts was evaluated with two different ADTs. The measurements were performed on fresh films. The first degradation test was 5000 fast cycles in the OER window, 1.2 to 1.6 V_{RHE}, 1V/s. The catalysts maintained a high activity after this test (Table 7). This ADT, while often performed in literature[72, 85, 121, 273], is, in our opinion, not severe enough to induce degradation mechanisms of the catalysts and thus longer tests are needed to observe effective degradation. In addition, the current target of the real device (WE) is to achieve a good current density. Hence, the second test was a chronopotentiometry (CP) protocol. A constant current of 2 mA/cm^2_{geo} was applied for two hours which is equivalent to 0.2-0.3 mA/ μg_{Ir} for the given loading on the electrode (around 6–9 $\mu g_{Ir}/cm^2$).

After the first ADT (cycling), the activity retention trend is Ir/Low-$TiON_x$/rGONRs > Ir/High-$TiON_x$/rGONRs > Ir/Middle-$TiON_x$/rGONRs. The most stable catalyst retains 99% of its initial activity while High- and Middle- analogues keep 93 and 87%, respectively. The stability trend under cycling is the opposite of the activity trend for the $TiON_x$-analogues. This is logical as the catalyst that is less active will reach a lower current during fast cycling in the same potential window than a highly active catalyst. Consequently, less oxygen is produced (which can involve dissolution of iridium[287]), less oxidation of the support/nanoparticles occurs and thus the more active the catalysts are, the harsher the cycling degradation test. Moreover, it was shown that the O_2 bubbles, formed during fast cycling, can block the active spots, and thus decrease the measured activity[288, 289]. This problem is also more impactful for more active catalysts. Nonetheless, the less active catalyst Ir/rGONRs is also the less stable under cycling with 84% activity retention. This could be due to the absence of stabilizing SMSI between Ir nanoparticle and the carbon support, oppositely to $TiON_x$ containing materials.

On the other hand, the stability trend after the CP-ADT is Ir/High-$TiON_x$/rGONRs > Ir/Low-$TiON_x$/rGONRs > Ir/rGONRs > Ir/Middle-$TiON_x$/rGONRs. Here, the good stability of Ir/rGONRs and Ir/Low-$TiON_x$/rGONRs, with 70 and 77% activity retention respectively, was surprising as the carbon was expected to heavily degrade. The 7% difference was attributed to the "Ti-doping" in Ir/Low-$TiON_x$/rGONRs. In the case of Ir/High-$TiON_x$/rGONRs, 85% of the activity remains after 2 hours, making it the most stable catalyst while the second-best catalyst in terms of activity. On the other hand, the most active catalyst, Ir/Middle-$TiON_x$/rGONRs, is the least stable one with a 36% loss of activity. However, its activity after degradation is still one of the highest in literature[85, 282, 283] with 3097 A/g_{Ir}.

Table 7: Remaining activity after ADTs.

Samples	A/g_{Ir} at 1.55 V_{RHE}	% of activity retained at 1.55 V_{RHE} after 2h at 2 mA/cm^2_{geo}	% of activity retained at 1.55 V_{RHE} after 5000 cycles (1.2 to 1.6 V_{RHE})
Ir/rGONRs	2361	84	70
Ir/Low-$TiON_x$/rGONRs	2827	99	77
Ir/Middle-$TiON_x$/rGONRs	5216	87	64
Ir/High-$TiON_x$/rGONRs	3227	93	85

In addition to the evaluation of activity before and after ADTs, the morphological changes were investigated with TEM. After 5000 cycles, no major structural changes were observed in Ir/Middle-$TiON_x$/rGONRs. The particles were still small and evenly dispersed on the support (Figure 5.21a-d). After the CP protocol, the particles start to agglomerate which reduces the ECSA and could explain the loss of activity (Figure 5.21e-h). The agglomeration occurs at the junction between rGONRs and $TiON_x$ as seen in EDXS (Figure 5.22e-h). In comparison, the most stable catalyst under CP (Ir/High-$TiON_x$/rGONRs) exhibits lower agglomeration and higher retention of the spherical shape of the nanoparticles (Figure 5.21i-l). Moreover, the carbon template remains covered by $TiON_x$ (Figure 5.22i-l).

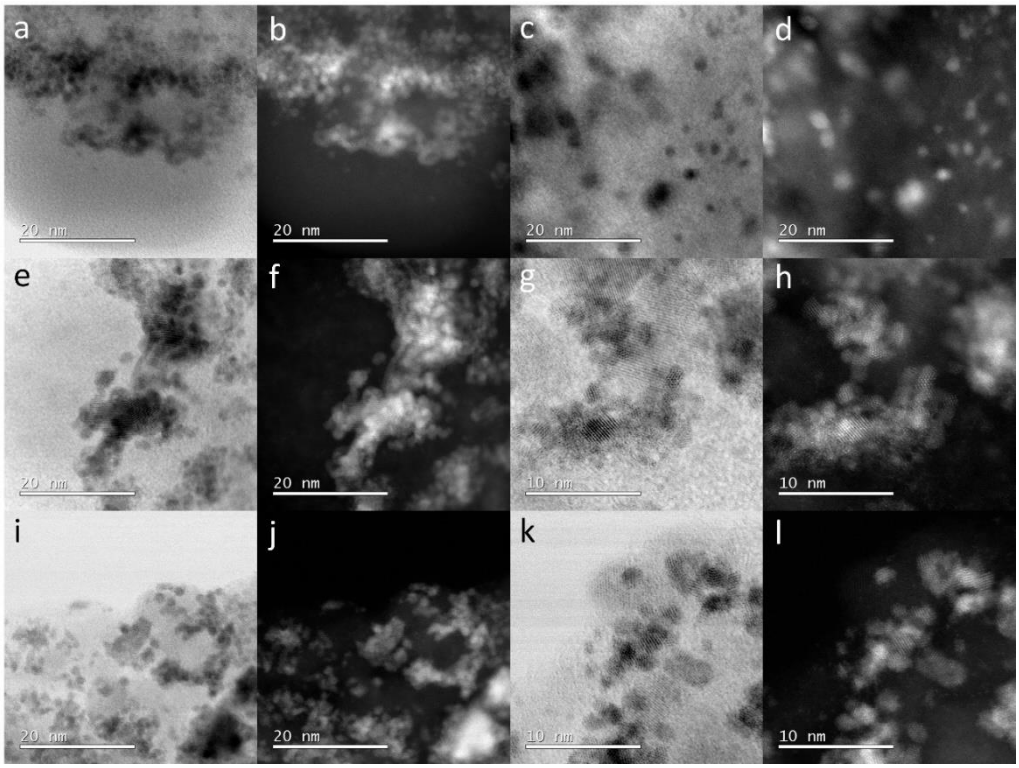

Figure 5.21: TEM pictures. a-d) Ir/Middle-$TiON_x$/rGONRs after 5000 cycles between 1.2 and 1.6 V_{RHE}. e-h) Ir/Middle-$TiON_x$/rGONRs after 2h at 2 mA/cm^2_{geo}. i-l) Ir/High-$TiON_x$/rGONRs after 2h at 2 mA/cm^2_{geo}.

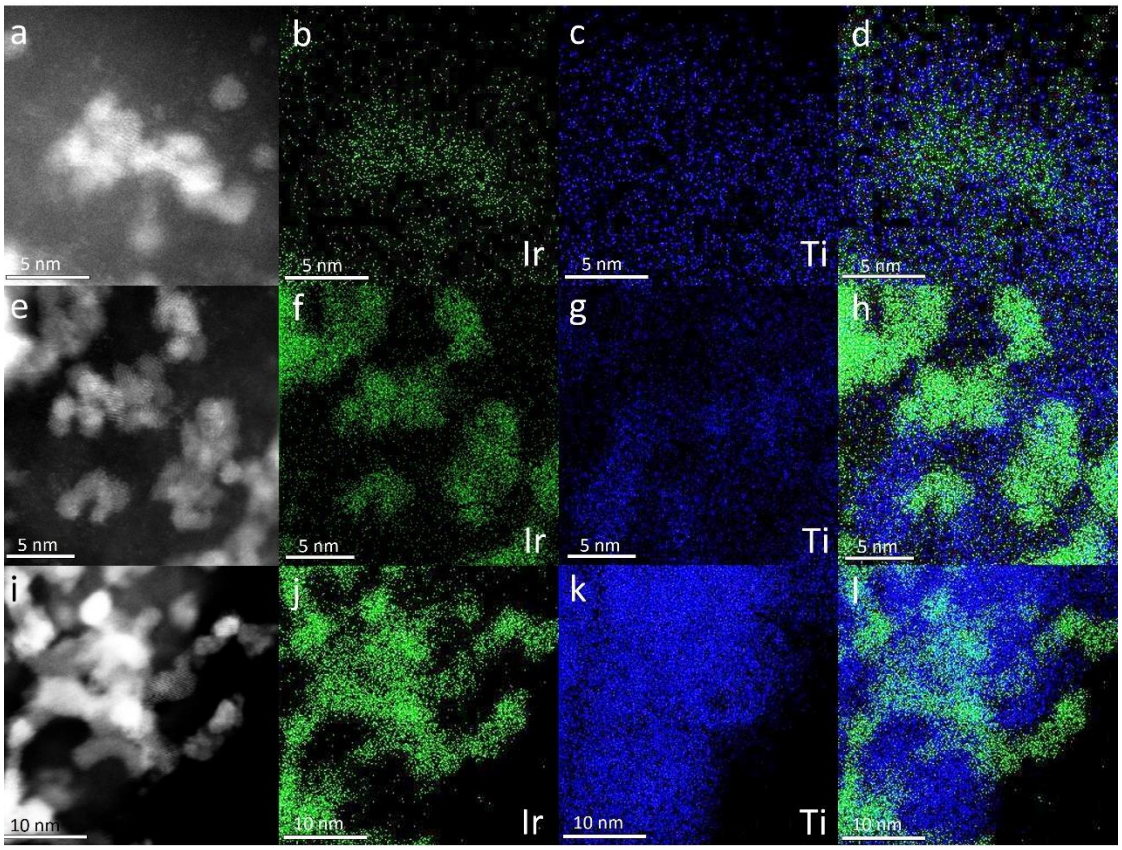

Figure 5.22: EDXS analysis. a-d) Ir/Middle-$TiON_x$/rGONRs after 5000 cycles between 1.2 and 1.6 V_{RHE}. e-h) Ir/Middle-$TiON_x$/rGONRs after 2h at 2 mA/cm^2_{geo}. i-l) Ir/High-$TiON_x$/rGONRs after 2h at 2 mA/cm^2_{geo}. Ir in green, Ti in blue.

5.4.3.2 CO_2 evolution – EC-MS

To better understand the degradation happening in each catalyst, additional techniques were performed. Namely, degradation of the carbon support was followed by recording the evolution of CO_2 with an EC-MS. The in-situ dissolution of the metals during OER cycling was detected by EFC-ICP-MS.

The protocol employed in the EC-MS consisted of an initial activation (10 potential cycles, 0.05 to 1.2 V_{RHE}, 200 mV/s) followed by three 5-minute-long degradation tests to get initial information about support degradation during different protocols. The first degradation consisted of 100 cycles between 1.2 and 1.5 V_{RHE}, the second protocol was a CP at 0.5 mA/cm^2 and the last one was a chronoamperometric (CA) protocol at 1.5 V_{RHE}. The integrated and normalized per carbon mass signals of CO_2 are visible in Figure 5.23. The catalyst with only 2.30 wt% of Ti (Ir/Low-$TiON_x$/rGONRs) evolved significantly less CO_2 than the analogue without Ti (Ir/rGONRs). Thus, such a small amount of Ti, doping-kind, has a clear stabilization effect on carbon. However, higher loadings of Ti lead to higher CO_2 release normalized by the mass of carbon in the samples, even compared to Ir/rGONRs. Therefore, the structure with $TiON_x$ flakes promotes faster carbon corrosion. This goes against the initial thought of $TiON_x$ protecting carbon from oxidizing. Nonetheless, Ir/High-$TiON_x$/rGONRs retains its OER activity the most after CP which would not occur if $TiON_x$ flakes were losing contact with the carbon support. Thus, the increase in carbon oxidation is more likely a consequence of the different morphology and surface chemistry of the graphene after the addition of titanium compounds during sample preparation and does not contribute to the loss of conductivity. Indeed, the SEM images

(Figure 5.16) show that the morphology of the nanoribbons changed significantly after the addition of $TiON_x$ flakes with a smaller average diameter and rougher surface, possibly due to carbon oxidation. The higher roughness and/or more oxygen functionalities could have led to the increase in CO_2 release. Nevertheless, after the initial release of this CO_2 from unstable parts of the nanoribbons, the activities for the catalysts containing $TiON_x$ flakes are still high (Ir/High-$TiON_x$/rGONRs and especially Ir/Middle-$TiON_x$/rGONRs). Therefore, an initial "break-in" protocol can be envisaged to lose the unstable carbon and then having these catalysts perform with a minimal activity loss.

The trend of carbon corrosion during the different electrochemical protocols is similar for all samples except one. Namely, CO_2 production drops in the order of CV > CP > CA. This is most likely due to the history of the sample than to the parameters of experiments. Indeed, it is common to observe less and less CO_2 the longer the degradation protocol (of any kind) is performed. Ir/Low-$TiON_x$/rGONRs is the only material with a unique response, with the most CO_2 produced during the second test (CP) which only suggests further that a low amount of $TiON_x$ in the carbon support has a distinctive impact on the corrosion of the latter. Overall, carbon degradation is not the main mechanism responsible for the loss of activity in the samples as the catalyst with the most CO_2 evolution per carbon in the sample is also one of the most stable ones in terms of activity retention. This could change if graphene-based carbon was not used.

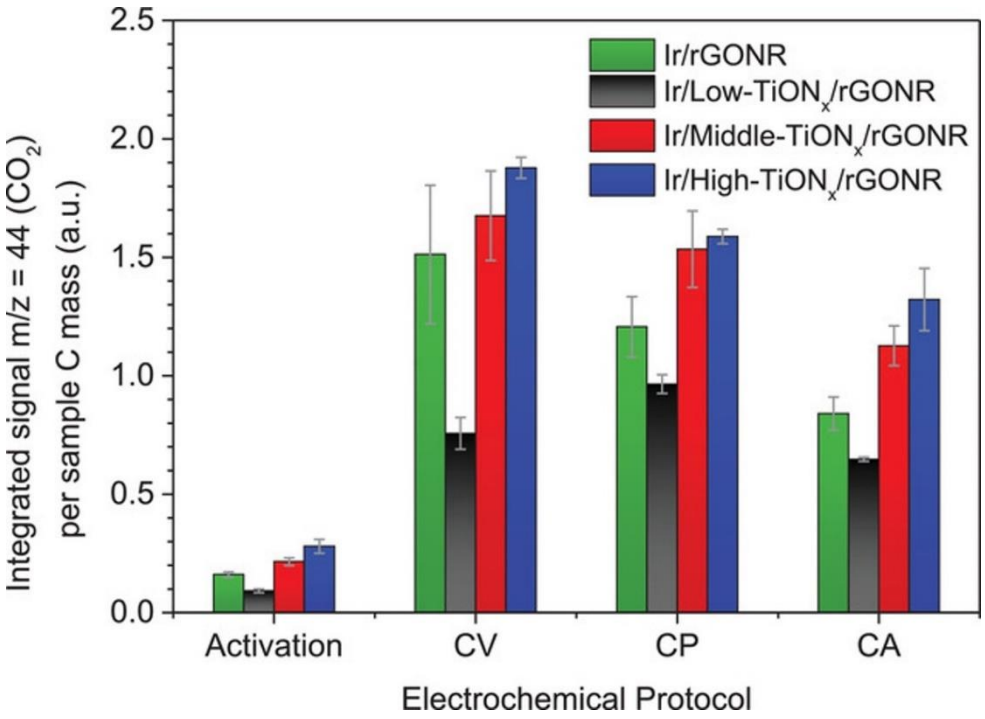

Figure 5.23: Results for carbon oxidation to CO_2. Integrated CO_2 signals evolved during the EC-MS electrochemical protocol (preconditioning, cyclic voltammetry (CV), chronopotentiometric (CP), and chronoamperometric (CA)), normalized per carbon mass. The amounts of released CO_2 were determined and averaged per two or three measurements.

5.4.3.3 Metal dissolution – EFC-ICP-MS

In the EFC-ICP-MS set-up, the catalysts were also preconditioned (10 cycles between 0.05 and 1.2 V_{RHE}, 200 mV/s) before two slow cycles (1.2 to 1.6 V_{RHE}, 20 mV/s) were applied to reveal the mechanism of dissolution of the metals present in the samples. Understanding

the fundamental dissolution behavior is relevant to predicting the long-term performance of the catalysts under prolonged operation.

5.4.3.3.1 Ti dissolution

The low Ti signal of Ir/rGONRs seen in Figure 5.24 is attributed to background noise as no Ti is present in the sample. The three other samples have the same mechanism of dissolution during the preconditioning step as the peaks have the same shape and position in Figure 5.24. First, a sharp increase in Ti dissolution is noticed. This is attributed to the cleaning of the surface. Afterwards, the Ti dissolves during each cycle with a decreasing trend. This dissolution is recognized as the transient dissolution occurring during the oxidation and reduction of metals[83, 108].

During the slow cycles, only one peak is observed for the three samples, even if a shoulder is visible, especially for Ir/High-$TiON_x$/rGONRs (in blue in Figure 5.24). This is due to the transient dissolution during oxidation/reduction reactions. However, the Pourbaix diagram of Ti shows that a passivated state of Ti is formed at OER conditions[136] and thus only little dissolution is expected once this TiO_2 passivated layer is present. This is observed with an already two-times lower dissolution in the second slow cycle. Therefore, $TiON_x$ can be stabilized by a TiO_2 layer and prevent any Ti dissolution after the adequate conditioning protocol[272, 290]. This can also partially explain a drop-in activity for $TiON_x$-containing samples if a too thick TiO_2 layer is formed[272].

In the case of Ir/Low-$TiON_x$/rGONRs, a relatively high dissolution of Ti was observed. It is attributed to the high active-surface area exposed for $TiON_x$ compared to its mass in the sample (due to the doping-like structure) with possibly its amorphous structure playing a role. In the same way, Ir/High-$TiON_x$/rGONR has the lowest dissolution per mass with the largest flakes observed and thus an expected lower surface area exposed per mass. A general conclusion can be that the Ti dissolution, normalized by the mass of Ti, decreases with the increase in coverage of carbon by $TiON_x$ patches, probably related to the exposed surface area of $TiON_x$.

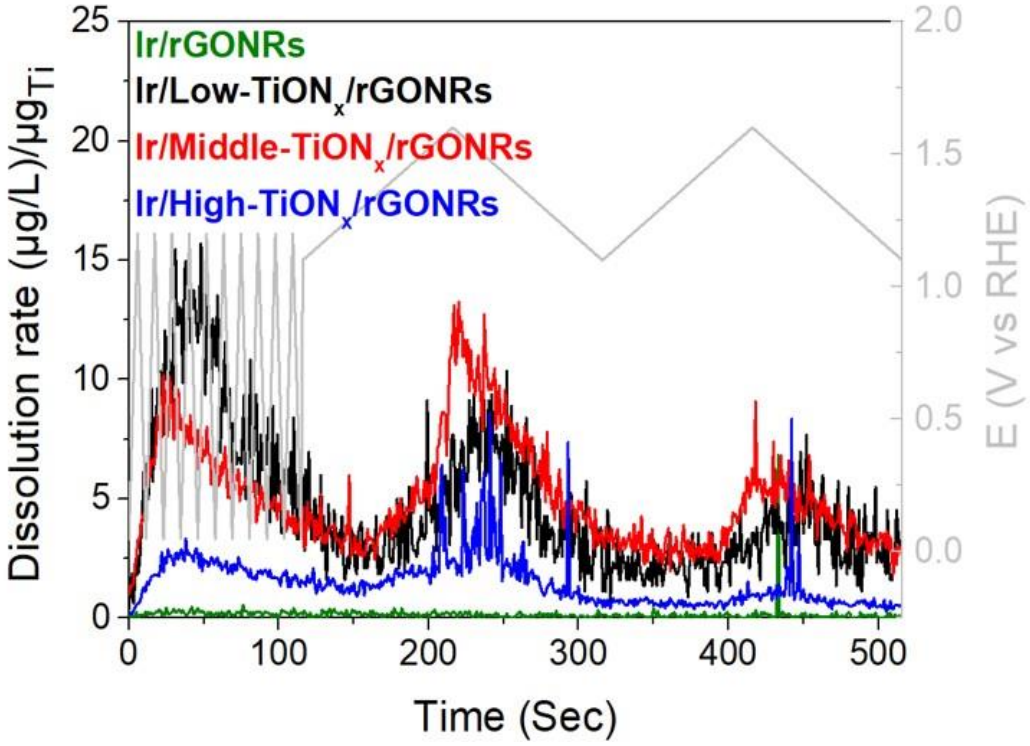

Figure 5.24: Dissolution of Ti in Ir/rGONRs (green), Ir/Low-$TiON_x$/rGONRs (black), Ir/Middle-$TiON_x$/rGONRs (red) and Ir/High-$TiON_x$/rGONRs (blue).

5.4.3.3.2 Ir dissolution

Iridium dissolves in all the samples during the preconditioning cycles (Figure 5.25). A steady dissolution is quickly reached for Ir/rGONRs while the Ti-containing samples exhibit an increasing dissolution in the order Ir/High-$TiON_x$/rGONRs $\leq$ Ir/Low-$TiON_x$/rGONRs $<$ Ir/Middle-$TiON_x$/rGONRs. Thus, a stable response is not reached for the Ti-containing samples. The particle size impacts the dissolution rate of precious metals. The smaller the particle, the higher the percentage of its atoms exposed (to oxidation or reduction) at the surface. Moreover, the size of the particle also influences the inherent stability of the surface atoms. Namely, smaller particles are expected to be less stable than large ones due to the Gibbs Thompson effect (e.g. Pt particles)[291, 292]. In our case, this explanation cannot be used to understand the trend observed during the preconditioning because Ir/rGONRs present the smaller Ir nanoparticles (2.35 ± 0.47) and not the worst stability. Another parameter that affects stability is related to the oxidation state of the nanoparticles. For example, the hydrous IrO_x is less stable than crystalline IrO_2[107, 121, 293, 294]. This was also shown when the particles were supported on the same support (ATO), IrO_x was dissolving more than its IrO_2 counterpart[109]. In our analogues, the XRD spectrum exhibits the same peak for Ir and thus it is likely to be in a similar oxidative state in all the materials.

Therefore, the difference in dissolution during the preconditioning is attributed to a different response of Ir under the electrochemical protocol applied. Considering the similar synthesis leading to a similar oxidative state in the "as-prepared" samples and the particle size difference being previously excluded as a possible explanation, the support effect needs to be considered to clarify the observed trend. Higher dissolution occurring in Ti-containing catalysts compared to Ir/rGONRs indicates that a less stable iridium oxide is formed[229], which is consistent with previously shown results of the SMSI effect (Chapter 5.2). In

addition, the Ti dissolution trend during conditioning (Low>Middle>High) and the Ir dissolution trend (Middle>High>Low) are different, implying that Ti dissolution in the support has a very low effect on the dissolution of nanoparticles (Ir).

The Ir dissolution during the first slow cycle between 1.2 and 1.6 V_{RHE} exhibits a peak of dissolution at the beginning of the anodic scan for Ir/Middle-$TiON_x$/rGONRs and Ir/High-$TiON_x$/rGONRs as well as a small shoulder for Ir/Low-$TiON_x$/rGONRs. On the other hand, Ir/rGONRs exhibits no anodic peak. This anodic peak corresponds to the transient dissolution happening during the oxidation of iridium surface[293, 294]. This peak is mostly visible for Middle- and High-analogues, indicating that the iridium is to a larger extent in a metallic/hydrous-oxide form in these catalysts compared to the already oxidized iridium after conditioning in Ir/rGONRs. This is visible in the CV of the conditioning where the H_{upd} (not present on Ir-oxides) and Ir reduction/oxidation peaks (between 0.4 and 0.6 V_{RHE}) are more pronounced for the Ti-containing samples, especially Ir/Middle-$TiON_x$/rGONRs (Figure 5.26). This was previously explained by the SMSI effect of TiONx on the formation of hydrous oxides. A second anodic peak, with an onset potential between 1.45 and 1.5 V_{RHE}, is observed for all samples. This peak is related to the OER and implies the dissolution of iridium during the reaction[290, 295].

The dissolution trend switches between the two cycles. Namely, during the first cycle, the trend is Ir/Middle-$TiON_x$/rGONRs > Ir/High-$TiON_x$/rGONRs ≥ Ir/rGONRs > Ir/Low-$TiON_x$/rGONRs while the dissolution trend becomes Ir/Middle-$TiON_x$/rGONRs > Ir/rGONRs > Ir/High-$TiON_x$/rGONRs ≥ Ir/Low-$TiON_x$/rGONRs during the second cycle. Hereby, a "doping-wise" amount of $TiON_x$ (Ir/Low-$TiON_x$/rGONRs) or a significant amount of $TiON_x$ (over 30 wt%, Ir/High-$TiON_x$/rGONRs) are added to the support to nicely cover the carbon, the stability of iridium increases during cycling, even after only two cycles. However, the Ir dissolution of Ir/Middle-$TiON_x$/rGONRs is the highest during the second cycle, where the background dissolution due to the conditioning protocol does not play a role anymore. Hence, the unique position of the nanoparticles in this sample negatively affects the stability while providing high activity. The second cycle is in adequation with the stability trend obtained after CA protocol. Ir/Middle-$TiON_x$/rGONRs has the lowest relative stability and Ir/rGONRs is the second worst catalyst while both Ir/Low-$TiON_x$/rGONRs and Ir/High-$TiON_x$/rGONRs reach a low dissolution and keep most of their activity after the ADT.

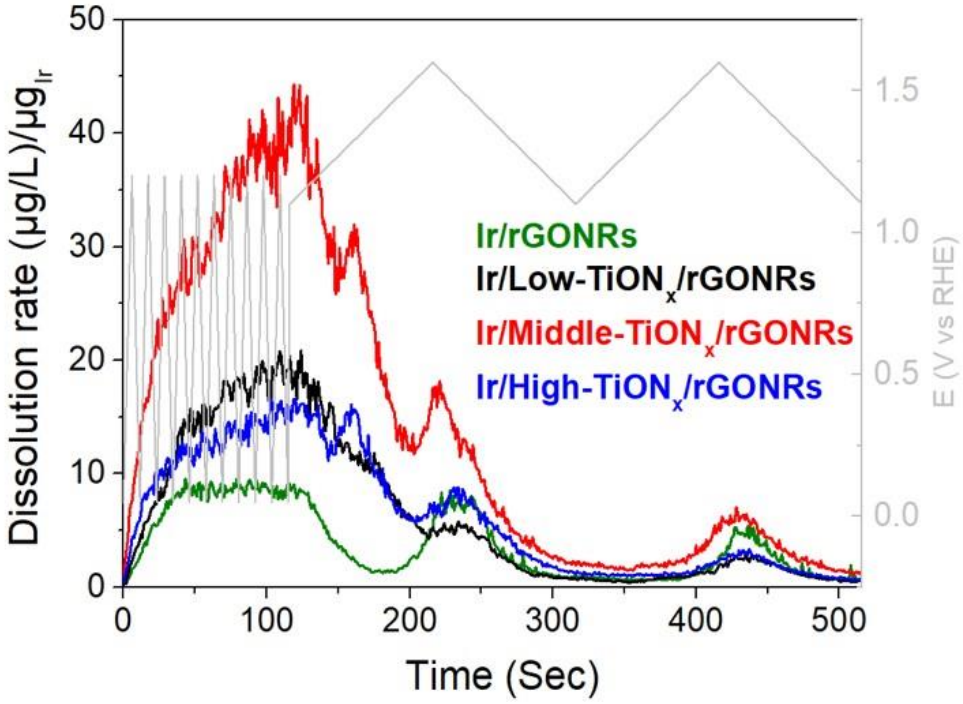

Figure 5.25: Dissolution of Ir in Ir/rGONRs (green), Ir/Low-TiON$_x$/rGONRs (black), Ir/Middle-TiON$_x$/rGONRs (red) and Ir/High-TiON$_x$/rGONRs (blue).

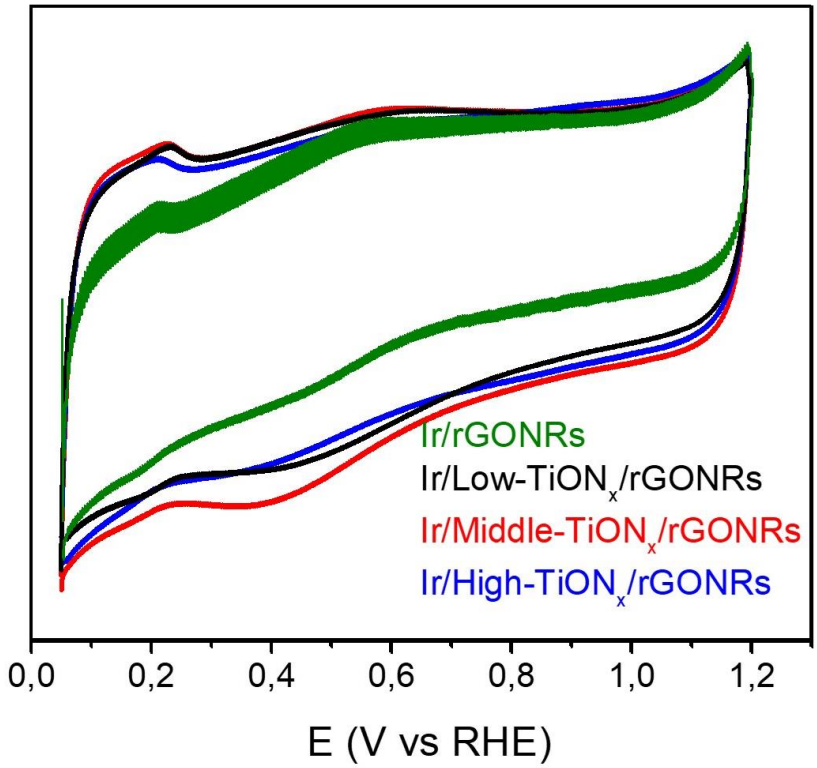

Figure 5.26: Preconditioning/cleaning cyclovoltamograms during ICP-MS measurements. Cycling between 0.05 and 1.2 V_{RHE}, 200 mV/s, cycle 10 presented.

5.4.4 Conclusion

Hereby, the catalysts made from a graphene-based template partially covered with $TiON_x$ flakes support exhibit excellent activity for OER. In fact, when sufficient amounts of Ti were covering the carbon, record activities were achieved with 4822 A/g_{Ir} and 3220 A/g_{Ir} at 1.55 V_{RHE} for Ir/Middle-$TiON_x$/rGONRs and Ir/High-$TiON_x$/rGONRs, respectively. The sample with the highest amount of $TiON_x$ flakes also displays the best stability under CP degradation test with an 85 % activity retention. In addition, even low loadings of Ti in the support, "doping-like", were shown to improve the activity and stability of OER catalyst. Namely, the Ir/Low-$TiON_x$/rGONRs catalyst beats the performance of Ir/rGONRs both in activity, with 2906 A/g_{Ir} vs 2453 A/g_{Ir} at 1.55 V_{RHE}, and in stability, 77% retention of activity over 70%, respectively.

The activity improvement for the samples was attributed to the SMSI between Ir and $TiON_x$. The enhancements of activity and stability are highly dependent on the composition ratio of the ceramic and carbon, and on the contact point between Ir nanoparticles and the support. Indeed, the highest activity was found when Ir was on the edges of $TiON_x$ and thus also in contact with the carbon (Ir/Middle-$TiON_x$/rGONRs). Therefore, it is possible to tune the OER performances by adjusting the interfacial contacts between a mix carbon/$TiON_x$ support and the Ir nanoparticles.

5.5 Conclusion

First, the $TiON_x$ material was shown to fit the electrocatalyst support requirements. Namely, a conductivity of 3-8 S/cm was measured for purely $TiON_x$, overpassing other proposed supports like ATO, by one order of magnitude. The good conductivity was accompanied by a sufficient surface area that allows a fine dispersion of nanoparticles. In practice, nanoparticles of iridium as small as 2 nm could be effectively deposited on the $TiON_x$ support.

Afterwards, the impact of the morphology of the support on the activity and stability of the electrocatalysts was studied. $TiON_x$ support was synthesized from anodically grown TiO_2 nanotubes and various morphologies were obtained by changing the time of the anodic grow step. Other parameters such as the Ir particle size and loading were kept constant. Two morphological features of the support were observed, nanotubular arrays and nanoparticulate agglomerates. When the nanotubular structure is predominant ($TiON_x$-1h-Ir), the OER activity is particularly good at low current densities while the nanoparticulate morphology ($TiON_x$-6h-Ir) becomes more efficient at higher current densities. The $TiON_x$ can be oxidized, causing higher electron resistance at the contact point for the nanoparticles compared to nanotubular arrays. However, this could also be positive to protect the interior of $TiON_x$ as long as the oxidized layer is thin enough to not induce high resistance. Nonetheless, the bubble formation/detachment cycle occurring during OER has a huge impact on activity, particularly at high reaction rates (i.e. higher potentials). The nanoparticulate agglomerates are more efficient in managing this cycle than the nanotubular morphology and thus better at higher potential. The support morphology for the best catalyst was made of a mixture of both ($TiON_x$-3h-Ir). This combination brings the best tradeoff between electron resistance and mass transport problems. In addition, Raman spectroscopy and electrochemical experiments revealed that a difference in the crystallinity of the TiO_2 in $TiON_x$ influences the activity but mainly the stability. Catalyst with a more crystalline TiO_2 ($TiON_x$-3h-Ir) exhibits better activity retention.

Finally, a graphene-based template was used to study the impact of the composition of the support on electrocatalytic performances. The different ratios between the graphene nanoribbons and Ti-precursor were investigated. The composition of the support induces a change in the environment of the Ir nanoparticles, therefore influencing their electrochemical performances. Combining domains of different chemical natures in the same material boosts OER performances. The presence of $TiON_x$, even in doping form, was inducing better activity compared to Ir/rGONRs. The best activity is observed when the Ir nanoparticles are in contact with both $TiON_x$ flakes and the carbon (4822 A/g_{Ir} at 1.55 V_{RHE} for Ir/Middle-$TiON_x$/rGONRs). The synergetic interaction in the three phase boundaries induces impressive activity. On the other hand, better stability was noticed when Ir nanoparticles were directly deposited on the $TiON_x$ flakes (85 % activity retention after 2 hours for Ir/High-$TiON_x$/rGONRs). Therefore, the composition of the support influences the environment of the nanoparticles and thus their interfacial interactions and consequently the (OER) electrochemical performances.

Hereby, $TiON_x$ is a suitable and promising support for electrocatalysts. It impacts the performances of the metal catalysts by the strong metal support interaction (SMSI). This impact on activity and stability can be tuned through the morphology of the $TiON_x$ (coming from the morphology of the TiO_2 precursor) and by its composition, with carbon (carbon-ceramic composite).

Chapter 6

Multifunctional Electrocatalysts on $TiON_x$/C Support for Unitized Regenerative Fuel Cell

Parts of the following text were published in ACS catalysis under the title "Synthesis and advanced electrochemical characterization of multifunctional electrocatalytic composite for unitized regenerative fuel cell". [296]

L. Moriau, M. Bele, A. Vižintin, F. Ruiz-Zepeda, U. Petek, P. Jovanovič, M. Šala, M. Gaberšček, and N. Hodnik**

As the first author, L. Moriau performed the electrochemical experiments and analysis. In addition, several rounds of multifunctional catalysts were synthesized by M. Bele and a constant exchange between the two researchers was needed to reach the material presented below. L. Moriau also prepared the first draft of the manuscript.

Diverse metals, namely PtCu, Ru and Ir, were deposited in the form of nanoparticles on $TiON_x$/C support to produce a multifunctional catalyst. The final material was investigated as an electrocatalyst for ORR and OER but also for HER and HOR. The activity was measured by electrochemistry while the stability was studied with a combination of advanced techniques such as online-ICP-MS and IL-TEM.

6.1 Introduction

Unitized reversible fuel cells (URFC) are an interesting alternative to FC and WE in order to reduce the amount of precious metal needed in the hydrogen cycle. Consequently, the development of efficient, low PGMs loading multifunctional catalysts is of primordial importance for the commercialization of URFCs[297]. The current state-of-the-art bifunctional catalyst for ORR and OER is a mix of Pt and Ir. Several approaches have been developed like the physical mixing of both metals[298-300], the deposition of Pt on Ir or Ir-oxide[301-304], and the deposition of Ir on Pt[305-308]. Nonetheless, all these strategies are entirely based on PGMs, and low loading will not be achievable with this kind of material. Therefore, the study of new materials containing a low amount of PGMs is required.

Hereby, a multifunctional catalyst was synthesized based on the obtained knowledge presented in the first parts of this thesis. First, an ORR Pt-alloy catalyst was chosen from the study conducted in Chapter 4. Therefore, PtCu nanoparticles were deposited on the

support as the ORR active catalyst sites in the multifunctional catalyst. For the OER catalyst, a mix of Ru and Ir nanoparticles was synthesized as the state-of-the-art metals used for this reaction. In addition, the presence of Ru and Pt allows the methanol oxidation reaction (MOR) to take place[309], which means that this material could also be used in direct methanol fuel cell (DMFC)[310]. To support these active materials, a graphene-based template – $TiON_x$ composite was chosen according to Chapter 5. The scheme of the final materials can be seen in Figure 6.1. Finally, the multifunctionality of the material will be shown by catalyzing not only the oxygen-evolved reactions but also HER and HOR. It would allow easier production of membrane electrode assemblies (MEA) as the same catalyst could be used for anode and cathode.

Furthermore, the stability and shortcoming of this material, and of multifunctional catalysts in general, will be revealed by advanced in-depth stability study.

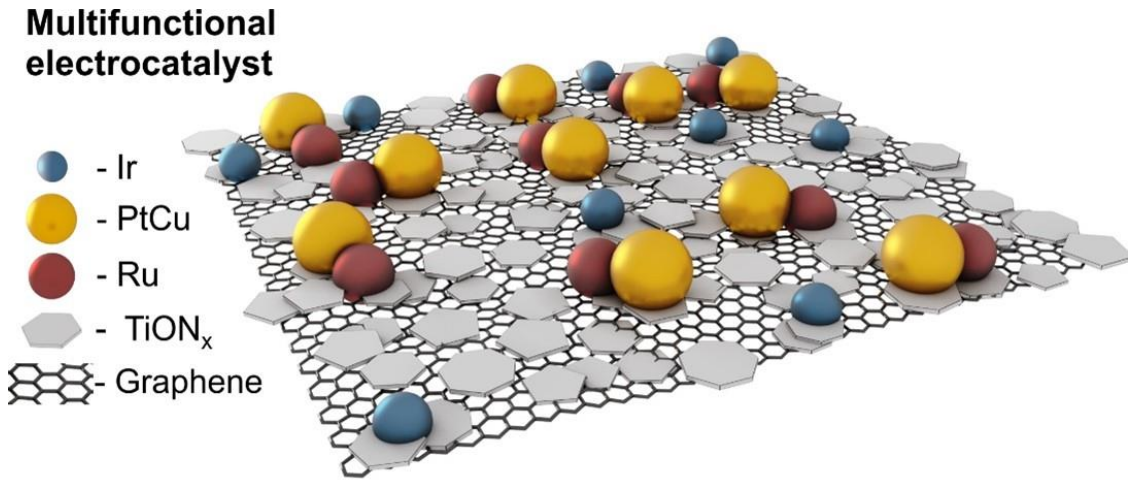

Figure 6.1: Scheme of the multifunctional catalyst. PtCu in yellow, Ru in red and Ir in blue. All the nanoparticles are supported on $TiON_x$ flakes deposited on a graphene template.

6.2 Results and Discussion

6.2.1 Physical characterization

As previously described in Chapter 3.1.1.4, the synthesis of the catalysts consists of four consecutive steps. The three last steps were followed by XRD to assure the successful synthesis of the support and metallic nanoparticles (Figure 6.2). First, the good formation of a $TiON_x$ layer on the graphene template was checked (Figure 6.2a). The TiO_2 (01-073-08760)[250] and $TiN_{0.6}O_{0.4}$ (00-049-1325)[250]spectra are used as references. The very broad peak of $TiON_x$ at 25° is attributed to the amorphous graphene used as a template. The other peaks, at 37°and 43.5°, are associated with $TiON_x$ phase, close to $TiN_{0.6}O_{0.4}$ spectra. No characteristic peak of TiO_2 was observed, indicating that if there is a TiO_2 phase in the support, it is either too small to be detected or not in a crystalline form. Afterwards, the deposition of Pt-Cu and Ru nanoparticles was verified (Figure 6.2b). Peaks from the support (25°, 37°, and 43.5°) are still visible but lower in intensities. In addition, the peak at 43.5° is now surrounded by a higher peak at 42-43° and another one at 44-45°. They are attributed to $PtCu_3$ (00-035-1358)[250] and Ru (04-003-6760)[250], respectively. The small peak at 38.5° is characteristic of Ru while the one at 49° is associated to $PtCu_3$. Finally, the last

step of the synthesis, the deposition of Ir nanoparticles, results in overlapping of many peaks. Nonetheless, the visible peak around 41° corresponds to Ir (04-016-112)[250]. The peak at 50° became broader to the lower angles with the addition of Ir, due to a characteristic peak of it at 48°. The broad peaks are also an indication of relatively small nanoparticles. Thus, the deposition of PtCu, Ru and Ir nanoparticles on a $TiON_x$/graphene composite support was successful.

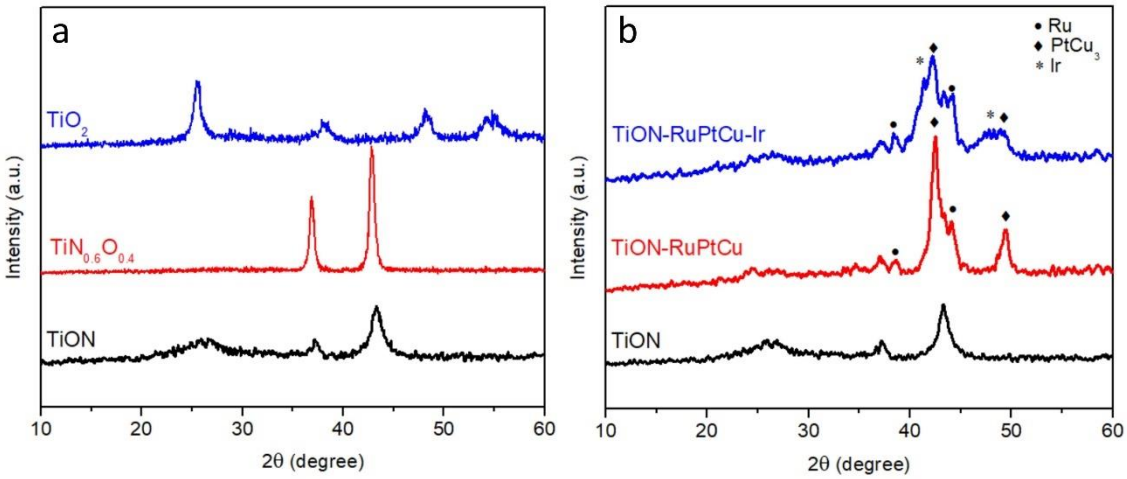

Figure 6.2: a) XRD pattern of the synthetized $TiON_x$ (black) compared to reference TiO_2 (blue) and $TiO_{0.4}N_{0.6}$ (red). b) XRD pattern of $TiON_x$ (black), TiON-RuPtCu (red) and TiON-RuPtCu-Ir (blue).

Afterwards, the catalyst was analyzed with TEM and EDXS. Three kinds of nanoparticles can be observed. The size and shape of these nanoparticles depend on their chemical nature (Figure 6.3). Some particles are above 10 nm while others are under 5 nm. The bigger particles that exhibit porosity are Pt-Cu alloy as indicated by the chemical mapping (Figure 6.3e). They present irregular shapes. The formation of an alloy is in accordance with the range of temperature used during synthesis[175]. Among the bigger particles, some are more spherical and do not have visible porosity. These are Ru nanoparticles. No alloying with Pt-Cu was expected from the phase diagrams library[311]. Interestingly, the Ru particles are in contact with Pt-Cu ones. On the other hand, the small nanoparticles are pure iridium. No mixing with the other metals was expected due to the separate step during synthesis and the immiscibility predicted by phase diagrams of iridium[312].

The coverage of the graphene template with $TiON_x$ was observed by EDXS (Figure 6.3). The metallic nanoparticles are seen to sit on the $TiON_x$ flakes. In the bifunctional catalysts, it is important to prevent Pt and carbon contact as the precious metal is known to catalyze the oxidation of carbon into CO_2 at higher potentials[89, 194, 195].

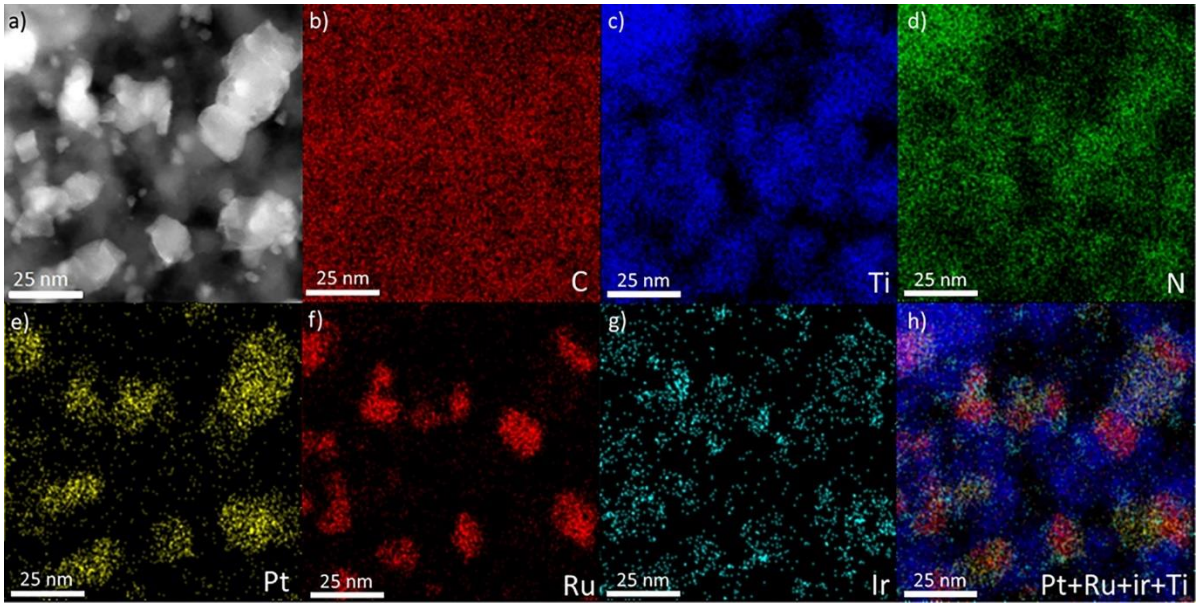

Figure 6.3: (a) STEM ADF image. (b) EDX mapping of carbon (red), (c) titanium (purple), (d) nitrogen (green), (e) platinum (yellow), (f) ruthenium (red), (g) iridium (blue), and (h) overlay of platinum, ruthenium, iridium, and titanium from the composite TiON-RuPtCu-Ir.

The exact amount of metals present in the catalyst was obtained by ICP-OES (Table 8). Altogether, the precious metals used only represent one fifth of the total mass of the catalyst.

Table 8: Weight and Atomic Percent of Catalytic Metals as Determined by ICP-MS in TiON-RuPtCu-Ir.

Elements	Weight (%)	Atomic (%)	Ratio (atomic)
Cu	6.74	1.06	2.5
Pt	7.68	0.39	0.925
Ru	2.81	0.28	0.65
Ir	3.5	0.18	0.425
Total	20.73	1.91	

6.2.2 Electrochemical Characterization

A cyclic voltammogram (CV) was recorded between 0.4 and 1.6 V_{RHE} in an oxygen-saturated 0.1 M $HClO_4$ electrolyte (Figure 6.4). For comparison purposes, Pt/C and Ir black CVs are also included. For both reactions, the onset is close to the onset of the respective benchmark (Pt for ORR and Ir for OER). The activity presented in Figure 6.4 is not normalized and thus the lower activity of our material is related to the 5-times lower total amount of metal. Once a mass-normalization is performed, the bifunctional catalyst shows a current density almost three times better than the ORR benchmark (at 0.9 V_{RHE} Figure 6.5a) and ten times higher than the OER benchmark (at 1.55 V_{RHE}, Figure 6.5b). It should be noted that ORR activity of bifunctional catalysts is often evaluated at 0.85 V_{RHE} due to poorer performances than monofunctional catalysts. In comparison with literature (mix of Pt and Ir), our material has an ORR current density in the same order

of magnitude and a two order of magnitude better OER current density, most likely due to the presence of Ru (Table 9). Another way of comparing bifunctional catalysts is by looking at the difference between the potentials (Δ E) needed to reach a current density of 1 mA/cm$^2_{geo}$ for ORR and 10 mA/cm$^2_{geo}$ for OER (violet lines in Figure 6.4)[39, 313]. The lower the Δ E, the more performant is the bifunctional catalyst. Both benchmarks are poor bifunctional catalysts as they do not show good activity for the other reaction (Pt not active for OER and Δ E of 0.872 V for Ir). The difference in potential of the presented bifunctional catalyst is 0.651 V while the mixed Pt/Ir catalysts from literature sometimes supported on TiO_2 or carbon-based support exhibit values between 0.67 and 0.75 V (Table 9). Therefore, we can conclude that the synthesized multifunctional catalyst will also exhibit excellent activity in the regenerative fuel cell.

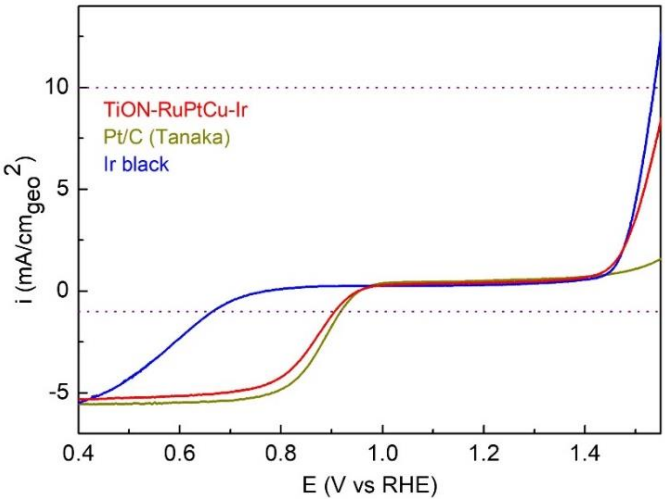

Figure 6.4: Comparison of our catalyst with the benchmarks for ORR and OER. Two violet vertical lines indicate the current densities where activity can be extracted. The polarization curves were recorded at 20 mV/s, in 0.1 M $HClO_4$, 1600 rpm, under O_2 atmosphere.

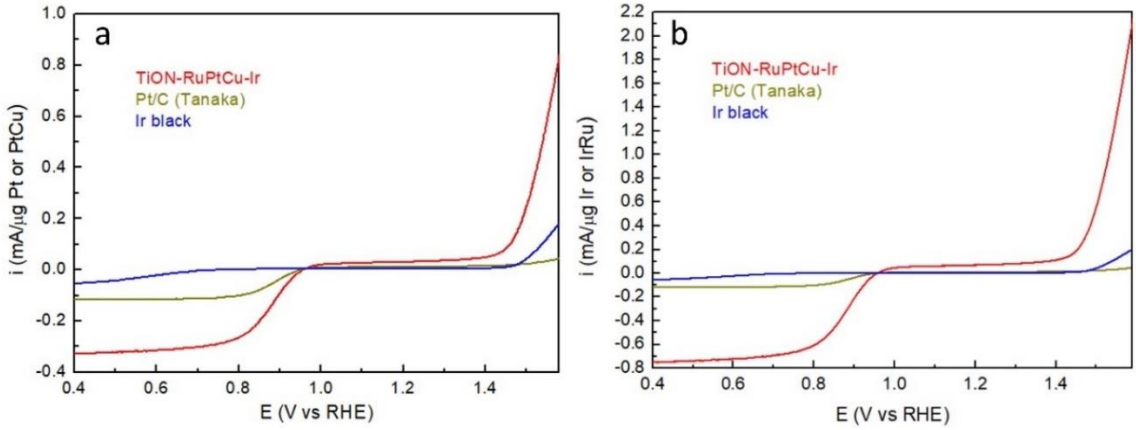

Figure 6.5: a) ORR and OER polarization curves normalized by the mass of Pt/PtCu. Comparison with the benchmark. b) ORR and OER polarization curves normalized by the mass of Ir/IrRu. Comparison with the benchmark.

Table 9: Performance of our catalyst, monofunctional benchmarks catalysts for ORR and OER and bifunctional catalysts from literature.

	ORR at 0.85 V[a] or 0.9 V_{RHE}		OER at 1.55 V_{RHE}		ORR at 1 mA/cm^2	OER at 10 mA/cm^2	ΔE
	j (mA/cm^2)	j_m (mA/mg_{Pt} or mA/mg_{PtCu})	j (mA/cm^2)	j_m (mA/mg_{Ir} or mA/mg_{IrRu})	E (V_{RHE})	E (V_{RHE})	
Pt/C	1.710	36.03	1.591	n.d.	0.917	n.d.	
Ir black	0.2401	n.d.	12.711	124.56	0.665	1.537	0.872
TiON-RuPtCu-Ir	1.348	91.61 (20.1[a])	8.586	1333.27	0.911	1.563	0.651
Pt/IrO_2 [314]		15.1 [a]		142.5 [b]			
Pt-Ir/IrO_2-PtO_2 [314]		27.4 [a]		207.3 [b]			
Pt/IrO_2 [303]		7.1		34.8			
Pt/IrO_x 1:9 [302]		10.1 [a]		58.9			
Pt/IrO_x 3:7 [302]		8.8 [a]		58.5			
Pt/IrO_x 1:1 [302]		7.5 [a]		61.3			
Pt/IrO_x [315]		9.8 [a]		60.4	0.86	1.54	0.68 [c]
Pt/IrO_2 [315]		35.1 [a]		24.5	0.9	1.58	0.68 [c]
Pt/IrO_2 1:9 [301]		107.4 [a]		25.0	0.87	1.56	0.69 [c]
Pt/IrO_2 3:7 [301]		44.7 [a]		20.3	0.89	1.575	0.685 [c]
Pt/IrO_2 1:1 [301]		35.7 [a]		18.8	0.9	1.585	0.685 [c]
Pt-Ir/rGO_P600 [316]					0.89	1.58	0.69 [c]
Pt-Ir/TiC[269]		164		18.4	0.955	1.635	0.68 [c]
$PtIr/Ti_4O_7$ [119]					0.905	1.63	0.725 [c]
$Pt_{90}Ir_{10}/TiO_2$ [317]					0.856	1.54	0.684 [c]
$Pt_{80}Ir_{20}/TiO_2$ [317]					0.848	1.55	0.702 [c]
$Pt_{70}Ir_{30}/TiO_2$ [317]					0.836	1.59	0.754 [c]

a values obtained at $0.85V_{RHE}$
b values obtained at $1.6V_{RHE}$
c values extracted from graphs

The precious metals from the PGMs group are not only good for ORR (Pt) and OER (Ir, Ru) but also for the hydrogen-involved reactions (hydrogen oxidation reaction, HOR and hydrogen evolution reaction, HER). Therefore, a bifunctional catalyst for ORR and OER can also perform well for the two other reactions of the URFC. The performance of the catalyst for these reactions is presented in Figure 6.6a. An activity comparable to the 50 wt% Pt benchmark was reached with only 20 wt% precious metal (and less than 8 wt% Pt). Therefore, this catalyst could be used on both electrodes of the URFC, being usable for URFC that works in both modes A and B (see Introduction, Chapter 1).

Moreover, the multifunctional catalyst also presented a similar MOR activity as the PtRu/C benchmark (Figure 6.6b), with less precious metal involved. This indicates possible use in direct methanol fuel cell and proves the multifunctionality of the low-PGMs loading material.

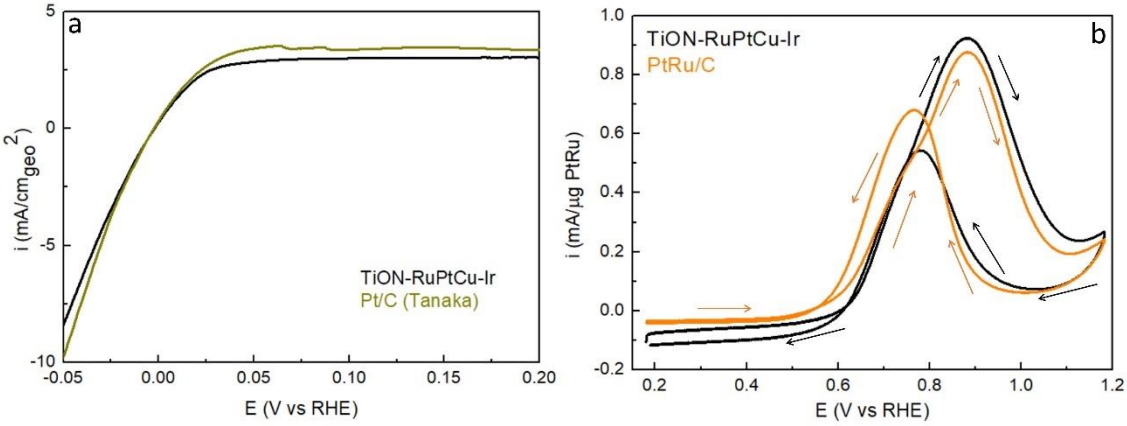

Figure 6.6: a) HOR/HER polarization curve at 20 mV/s, in 0.1 M $HClO_4$, 1600 rpm, under H_2 atmosphere. b) MOR polarization curve in 1 M CH_3OH + 0.1 M $HClO_4$, 1600 rpm, and a scan rate of 20 mV/s.

6.2.3 Stability studies

A bifunctional (multifunctional) catalyst should be active for all the reactions of interest but also stable under all the different conditions. Hereby, the degradation tests were chosen to cover the wide potential range of URFC operation. Namely, three protocols were applied to cover the oxygen-involved reactions, i.e. one for ORR (0.4 to 1.0 V_{RHE}), one for OER (1.2 to 1.6 V_{RHE}) and the last one for both ORR&OER (0.4 to 1.6 V_{RHE}). The latter simulates the switch from fuel cell (FC) mode to water electrolyzer (WE) mode. Indeed, in real devices, the degradation is investigated by switching from FC mode (constant current of 0.5 A/cm^2, around 0.7 V_{RHE}) and WE mode (constant current of 0.5 A/cm^2, around 1.6 V_{RHE})[300, 304, 318]. The impact of each degradation test was studied with RDE for activity changes, IL-SEM or IL-TEM for compositional, morphological and structural changes and EFC-ICP-MS. For RDE and microscopy studies, 10 000 CVs were performed while only 5 cycles were done in the EFC-ICP-MS set-up to get an idea of the mechanism of dissolution. Prior to the degradation test, an electrochemical activation protocol (200 cycles, 0.05 to 1.2 V_{RHE}, 300 mV/s) was performed on the catalyst both in RDE and EFC-ICP-MS set-ups. The impact of this step was also checked with IL-microscopy.

6.2.3.1 Activation protocol

This step is necessary to reach a good activity for Pt-Cu alloy[137]. The dissolution profiles have different shapes for all the metals present in the sample (Figure 6.7). Cu dissolves

heavily from the start of the protocol (reaching 200 ppb), which was intended as the activation triggers dealloying of Pt-Cu nanoparticles. Cu is selectively leached from the Pt-alloy surface, forming a Pt-rich layer on the particle surface that protects the Cu in the bulk[128]. In addition to the protection, a Cu-bulk rich cover with Pt-rich surface induces enhanced ORR activity compared to Pt alone due to the so-called ligand and/or strain effects[48, 128, 132, 152].

All the other metals present one order of magnitude lower dissolution than Cu. Their dissolution is mostly due to the transient mechanism of dissolution occurring during the oxidation or reduction of noble metal oxides[83, 319]. Moreover, native oxides are formed (spontaneous surface oxidation) when the metal is at OCP or exposed to air. Therefore, Ir and Pt exhibit a big dissolution peak during the first cycles due to the reduction of native oxides before decreasing into a steady state of low dissolution[319]. In the case of Ru, the dissolution starts low but increases with the number of cycles. At 1.2 V_{RHE}, Ru is already heavily oxidizing[275] and thus the transient dissolution for Ru is increasing with the number of cycles compared to other precious metals. Some Ti is also dissolving during the activation. This is most likely due to the removal of some unstable superficial Ti as less than 3% of the total Ti present in the catalyst (43.67 wt% of the catalyst) is dissolved.

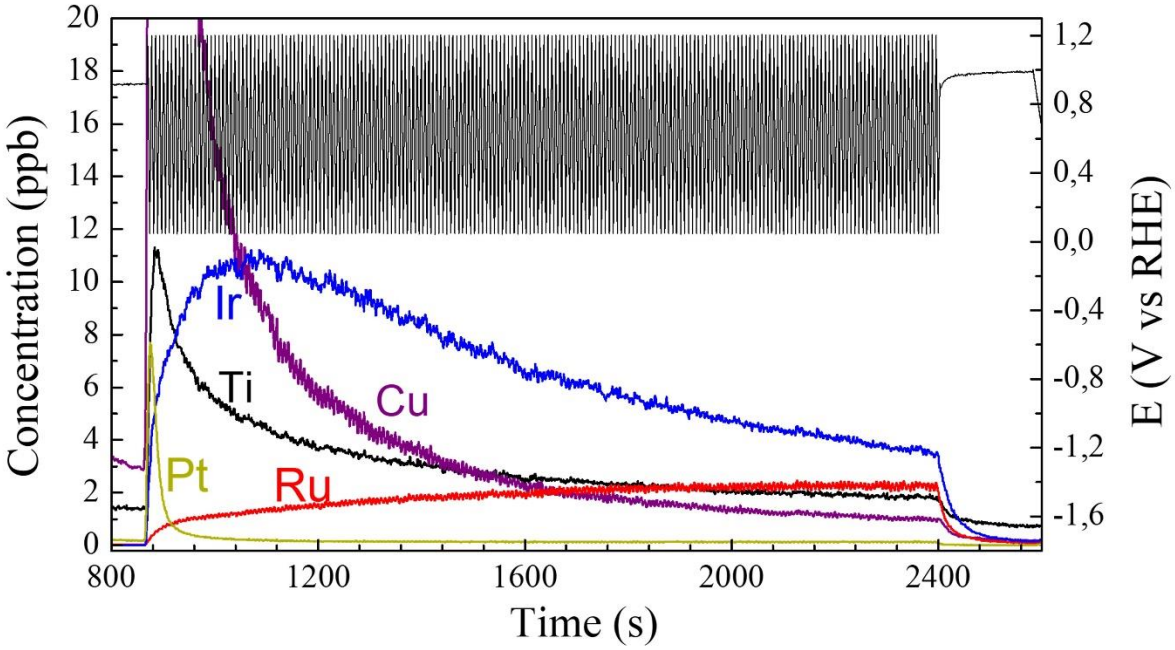

Figure 6.7: The dissolution profile of precious metals during the activation protocol (200 cycles, 300 mV/s, 0.05 to 1.2 V_{RHE}).

6.2.3.2 Degradation during ORR protocol (cycling between 0.4 and 1.0 V)

The activity for the reactions of interest (ORR, OER and HOR/HER) was investigated after 10 000 fast cycles (1 V/s) in the ORR region, i.e. 0.4 to 1.0 V_{RHE}. The dissolution mechanism in this region was studied by EFC-ICP-MS during 5 slower cycles (20 mV/s). The polarization curves before and after ADT can be seen in Figure 6.8a-c. The ADT has a different effect on the activity of the different reactions. Namely, the ORR activity is better after the degradation protocol while the OER activity is worse. For HER, the onset is similar, but the slope of the reaction decreases.

The dissolution profiles show that some Ru, Ir and Cu are dissolved in extremely low amounts during ORR cycling while Pt dissolution is almost zero. Therefore, the changes in activity can be related to the loss of the different metals. Namely, a small decrease in OER activity is understandable as some OER catalysts dissolved[273, 275, 320]. In the same way, HER activity decreased, especially at higher overpotentials, due to the loss of Ru/Ir. Indeed, while Pt is the best catalyst for this reaction, Ir and Ru have been shown to be able to catalyze it too. More specifically, Ir supported on carbon[117] and Ru in contact with Pt are good catalysts for HER[321]. Therefore, the slight loss of these metals induces a diminution of catalytic activity for HER at high overpotentials. Oppositely to OER and HER, the activity for ORR and HOR (low current density in Figure 6.8c) is better after ADT. This is due to larger availability of Pt. Indeed, the Ru, which was shown to be in contact with Pt-Cu by chemical mapping (Figure 6.3), dissolved and "freed" or exposed some new Pt active sites.

In more detail, Pt and Cu present a peak of dissolution during the anodic part of the scan (oxidation). However, the oxidation of Pt is low when cycling to 1.0 V, explaining the background level observed. On the other hand, Ir and Ru dissolution peaks reach a maximum during the reduction (cathodic). This dissolution is due to the reduction of oxides still present after activation[275, 322]. In addition, less and less of Ir is dissolved with each cycle indicating that no new oxide is formed during cycling to 1.0 V_{RHE} for this metal. For Ru, the dissolution is constant after a few cycles implying the production of oxides and their consequent reduction.

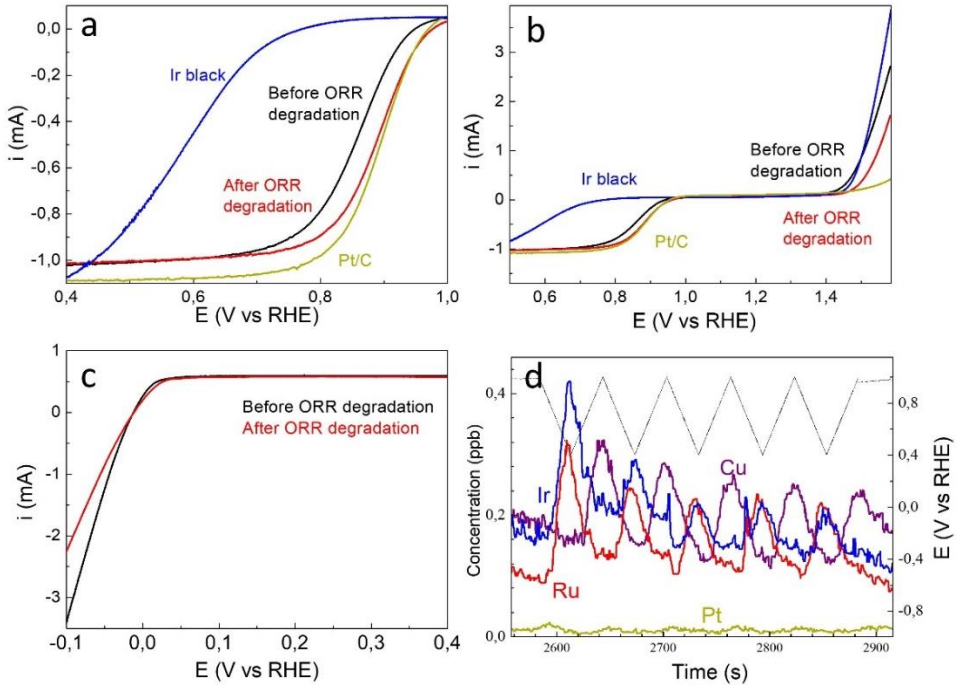

Figure 6.8: a) ORR polarization curves before and after degradation – ORR protocol. b) OER polarization curves before and after degradation – ORR protocol. c) HOR/HER polarization curves before and after degradation – ORR protocol. d) The dissolution profile of the precious metal during five cycles from 0.4 to 1.0 V_{RHE}. The curves were obtained at 20 mV/s, in 0.1 M $HClO_4$, 1600 rpm, under O_2 (a and b) or H_2 (c) atmosphere.

Furthermore, the morphological, structural, and compositional changes were followed by IL-STEM. Pictures and EDX spectra taken at the same location of the as-prepared samples, after activation (only TEM picture) and after degradation, are presented in

Figures 6.9 and 6.10. After the degradation protocol, no significant change in composition is visible by EDXS, as expected from the low and decreasing dissolution of metal in the EFC-ICP-MS (Figure 6.9). In the pictures, higher porosity of Pt-Cu alloy nanoparticles can be observed after activation (Figure 6.10b). However, no big change is visible after ADT. Especially, coarsening of the porous Pt-Cu did not happen even if it was shown to be common for Pt-alloy in these conditions[143]. Therefore, the pores are stabilized, maybe due to the presence of Ru and Ir.

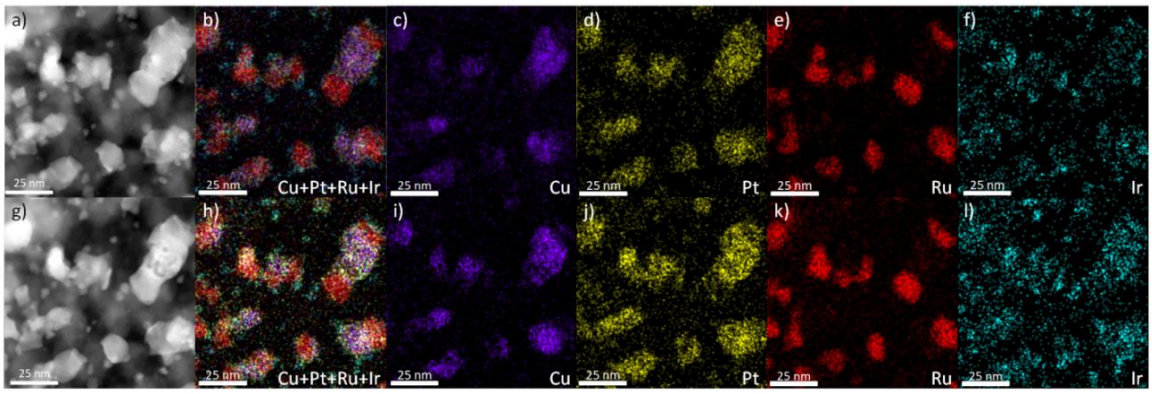

Figure 6.9: IL-EDX of TiON-RuPtCu-Ir. a-f) As-prepared, g-l) After ORR degradation. a) and g) STEM ADF images. b) and h) Overlapping of copper (purple), platinum (yellow), ruthenium (red) and iridium (blue).

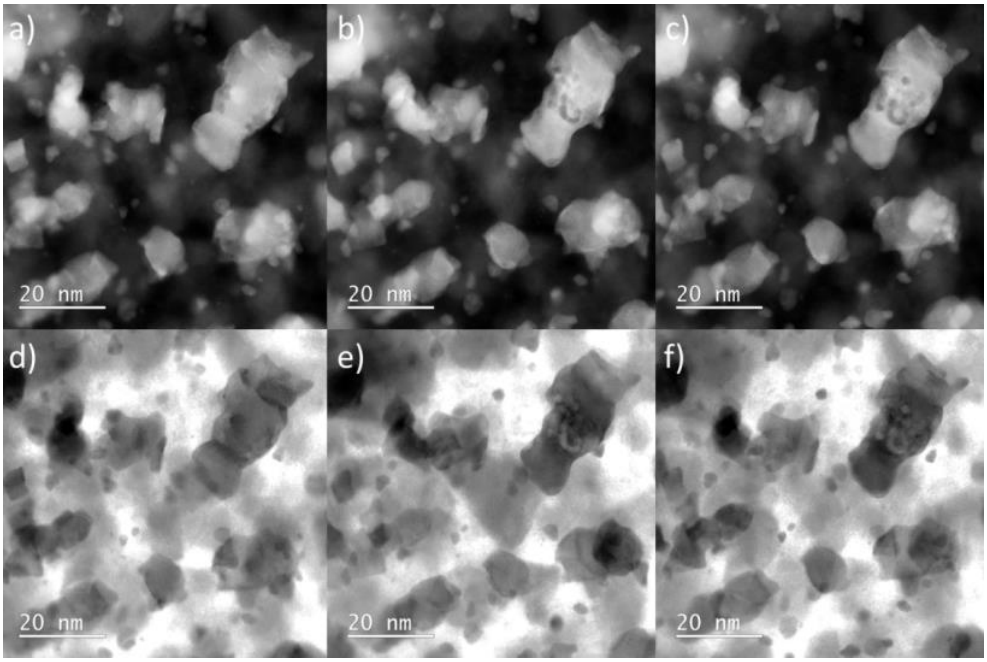

Figure 6.10: IL-STEM ADF and BF images of TiON-RuPtCu-Ir. a) and d) As-prepared, b) and e) after activation (between 0.05 and 1.2 V_{RHE}), c) and f) after ORR protocol (10 000 cycles between 0.4 and 1.0 V_{RHE}).

6.2.3.3 Degradation during OER protocol (cycling between 1.2 and 1.6 V)

A fresh film was used to study the stability during OER (10 000 cycles, 1.2 to 1.6 V_{RHE}, 1V/s). After the OER ADT, the ORR activity is almost similar as before (Figure 6.11a).

A slight increase of 9% was measured. On the contrary, a strong decline in OER activity is observed with a more than 60% decrease (Figure 6.11b). In the case of HER, an improvement in activity is noticed, especially at high overpotentials.

The metals exhibit a similar dissolution profile but with different orders of magnitude (Figure 6.11d and e). Namely, one anodic peak related to the oxidation of metal is visible for all metals and no cathodic peak is observed. In the case of Ru, this peak can reach 200 ppb and is due to the formation of the unstable RuO_4. RuO_4 is formed during the OER mechanism[82, 275]. The loss of Ru is in accordance with the decrease in OER activity. Some activity for OER is left after 10 000 cycles as Ir is still present in the catalyst. Indeed, Ir shows some low dissolution that lowers with each cycle. The dissolution is due to a mild dissolution during OER and/or the transient dissolution happening during oxidation[273, 295, 320]. Nonetheless, more and more irreversible Ir-oxides are formed that protect Ir from further dissolution. Pt has the same order of magnitude of dissolution as Ir except that it is only due to transient dissolution as Pt is a bad catalyst for OER. The dissolution of Cu is mechanistically linked to Pt. When Pt is dissolved and removed from the surface of Pt-Cu nanoparticles, the Cu underneath is uncovered and dissolved directly at these potentials in acidic conditions. One would think that the loss of some Pt (and Cu) would result in a lower ORR activity, but the opposite is observed. Indeed, Pt dissolution is quickly reaching a low amount so the loss of activity would be minimum while at the same time an extensive amount of Ru is lost in 10 000 cycles, exposing more Pt fresh. The balance of these two phenomena results in a slightly improved ORR activity.

The same explanation can be used to understand the HER trend. Namely, at high current densities, the activity is better after degradation while it is very close to before at low current densities. When a little of Ru or Ir is removed, the activity is worse at high current densities but when almost all Ru is gone, a lot of new Pt active sites are now available, increasing the activity. The same explanation can be done for the improvement of HOR. This counter-balances the loss of activity due to some Pt dissolution or reshaping/agglomeration of nanoparticles.

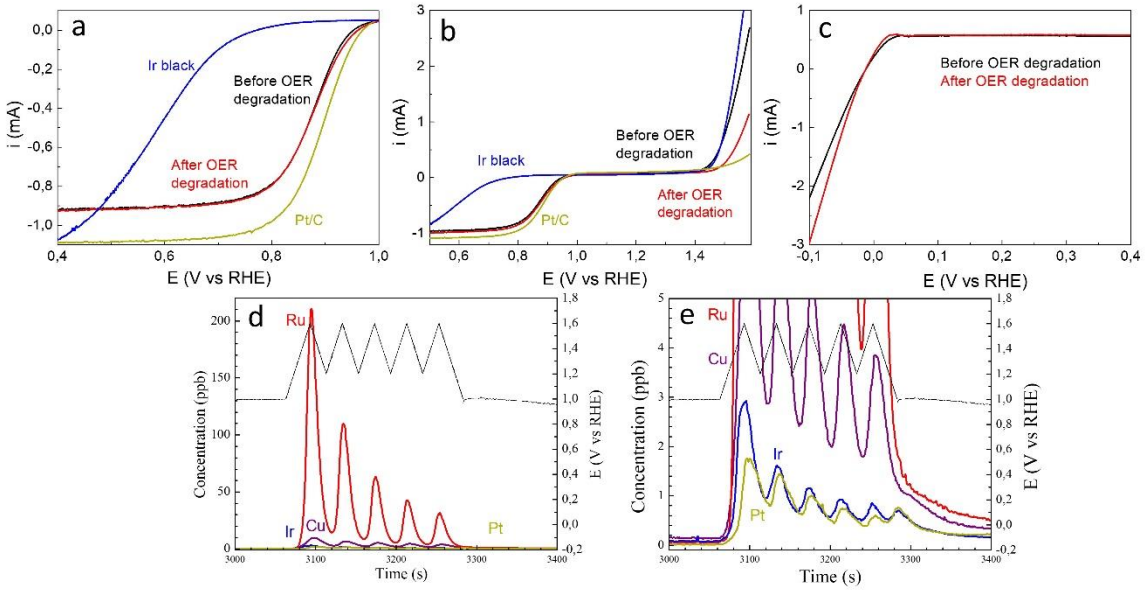

Figure 6.11: a) ORR polarization curves before and after degradation – OER protocol. b) OER polarization curves before and after degradation – OER protocol. c) HOR/HER polarization curves before and after degradation – OER protocol. d) The dissolution profile of the precious metal during five cycles from 1.2 to 1.6 V_{RHE}. e) Enlarged view of Pt and Ir

dissolution profiles. The curves were obtained at 20 mV/s, in 0.1 M $HClO_4$, 1600 rpm, under O_2 (a and b) or H_2 (c) atmosphere.

Once again, TEM pictures and EDX spectra are taken on the same spot for the as-prepared sample, after activation, after 10 cycles in OER potential window and after degradation (Figures 6.12 and 6.13). Ru is already massively dissolved after 10 cycles in the OER potential window as pointed out by the red circles in Figure 6.12. Most of Ru particles are gone after the 10 000 cycles, as pointed out by EDXS (Figure 6.13). In addition, noticeable morphological changes in nanoparticles are observed, especially for the Pt-Cu nanoparticles. The size and shape of these nanoparticles are different after degradation due to migration and agglomeration (Figure 6.12). The agglomeration can be expected after ADT while the migration is probably due to the loss of Ru. Pt particles probably migrate to new stable positions on the support after the removal of Ru.

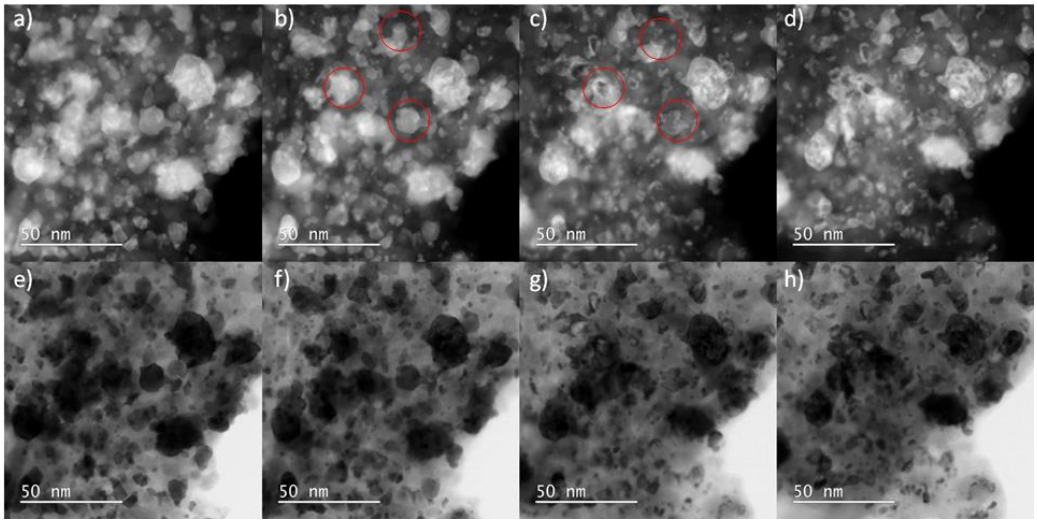

Figure 6.12: IL-STEM ADF and BF images of TiON-RuPtCu-Ir. a-e) As-prepared. b-f. After activation. c-g) after 10 cycles OER protocol. d-h) After 10 000 cycles OER protocol.

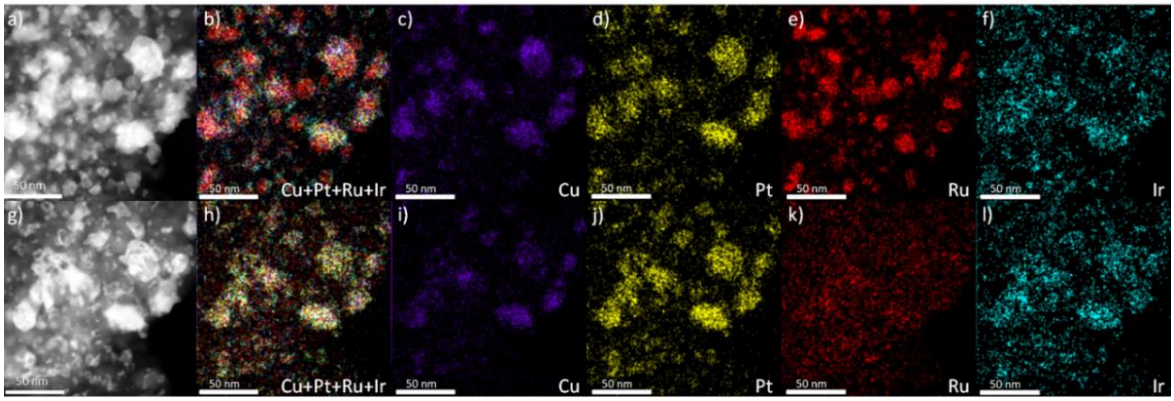

Figure 6.13: IL-EDX of TiON-RuPtCu-Ir. a-f) As-prepared, g-l) After OER degradation. a) and g) STEM ADF images. b) and h) Overlapping of copper (purple), platinum (yellow), ruthenium (red) and iridium (blue).

6.2.3.4 Degradation during ORR & OER protocol (cycling between 0.4 and 1.6 V)

Finally, a degradation test covering both potential windows (from 0.4 to 1.6 V_{RHE}) was conducted on a fresh film. The resulting activities are presented in Figure 6.14. There is obviously no activity left for ORR and HER. The polarization curve for ORR does not exhibit any characteristic features of Pt-based catalyst and is even worse than Ir black benchmark while the HER polarization curve is close to a current of zero. In the case of OER, around a 6-time decrease in activity is noticed after ADT.

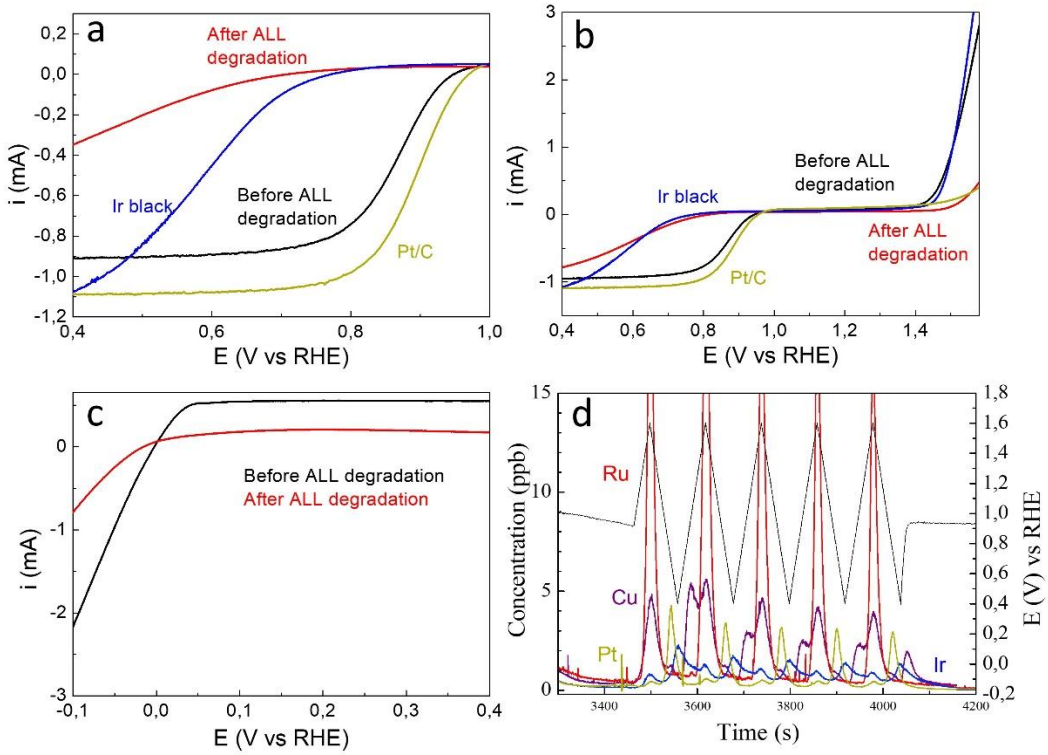

Figure 6.14: a) ORR polarization curves before and after degradation – ORR & OER protocol. b) OER polarization curves before and after degradation – ORR & OER protocol. c) HOR/HER polarization curves before and after degradation – ORR & OER protocol. d) Dissolution profile of the precious metal during five cycles from 1.2 to 1.6 V_{RHE}. The curves were obtained at 20 mV/s, in 0.1 M $HClO_4$, 1600 rpm, under O_2 (a and b) or H_2 (c) atmosphere.

The dissolution profiles of the metal are more diverse, however two peaks, one anodic and one cathodic, are always visible (the cathodic peak of Ru is extremely low compared to its anodic peak) in Figure 6.15. In the case of Pt (Figure 6.15a), a low anodic peak and a high cathodic peak are observed similarly to Pt in Chapter 4. The intensity of peaks decreases after a few cycles until reaching a steady amount, indicating a total reduction of surface oxide upon cycling. The Cu present in the bulk of the nanoparticle dissolves after the protecting layer of Pt on the surface gets dissolved (Figure 6.15a). The Cu dissolution profile follows the same trend noticed with the Pt-Cu benchmark in Chapter 4. Namely, three peaks are observed after the second cycle. Indeed, the first anodic peak, due to Cu_{udp}, is not present in the first cycle. Then, a predominant anodic peak is visible followed by a lower cathodic peak[138]. Among all the metals, Ru exhibits the highest dissolution, almost exclusively due to an anodic dissolution peak (Figure 6.15b). The cathodic and anodic peaks are well separated. Once again, the dissolution is due to the unstable RuO_4 formation.

Similarly, the Ir dissolution profile presents well defined anodic and cathodic peaks for the same cycle with the particularity of significant dissolution in between (dissolution does not fall to background level, Figure 6.15c). This causes the merging of the cathodic peak of one cycle with the anodic peak of the following cycle. This suggests that the reduction of oxide is not complete, accordingly to the formation of irreversible Ir-oxide at high potentials[83]. In addition, the dissolution is 10-times lower than for Ru and the cathodic peak of Ir is higher than the anodic one, oppositely to Ru. Also, the intensity of the peak decreases with each cycle. The Ti dissolution was recorded to understand if $TiON_x$ is responsible for the support corrosion. One anodic peak and one smaller cathodic peak are observed (Figure 6.15d). This dissolution follows the dissolution of other metals. Namely, higher amounts of precious metals are lost during the anodic part of the cycle. Consequently, new/fresh surfaces of the Ti-support are exposed and thus prone to be dissolved.

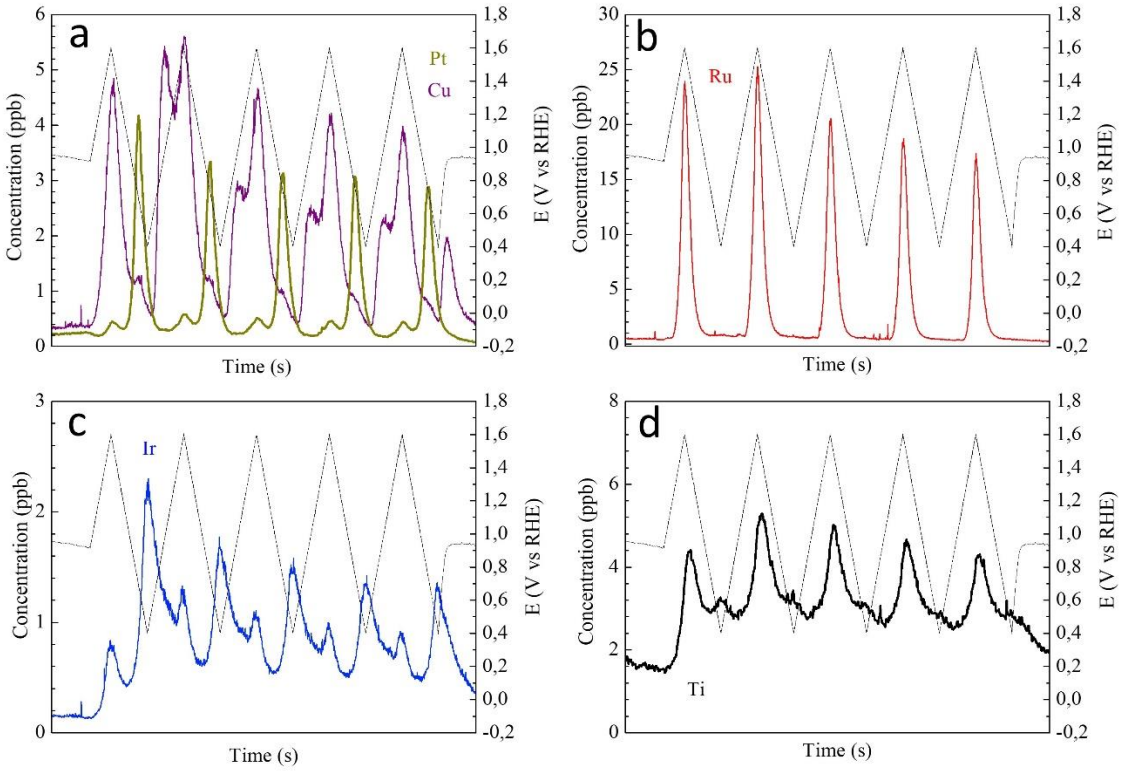

Figure 6.15: Dissolution profile of the precious metal during five cycles from 0.4 to 1.6 V_{RHE}. a) Platinum (yellow) and copper (purple). b) Ruthenium. c) Iridium. d) Titanium.

Moreover, the catalyst was studied with IL-SEM, IL-TEM and EDXS. Most particles are not present after the degradation test, and they are mostly Ir nanoparticles (Figures 6.16 and 6.17). The EDXS data confirm the faster dissolution of Cu and Ru compared to Pt and Ir, with Ir being the most stable metal among the four (Table 10). In addition, the support seems to have undergone severe degradation (Figure 6.16).

Therefore, the absence of activity for ORR and HER is correlated to the corrosion of Pt-Cu nanoparticles but also to some loss due to support degradation. On the other hand, the decrease in OER is strongly related to the complete loss of Ru. There is still some activity due to the presence of Ir nanoparticles after ADT.

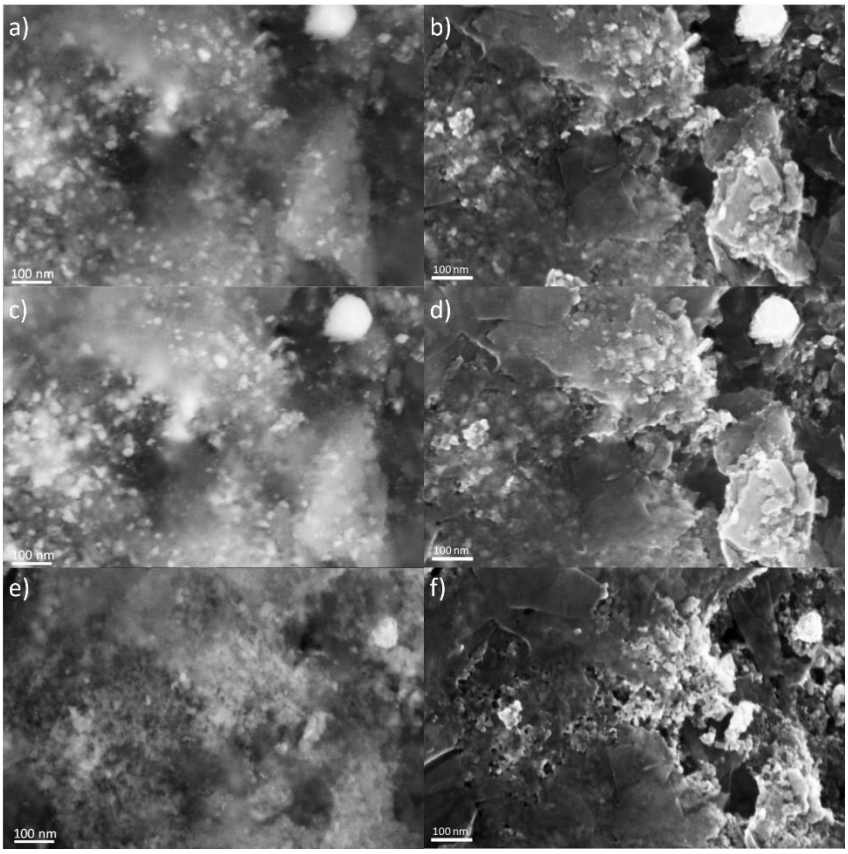

Figure 6.16: IL-SEM pictures of $TiON_x$-RuPtCu-Ir. a-b) As-prepared. c-d) After activation. e-f) After ORR&OER degradation. a-c-e) Secondary and b-d-f) in-lens detector.

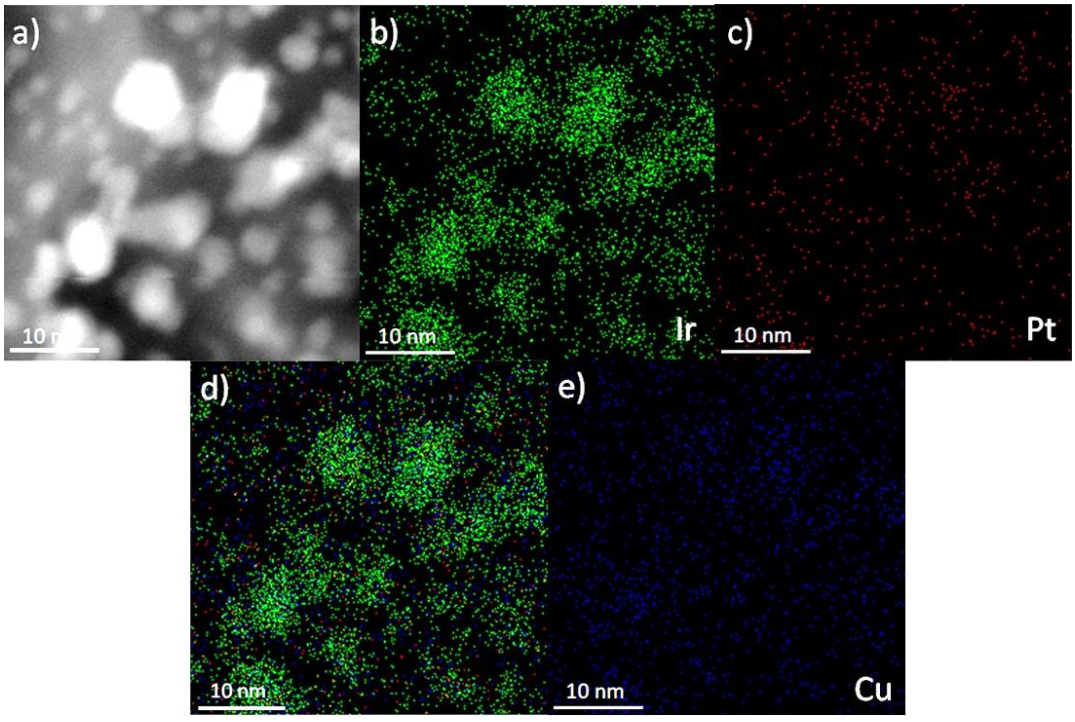

Figure 6.17: a) STEM ADF. b) Iridium. c) Platinum. d) Overlapping. e) Copper.

Table 10: Atomic ratio of the precious metal as-prepared, after activation and after the ORR & OER degradation protocol.

Atomic ratio	Cu	Ru	Ir	Pt
As-prepared	6	1.8	1	1.9
Activated	3.4	1.8	1	2
Degraded	0	0.04	1	0.4

TiON-RuPtCu-Ir is an efficient catalyst for ORR, OER and HER/HOR but the stability of the different metals depends highly on the potential window. Namely, the catalyst is stable for ORR and semi-stable for OER (as only Ru is lost) but a broad window (ORR&OER) should be avoided at all costs as all the metals, as well as the support, are corroded in this potential window.

6.3 Conclusion

Hereby, a multifunctional catalyst for ORR, OER and HER/HOR was synthesized based on a new design. Namely, a graphene template evenly covered with $TiON_x$ was used as electrocatalyst support for Pt-Cu alloy, Ru and Ir nanoparticles. The multifunctional catalyst presents a 3-times higher activity than Pt/C for ORR and 10-times better activity than Ir/C for OER. As a bifunctional it exhibits an overpotential window (ΔE) of 0.651 V, beating Pt-Ir state-of-the-art mixture from literature. It also shows good activity for HER/HOR.

The physical characteristics of the catalyst were analyzed with various techniques such as XRD, TEM, ICP-OES, and EDXS. The presence of Pt-Cu alloy and of Ru and Ir independent nanoparticles, as well as $TiON_x$, was proven by XRD where the characteristic peaks of these materials were observed. The particle size and morphology of the nanoparticles, i.e. under 5 nm for Ir, above 10 nm for Ru and above 10 nm but porous for Pt-Cu, were examined by TEM. At the same time, the coverage of the graphene by $TiON_x$, essential for good stability during OER, was proven by EDXS. Finally, the low amount of precious metal used in the catalyst was measured by ICP-OES, with Ir, Pt, Cu and Ru accounting for only up to 20 wt% of the catalyst.

Afterwards, the stability of the catalyst under different potential windows was investigated. The dissolution of metals was studied with EFC-ICP-MS while the structural and morphological changes were examined with IL-TEM. Three different ADT protocols were chosen to represent ORR (0.4 to 1.0 V_{RHE}), OER (1.2 to 1.6 V_{RHE}) and ORR&OER (0.4 to 1.6 V_{RHE}) potential windows. The activity after the different protocols is summarized in Table 11. After ORR degradation test, the catalyst was still active for all the reactions, with an even better activity for HER and ORR due to fresh Pt exposed after the loss of some Ru. The OER activity was lower but still 5-times better than the Ir black benchmark. In the case of ADT in OER potential window, Ru was almost completely dissolved inducing a huge decrease in OER activity as well as a small improvement for Pt and HER. The last ADT was the harsher of the three. Almost all activity was lost after cycling in this broader region, only some Ir nanoparticles survived, and consequently some OER activity. Therefore, the importance of the degradation protocol as well as the protocol chosen in real devices is highlighted. Indeed, good activities are still present after extensive ORR or OER catalyzation but the shift from ORR potential to OER potential is particularly destructive for the catalyst. A potential ramp between these two windows should be avoided in the real devices. Moreover, this ADT should be considered while synthetizing new bifunctional catalysts as it is the main potential degradation cause.

Table 11: Resume of the change in activity after the diverse AST protocols.

Protocols	ORR activity	OER activity	HER activity
ORR	Increase (+ 110.9%)	Decrease (- 44.9%)	Decrease
OER	Increase (+ 9.0%)	Decrease (- 61.3%)	Increase
ORR&OER	No activity	Decrease strongly (-85.38%)	Almost zero

Chapter 7

Conclusions

A transition to renewable energy sources is inevitable and should be accelerated without a doubt. However, technological drawbacks are hindering the passage to a green hydrogen economy. Notably, the high price and scarcity of PGMs, the still-too-low efficiency of non-noble catalysts, and the lack of suitable support for acidic OER catalysts.

In the first step, it was shown how "similar" commercial state-of-the-art Pt-M/C alloys are difficult to compare. The study of commercial catalysts was supposed to highlight the advantages and disadvantages of each transition metal (Co, Fe, Ni, Cu) without any other different parameters. However, the reality of Pt-M/C is that the same synthesis does not lead to similar catalysts, with, for example, a pure phase present for Fe, Co, and Ni containing alloys or different carbon encapsulation (especially for Ni and Co). Nonetheless, these results highlighted the extensive approach used in our group to study and understand electrocatalysts, with deep, in-situ, nanoscale resolved techniques. Furthermore, global conclusions and selection of one Pt-M/C alloy to use in the multifunctional catalysts were carried out. The choice was based on M-leached impact in a real device, synthesis parameters but also ethical choices. Specifically, Fe was ruled out because of the Fenton reaction occurring in the PEMFC and destroying the membrane, Ni was dismissed because of the high encapsulating carbon layer due to the current synthesis process and thus the complication in further bifunctional catalyst synthesis. Finally, while the most promising with Cu, Co was excluded due to the ethical problem coming from Co mining. Therefore, Pt-Cu alloy was selected as the ORR catalyst for a further bifunctional study.

Afterwards, the lack of suitable material to support iridium nanoparticles during the OER was tackled down by proposing $TiON_x$ support. It was shown that $TiON_x$ fulfills the requirement for electrocatalyst support, i.e. conductivity, sufficient stability in OER conditions and the ability to finely disperse iridium nanoparticles. In addition, a SMSI effect was noticed which improved the intrinsic activity and stability of iridium nanoparticles. Furthermore, it was found that the morphology of the support also impacts the electrochemical performances. Namely, a nanotubular morphology is more adequate in terms of conductivity, as there are fewer resistance points and better conductivity in z plane. This is beneficial for the activity, particularly at low current densities. However, at high current densities, when the oxygen evolution is pushed forward, a bubble management issue is rising and becomes a predominant factor to establish good activity. In other words, the aptitude of the catalyst to free the formed bubbles becomes more important. In this case, the nanoparticulate morphology of the support was found to be more efficient and thus a more adequate support for Ir nanoparticles at high current densities. In the end, a mix of both morphologies in the support is ideal and the subsequent electrocatalyst presents the best activity at high current densities and good activity at low current densities. Furthermore, the stability of this "mix" morphology-support containing catalysts ($TiON_x$-

3h-Ir) was found to be the best among the different morphologies. It was ascribed to its specific morphology and to a crystalline TiO_2 layer, as determined by Raman.

Another parameter to improve Ir on $TiON_x$ support was the utilization of a graphene template. Therefore, different ratios between the Ti-precursor and the reduced graphene nanoribbons were used in the synthesis to make $TiON_x$/rGONRs. The different ratios resulted in different coverage of the graphene template by $TiON_x$. Namely, the "Low" ratio (1/140) led to a Ti-doped graphene support while the two others, "Middle" (1/70) and "High" (1/35), resulted in $TiON_x$ flakes over the graphene. Bigger and more covering flakes were observed for the "High" sample. After the deposition of iridium nanoparticles, Ir/Middle-$TiON_x$/rGONRs appeared to be the most active catalyst. It also surpassed the activity of the best catalysts from literature. The exceptional activity was ascribed to the particular position of the iridium nanoparticles. Indeed, instead of being on the $TiON_x$ flakes, like in Ir/High-$TiON_x$/rGONRs sample, they were present in the intersection of graphene and $TiON_x$. Consequently, the contact point and chemical environment of the iridium was different in those samples, leading to a different SMSI. The latter was considered as the cause of the improved activity. In terms of stability, the catalyst with the higher amount of $TiON_x$ possessed the highest activity retention after cycling. Hence, the activity is tunable by the chemical environment of iridium nanoparticles and a higher amount of $TiON_x$ is preferable for good stability.

Finally, the previously acquired knowledge on OER-suitable support and Pt-M alloy was used to synthesize a multifunctional catalyst. First, a graphene template was covered with $TiON_x$. Afterwards, Pt-Cu was deposited on it as ORR catalyst while Ru and Ir nanoparticles were used as OER catalysts. The total amount of precious metal on the catalysts was 20 wt% as measured by ICP-OES. Even with this low amount, the ΔE of 0.651 V between ORR ($1 mA/cm^2_{geo}$) and OER ($10 mA/cm^2_{geo}$) was lower than any Pt+Ir bifunctional catalysts from the literature. In addition, this material was shown to be able to catalyze other reactions like HOR, HER and MOR, simplifying the potential production of URFCs. The stability of the composite was then tested in three different potential windows, 0.4 to 1.0 V_{RHE} (ORR), 1.2 to 1.6 V_{RHE} (OER), and 0.4 to 1.6 V_{RHE} (ORR and OER). After the ADTs in the ORR window and in the OER window, good activities are still visible. The material could thus be used in a URFC device. Interestingly, the catalyst was almost totally destroyed after cycling between ORR and OER potential windows. This indicates that the transition between FC and WE mode should be controlled in the real device and that cycling between both should be avoided.

In the future, further development and testing of supported bifunctional catalysts are needed, especially in real devices. Before that, a material able to withstand the real conditions of WE and to support iridium nanoparticles should be developed, not only in lab conditions as was $TiON_x$/C. Indeed, URFC and supporting iridium are two of the best short/middle-term options to decrease the price of the green hydrogen economy and are intrinsically linked. Finding appropriate support for OER conditions would also benefit the URFC technology.

References

[1] W. M. Organization, "Weather related disasters increase over past 50 years causing more damage fewer," WMO, 2022. [Online]. Available: https://public.wmo.int/en/media/press-release/weather-related-disasters-increase-over-past-50-years-causing-more-damage-fewer. [Accessed 26 April 2022].

[2] H. Ritchie and M. Roser, "CO2 emissions," Our world in data, [Online]. Available: https://ourworldindata.org/co2-emissions. [Accessed 26 April 2022].

[3] A. Blinken, "Intergovernmental panel on climate change working group I contribution to the sixth assessment report," US Department of State, 9 August 2021. [Online]. Available: https://www.state.gov/intergovernmental-panel-on-climate-change-working-group-i-contribution-to-the-sixth-assessment-report/. [Accessed 26 April 2022].

[4] Enerdata, "Long term energy forecasting scenarios," Enerdata, 14 March 2018. [Online]. Available: https://www.enerdata.net/publications/reports-presentations/long-term-energy-forecasting-scenarios-2018.html. [Accessed 26 April 2022].

[5] "World energy outlook 2021," International Energy Agency, [Online]. Available: https://www.iea.org/reports/world-energy-outlook-2021/executive-summary. [Accessed 26 April 2022].

[6] A. Mejean, C. Guivarcj, J. Lefevre and M. Hamdi-Cherif, "The transition in energy demand sectors to limit global warming to 1.5°C," *Energy Effic.*, vol. 12, pp. 441-462, July 2019.

[7] A. Energiewende, "Electricity Data," Agora Energiewende, [Online]. Available: https://www.agora-energiewende.de/en/service/recent-electricity-data/chart/power_generation/29.08.2022/29.09.2022/today/. [Accessed 29 September 2022].

[8] E. Tzimas, C. Filiou, S. Peteves and J.-B. Veyret, "Hydrogen storage: state-of-the-art and future perspective," European Commision, Petten, 2003.

[9] I. E. Agency, "The future of hydrogen," International Energy Agency, 2019.

[10] R. Kothari, D. Buddhi and R. Sawhney, "Comparison of environmental and economic aspects of various hydrogen production methods," *Renew. Sust. Energ. Rev.*, vol. 12, no. 2, pp. 553-563, 2008.

[11] S. Onorato and J. Krutz, "NREL fuel cell and hydrogen systems research," 16 October 2018. [Online]. Available: https://www.nrel.gov/docs/fy19osti/72776.pdf. [Accessed 26 April 2022].

[12] I. Katsounaros and M. Koper, "Hydrogen economy," in *Electrochemical Science for a Sustainable Society,* Ed., Springer, 2017, pp. 23-50.

[13] I. Katsounaros, S. Cherevko, A. Zeradjanin and K. Mayrhofer, "Oxygen electrochemistry as a cornerstone for sustainable energy conversion," *Angew. Chem. Int. Ed.,* vol. 53, no. 1, pp. 102-121, 2014.

[14] J. Turner, "A realizable renewable energy future," *Science*, vol. 285, pp. 687-689, 1999.

[15] M. Ball and M. Wietschel, The hydrogen economy: opportunities and challenges, Ed., Cambridge University Press, 2010.

[16] K.-F. Aguey-Zinsou, "About hydrogen energy," MERlin, [Online]. Available: http://www.merlin.unsw.edu.au/energyh/about-hydrogen-energy/. [Accessed 16 January 2021].
[17] M. Koper, "Thermodynamic theory of multi-electron transfer reactions: Implications for electrocatalysis," *J. Electroanal. Chem.*, vol. 660, no. 2, pp. 254-260, 2011.
[18] J. Rossmeisl, Z.-W. Qu, H. Zhu, G.-J. Kroes and J. Norskov, "Electrolysis of water on oxide surfaces," *J. Electroanal. Chem.*, vol. 607, no. 1-2, pp. 83-89, 2007.
[19] J. K. Nørskov, J. Rossmeisl, A. Logadottir, L. Lindqvist, J. Kitchin, T. Bligaard and H. Jónsson, "Origin of the Overpotential for Oxygen Reduction at a Fuel-Cell Cathode," *J. Phys. Chem. B*, vol. 108, no. 46, pp. 17886-17892, 2004.
[20] E. Commision, "Critical raw materials," European Commision, 2020. [Online]. Available:http://ec.europa.eu/growth/sectors/raw-materials/specific-interest/critical_en. [Accessed 26 April 2022].
[21] L. Carrette, K. A. Friedrich and U. Stimming, "Fuel cells: principles, types, fuels, and applications," *ChemPhysChem*, vol. 1, pp. 162-193, 2000.
[22] L. Perry and T. Fueller, "A Historical Perspective of Fuel Cell Technology in the 20th Century," *J. Electrochem. Soc.*, vol. S59, p. 149, 2002.
[23] T. Ferriday and P. Middleton, "Alkaline fuel cell technology - A review," *Inter. J. Hydrog. Energy*, vol. 46, no. 35, pp. 18489-18510, 2021.
[24] S. Lu, J. Pan, A. Huang, L. Zhuang and J. Lu, "Alkaline polymer electrolyte fuel cells completely free from noble metal catalysts," *Proc. Natl. Acad. Sci.*, vol. 105, no. 52, pp. 20611-20614, 2008.
[25] G. McLean, T. Niet, S. Prince-Richard and N. Djilali, "An assessment of alkaline fuel cell technology," *Inter. J. Hydrog. Energy*, vol. 27, no. 5, pp. 504-526, 2002.
[26] T. Von Unwerth, Conference in Mikulov, 2021.
[27] V. Vishnyakov, "Proton exchange membrane fuel cells," *Vaccum*, vol. 80, no. 10, pp. 1053-1065, 2006.
[28] O. Sharaf and M. Orhan, "An overview of fuel cell technology: Fundamentals and applications," *Renew. Sust. Energ. Rev.*, vol. 32, pp. 810-853, 2014.
[29] D. Banham and S. Ye, "Current status and future development of catalyst materials and catalyst layers for proton exchange membrane fuel cells: an industrial perspective.," *ACS Energy Lett.*, vol. 2, no. 3, pp. 629-638, 2017.
[30] X. Ren, Q. Lv, L. Liu, B. Liu, Y. Wang, A. Liu and G. Wu, "Current progress of Pt and Pt-based electrocatalysts used for fuel cells," *Sustain. Energy Fuels*, vol. 4, pp. 15-30, 2020.
[31] Fuel cell technology office, "Multi-year research, development and demonstration plan," US Department of energy, 2012.
[32] J. Durst, A. Siebel, C. Simon, F. Hasche, J. Herranz and H. Gasteiger, "New insights into the electrochemical hydrogen oxidation and evolution reaction mechanism," *Energy Environ. Sci.*, vol. 7, pp. 2255-2260, 2014.
[33] S. Trasatti, "Work function, electronegativity, and electrochemical behaviour of metals," *J. Electroanal. Chem.*, vol. 39, pp. 163-184, 1972.
[34] J. N. Hansen, H. Prats, K. Toudahl, N. Secher, K. Chan, J. Kibsgaard and I. Chorkendorff, "Is There Anything Better than Pt for HER?," *ACS Energy Lett.*, vol. 6, no. 4, pp. 1175-1180, 2021.
[35] J. Zhu, L. Hu, P. Zhao, L. Lee and K.-Y. Wong, "Recent Advances in Electrocatalytic Hydrogen Evolution Using Nanoparticles,, *Chem. Rev.*, vol. 120, no. 2, pp. 851-918, 2020.
[36] H. S. Wroblowa, Yen-Chi-Pan and G. Razumney, "Electroreduction of oxygen: A new mechanistic criterion," *J. Electroanal. Chem.*, vol. 69, no. 2, pp. 195-201, 1976.

[37] I. Katsounaros, W. B. Schneider, J. Meier, U. Benedikt, P. Biedermann, A. Cuesta, A. Auerb and K. Mayrhofer, "The impact of spectator species on the interaction of H2O2 with platinum – implications for the oxygen reduction reaction pathways," *Phys. Chem. Phys. Chem.*, vol. 15, pp. 8058-8068, 2013.
[38] N. Ramaswamy, N. Hakim and S. Mukerjee, "Degradation mechanism study of perfluorinated proton exchange membrane under fuel cell operating conditions," *Electrochim. Acta*, vol. 53, pp. 3279-3295, 2008.
[39] Y. Jiao, Y. Zheng, M. Jaroniec and S. Z. Qiao, "Design of electrocatalysts for oxygen- and hydrogen- involving energy conversion reactions," *Chem. Soc. Rev.*, vol. 44, pp. 2060-2086, 2015.
[40] V. Zhdanov and B. Kaserno, "Kinetics of electrochemical O2 reduction on Pt," *Electrochem. Comm.*, vol. 8, no. 7, pp. 1132-1136, 2006.
[41] V. Tripkovic and T. Vegge, "Potential- and Rate-Determining Step for Oxygen Reduction on Pt(111)," *J. Phys. Chem. C*, vol. 121, no. 48, pp. 26785-26793, 2017.
[42] J. Rossmeisl, A. Logadottir and J. Nørskov, "Electrolysis of water on (oxidized) metal surfaces," *Chem. Phys.*, vol. 319, no. 1-3, pp. 178-184, 2005.
[43] J. Wang, N. Markovic and R. Adzic, "Kinetic Analysis of Oxygen Reduction on Pt(111) in Acid Solutions: Intrinsic Kinetic Parameters and Anion Adsorption Effects," *J. Phys. Chem. B*, vol. 108, no. 13, pp. 4127-4133, 2004.
[44] P. Sabatier, La catalyse en chimie organique, Ed., *Librairie Polytechnique*, Paris et Liège, 1920.
[45] V. Stamenkovic, B. Mun, M. Arenz, K. Mayrhofer, C. Lucas, G. Wang, P. Ross and N. Markovic, "Trends in electrocatalysis on extended and nanoscale Pt-bimetallic alloy surface," *Nat. Mater.*, vol. 6, pp. 241-247, 2007.
[46] V. Stamenkovic, B. Moon, K. Mayrhofer, P. Ross, N. Markovic, J. Rossmeis, J. Greeley and J. Nørskov, "Changing the Activity of Electrocatalysts for Oxygen Reduction by Tuning the Surface Electronic," *Angew. Chem. Int. Ed.*, vol. 118, no. 18, pp. 2936-2967, 2006.
[47] J. Greeley, I. Stephens, A. Bondarenka, T. Johansson, H. Hansen, T. Jaramillo, J. Rossmeisl, I. Chorkendorff and J. Nørskov, "Alloys of platinum and early transition metals as oxygen reduction electrocatalysts," *Nat. Chem.*, vol. 1, pp. 552-556, 2009.
[48] P. Strasser, S. Koh, T. Anniyev, J. Greeley, K. More, C. Yu, Z. Liu, S. Kaya, D. Nordlund, H. Ogasawara, M. Toney and A. Nilsson, "Lattice-strain control of the activity in the dealloyed core-shell fuel cell catalysts," *Nat. Chem.*, vol. 2, pp. 454-460, 2010.
[49] M.-H. Shao, K. Sasaki and R.R. Adzic, "Pd-Fe nanoparticles as electrocatalysts for oxygen reduction," *J. Am. Chem. Soc.*, vol. 128, no. 11, pp. 3526-3527, 2006.
[50] P. Mani, R. Srivastava and P. Strasser, "Dealloyed Pt−Cu Core−Shell Nanoparticle Electrocatalysts for Use in PEM Fuel Cell Cathodes," *J. Phys. Chem. C*, vol. 112, pp. 2770-2778, 2008.
[51] C. Wang, N. Markovic and V. Stamenkovic, "Advanced Platinum Alloy Electrocatalysts for the Oxygen Reduction Reaction," *ACS Catal.*, vol. 2, no. 5, pp. 891-898, 2012.
[52] K. Kinoshita, Carbon: Electrochemical and Physicochemical Properties, Ed., *John Wiley & Sons*, New York, 1988.
[53] S. Tauster, S.C. Fung and R.L. Garten, "Strong metal-support interactions. Group 8 noble metals supported on titanium dioxide," *J. Am. Chem. Soc.*, vol. 100, no. 1, pp. 170-175, 1978.
[54] C. Campbell, "Electronic perturbations," *Nat. Chem.*, vol. 4, pp. 597-598, 2012.
[55] A. Bruix, J. Rodriguez, P. Ramirez, S. Senanayake, J. Evans, J. Park, D. Stacchiola, P. Liu, J. Hrbek and F. Illas, "A New Type of Strong Metal–Support Interaction

and the Production of H2 through the Transformation of water on Pt/CeO2(111) and Pt/CeOx/TiO2(110) catalysts," *J. Am. Chem. Soc.*, vol. 134, no. 21, pp. 8968-8974, 2012.
[56] J. Yang, W. Li, D. Wang and Y. Li, "Electronic Metal–Support Interaction of Single-Atom Catalysts and Applications in Electrocatalysis," *Adv. Mat.*, vol. 32, no. 49, p. 2003300, 2020.
[57] J. Wang, D. Cheng, M. Gao, Q. Li, Y. Yin, N. Zhang, Z. Zhang, X. Yu, Z. Zhao and K. Zhou, "Modulation of the superficial electronic structure via metal–support interaction for H2 evolution over Pd catalysts," *Chem Sci.*, vol. 12, no. 9, pp. 3245-3252, 2021.
[58] N. Hodnik, G. Dehm and K. Mayrhofer, "Importance and Challenges of Electrochemical in Situ Liquid Cell Electron Microscopy for Energy Conversion Research," *Acc. Chem. Res.*, vol. 49, no. 9, pp. 2015-2022, 2016.
[59] R. Borup, J. Meyers, B. Pivovar, Y. Kim, R. Mukundan, N. Garland, D. Myers, M. Wilson, F. Garzon, D. Wood, P. Zelenay, K. More, K. Stroh, T. Zawodzinski, J. Boncella, J. McGrath, M. Inaba, K. Miyatake, M. Hori, K. Ota, Z. Ogumi, S. Miyata, A. Nishikata, Z. Siroma, Y. Uchimoto, K. Yasuda, K.-I. Kimijima and N. Iwashita, "Scientific ascpects of polymer electrolyte fuel cell durability and degradation," *Chem. Rev.*, vol. 107, no. 10, pp. 3904-3951, 2007.
[60] J. Meier, C. Galeano, I. Katsounaros, J. Witte, H. Bongard, A. Topalov, C. Baldizzone, S. Mezzavilla, F. Schüth and K. Mayrhofer, "Design criteria for stable Pt/C fuel cell catalysts," *Beilstein J. Nanotechnol.*, vol. 5, pp. 44-67, 2014.
[61] A. Topalov, S. Cherevko, A. Zeradjanin, J. Meier, I. Katsounaros and K. Mayrhofer, "Towards a comprehensive understanding of platinum dissolution in acidic media," *Chem. Sci.*, vol. 5, pp. 631-638, 2014.
[62] N. Linse, L. Gubler, G. Scherer and A. Wokaun, "The effect of platinum on carbon corrosion behavior in polymer electrolyte fuel cells," *Electrochim. Acta*, vol. 56, no. 22, pp. 7541-7549, 2011.
[63] H. Schulenburg, B. Schwanitz, N. Linse, G. Scherer, A. Wokaun, J. Krbanjevic, R. Grothausmann and I. Manke, "3D Imaging of Catalyst Support Corrosion in Polymer Electrolyte Fuel Cells," *J. Phys. Chem. C*, vol. 115, no. 29, p. 14236–14243, 2011.
[64] N. Hodnik, M. Zorko, M. Bele, S. Hočevar and M. Gaberšček, "Identical Location Scanning Electron Microscopy: A Case Study of Electrochemical Degradation of PtNi Nanoparticles Using a New Nondestructive Method," *J. Phys. Chem. C*, vol. 116, no. 40, pp. 21326-21333, 2012.
[65] K. Schlögl, K. Mayrhofer, M. Hanzlik and M. Arenz, "Identical-location TEM investigations of Pt/C electrocatalyst degradation at elevated temperatures," *J. Electroanal. Chem.*, vol. 15, no. 2, pp. 355-360, 2011.
[66] Y. Shao-Horn, P. Ferreira, G. L. O', D. Morgan, H. Gasteiger and R. Makharia, "Coarsening of Pt Nanoparticles in Proton Exchange Membrane Fuel Cells upon Potential Cycling," *ECS Trans.*, vol. 1, no. 8, pp. 185-195, 2006.
[67] E. Antolini, J. Salgado and E. Gonzalez, "The stability of Pt–M (M = first row transition metal) alloy catalysts and its effect on the activity in low temperature fuel cells: A literature review and tests on a Pt–Co catalyst," *J. Power Sources*, vol. 160, no. 2, pp. 957-968, 2006.
[68] F. Hasche, M. Oezaslan and P. Strasser, "Activity, Stability, and Degradation Mechanisms of Dealloyed PtCu3 and PtCo3 Nanoparticle Fuel Cell Catalysts," *ChemCatChem*, vol. 3, no. 11, pp. 1805-1813, 2011.
[69] L. Moriau, A. Hrnjic, A. Pavlisic, A. Kamsek, U. Petek, F. Ruiz-Zepeda, M. Sala, L. Pavko, V. Selih, M. Bele, P. Jovanovic, M. Gatalo and N. Hodnik, "Resolving the

nanoparticles' structure-property relationships at the atomic level: a study of Pt-based electrocatalysts," *iScience*, vol. 24, no. 2, p. 102102, 2021.
[70] T. Reier, H. Nong, D. Teschner, R. Schlogl and P. Strasser, "Electrocatalytic Oxygen Evolution Reaction in Acidic Environments – Reaction Mechanisms and Catalysts," *Adv. Energy Mater.*, vol. 7, no. 1, p. 1601275, 2017.
[71] C. McCrory, S. Jung, J. Peters and T. Jaramillo, "Benchmarking Heterogeneous Electrocatalysts for the Oxygen Evolution Reaction," *J. Am. Chem. Soc.*, vol. 135, no. 45, pp. 16977-16987, 2013.
[72] S. Alia and G. Anderson, "Iridium Oxygen Evolution Activity and Durability Baselines in Rotating disk Electrode Half-Cells," *J. Electrochem. Soc.*, vol. 166, no. 4, pp. F282-F294, 2019.
[73] C. F. da Silva, F. Claudel, V. Martin, R. Chattot, S. Abbou, K. Kumar, I. Jiménez-Morales, S. Cavaliere, D. Jones, J. Rozière, L. Sola-Hernandez, C. Beauger, M. Faustini, J. Peron, B. Gilles, T. Encinas, L. Piccolo, F. Barros de Lima, L. Dubau and F. Maillard, "Oxygen Evolution Reaction Activity and Stability Benchmarks for Supported and Unsupported IrOx Electrocatalysts," *ACS Catal.*, vol. 11, no. 7, pp. 4107-4116, 2021.
[74] J. Nørskov, T. Bligaard, A. Logadottir, J. Kitchin, J. Chen, S. Pandelov and U. Stimming, "Trends in the Exchange Current for Hydrogen Evolution," *J. Electrochem. Soc.*, vol. 152, no. 3, pp. J23-J26, 2005.
[75] Y. Zheng, Y. Jiao, Y.Zhu, L. H. Li, Y. Han, Y. Chen, A. Du, M. Jaroniec and S. Z. Qiao, "Hydrogen evolution by a metal-free electrocatalyst," *Nat. Comm.*, vol. 5, p. 3783, 2014.
[76] J. Kibsgaard and I. Chorkendorff, "Considerations for the scaling-up of water splitting catalysts," *Nat. Energy*, vol. 4, pp. 430-433, 2019.
[77] Y. Ping, R. Nielsen and W. Goddart, "The reaction mechanism with free energy barriers at constant potentials for the oxygen evolution reaction at the IrO2 (110) surface," *J. Am. Chem. Soc.*, vol. 139, no. 1, pp. 149-155, 2017.
[78] A. Bard and L. Faulkner, Electrochemical Methods. Fundamentals and Applications, New York: Wiley, 2001.
[79] J. O. Bockris, "Kinetics of Activation Controlled Consecutive Electrochemical Reactions: Anodic Evolution of Oxygen," *J. Chem. Phys.*, vol. 24, no. 4, pp. 817-827, 1956.
[80] I. Man, H.-Y. Su, F. Calle-Vallejo, H. Hansen, J. Martinez, N. Inoglu, J. Kitchin, T. Jaramillo, J. Nørskov and J. Rossmeisl, "Universality in oxygen evolution electrocatalysis on oxide surfaces," *ChemCatChem*, vol. 3, no. 7, pp. 1159-1165, 2011.
[81] S. Fierro, T. Nagel, H. Baltruschat and C. Comninellis, "Investigation of the oxygen evolution reaction on Ti/IrO2 electrodes using isotope labelling and on-line mass spectrometry," *Electrochem. Commun.*, vol. 9, no. 8, pp. 1969-1974, 2007.
[82] R. Kötz, S. Stucki, D. Scherson and D. Kolb, "In situ identification of RuO4 as the corrosion product during oxygen evolution on ruthenium in acid media," J. Electroanal. *Chem. Interfacial Electrochem.*, vol. 172, no. 1-2, pp. 211-219, 1984.
[83] S. Cherevko, A. Zeradjanin, A. Topalov, N. Kulyk, I. Katsounaros and K. Mayrhofer, "Dissolution of Noble metals during oxygen evolution in acidic media," *ChemCatChem*, vol. 6, no. 8, pp. 2219-2223, 2014.
[84] T. Reier, Z. Pawolek, S. Cherevko, M. Bruns, T. Jones, D. Teschner, S. Selve, A. Bergmann, H. Nong, R. Schlögl, K. Mayrhofer and P. Strasser, "Molecular Insight in Structure and Activity of Highly Efficient, Low-Ir Ir-Ni oxide catalysts for electrochemical water splitting (OER)," *J. Am. Chem. Soc.*, vol. 167, no. 40, pp. 13031-13040, 2015.
[85] S. Alia, S. Shulda, C. Ngo, S. Pylypenko and B. Pivovar, "Iridium-Based Nanowires as Highly Active, Oxygen Evolution Reaction Electrocatalysts," *ACS Catal.*, vol. 8, no. 3, pp. 2111-2120, 2018.

[86] W. Hu, H. Zhong, W. Liang and S. Chen, "Ir-Surface Enriched Porous Ir–Co Oxide Hierarchical Architecture for High Performance Water Oxidation in Acidic Media.," *ACS Appl. Mater. Interfaces*, vol. 6, no. 15, pp. 12729-12736, 2014.
[87] S. Chatterjee, S. Intikhab, L. Profitt, Y. Li, V. Natu, R. Gawas and J. Snyder, "Nanoporous multimetallic Ir alloys as efficient and stable electrocatalysts for acidic oxygen evolution reactions," *J. Catal.*, vol. 393, pp. 303-312, 2021.
[88] H. Nong, H. Oh, T. Reier, E. Willinger, M.-G. Willinger, V. Petkov, D. Teschner and P. Strasser, "Oxide-Supported IrNiOxCore–Shell Particles as Efficient, Cost-Effective, and Stable Catalysts for Electrochemical water splitting," *Angew. Chem. Int. Ed.*, vol. 54, no. 10, pp. 2975-2979, 2015.
[89] S. Maass, F. Finsterwalder, G. Frank, R. Hartmann and C. Merten, "Carbon support oxidation in PEM fuel cell cathodes," *J. Power Sources*, vol. 176, no. 2, pp. 444-451, 2008.
[90] L. Moriau, M. Smiljanic, A. Loncar and N. Hodnik, *ChemCatChem*, , vol. Accepted, Online version https://chemistry-europe.onlinelibrary.wiley.com/doi/10.1002/cctc.202201123.
[91] L. Ma, S. Sui and Y. Zhai, "Preparation and characterization of Ir/TiC catalyst for oxygen evolution," *J. Power Sources*, vol. 177, no. 2, pp. 470-477, 2008.
[92] F. Karimi and B. Peppley, "Metal Carbide and Oxide Supports for Iridium-Based Oxygen Evolution Reaction Electrocatalysts for Polymer-Electrolyte-Membrane Water Electrolysis," *Electrochim. Acta*, vol. 246, pp. 654-670, 2017.
[93] H. Song, H. Yoon, B. Ju and D.-W. Kim, "Highly Efficient Perovskite-Based Electrocatalysts for Water Oxidation in Acidic Environments: A Mini Review," *Adv. Energy Mater.*, vol. 11, no. 27, p. 2002428, 2021.
[94] G. Li, K. Li, L. Yang, J. Chang, R. Ma, Z. Wu, J. Ge, C. Liu and W. Xing, "Boosted Performance of Ir Species by Employing TiN as the Support toward Oxygen Evolution Reaction," *ACS Appl. Mater. Interfaces*, vol. 10, no. 44, pp. 38117-38124, 2018.
[95] A. Nikiforov, C. Prag, J. Polonský, I. Petrushina, E. Christensen and N. Bjerrum, "Development of Refractory Ceramics for the Oxygen Evolution Reaction (OER) Electrocatalyst Support for Water Electrolysis at Elevated Temperatures," *ECS Trans.*, vol. 41, no. 42, pp. 115-124, 2012.
[96] J. Xu, G. Liu, J. Li and X. Wang, "The electrocatalytic properties of an IrO2/SnO2 catalyst using SnO2 as a support and an assisting reagent for the oxygen evolution reaction," *Electrochim. Acta*, vol. 59, pp. 105-112, 2012.
[97] B. Han, M. Risch, S. Belden, S. Lee, D. Bayer, E. Mutoro and Y. Shao-Horn, "Screening Oxide Support Materials for OER Catalysts in Acid," *J. Electrochem. Soc.*, vol. 165, no. 10, pp. F813-F820, 2018.
[98] H.-S. Oh, H. Nong, T. Reier, A. Bergmann, M. Gliech, J. F. d. Araújo, E. Willinger, R. Schlögl, D. Teschner and P. Strasser, "Electrochemical Catalyst–Support Effects and Their Stabilizing Role for IrOx Nanoparticle catalysts during the oxygen evolution reaction," *J. Am. Chem. Soc.*, vol. 138, no. 38, pp. 12552-12563, 2016.
[99] M. Ledendecker, S. Geiger, K. Hengge, J. Lim, S. Cherevko, A. Mingers, D. Göhl, G. Fortunato, D. Jalalpoor, F. Schüth, C. Scheu and K. Mayrhofer, "Towards maximized utilization of iridium for the acidic oxygen evolution reaction," *Nano Res.*, vol. 12, pp. 2275-2280, 2019.
[100] E. Oakton, D. Lebedev, M. Povia, D. Abbott, E. Fabbri, A. Fedorov, M. Nachtegaal, C. Copéret and T. Schmidt, " IrO2 TiO2: A High-Surface-Area, Active, and Stable Electrocatalyst for the Oxygen Evolution Reaction," *ACS Catal.*, vol. 7, no. 4, pp. 2346-2352, 2017.

[101] G. Chen, S. Bare and T. Mallouk, "Development of Supported Bifunctional Electrocatalysts for Unitized Regenerative Fuel Cells," *J. Electrochem. Soc.*, vol. 149, no. 8, pp. A1092-A1099, 2002.
[102] Z. Wang, W. Gao, Q. Xi, X. Ren, S. Xu, S. Zhu, X. Niu, X. Li, R. Zhao, Y. Han, G. Li and Q. Wang, "Influence of the MnO2 Phase on Oxygen Evolution Reaction Performance for Low-Loading Iridium Electrocatalysts," *ChemElectroChem*, vol. 8, no. 2, pp. 418-424, 2021.
[103] A. Hartig-Weiss, M. Miller, H. Beyer, A. Schmitt, A. Siebel, A. Freiberg, H. Gasteiger and H. El-Sayed, "Iridium Oxide Catalyst Supported on Antimony-Doped Tin Oxide for High Oxygen Evolution Reaction Activity in Acidic Media," *ACS Appl. Nano Mater.*, vol. 3, no. 3, pp. 2185-2196, 2020.
[104] L. Wang, F. Song, G. Ozouf, D. Geiger, T. Morawietz, M. Handl, P. Gazdzicki, C. Beauger, U. Kaiser, R. Hiesgen, A. Gago and K. Friedrich, "Improving the activity and stability of Ir catalysts for PEM electrolyzer anodes by SnO2:Sb aerogel supports: does V addition play an active role in electrocatalysis?," *J. Mater. Chem. A*, vol. 5, pp. 3172-3178, 2017.
[105] H. Ohno, S. Nohara, K. Kakinuma, M. Uchida, A. Miyake, S. Deki and H. Uchida, "Remarkable Mass Activities for the Oxygen Evolution Reaction at Iridium Oxide Nanocatalysts Dispersed on Tin Oxides for Polymer Electrolyte Membrane Water Electrolysis," *J. Electrochem. Soc.*, vol. 164, no. 9, pp. F944-F947, 2017.
[106] S. Geiger, O. Kasian, A. Mingers, K. Mayrhofer and S. Cherevko, "Stability limits of tin-based electrocatalyst supports," *Sci. Rep.*, vol. 7, pp. 4595-4601, 2017.
[107] G. Silva, S. Venturini, S. Zhang, M. Löffler, C. Scheu, K. Mayrhofer, E. Ticianelli and S. Cherevko, "Oxygen Evolution Reaction on Tin Oxides Supported Iridium Catalysts: Do We Need Dopants?," *ChemElectroChem*, vol. 7, no. 10, pp. 2330-2339, 2020.
[108] V. Puthiyapura, M. Mamlouk, S. Pasupathi, B. Pollet and K. Scott, " Physical and electrochemical evaluation of ATO supported IrO2 catalyst for proton exchange membrane water electrolyser," *J. Power Sources*, vol. 269, pp. 451-460, 2014.
[109] P. Biddyut and A. John, "PEM Unitised Reversible/Regenerative Hydrogen Fuel Cell Systems: State of the Art and Technical Challenges," *Renew. Sust. Energ. Rev.*, vol. 79, pp. 585-599, 2017.
[110] D. Bents, V. Scullin, B. Chang, C. G. D.W. Johnson and I. Jakupca, "Hydrogen-oxygen PEM regenerative fuel cell development at NASA Glenn Research Center," *Fuel Cells Bulletin*, vol. 2006, no. 1, pp. 12-14, 2006.
[111] S. Park, Y. Shao, J. Liu and Y. Wang, "Oxygen electrocatalysts for water electrolyzers and reversible fuel cells: status and perspective," *Energy Environ. Sci.*, vol. 5, pp. 9331-9344, 2012.
[112] S. Grigoriev, P. Millet, K. Dzhus, H. Middleton, T. Saetre and V. Fateev, "Design and characterization of bi-functional electrocatalytic layers for application in PEM unitized regenerative fuel cells," *Int. J. Hydrogen Energy*, vol. 35, no. 10, pp. 5070-5076, 2010.
[113] J. Pettersson, B. Ramsey and D. Harrison, "A review of the latest developments in electrodes for unitised regenerative polymer electrolyte fuel cells," *J. Power Sources*, vol. 157, no. 1, pp. 28-34, 2006.
[114] S.-D. Yim, W.-Y. Lee, Y.-G. Yoon, Y.-J. Sohn, G.-G. Park, T.-H. Yang and C.-S. Kim, "Optimization of bifunctional electrocatalyst for PEM unitized regenerative fuel cell," *Electrochim. Acta*, vol. 50, no. 2-3, pp. 713-718, 2004.
[115] Y. Shao, J. Liu, Y. Wang and Y. Lin, "Novel catalyst support materials for PEM fuel cells: current status and future prospects," *J. Mater. Chem.*, vol. 19, pp. 46-59, 2009.

[116] F.-D. Kong, S. Zhang, G.-P. Yin, N. Zhang, Z.-B. Wang and C.-Y. Du, "Pt/porous-IrO2 nanocomposite as promising electrocatalyst for unitized regenerative fuel cell," *Electrochem. Comm.*, vol. 14, no. 1, pp. 63-66, 2012.
[117] J. Zhang, G. Wang, Z. Liao, P. Zhang, F. Wang, X. Zhuang, E. Zschech and X. Feng, " Iridium Nanoparticles Anchored on 3D Graphite Foam as a Bifunctional Electrocatalyst for Excellent Overall Water Splitting in Acidic Solution," *Nano Energy*, vol. 40, pp. 27-33, 2017.
[118] S. Roy, K. Akbar, J. Jeon, S.-K. Jerng, L. Truong, K. Kim, Y. Yi and S.-H. Chun, "Iridium on vertical graphene as an all-round catalyst for robust water splitting reactions.," *J. Mater. Chem. A*, vol. 7, pp. 20590-20596, 2019.
[119] J.-E. Won, D.-H. Kwak, S.-B. Han, H.-S. Park, J.-Y. Park, K.-B. Ma, D.-H. Kim and K.-W. Park, "PtIr/Ti4O7 as a Bifunctional Electrocatalyst for Improved Oxygen Reduction and Oxygen Evolution Reactions," *J. Catal.*, vol. 358, pp. 287-294, 2018.
[120] D. C. Marcano, D. V. Kosynkin, J. M. Berlin, A. Sinitskii, Z. Sun, A. Slesarev, L. B. Alemany, W. Lu and J. M. Tour, "Improved Synthesis of Graphene Oxide," *ACS Nano*, vol. 4, no. 8, pp. 4806-4814, 2010.
[121] G. C. Da Silva, N. Perini and E.A. Ticianelli, "Effect of temperature on the activities and stabilities of hydrothermally prepared IrOx nanocatalyst layers for the oxygen evolution reaction," *Appl. Catal. B*, vol. 218, no. 5, pp. 287-297, 2017.
[122] C. Du, Q. Tan, G. Yin and J. Zhang, "Rotating Disk Electrode Method," in *Rotating Electrode Methods and Oxygen Reduction Electrocatalysts*, Ed., Elsevier, 2017, pp. 171-198.
[123] K. Mayrhofer, Oxygen Reduction and Carbon Monoxide Oxidation on Pt - from Model to Real Systems for Fuel Cell Electrocatalysis, Doctoral Thesis, 2006.
[124] D. van der Vliet, D. S. Strmcnik, C. Wang, V. R. Stamenkovic, N. M. Markovic and M. T. M. Koper, "On the Importance of Correcting for the Uncompensated Ohmic Resistance in Model Experiments of the Oxygen Reduction Reaction," *J. Electroanal. Chem.*, vol. 647, no. 1, pp. 29-34, 2010.
[125] K. Mayrhofer, D. Strmcnik, B. Blizanac, V. Stamenkovic, M. Arenz and N. Markovic, "Measurement of oxygen reduction activities via the rotating disc electrode method: From Pt model surfaces to carbon-supported high surface area catalysts," *Electrochim. Acta*, vol. 53, no. 7, pp. 3181-3188, 2008.
[126] C. Spöri, J. T. H. Kwan, A. Bonakdarpour, D. P. Wilkinson and P. Strasser, "The Stability Challenges of Oxygen Evolving Catalysts: Towards a Common Fundamental Understanding and Mitigation of Catalyst Degradation," *Angew. Chem. Int. Ed.*, vol. 56, no. 22, pp. 5994-6021, 2017.
[127] N. Hodnik, C. Jeyabharathi, J. C. Meier, A. Kostka, K. L. Kanala L. Phani, A. Rečnik, M. Bele, S. Hočevar, M. Gaberšček and K. J. J. Mayrhofer, "Effect of Ordering of PtCu3 Nanoparticle Structure on the Activity and Stability for the Oxygen Reduction reaction," *Phys. Chem. Chem. Phys.*, vol. 16, pp. 13610-13615, 2014.
[128] M. Gatalo, P. Jovanović, F. Ruiz-Zepeda, A. Pavlišič, A. Robba, M. Bele, G. Dražić, M. Gaberšček and N. Hodnik, "Insights into Electrochemical Dealloying of Cu out of Au-doped Pt-alloy Nanoparticles at the Sub-Nano-Scale," *J. Electrochem. Sci. Eng.*, vol. 8, pp. 87-100, 2018.
[129] P. Jovanovič, A. Pavlišič, V. S. Šelih, M. Šala, N. Hodnik, M. Bele, S. Hočevar and M. Gaberšček, "New insight into platinum dissolution from nanoparticulate platinum-based electrocatalysts using highly sensitive in situ concentrentration measurements," *ChemCatChem*, vol. 6, no. 2, pp. 449-453, 2014.
[130] DOE, "DOE Hydrogen and Fuel Cells Program Record," USA Department of Energy, 2017.

[131] M. Escudero-Escribano, K. Jensen and A. Jensen, "Recent advances in bimetallic electrocatalysts for oxygen reduction: design principles, structure-function relations and active phase elucidation," *Curr. Opin. Electrochem.*, vol. 8, pp. 135-146, 2018.
[132] V. R. Stamenkovic, B. Fowler, B. S. Mun, G. Wang, P. N. Ross, C. A. Lucas and N. M. 2. 3. 4.-4. Markovic, "Improved Oxygen Reduction Activity on Pt3Ni(111) via Increased Surface Site Availability," *Science*, vol. 315, no. 5811, pp. 493-497, 2007.
[133] L. Bu, N. Zhang, S. Guo, X. Zhang, J. Li, J. Yao, T. Wu, G. Lu, J.-Y. Ma, D. Su and X. Huang, "Biaxially strained PtPb/Pt core/shell nanoplate boosts oxygen reduction catalysis," *Science*, vol. 354, no. 6318, pp. 1410-1414, 2016.
[134] S. Mezzavilla, C. Baldizzone, A.-C. Swertz, N. Hodnik, E. Pizzutilo, G. Polymeros, G. Keeley, J. Knossalla, M. Heggen, K. Mayrhofer and F. Schuth, "Structure–activity–stability relationships for space-confined PtxNiy nanoparticles in the oxygen reduction reaction," *ACS Catal.*, vol. 6, no. 12, pp. 8058-8068, 2016.
[135] M. Oezaslan, F. Hasche and P. Strasser, "PtCu3, PtCu and Pt3Cu alloy nanoparticle electrocatalysts for oxygen reduction reaction in alkaline and acidic media," *J. Electrochem. Soc.*, vol. 159, no. 4, pp. 444-454, 2012.
[136] M. Pourbaix, "Atlas of Electrochemical Equilibria," in *Aqueous Solution*, Ed., National Association of Corrosion Engineers, 1974, p. 343.
[137] M. Gatalo, L. Moriau, U. Petek, F. Ruiz-Zepeda, M. Sala, M. Grom, T. Galun, P. Jovanovic, A. Pavlisic, M. Bele, N. Hodnik and M. Gaberscek, "CO-assisted ex-situ chemical activation of Pt-Cu/C oxygen reduction reaction electrocatalyst," *Electrochim. Acta*, vol. 306, pp. 377-386, 2019.
[138] M. Gatalo, P. Jovanovic, U. Petek, M. Sala, V. S. Selih, F. Ruiz-Zepeda, M. Bele, N. Hodnik and M. Gaberscek, "Comparison of Pt–Cu/C with Benchmark Pt–Co/C: Metal Dissolution and Their Surface Interactions," *ACS Appl. Energy Mater.*, vol. 2, no. 5, pp. 3131-3141, 2019.
[139] R. Ahluwalia, X. Wang, J.-K. Peng, N. Kariuki, D. Myers, S. Rasouli, P. Ferreira, Z. Yang, A. Martinez-Bonastre, D. Fongalland and J. Sharman, "Durability of de-alloyed platinum-nickel cathode catalyst in low platinum loading membrane-electrode assemblies subjected to accelerated stress tests," *J. Electrochem. Soc.*, vol. 165, no. 6, pp. F3316-F3327, 2018.
[140] J. Braaten, X. Xu, Y. Cai, A. Kongkanand and S. Litster, "Contaminant cation effect on oxygen transport through the ionomers of polymer electrolyte membrane fuel cells," *J. Electrochem. Soc.*, vol. 166, no. 16, pp. F1337-F1343, 2019.
[141] H. Gasteiger, S. Kocha, B. Sompalli and F. Wagner, "Activity benchmarks and requirements for Pt, Pt-alloy, and non-Pt oxygen reduction catalysts for PEMFCs," *Appl. Catal. B Environ.*, vol. 56, no. 1-2, pp. 9-35, 2005.
[142] B. Han, C. Carlton, A. Kongkanand, R. Kukreja, B. Theobald, L. Gan, R. O'Malley, P. Strasser, F. Wagner and Y. Shao-Horn, "Record activity and stability of dealloyed bimetallic catalysts for proton exchange membrane fuel cells," *Energy Environ. Sci.*, vol. 8, pp. 259-266, 2015.
[143] C. Baldizzone, L. Gan, N. Hodnik, G. Keeley, A. Kostka, M. Heggen, P. Strasser and K. Mayrhofer, "Stability of Dealloyed Porous Pt/Ni Nanoparticles," *ACS Catal.*, vol. 5, no. 9, pp. 5000-5007, 2015.
[144] D. Li, C. Wang, D. Strmcnik, D. Tripkovic, X. Sun, Y. Kang, M. Chi, J. Snyder, D. v. d. Vliet, V. S. Y. Tsai and N. M. S. Sun, "Functional links between Pt single crystal morphology and nanoparticles with different size and shape: the oxygen reduction reaction case," *Energy Environ. Sci.*, vol. 7, pp. 4061-4069, 2014.

[145] M. Oezaslan, M. Heggen and P. Strasser, "Size-dependent morphology of dealloyed bimetallic catalysts: linking the nano to the macro scale," *J. Am. Chem. Soc.*, vol. 134, no. 1, pp. 514-524, 2012.
[146] F. Calle-Vallejo, J. Tymoczko, V. Colic, Q. Vu, M. Pohl, K. Morgenstern, D. Loffreda, P. Sautet, W. Schuhmann and A. Bandarenka, "Finding optimal surface sites on heterogeneous catalysts by counting nearest neighbors," *Sciences*, vol. 350, no. 6257, pp. 185-189, 2015.
[147] J. Aarons, L. Jones, A. Varambhia, K. MacArthur, D. Ozkaya, M. Sarwar, C.-K. Skylaris and P. Nellist, "Predicting the Oxygen-Binding Properties of Platinum Nanoparticle Ensembles by Combining High-Precision Electron Microscopy and Density Functional Theory," *Nano Lett.*, vol. 17, no. 7, pp. 4003-4012, 2017.
[148] M. Rück, A. Bandarenka, F. Calle-Vallejo and A. Gagliardi, "Fast identification of optimal pure platinum nanoparticle shapes and sizes for efficient oxygen electroreduction," *Nanoscale Adv.*, vol. 1, pp. 2901-2909, 2019.
[149] C. Zalitis, A. Kucernak, X. Lin and J. Sharman, "Electrochemical measurement of intrinsic oxygen reduction reaction activity at high current densities as a function of particle size for Pt4–xCox/C (x = 0, 1, 3) catalysts," *ACS Catal.*, vol. 10, no. 7, pp. 4361-4376, 2020.
[150] Y. Xiong, Y. Yang, H. Joress, E. Padgett, U. Gupta, V. Yarlagadda, D. Agyeman-Budu, X. Huang, T. Moylan, R. Zeng, A. Kongkanand, F. Escobedo, J. Brock, F. DiSalvo, D. Muller and H. Abruna, "Revealing the atomic ordering of binary intermetallics using in situ heating techniques at multilength scales," *Proc. Natl. Acad. Sci.*, vol. 116, no. 6, pp. 1974-1983, 2019.
[151] Y. Yang, C.-C. Chen, M. Scott, C. Ophus, R. Xu, A. Pryor, L. Wu, F. Sun, W. Theis, J. Zhou, M. Eisenbach, P. Kent and H. Z. P. E. J. M. R. F. Sabirianov, "Deciphering chemical order/disorder and material properties at the single-atom level," *Nature*, vol. 542, pp. 75-79, 2017.
[152] A. Pavlisič, P. Jovanovic, V. S. Šelih, M. Šala, M. Bele, G. Dražič, I. Arcon, S. Hocevar, A. Kokalj, N. Hodnik and M. Gaberšček, "Atomically Resolved Dealloying of Structurally Ordered Pt Nanoalloy as an Oxygen Reduction Reaction Electrocatalyst," *ACS Catal.*, vol. 6, no. 8, pp. 5530-5534, 2016.
[153] R. Chattot, O. L. Bacq, V. Beermann, S. Kühl, J. Herranz, S. Henning, L. Kühn, T. Asset, L. Guétaz, G. Renou, J. Drnec, P. Bordet, A. Pasturel, A. Eychmuller, T. Schmidt, P. Strasser, L. Dubau and F. Maillard, "Surface distortion as a unifying concept and descriptor in oxygen reduction reaction electrocatalysis," *Nat. Mater.*, vol. 17, pp. 827-833, 2018.
[154] M. Li, Z. Zhao, T. Cheng, A. Fortunelli, C.-Y. Chen, R. Yu, Q. Zhang, L. Gu, B. Merinov, Z. Lin, E. Zhu, T. Yu, Q. Jia, J. Guo, L. Zhang, W. Goddard, Y. Huand and X. Duan, "Ultrafine jagged platinum nanowires enable ultrahigh mass activity for the oxygen reduction reaction," *Science*, vol. 354, no. 6318, pp. 1414-1419, 2016.
[155] L. Gan, M. Heggen, C. Cui and P. Strasser, "Thermal facet healing of concave octahedral Pt–Ni nanoparticles imaged in situ at the atomic scale: implications for the rational synthesis of durable high-performance ORR electrocatalysts," *ACS Catal.*, vol. 6, no. 2, pp. 692-695, 2016.
[156] F. Ruiz-Zepeda, M. Gatalo, A. Pavlišič, G. Dražić, P. Jovanovič, M. Bele, M. Gaberšček and N. Hodnik, "Atomically resolved anisotropic electrochemical shaping of nano-electrocatalyst," *Nano Lett.*, vol. 19, no. 8, pp. 4919-4927, 2019.
[157] K. Matsutani, T. Tomoyuki and K. Hayakawa, "Effect of particle size of platinum and platinum-cobalt catalysts on stability against load cycling," Platin. Met. Rev., vol. 54, p. 233, 2010.

[158] S. Taylor, E. Fabbri, P. Levecque, T. Schmidt and O. Conrad, "The effect of platinum loading and surface morphology on oxygen reduction activity," *Electrocatalysis*, vol. 7, pp. 287-297, 2016.
[159] A. Anonymous, "Product Page of Pt-Fe/C from FCS," 2020. [Online]. Available: https://www.fuelcellstore.com/20-platinum-iron-vulcan (2020). [Accessed 26 April 2022].
[160] C. Baldizzone, S. Mezzavilla, H. Carvalho, J. Meier, A. Schuppert, M. Heggen, C. Galeano, J.-D. Grunwaldt, F. Schüth and K. Mayrhofer, "Confined-space alloying of nanoparticles for the synthesis of efficient PtNi fuel-cell catalysts," *Angew. Chem. Int. Ed.*, vol. 53, no. 51, pp. 14250-14254, 2014.
[161] L. Chong, J. Wen, J. Kubal, F. Sen, J. Zou, J. Greeley, M. Chan, H. Barkholtz, W. Ding and D.-J. Liu, "Ultralow-loading platinum-cobalt fuel cell catalysts derived from imidazolate frameworks," *Science*, vol. 362, no. 6420, pp. 1276-1281, 2018.
[162] X. Wang, M. Swihart and G. Wu, "challenges and perspectives on cathode catalysts in proton exchange membrane fuel cells for transportation," *Nat. Catal.*, vol. 2, pp. 578-589, 2019.
[163] X. Li, W. Cai, J. An, S. Kim, J. Nah, D. Yang, R. Piner, A. Velamakanni, I. Jung, E. Tutuc, S. Banerjee, L. Colombo and R. Ruoff, "Large-area synthesis of high-quality and uniform graphene films on copper foils," *Science*, vol. 324, no. 5930, pp. 1312-1314, 2009.
[164] S.S. Kocha, Y. Garsany and D. Myers "Testing oxygen reduction reaction activity with the rotating disc electrode technique," 12 March 2013. [Online]. Available: https://www.energy.gov/sites/prod/files/2014/03/f12/webinarslides_rde_technique_031213.pdf. [Accessed 26 April 2022].
[165] D. van der Vliet, C. Wang, D. Li, A. Paulikas, J. Greeley, R. Rankin, D. Strmcnik, D. Tripkovic, N. Markovic and V. Stamenkovic, "Unique electrochemical adsorption properties of Pt-skin surface," *Angew. Chem. Int. Ed.*, vol. 51, no. 13, pp. 3139-3142, 2012.
[166] K. Mayrhofer, D. Strmcnik, B. Blozanac, V. Stamenkovic, M. Arenz and N. Markovic, "Measurement of oxygen reduction activities via the rotating disc electrode method: From Pt model surfaces to carbon-supported high surface area catalysts," *Electrochim. Acta*, vol. 53, no. 7, pp. 3181-388, 2008.
[167] S. Klemm, A. Topalov, C. Laska and K. Mayrhofer, "Coupling of a high throughput microelectrochemical cell with online multielemental trace analysis by ICP-MS," *Electro. Comm.*, vol. 13, no. 12, pp. 1533-1535, 2011.
[168] R. Ahluwalia, D. Papadias, N. Kariuki, J.-K. Peng, X. Wang, Y. Tsai, D. Graczyk and D. Myers, "Potential dependence of Pt and Co dissolution from platinum-cobalt alloy PEFC catalysts using time-resolved measurements," *J. Electrochem. Soc.*, vol. 165, no. 6, pp. F3024-F3035, 2018.
[169] S. Cherevko, N. Kulyk and K. Mayrhofer, "Durability of platinum-based fuel cell electrocatalysts: dissolution of bulk and nanoscale platinum," *Nano Energy*, vol. 29, pp. 275-298, 2016.
[170] A. Topalov, I. Katsounaros, M. Auinger, S. Cherevko, J. Meier, S. Klemm and K. Mayrhofer, "Dissolution of platinum: limits for the deployment of electrochemical energy conversion?," *Angew. Chem. Int. Ed.*, vol. 51, no. 50, pp. 12613-12615, 2012.
[171] D. Chung, S. Park, H. Lee, H. Kim, Y.-H. Chung, J. Yoo, D. Ahn, S.-H. Yu, K.-S. Lee, M. Ahmadi, H. Ju, H. Abruna, S. Yoo, B. Mun and Y.-E. Sung, "Activity–stability relationship in Au@Pt nanoparticles for electrocatalysis," *ACS Energy Lett.*, vol. 5, no. 9, pp. 2827-2834, 2020.
[172] M. Gatalo, P. Jovanovič, G. Polymeros, J.-P. Grote, A. Pavlišič, F. R.-. Zepeda, V. Šelih, M. Šala, S. Hočevar, M. Bele, K. Mayrhofer, N. Hodnik and M. Gaberscek, "Positive effect of surface doping with Au on the stability of Pt-based electrocatalysts," *ACS Catal.*, vol. 6, no. 3, pp. 1630-1634, 2016.

[173] K. Kodama, R. Jinnouchi, N. Takahashi, H. Murata and Y. Morimoto, "Activities and stabilities of Au-modified stepped-Pt single-crystal electrodes as model cathode catalysts in polymer electrolyte fuel cells," *J. Am. Chem. Soc.*, vol. 138, no. 12, pp. 4194-4200, 2016.
[174] P. Lopes, D. Li, H. Lv, C. Wang, D. Tripkovic, Y. Zhu, R. Schimmenti, H. Daimon, Y. Kang, J. Snyder, N. Becknell, K. More, D. Strmcnik, N. Markovic and V. S. M. Mavrikakis, "Eliminating dissolution of platinum-based electrocatalysts at the atomic scale," *Nat. Mater.*, vol. 19, pp. 1207-1214, 2020.
[175] M. Bele, P. Jovanovič, A. Pavlišič, B. Jozinović, M. Zorko, A. Rečnik, E. Chernyshova, S. Hočevar, N. Hodnik and M. Gaberšček, "A highly active PtCu3 intermetallic core–shell, multilayered Pt-skin, carbon embedded electrocatalyst produced by a scale-up sol–gel synthesis," *Chem. Commun.*, vol. 50, pp. 13124-13126, 2014.
[176] Z. Yu, J. Zhang, Z. Liu, J. Ziegelbauer, H. Xin, I. Dutta, D. Muller and F. Wagner, "Comparison between dealloyed PtCo3 and PtCu3 cathode catalysts for proton exchange membrane fuel cells," *J. Phys. Chem. C*, vol. 116, no. 37, pp. 19877-19885, 2012.
[177] F. Zhu, A. Wu, L. Luo, C. Wang, F. Yang, G. Wei, G. Xia, J. Yin and J. Zhang, "The asymmetric effects of Cu2+ contamination in a proton exchange membrane fuel cell (PEMFC)," *Fuel Cells*, vol. 20, no. 2, pp. 196-202, 2020.
[178] W. Tu, W. Luo, C. Chen, K. Chen, E. Zhu, Z. Zhao, Z. Wang, T. Hu, H. Zai, X. Ke, M. Sui, P. Chen, Q. Zhang, Q. Chen, Y. Li and Y. Huang, "Tungsten as “adhesive” in Pt2CuW0.25 ternary alloy for highly durable oxygen reduction electrocatalysis," *Adv. Funct. Mater.*, vol. 30, no. 6, p. 1908230, 2020.
[179] Q. Liu, L. Du, G. Fu, Z. Cui, Y. Li, D. Dang, X. Gao, Q. Zheng and J.B. Goodenough, "Structurally ordered Fe3Pt nanoparticles on robust nitride support as a high-performance catalyst for the oxygen reduction reaction," *Adv. Energy Mater.*, vol. 9, no. 3, p. 1803040, 2019.
[180] Z. Wang, X. Yao, Y. Kang, L. Miao, D. Xia and L. Gan, "Structurally ordered low-Pt intermetallic electrocatalysts toward durably high oxygen reduction reaction activity," *Adv. Funct. Mater.*, vol. 29, no. 35, p. 1902987, 2019.
[181] M. Strlič, J. Kolar, V.-S. Šelih, D. Kočar and B. Pihlar, "A comparative study of several transition metals in fenton-like reaction system at circum-neutral pH," *Acta Chim. Slov.*, vol. 50, pp. 619-632, 2003.
[182] H. Yamada, H. Kato and K. Kodama, "Cell performance and durability of Pt/C cathode catalyst covered by dopamine derived carbon thin layer for polymer electrolyte fuel cells," *J. Electrochem. Soc.*, vol. 167, p. 84508, 2020.
[183] C. Baldizzone, S. Mezzavilla, N. Hodnik, A. Zeradjanin, A. Kostka, F. Schuth and K. Mayrhofer, "Activation of carbon-supported catalysts by ozonized acidic solutions for the direct implementation in (electro-)chemical reactors," *Chem. Commun.*, vol. 51, pp. 1226-1229, 2015.
[184] F. Dionigi, C. Weber, M. Primbs, M. Gocyla, A. Bonastre, C. Spöri, H. Schmies, E. Hornberger, S. Kühl, J. Drnec, M. Heggen, J. Sharman, R. E. D.-. Borkowski and P. Strasser, "Controlling Near-Surface Ni Composition in Octahedral PtNi(Mo) Nanoparticles by Mo Doping for a Highly Active Oxygen Reduction Reaction Catalyst," *Nano Lett.*, vol. 19, no. 10, pp. 6876-6885, 2019.
[185] H. Lohse-Busch, M. Duoba, K. Stutenberg, S. Iliev and M. Kern, "Technology assessment of a fuel cell vehicle: 2017 Toyota Mirai," US Department of Energy, 2018.
[186] T. Yoshida and K. Kojima, "Toyota MIRAI fuel cell vehicle and progress toward a future hydrogen society," *Electrochem. Soc. Interface*, vol. 24, pp. 45-49, 2015.
[187] A. Kongkanand, "Highly-Accessible Catalysts for Durable High-Power Performance," General Motors LLC, 2020.

[188] J. Braaten, A. Kongkanand and S. Litster, "Oxygen transport effects of cobalt cation contamination of ionomer thin films in proton exchange membrane fuel cells," *ECS Trans.*, vol. 80, no. 8, pp. 293-290, 2017.
[189] J. Calma, "Tesla to make EV battery cathodes without cobalt," 22 September 2020. [Online]. Available: https://www.theverge.com/2020/9/22/21451670/tesla-cobalt-free-cathodes-mining-battery-nickel-ev-cost. [Accessed 30 April 2022].
[190] E. Antolini, "Carbon supports for low-temperature fuel cell catalysts," *Appl. Catal. B Environ.*, vol. 88, no. 1-2, pp. 1-24, 2009.
[191] L. Castanheira, L. Dubau, M. Mermoux, G. Berthomé, N. Caqué, E. Rossinot, M. Chatenet and F. Maillard, "Carbon corrosion in proton-exchange membrane fuel cells: from model experiments to real-life operation in membrane electrode assemblies," *ACS Catal.*, vol. 4, no. 7, pp. 2258-2267, 2014.
[192] J. Tang, J. Liu, N. Torad, T. Kimura and Y. Yamauchi, "Tailored design of functional nanoporous carbon materials toward fuel cell applications," *Nano Today*, vol. 9, no. 3, pp. 305-323, 2014.
[193] V. Yarlagadda, M. Carpenter, T. Moylan, R. Kukreja, R. Koestner, W. Gu, L. Thompson and A. Kongkanand, "Boosting fuel cell performance with accessible carbon mesopores," *ACS Energy Lett.*, vol. 3, no. 3, pp. 618-621, 2018.
[194] N. Maselj, M. Gatalo, F. Ruiz-Zepeda, A. Kregar, P. Jovanovič, N. Hodnik and M. Gaberšček, "The importance of temperature and potential window in stability evaluation of supported Pt-based oxygen reduction reaction electrocatalysts in thin film rotating disc electrode set-up," *J. Electrochem. Soc.*, vol. 167, p. 114506, 2020.
[195] E. Pizzutilo, S. Geiger, J.-P. Grote, A. Mingers, K. Mayrhofer, M. Arenz and S. Cherevko, "On the need of improved accelerated degradation protocols (ADPs): examination of platinum dissolution and carbon corrosion in half-cell tests," *J. Electrochem. Soc.*, vol. 163, no. 14, pp. F1510-F1514, 2016.
[196] D. Trimarco, T. Pedersen, O. Hansen, I. Chorkendorff and P. Vesborg, "Fast and sensitive method for detecting volatile species in liquids," *Rev. Sci. Instrum.*, vol. 86, p. 75006, 2015.
[197] N. Hodnik and S. Cherevko, "Spot the difference at the nanoscale: identical location electron microscopy in electrocatalysis," *Curr. Opin. Electrochem.*, vol. 15, pp. 73-82, 2019.
[198] J. Meier, I. Katsounaros, C. Galeano, H. Bongard, A. Topalov, A. Kostka, A. Karschin, F. Schuth and K. Mayrhofer, "Stability investigations of electrocatalysts on the nanoscale," *Energy Environ. Sci.*, vol. 5, pp. 9319-9330, 2012.
[199] A. Hrnjic, A. R. Kamšek, A. Pavlišič, M. Šala, M. Bele, L. Moriau, M. Gatalo, F. Ruiz-Zepeda, P. Jovanovič and N. Hodnik, "Observing, tracking and analysing electrochemically induced atomic-scale structural changes of an individual Pt-Co nanoparticle as a fuel cell electrocatalyst by combining modified floating electrode and identical location electron microscopy," *Electrochim. Acta*, vol. 388, pp. 138513, 2021.
[200] G. Koderman Podboršek, A. R. Kamšek, A. Lončar, M. Bele, L. Suhadolnik, P. Jovanovič and N. Hodnik, "Atomically-resolved structural changes of ceramic supported nanoparticulate oxygen evolution reaction Ir catalyst," *Electrochim. Acta*, vol. 426, pp. 140800, 2022.
[201] C. Hao, H. Lv, Q. Zhao, B. Li, C. Zhang, C. Mi, Y. Song and J. Ma, "Investigation of V-doped TiO2 as an anodic catalyst support for SPE water electrolysis," *Int. J. Hydrogen Energ.*, vol. 42, no. 15, pp. 9384-9395, 2017.
[202] W. Hu, S. Chen and Q. Xia, "IrO2/Nb–TiO2 electrocatalyst for oxygen evolution reaction in acidic medium.," *Int. J. Hydrogen Energ.*, vol. 39, no. 13, pp. 6967-6976, 2014.
[203] J. Cheng, J. Yang, S. Kitano, G. Juhasz, M. Higashi, M. Sadakiyo, K. Kato, S. Yoshioka, T. Sugiyama, M. Yamauchi and N. Nakashima, "Impact of Ir-Valence Control

and Surface Nanostructure on Oxygen Evolution Reaction over a Highly Efficient Ir–TiO2 Nanorod Catalyst," *ACS Catal.*, vol. 9, no. 8, pp. 6974-6986, 2019.
[204] K. Zhang, W. Mai, J. Li, H. Wang, G. Li and W. Hu, "Highly scattered Ir oxides on TiN as an efficient oxygen evolution reaction electrocatalyst in acidic media," *J. Mater. Sci.*, vol. 55, pp. 3507-3520, 2020.
[205] J. Polonsky, P. Mazur, M. Paidar, E. Christensen and K. Bouzek, "Performance of a PEM water electrolyser using a TaC-supported iridium oxide electrocatalyst," *Int. J. Hydrog. Energy*, vol. 39, no. 7, pp. 3072-3078, 2014.
[206] O. Diaz-Morales, S. Raaijman, R. Kortlever, P. Kooyman, T. Wezendonk, J. Gascon, W. Fu and M. Koper, "Iridium-based double perovskites for efficient water oxidation in acid media," *Nat. Commun.*, vol. 7, p. 12363, 2016.
[207] H. Ohno, S. Nohara, K. Kakinuma, M. Uchida and H. Uchida, "Effect of Electronic Conductivities of Iridium Oxide/Doped SnO2 Oxygen-Evolving Catalysts on the Polarization Properties in Proton Exchange Membrane Water Electrolysis," *Catalysts*, vol. 9, no. 1, p. 74, 2019.
[208] L. Sola-Hernandez, F. Claudel, F. Maillard and C. Beauger, "Doped tin oxide aerogels as oxygen evolution reaction catalyst supports," *Int. J. Hydrog, Energy*, vol. 44, no. 45, pp. 24331-24341, 2019.
[209] M. Datta, K. Kadakia, O. Velikokhatnyi, P. Jampani, S. Chung, J. Poston, A. Manivannan and P. Kumta, "High performance robust F-doped tin oxide-based oxygen evolution electro-catalysts for PEM based water electrolysis," *J. Mater. Chem. A*, vol. 1, pp. 4026-4037, 2013.
[210] S. Tauster, S. Fung, R. Baker and J. Horsley, "Strong Interactions in Supported-Metal Catalysts," *Science*, vol. 211, no. 4487, pp. 1121-1125, 1981.
[211] A. Trenczek-Zajac, M. Radecka, K. Zakrzewska, A. Brudnik, E. Kusior, S. Bourgeois, M. C. Marco De Lucas and L. Imhoff, "Structural and Electrical Properties of Magnetron Sputtered Ti(ON) Thin Films: The Case of TiN Doped in Situ with Oxygen," *J. Power Sources*, vol. 194, no. 1, pp. 93-103, 2009.
[212] M. Sluban, P. Umek, Z. Jagličić, J. Buh, P. Šmitek, A. Mrzel, C. Bittencourt, P. Guttmann, M.-H. Delville, D. Mihailović and D. Arčon, "Controlling Disorder and Superconductivity in Titanium Oxynitride Nanoribbons with Anion Exchange.," *ACS Nano*, vol. 9, no. 10, pp. 10133-10141, 2015.
[213] K. A. Soliman, A. F. Zedan, A. Khalifa, H. A. El-Sayed, A. S. Aljaber, S. Y. AlQaradawi and N. K. Allam, "Silver Nanoparticles-Decorated Titanium Oxynitride Nanotube Arrays for Enhanced Solar Fuel Generation," *Sci. Rep.*, vol. 7, p. 1913, 2017.
[214] L. Yan, G. Chen, S. Tan, M. Zhou, G. Zou, S. Deng, S. Smirnov and H. Luo, "Titanium Oxynitride Nanoparticles Anchored on Carbon Nanotubes as Energy Storage Materials," *ACS Appl. Mater. Interfaces*, vol. 7, no. 43, pp. 24212-24217, 2015.
[215] M. A. Rafiee, W. Lu, A. Thomas, A. Zandiatashbar, J. Rafiee, J. Tour and N. Koratkar, "Graphene nanoribbon composites," *ACS Nano*, vol. 4, no. 12, pp. 7415-7420, 2010.
[216] B. Xiao, X. Li, X. Li, B. Wang, C. Langford, R. Li and X. Sun, "Graphene Nanoribbons Derived from the Unzipping of Carbon Nanotubes: Controlled Synthesis and Superior Lithium Storage Performance," *J. Phys. Chem. C*, vol. 118, no. 2, pp. 881-890, 2014.
[217] M. Bele, K. Stojanovski, P. Jovanovic, L. Moriau, G. K. Podborsek, J. Moskon, P. Umek, M. Sluban, G. Drazic, N. Hodnik and M. Gaberscek, "Towards stable and conductive Titanium oxynitride high surface area support for Iridium nanoparticles as OER electrocatalysts," *ChemCatChem*, vol. 11, no. 20, pp. 5038-5044, 2019.

[218] R. O. Grisdale, "The properties of carbon contact," *J. Appl. Phys.*, vol. 24, pp. 1288-1296, 1953.
[219] F. C. Cowlard and J. C. Lewis, "Vitreous carbon - a new form of carbon," *J. Mater. Sci.*, vol. 2, pp. 507-512, 1967.
[220] D. McKee, "Carbon and Graphite science," *Annu. Rev. Mater. Sci.*, vol. 3, pp. 195-231, 1973.
[221] I. Spain, "Electronic Transport Properties of Graphite, Carbons, and Related Materials," in *Chemistry and Physics of Carbon*, Ney Work, P.L. Walker, 1988, pp. 130-164.
[222] J. Moskon, R. Dominko, M. Gaberscek, R. Cerc-Korosec and J. Jamnik, "Citrate-Derived Carbon Nanocoatings for Poorly Conducting Cathode: A Detailed Study Using TiO2 Substrate Materials.," *J. Electrochem. Soc.*, vol. 153, no. 10, pp. A1805-A1811, 2006.
[223] K. L. I. Park, Y. Cho, D. Jung, N. Jung, H. Park and Y. Sung, "Electrocatalytic activity and stability of Pt supported on Sb-doped SnO2 nanoparticles for direct alcohol fuel cells.," *J. Catal.*, vol. 258, no. 1, pp. 143-152, 2008.
[224] S. Alia, B. Rasimick, C. Ngo, K. Neyerlin, S. Kocha, S. Pylypenko, H. Xu and B. Pivovar, "Activity and Durability of Iridium Nanoparticles in the Oxygen Evolution Reaction.," *J. Electrochem. Soc.*, vol. 163, no. 11, p. F3105–F3112. , 2016.
[225] R. Frydendal, E. Paoli, B. Knudsen, B. Wickman, P. Malacrida, I. Stephens and I. Chorkendorff, "Benchmarking the Stability of Oxygen Evolution Reaction Catalysts: The Importance of Monitoring Mass Losses.," *ChemElectroChem*, vol. 1, no. 12, pp. 2075-2081, 2014.
[226] P. Pickup and V. Birss, "A model for anodic hydrous oxide growth at iridium," *J. Electroanal. Chem. Interfacial Electrochem.*, vol. 220, no. 1, pp. 83-100, 1987.
[227] V. A. Saveleva, L. Wang, O. Kasian, M. Batuk, J. Hadermann, J. J. Gallet, F. Bournel, N. Alonso-Vante, G. Ozouf, C. Beauger, K. Mayrhofer, S. Cherevko, A. Gago, K. Friedrich, S. Zafeiratos and E. Savinova, "Insight into the Mechanisms of High Activity and Stability of Iridium Supported on Antimony-Doped Tin Oxide Aerogel for anodes of proton exchange membrane water electrolyzers," *ACS Catal.*, vol. 10, no. 4, pp. 2508-2516, 2020.
[228] T. Reier, D. Teschner, T. Lunkenbein, A. Bergmann, S. Selve, R. Kraehnert, R. Schlögl and P. Strasser, "Electrocatalytic Oxygen Evolution on Iridium Oxide: Uncovering Catalyst-Substrate Interactions and Active Iridium Oxide Species," *J. Electrochem. Soc.*, vol. 161, no. 9, pp. F876-F882, 2014.
[229] V. Pfeifer, T. Jones, J. V. Vélez, C. Massué, M. Greiner, R. Arrigo, D. Teschner, F. Girgsdies, M. Scherzer, J. Allan, M. Hashagen, G. Weinberg, S. Piccinin, M. Hävecker, A. Knop-Gericke and R. Schlögl, "The electronic structure of iridium oxide electrodes active in water splitting," *Phys. Chem. Chem. Phys.*, vol. 18, pp. 2292-2296, 2016.
[230] A. Minguzzi, C. Locatelli, O. Lugaresi, E. Achilli, G. Cappelletti, M. Scavini, M. Coduri, P. Masala, B. Sacchi, A. Vertova, P. Ghigna and S. Rondinini, "Easy Accommodation of Different Oxidation States in Iridium Oxide Nanoparticles with Different Hydration Degree as Water Oxidation Electrocatalysts," *ACS Catal.*, vol. 5, no. 9, p. 5104–5115, 2015.
[231] A. Minguzzi, O. Lugaresi, E. Achilli, C. Locatelli, A. Vertova, P. Ghigna and S. Rondinini, "Observing the oxidation state turnover in heterogeneous iridium-based water oxidation catalysts," *Chem. Sci.*, vol. 5, pp. 3591-3597, 2014.
[232] V. Pfeifer, T. Jones, S. Wrabetz, C. Massué, J. V. Vélez, R. Arrigo, M. Scherzer, S. Piccinin, M. Hävecker, A. Knop-Gericke and R. Schlögl, "Reactive oxygen species in iridium-based OER catalysts," *Chem. Sci.*, vol. 7, pp. 6791-6795, 2016.

[233] V. Pfeifer, T. Jones, J. V. Vélez, R. Arrigo, S. Piccinin, M. Hävecker, A. Knop-Gericke and R. Schlögl, "In situ observation of reactive oxygen species forming on oxygen-evolving iridium surfaces.," *Chem. Sci.*, vol. 8, pp. 2143-2149, 2017.
[234] L. Moriau, M. Bele, Z. Marinko, F. Ruiz-Zepeda, G. K. Podboršek, M. Šala, A. Šurca, J. Kovač, I. Arčon, P. Jovanovič, N. Hodnik and L. Suhadolnik, "Effect of the Morphology of the High-Surface-Area Support on the Performance of the Oxygen-Evolution Reaction for Iridium Nanoparticles," *ACS Catal.*, vol. 11, no. 2, pp. 670-681, 2021.
[235] A. Zeradjanin, E. Ventosa, A. Bondarenka and W. Schuhmann, "Evaluation of the Catalytic Performance of Gas-Evolving Electrodes Using Local Electrochemical Noise Measurements," *ChemSusChem.*, vol. 5, no. 10, pp. 1905-1911, 2012.
[236] X. Chen, A. Maljusch, R. Rincón, A. Battistel, A. Bandarenka and W. Schuhmann, "Local Visualization of Catalytic Activity at Gas Evolving Electrodes Using Frequency-Dependent Scanning Electrochemical Microscopy," *Chem. Commun.*, vol. 50, no. 87, pp. 13250-13253, 2014.
[237] A. Zeradjanin, A. Topalov, Q. Van Overmeere, S. Cherevko, X. Chen, E. Ventosa, W. Schuhmann and K. Mayrhofer, "Rational Design of the Electrode Morphology for Oxygen Evolution-Enhancing the Performance for Catalytic Water Oxidation," *RSC Adv.*, vol. 4, pp. 9579-9587, 2014.
[238] A. Zeradjanin, F. La Mantia, J. Masa and W. Schuhmann, "Utilization of the Catalyst Layer of Dimensionally Stable Anodes—Interplay of Morphology and Active Surface Area," *Electrochim. Acta*, vol. 82, no. 1, pp. 408-414, 2012.
[239] F. Hegge, F. Lombeck, E. Cruz Ortiz, L. Bohn, M. von Holst, M. Kroschel, J. Hübner, M. Breitwieser, P. Strasser and S. ž. Vierrath, "Efficient and Stable Low Iridium Loaded Anodes for PEM Water Electrolysis Made Possible by Nanofiber Interlayers," *ACS Appl. Energy Mater.*, vol. 3, no. 9, pp. 8276-8284, 2020.
[240] J. Macak, H. Tsuchiya, A. Ghicov, K. Yasuda, R. Hahn, S. Bauer and P. Schmuki, "TiO2 Nanotubes: Self-Organized Electrochemical Formation, Properties and Applications," *Curr. Opin. Solid State Mater. Sci.*, vol. 11, no. 1, pp. 3-18, 2007.
[241] J. Han and J. Bang, "Hollow Titanium Oxynitride Nanorod Array as an Electrode Substrate Prepared by the Hot Ammonia-Induced Kirkendall Effect," *J. Mater. Chem. A*, vol. 2, pp. 10568-10576, 2014.
[242] V. Pfeifer, T. Jones, J. V. Vélez, C. Massué, R. Arrigo, D. Teschner, F. Girgsdies, M. Scherzer, M. Greiner, J. Allan, M. Hashagen, G. Weinberg, S. Piccinin, M. Havecker, A. Knop-Gericke and R. Schlogl, "The Electronic Structure of Iridium and Its Oxides," *Surf. Interface Anal.*, vol. 48, pp. 261-273, 2016.
[243] T. Ohsaka, F. Izumi and Y. Fujiki, "Raman Spectrum of Anatase, TiO2," *J. Raman Spectrosc.*, vol. 7, no. 6, pp. 321-324, 1978.
[244] A. Kontos, A. Kontos, Y. Raptis and P. Falaras, "Nitrogen Modified Nanostructured Titania: Electronic, Structural and Visible-Light Photocatalytic Properties," *Phys. status solidi – Rapid Res. Lett.*, vol. 2, no. 2, pp. 83-85, 2008.
[245] E. György, A. Pérez Del Pino, P. Serra and J. Morenza, "Surface Nitridation of Titanium by Pulsed Nd:YAG Laser Irradiation," *Appl. Surf. Sci.*, vol. 186, no. 1-4, pp. 130-134, 2002.
[246] Z. Ding, B. Yao, L. Qiu and T. Lv, "Raman Scattering Investigation of Nanocrystalline δ-TiNx Synthesized by Solid-State Reaction," *J. Alloys Compd.*, vol. 421, no. 1-2, pp. 247-251, 2006.
[247] W. Spengler, R. Kaiser, A. Christensen and G. Müller-Vogt, "Raman Scattering, Superconductivity, and Phonon Density of States of Stoichiometric and Nonstoichiometric TiN," *Phys. Rev. B*, vol. 17, no. 3, pp. 1095-1101, 1978.

[248] S. Prokes, J. Gole, X. Chen, C. Burda and W. Carlos, "Defect-Related Optical Behavior in Surface-Modified TiO2 Nanostructures," *Adv. Funct. Mater.*, vol. 15, no. 1, pp. 161-167, 2005.
[249] A. Korotcov, Y. Huang, D. Tsai and K. Tiong, "Raman Scattering Characterization of Vertical Aligned 1D IrO2 Nanocrystals Grown on Single Crystal Oxide Substrates," *Solid State Commun.*, vol. 137, no. 6, pp. 310-314, 2006.
[250] S. Kabekkodu, "Powder diffraction file," International Centre for Diffraction Data, Newton Square, Pennsylvania, 2019.
[251] Y. T. Kim, P. P. Lopes, S. A. Park, A. Y. Lee, J. Lim, H. Lee, S. Back, Y. Jung, N. Danilovic, V. Stamenkovic, J. Erlebacher, J. Snyder and N. Markovic, "Balancing Activity, Stability and Conductivity of Nanoporous Core-Shell Iridium/Iridium Oxide Oxygen Evolution Catalysts," *Nat. Commun.*, vol. 8, no. 1, pp. 1-8, 2017.
[252] L. Seitz, C. Dickens, K. Nishio, Y. Hikita, J. Montoya, A. Doyle, C. Kirk, A. Vojvodic, H. Hwang, J. Norskov and T. Jaramillo, "A Highly Active and Stable IrOx/SrIrO3 Catalyst for the Oxygen Evolution Reaction," *Science*, vol. 353, no. 6303, pp. 1011-1014, 2016.
[253] S. Chang, N. Danilovic, K.-C. Chang, R. Subbaraman, A. Paulikas, D. Fong, M. Highland, P. Baldo, V. Stamenkovic, J. Freeland, J. Eastman and N. Markovic, "Functional links between stability and reactivity of strontium ruthenate single crystals during oxygen evolution," *Nat. Commun.*, vol. 5, p. 4191, 2014.
[254] T. Reier, M. Oezaslan and P. Strasser, "Electrocatalytic Oxygen Evolution Reaction (OER) on Ru, Ir, and Pt Catalysts: A Comparative Study of Nanoparticles and Bulk Materials," *ACS Catal.*, vol. 2, no. 8, pp. 1765-1772, 2012.
[255] S. Chang, J. Connell, N. Danilovic, R. Subbaraman, K.-C. Chang, V. Stamenkovic and N. Markovic, "Activity–Stability Relationship in the Surface Electrochemistry of the Oxygen Evolution Reaction," *Faraday Discuss.*, vol. 176, pp. 125-133, 2014.
[256] H. Nong, T. Reier, H. Oh, M. Gliech, P. Paciok, T. Vu, D. Teschner, M. Heggen, V. Petkov, R. Schlögl, T. Jones and P. Strasser, "A Unique Oxygen Ligand Environment Facilitates Water Oxidation in Hole-Doped IrNiOx Core–Shell Electrocatalysts," *Nat. Catal.*, vol. 1, pp. 841-851, 2018.
[257] O. Kasian, T. Li, A. Mingers, K. Schweinar, A. Savan, A. Ludwig and K. Mayrhofer, "Stabilization of an Iridium Oxygen Evolution Catalyst by Titanium Oxides," *J. Phys. Energy*, vol. 3, no. 3, p. 034006, 2020.
[258] I. Katsounaros, J. C. Meier, S. O. Klemm, A. A. Topalov, P. U. Biedermann, M. Auinger and K. J. J. Mayrhofer, "The Effective Surface PH during Reactions at the Solid-Liquid Interface," *Electrochem. Commun.*, vol. 13, no. 6, pp. 634-637, 2011.
[259] V. Trieu, B. Schley, H. Natter, J. Kintrup, A. Bulan and R. Hempelmann, "RuO 2-Based Anodes with Tailored Surface Morphology for Improved Chlorine Electro-Activity," *Electrochim. Acta*, vol. 78, pp. 188-194, 2012.
[260] J. Li, Y. Zhu, W. Chen, Z. Lu, J. Xu, A. Pei, Y. Peng, X. Zheng, Z. Zhang, S. Chu and Y. Cui, "Breathing-mimicking electrocatalysis for oxygen evolution and reduction," *Joule*, vol. 3, no. 2, pp. 557-569, 2019.
[261] A. Scheuermann, J. Prange, M. Gunji, C. Chidsey and P. McIntyre, "Effects of Catalyst Material and Atomic Layer Deposited TiO2 Oxide Thickness on the Water Oxidation Performance of Metal-Insulator-Silicon Anodes," *Energy Environ. Sci.*, vol. 6, pp. 2487-2496, 2013.
[262] C. Gebauer, P. Fischer, M. Wassner, T. Diemant, Z. Jusys, N. Hüsing and R. Behm, "Performance of Titanium Oxynitrides in the Electrocatalytic Oxygen Evolution Reaction," *Nano Energy*, vol. 29, pp. 136-148, 2016.

[263] M. Hannula, H. Ali-Löytty, K. Lahtonen, E. Sarlin, J. Saari and M. Valden, "Improved Stability of Atomic Layer Deposited Amorphous TiO2 Photoelectrode Coatings by Thermally Induced Oxygen Defects," *Chem. Mater.*, vol. 30, no. 4, pp. 1199-1208, 2018.
[264] A. Marshall and R. Haverkamp, "Electrocatalytic Activity of IrO2-RuO2 Supported on Sb-Doped SnO2 Nanoparticles," *Electrochim. Acta*, vol. 55, no. 6, pp. 1978-1984, 2010.
[265] H.-S. Oh, H. Nong, T. Reier, M. Gliech and P. Strasser, "Oxide-Supported Ir Nanodendrites with High Activity and Durability for the Oxygen Evolution Reaction in Acid PEM Water Electrolyzers," *Chem. Sci.*, vol. 6, no. 6, pp. 3321-3328, 2015.
[266] G. Liu, J. Xu, Y. Wang and X. Wang, "An Oxygen Evolution Catalyst on an Antimony Doped Tin Oxide Nanowire Structured Support for Proton Exchange Membrane Liquid Water Electrolysis," *J. Mater. Chem. A*, vol. 3, no. 41, pp. 20791-20800, 2015.
[267] Y. Kamegaya, K. Sasaki, M. Oguri, T. Asaki, H. Kobayashi and T. Mitamura, "Improved Durability of Iridium Oxide Coated Titanium Anode with Interlayers for Oxygen Evolution at High Current Densities," *Electrochim. Acta*, vol. 40, no. 7, pp. 889-895, 1995.
[268] C. V. Pham, M. Buhler, J. Knoppel, M. Bierling, D. Seeberger, D. Escalera-Lopez, K. J. J. Mayrhofer, S. Cherevko and S. Thiele, "IrO2 coated TiO2 core-shell microparticles advance performance of low loading proton exchange membrane water electrolyzers," *Appl. Catal. B*, vol. 269, p. 118762, 2020.
[269] R. Fuentes, H. Colon-Mercado and M. Martinez-Rodriguez, "Pt-Ir/TiC Electrocatalysts for PEM Fuel Cell/Electrolyzer Process," *J. Electrochem. Soc.*, vol. 161, no. 1, pp. F77-F82, 2014.
[270] H. A. El-Sayed, A. Weiß, L. F. Olbrich, G. P. Putro and H. A. Gasteiger, "OER Catalyst Stability Investigation Using RDE Technique: A Stability Measure or an Artifact?," *J. Electrochem. Soc.*, vol. 166, no. 8, pp. F485-F464, 2019.
[271] P. Jovanovič, K. Stojanovski, M. Bele, G. Dražić, G. Koderman Podboršek, L. Suhadolnik, M. Gaberšček and N. Hodnik, "Methodology for Investigating Electrochemical Gas Evolution Reactions: Floating Electrode as a Means for Effective Gas Bubble Removal," *Anal. Chem.*, vol. 91, no. 16, pp. 10353-10356, 2019.
[272] M. Bele, P. Jovanovič, Z. Marinko, S. Drev, V. Simon Šelih, J. Kovač, M. Gaberšček, G. Koderman Podboršek, G. Dražić, N. Hodnik, A. Kokalj and L. Suhadolnik, "Increasing the Oxygen-Evolution Reaction Performance of Nanotubular Titanium Oxynitride-Supported Ir Nanoparticles by a Strong Metal–Support Interaction," *ACS Catal.*, vol. 10, no. 22, pp. 13688-13700, 2020.
[273] P. Jovanovič, N. Hodnik, F. Ruiz-Zepeda, I. Arčon, B. Jozinović, M. Zorko, M. Bele, M. Šala, V. S. Šelih, S. Hočevar and M. Gaberscek, "Electrochemical Dissolution of Iridium and Iridium Oxide Particles in Acidic Media: Transmission Electron Microscopy, Electrochemical Flow Cell Coupled to Inductively Coupled Plasma Mass Spectrometry, and X-ray Absorption Spectroscopy Study," *J. Am. Chem. Soc.*, vol. 139, no. 36, pp. 12837-12846, 2017.
[274] S. Geiger, O. Kasian, B. R. Shrestha, A. M. Mingers, K. J. J. Mayrhofer and S. Cherevko, "Activity and Stability of Electrochemically and Thermally Treated Iridium for the Oxygen Evolution Reaction," *J. Electrochem. Soc.*, vol. 163, no. 11, pp. F3132-F3138, 2016.
[275] N. Hodnik, P. Jovanovič, A. Pavlišič, B. Jozinović, M. Zorko, M. Bele, V. S. Šelih, M. Šala, S. Hočevar and M. Gaberšček, "New Insights into Corrosion of Ruthenium and Ruthenium Oxide Nanoparticles in Acidic Media," *J. Phys. Chem. C*, vol. 119, no. 18, pp. 10140-10147, 2015.
[276] L. Moriau, G. K. Podborsek, A. Surca, S. S. Parapari, M. Sala, U. Petek, M. Bele, P. Jovanovic, B. Genorio and N. Hodnik, "Enhancing Iridium Nanoparticles' Oxygen Evolution Reaction Activity and Stability by Adjusting the Coverage of Titanium

Oxynitride Flakes on Reduced Graphene Oxide Nanoribbons' Support," *Adv. Mater. Inter.*, vol. 8, no. 17, p. 2100900, 2021.
[277] S. D. Gates-Rector and T. N. Blanton, The Powder Diffraction File: a quality materials characterization database, Ed., Cambridge University Press, 2019.
[278] T. Zhang, S.-C. Li, W. Zhu, Z.-P. Zhang, J. Gu and Y.-W. Zhang, "Shape-tunable Pt–Ir alloy nanocatalysts with high performance in oxygen electrode reactions," *Nanoscale*, vol. 9, pp. 1154-1165, 2017.
[279] G. Buvat, M. Eslamibidgoli, A. Youssef, S. Garbarino, A. Ruediger, M. Eikerling and D. Guay, "Effect of IrO6 Octahedron Distortion on the OER Activity at (100) IrO2 Thin Film," *ACS Catal.*, vol. 10, no. 1, pp. 806-817, 2020.
[280] K. Stoerzinger, L. Qiao, M. Biegalski and Y. Shao-Horn, "Orientation-Dependent Oxygen Evolution Activities of Rutile IrO2 and RuO2," *J. Phys. Chem. Lett.*, vol. 5, no. 10, pp. 1636-1641, 2014.
[281] M. Bernicke, E. Ortel, T. Reier, A. Bergmann, J. F. D. Araujo, P. Strasser and R. Kraehnert, "Iridium Oxide Coatings with Templated Porosity as Highly Active Oxygen Evolution Catalysts: Structure-Activity Relationships," *ChemSusChem*, vol. 8, no. 11, pp. 1908-1915, 2015.
[282] J. Xu, Z. Lian, B. Wei, Y. Li, O. Bondarchuk, N. Zhang, Z. Yu, A. Araujo, I. Amorim, Z. Wang, B. Li and L. Liu, "Strong Electronic Coupling between Ultrafine Iridium–Ruthenium Nanoclusters and Conductive, Acid-Stable Tellurium Nanoparticle Support for Efficient and Durable Oxygen Evolution in Acidic and Neutral Media," *ACS Catal.*, vol. 10, no. 6, pp. 3571-3579, 2020.
[283] J. Zhang, H. Tao, M. Kuang, H. Yang, W. Cai, Q. Yan, Q. Mao and B. Liu, " Advances in Thermodynamic-Kinetic Model for Analyzing the Oxygen Evolution Reaction," *ACS Catal.*, vol. 10, no. 15, pp. 8597-8610, 2020.
[284] S. Anantharaj, S. Noda, M. Driess and P. Menezes, "The Pitfalls of Using Potentiodynamic Polarization Curves for Tafel Analysis in Electrocatalytic Water Splitting," *ACS Energy Lett.*, vol. 6, no. 4, pp. 1067-1611, 2021.
[285] T. Shinagawa, A. Garcia-Esparza and K. Takanabe, "Insight on Tafel slopes from a microkinetic analysis of aqueous electrocatalysis for energy conversion," *Sci. Rep.*, vol. 5, p. 13801, 2015.
[286] A. Jensen, G. Sievers, K. Jensen, J. Quinson, J. Arminio-Ravelo, V. Bruser, M. Arenz and M. Escudero-Escribano, "Self-supported nanostructured iridium-based networks as highly active electrocatalysts for oxygen evolution in acidic media," *J. Mater. Chem. A*, vol. 8, pp. 1066-1071, 2020.
[287] A. Loncar, D. Escalera-Lopez, S. Cherevko and N. Hodnik, "Inter-relationships between Oxygen Evolution and Iridium Dissolution Mechanisms.," *Angew. Chem. Int. Ed.*, vol. 61, no. 14, p. e202114437, 2022.
[288] A. Hartig-Weib, M. F. Tovini, H. Gasteiger and H. El-Sayed, "OER Catalyst Durability Tests Using the Rotating Disk Electrode Technique: The Reason Why This Leads to Erroneous Conclusions," *ACS Appl. Energy Mater.*, vol. 3, no. 11, pp. 10323-10327, 2020.
[289] M. F. Tovini, A. Hartig-Weib, H. Gasteiger and H. El-Sayed, "The Discrepancy in Oxygen Evolution Reaction Catalyst Lifetime Explained: RDE vs MEA - Dynamicity within the Catalyst Layer Matters," *J. Electrochem. Soc.*, vol. 168, no. 1, p. 014512, 2021.
[290] B. Avasarala and P. Haldar, "Electrochemical oxidation behavior of titanium nitride based electrocatalysts under PEM fuel cell conditions," *Electrochim. Acta*, vol. 55, no. 28, pp. 9024-9034, 2010.
[291] P. Jovanovic, A. Pavlišič, V. Selih, M. Šala, N. Hodnik, M. Bele, S. Hočevar and M. Gaberšček, "New Insight into Platinum Dissolution from Nanoparticulate Platinum-

Based Electrocatalysts Using Highly Sensitive In Situ Concentration Measurements," *ChemCatChem*, vol. 6, no. 2, pp. 449-453, 2014.
[292] Y. Shao-Horn, W. Sheng, S. Chen, P. Ferreira, E. Holby and D. Morgan, "Instability of Supported Platinum Nanoparticles in Low-Temperature Fuel Cells," *Top. Catal.*, vol. 46, pp. 285-305, 2007.
[293] S. Cherevko, S. Geiger, O. Kasian, A. Mingers and K. Mayrhofer, "Oxygen evolution activity and stability of iridium in acidic media. Part 2. – Electrochemically grown hydrous iridium oxide," *J. Electroanal. Chem.*, vol. 774, pp. 102-110, 2016.
[294] S. Cherevko, T. Reier, A. Zeradjanin, Z. Pawolek, P. Strasser and K. Mayrhofer, "Stability of nanostructured iridium oxide electrocatalysts during oxygen evolution reaction in acidic environment," *Electrochem. Commun.*, vol. 48, pp. 81-85, 2014.
[295] O. Kasian, J.-P. Grote, S. Geiger, S. Cherevko and K. Mayrhofer, "The Common Intermediates of Oxygen Evolution and Dissolution Reactions during Water Electrolysis on Iridium," *Angew. Chem. Int. Ed.*, vol. 57, no. 9, pp. 2488-2491, 2018.
[296] L. Moriau, M. Bele, A. Vizintin, F. Ruiz-Zepeda, U. Petek, P. Jovanovic, M. Sala, M. Gaberscek and N. Hodnik, "Synthesis and advanced electrochemical characterization of multifunctional electrocatalytic composite for unitized regenerative fuel cell," *ACS Catal.*, vol. 9, no. 12, pp. 11468-11483, 2019.
[297] E. Antolini, "Iridium As Catalyst and Cocatalyst for Oxygen Evolution/Reduction in Acidic Polymer Electrolyte Membrane Electrolyzers and Fuel Cells," *ACS Catal.*, vol. 4, no. 5, pp. 1426-1440, 2014.
[298] S. Zhigang, Y. Baolian and H. Ming, "Bifunctional Electrodes with a Thin Catalyst Layer for Unitized Proton Exchange Membrane Regenerative Fuel Cell," *J. Power Sources*, vol. 79, no. 1, pp. 82-85, 1999.
[299] T. Ioroi, N. Kitazawa, K. Yasuda, Y. Yamamoto and H. Takenaka, "Iridium Oxide/Platinum Electrocatalysts for Unitized Regenerative Polymer Electrolyte Fuel Cells," *J. Electrochem. Soc.*, vol. 147, no. 6, pp. 2018-2022, 2000.
[300] H.-Y. Jung, S. Park and B. N. Popov, "Electrochemical Studies of an Unsupported PtIr Electrocatalyst as a Bifunctional Oxygen Electrode in a Unitized Regenerative Fuel Cell," *J. Power Sources*, vol. 191, no. 2, pp. 357-361, 2009.
[301] G. C. da Silva, M. R. Fernandes and E. A. Ticianelli, "Activity and Stability of Pt/IrO2 Bifunctional Materials as Catalysts for the Oxygen Evolution/Reduction Reactions," *ACS Catal.*, vol. 8, no. 3, pp. 2081-2092, 2018.
[302] G. C. da Silva, K. J. J. Mayrhofer, E. Ticianelli and S. Cherevko, "The Degradation of Pt/IrOx Oxygen Bifunctional Catalysts," *Electrochim. Acta*, vol. 308, pp. 400-409, 2019.
[303] F.-D. Kong, S. Zhang, G.-P. Yin, J. Liu and A.-X. Ling, "A Facile Route to Fabricate Effective Pt/IrO2 Bifunctional Catalyst for Unitized Regenerative Fuel Cell," *Catal. Lett.*, vol. 144, pp. 242-247, 2014.
[304] Y. Zhang, H. Zhang, Y. Ma, J. Cheng, H. Zhong, S. Song and H. Ma, "A Novel Bifunctional Electrocatalyst for Unitized Regenerative Fuel Cell," *J. Power Sources*, vol. 195, no. 1, pp. 142-145, 2010.
[305] T. Ioroi, N. Kitazawa, K. Yasuda, Y. Yamamoto and H. Takenaka, "IrO2-deposited Pt Electrocatalysts for Unitized Regenerative Polymer Electrolyte Fuel Cells," *J. Appl. Electrochem.*, vol. 31, pp. 1179-1183, 2001.
[306] V. Baglio, C. D'Urso, A. Di Blasi, R. Ornelas, L. G. Arriaga, V. Antonucci and A. S. Arico, "Investigation of IrO2/Pt Electrocatalysts in Unitized Regenerative Fuel Cells," *Int. J. Electrochemistry*, vol. 2011, p. 276205, 2011.
[307] F. Ye, C. Xu, G. Liu, J. Li, X. Wang, X. Du and J. K. Lee, "A Novel PtRuIr Nanoclusters Synthesized by Selectively Electrodepositing Ir on PtRu as Highly Active

Bifunctional Electrocatalysts for Oxygen Evolution and Reduction," *Energy Convers. Manag.*, vol. 155, pp. 182-187, 2018.
[308] C. Gutsche, C. J. Moeller, M. Knipper, H. Borchert, J. Parisi and T. Plaggenborg, "Synthesis, Structure, and Electrochemical Stability of Ir-decorated RuO2 Nanoparticles and Pt Nanorods as Oxygen Catalysts," *J. Phys. Chem. C*, vol. 120, no. 2, pp. 1137-1146, 2016.
[309] M. Watanabe, M. Uchida and S. Motoo, "Preparation of Highly Dispersed Pt + Ru Alloy Clusters and the Activity for the Electrooxidation of Methanol," *J. Electroanal. Chem. Interfacial Electrochem.*, vol. 229, no. 1-2, pp. 395-406, 1987.
[310] P. Joghee, J. Malik, S. Pylypenko and R. O'Hayre, "A review on direct methanol fuel cells–In the perspective of energy and sustainability," *MRS Energy & Sustainability*, vol. 2, p. e3, 2015.
[311] J. Hutchinson, "Solubility Relationships in the Ruthenium-Platinum System," *Platinum Met. Rev.*, vol. 16, no. 3, pp. 88-90, 1972.
[312] T. Massalski, H. Okamoto, P. Subramanian and L. Kacprzak, Binary Alloy Phase Diagrams, Ohio: ASM International, 1990.
[313] J. Masa, W. Xia, I. Sinev, A. Zhao, Z. Sun, S. Grutzke, P. Weide, M. M. and W. Schuhmann, "Mn(x)O(y)/NC and Co(x)O(y)/NC Nanoparticles Embedded in a Nitrogen-doped Carbon Matrix for High-performance Bifunctional Oxygen Electrodes," *Angew. Chem. Int. Ed.*, vol. 53, no. 32, pp. 8508-8512, 2014.
[314] F. D. Kong, J. Liu, A. X. Ling, Z. Q. Xu, M. J. Shi, Q. S. Kong and H. Y. Wang, "Overlapping Structure of Platinum-Iridium Oxide Layers and its Electrocatalytic Behavior on Bifunctional Oxygen Electrode," *Catal. Commun.*, vol. 90, pp. 19-22, 2017.
[315] G. C. da Silva, K. J. J. Mayrhofer, E. A. Ticianelli and S. Cherevko, "Dissolution Stability: The Major Challenge in the Regenerative Fuel Cells Bifunctional Catalysis," *J. Electrochem. Soc.*, vol. 165, no. 16, pp. F1376-F1384, 2018.
[316] I. G. Kim, I. W. Nah, I.-H. Oh and S. Park, "Crumpled rGO-supported Pt-Ir Bifunctional Catalyst Prepared by Spray Pyrolysis for Unitized Regenerative Fuel Cells," *J. Power Sources*, vol. 364, pp. 215-225, 2017.
[317] S.-Y. Huang, P. Ganesan, H.-Y. Jung and B. N. Popov, "Development of Supported Bifunctional Oxygen Electrocatalysts and Corrosion-Resistant Gas Diffusion Layer for Unitized Regenerative Fuel Cell Applications," *J. Power Sources*, vol. 198, pp. 23-29, 2012.
[318] B.-S. Lee, H.-Y. Park, M. Cho, J. W. Jung, H.-J. Kima, D. Henkensmeier, S. J. Yoo, J. Y. Kim, S. Park, K.-Y. Lee and J. Jang, "Development of Porous Pt/IrO2/Carbon Paper Electrocatalysts with Enhanced Mass Transport as Oxygen Electrodes in Unitized regenerative fuel cells," *Electrochem. Commun.*, vol. 64, pp. 14-17, 2016.
[319] S. Cherevko, "Electrochemical Dissolution of Noble Metals Native Oxides," *J. Electroanal. Chem.*, vol. 787, pp. 11-13, 2017.
[320] S. Siracusano, N. Hodnik, P. Jovanovic, F. Ruiz-Zepeda, M. Šala, V. Baglio and A. S. Aricò, "New insights into the Stability of a High-Performance Nanostructured Catalyst for Sustainable Water Electrolysis," *Nano Energy*, vol. 40, pp. 618-632, 2017.
[321] D. Strmcnik, M. Uchimura, C. Wang, R. Subbaraman, N. Danilovic, D. van der Vliet, A. P. Paulikas, V. R. Stamenkovic and N. M. Markovic, "Improving the Hydrogen Oxidation Reaction Rate by Promotion of Hydroxyl Adsorption," *Nat. Chem.*, vol. 5, pp. 300-306, 2013.
[322] S. Cherevko, S. Geiger, O. Kasian, N. Kulyk, J.-P. Grote, A. Savan, B. R. Shrestha, S. Merzlikin, B. Breitbach, A. Ludwig and K. J. J. Mayrhofer, "Oxygen and Hydrogen Evolution Reactions on Ru, RuO2, Ir, and IrO2 Thin Film Electrodes in Acidic and alkaline electrolytes: a comparative study on activity and stability," *Catal. Today*, vol. 262, pp. 170-180, 2016.

Bibliography

Publications Related to the Thesis

L. Moriau, A. Hrnjic, A. Pavlisic, A. Kamsek, U. Petek, F. Ruiz-Zepeda, M. Sala, L. Pavko, V. Selih, M. Bele, P. Jovanovic, M. Gatalo and N. Hodnik, "Resolving the nanoparticles' structure-property relationships at the atomic level: a study of Pt-based electrocatalysts," *iScience*, vol. 24, no. 2, p. 102102, 2021.

M. Bele, K. Stojanovski, P. Jovanovic, L. Moriau, G. K. Podborsek, J. Moskon, P. Umek, M. Sluban, G. Drazic, N. Hodnik and M. Gaberscek, "Towards stable and conductive Titanium oxynitride high surface area support for Iridium nanoparticles as OER electrocatalysts," *ChemCatChem*, vol. 11, no. 20, pp. 5038-5044, 2019.

L. Moriau, M. Bele, Z. Marinko, F. Ruiz-Zepeda, G. K. Podboršek, M. Šala, A. Šurca, J. Kovač, I. Arčon, P. Jovanovič, N. Hodnik and L. Suhadolnik, "Effect of the Morphology of the High-Surface-Area Support on the Performance of the Oxygen-Evolution Reaction for Iridium Nanoparticles," *ACS Catal.*, vol. 11, no. 2, pp. 670-681, 2021.

L. Moriau, G. K. Podborsek, A. Surca, S. S. Parapari, M. Sala, U. Petek, M. Bele, P. Jovanovic, B. Genorio and N. Hodnik, "Enhancing Iridium Nanoparticles' Oxygen Evolution Reaction Activity and Stability by Adjusting the Coverage of Titanium Oxynitride Flakes on Reduced Graphene Oxide Nanoribbons' Support," *Adv. Mater. Inter.*, vol. 8, no. 17, p. 2100900, 2021.

L. Moriau, M. Bele, A. Vizintin, F. Ruiz-Zepeda, U. Petek, P. Jovanovic, M. Sala, M. Gaberscek and N. Hodnik, "Synthesis and advanced electrochemical characterization of multifunctional electrocatalytic composite for unitized regenerative fuel cell," *ACS Catal.*, vol. 9, no. 12, pp. 11468-11483, 2019.

Other Publications

M. Gatalo, L. Moriau, U. Petek, F. Ruiz-Zepeda, M. Šala, M. Grom, T. Galun, P. Jovanovič, A. Pavlišič, M. Bele, N. Hodnik and M. Gaberšček, "CO-assisted ex-situ chemical activation Pt-Cu/C oxygen reduction reaction electrocatalyst," *Electrochim. Acta*, vol. 306, pp. 377-386, 2019.

D. Menga, F. Ruiz-Zepeda, L. Moriau, M. Šala, F. Wagner, B. Koyuturk, M. Bele, U. Petek, M. Gaberšček and T.-P. Fellinger, "Active-site imprinting: preparation of Fe-N-C catalysts from zinc ion-templated ionothermal nitrogen-doped carbons," *Adv. Energy Mater.*, vol. 9, no. 43, pp. 1902412, 2019.

A. Lončar, L. Moriau, K. Stojanovski, F. Ruiz-Zepeda, P. Jovanovič, M. Bele, M. Gaberšček and N. Hodnik, "Ir/TiONx/C high-performance oxygen evolution reaction nanocomposite electrocatalysts in acidic media: synthesis, characterization and electrochemical benchmarking protocol," *JPhys. Energy*, vol. 2, no. 2, pp. 02LT01, 2020.

A. Hrnjic, A.R. Kamšek, A. Pavlišič, M. Šala, M. Bele, L. Moriau, M. Gatalo, F. Ruiz-Zepeda, P. Jovanovič and N. Hodnik, "Observing, tracking and analysing electrochemically induced atomic-scale structural changes of an individual Pt-Co nanoparticle as fuel cell electrocatalyst by combining modified floating electrode and identical location electron microscopy," *Electrochim. Acta*, vol. 388, pp. 138513, 2021.

M. Smiljanić, M. Bele, L. Moriau, F. Ruiz-Zepeda, M. Šala and N. Hodnik, "Electrochemical stability and degradation of commercial Pd/C catalyst in acidic media," *J. Phys. Chem. C.*, vol. 125, no. 50, pp. 27534-27542, 2021.

T. Đukić, L. Moriau, L. Pavko, M. Kostelec, M. Prokop, F. Ruiz-Zepeda, M. Šala, G. Dražić, M. Gatalo and N. Hodnik, "Understanding the crucial significance of the temperature and potential window on the stability of carbon supported Pt-alloy nanoparticles as oxygen reduction reaction electrocatalysts," *ACS Catal.*, vol. 12, no. 1, pp. 101-115, 2021.

M. Smiljanic, M. Bele, L. Moriau, J. Velez Santa, S. Menart, M. Sala, A. Hrnjic, P. Jovanovic, F. Ruiz-Zepeda, M. Gaberscek and N. Hodnik, "Suppressing platinum electrocatalyst degradation via a high-surface-area organic matrix support," *ACS Omega*, vol. 7, no. 4, pp. 3540-3548, 2022.

L. Moriau, M. Smiljanić, A. Lončar and N. Hodnik, "Supported iridium-based oxygen evolution reaction electrocatalysts – recent developments", *ChemCatChem*, pp. e202200586, 2022.

Biography

I was born on the 20th of April 1992 in Brussels, Belgium. After finishing elementary (Sept Bonnier, Forest) and secondary schools (Athénée Charles Janssens, Ixelles) which resulted in a high school diploma, options Latin-Science-Mathematics, I enrolled in the Chemistry science section of Université Libre de Bruxelles in 2010. In 2013, I finished my Bachelor degree with honours followed up by a Master degree with honours in 2015.

During my Master degree, I had the opportunity to do a four-month internship in research and development at Cardiatis (www.cardiatis.com). There, I focused on organic treatment of a multilayer flow modulator. This technology is meant to prevent aneurysm and is composed of metal alloys. To prevent any contamination, its surface needs to be covered with bio-compatible material. On the other hand, my Master thesis, under the supervision of Prof. Thomas Doneux, was focused on the modification of gold electrodes by a diazonium calixarene in order to immobilize a peptide aptamer. The modified electrode could then be used as a biosensor for Mdm2 protein, present in some cancers.

After my study, I took one year to travel around Europe as a volunteer as well as working as a judo teacher in my childhood club (20 years of judo training, black belt) when I was in Belgium. It is during this volunteering period that I travelled first to Slovenia and met the people of the National Institute of Chemistry of Slovenia.

The year after I worked there for a few months as a fellow expert (June to September 2017) at the Department of Catalysis and Chemical Reaction Engineering (National Institute of Chemistry of Slovenia) before officially starting my Ph.D. under the supervision of Prof. Nejc Hodnik on the topic of fuel cell and electrolyzer reactions.

During my Ph.D., I successfully published several articles which are listed above and currently cited 182 times, resulting in a h-index of 8 (Google Scholar).